# Towards Stable Perovskite Materials for Photovoltaics


Rebecca Jane Sutton

St Edmund Hall

University of Oxford

A thesis submitted in fulfilment of the requirements for the degree of

*Doctor of Philosophy*

August 2018

# Towards Stable Perovskite Materials for Photovoltaics

Rebecca J. Sutton, St Edmund Hall

A thesis submitted in fulfilment of the requirements for the degree of Doctor of Philosophy at the University of Oxford, Trinity Term, 2018.

## Abstract

This thesis explores a range of photoactive metal halide perovskite materials for use in photovoltaic applications. These materials are of huge interest due to their outstanding optoelectronic properties which result in high photovoltaic power conversion efficiencies. In particular, this thesis discusses perovskites with stoichiometry $ABX_3$ where A is a singly charged cation, for example methylammonium (MA), B is predominantly lead ($Pb^{2+}$), and X is iodide ($I^-$) and/or bromide ($Br^-$). At present the commercial applications of these materials are limited by the chemical instability of the A-site cation. In this thesis, the effect of chemical substitution of the A-site is investigated as a way to increase the stability of the perovskite material. Full replacement with the inorganic cation caesium ($Cs^+$) is shown to significantly improve the chemical stability. However, the inorganic lead halide perovskites with ideal bandgaps for photovoltaic applications exhibit structural instability. Routes to achieve both chemical and structural stability for these perovskites are discussed. Consequently, this thesis represents pioneering work in the field of inorganic halide perovskites and will greatly assist the development of stable inorganic perovskite materials for optoelectronic applications such as tandem photovoltaics and LEDs.

Chapters 1 and 2 of this thesis present the motivation for perovskite materials to be used in solar cells, along with relevant background information about these materials and solar cell operation in general. Chapter 3 details the methods utilised in the experimental results chapters which follow. The first experimental results chapter, Chapter 4, shows how incorporation of $Br^-$ in place of $I^-$ in $CsPbI_3$ leads to increased ambient stability of the perovskite structure, and the first solar cells with $CsPbI_2Br$ as the absorbing photovoltaic material are reported. Chapter 5 remedies the deficit of information about the optoelectronic properties of the $CsPbI_{3-x}Br_x$ ($0 \leq x \leq 3$) perovskites through magneto-optical measurements on thin-films. These measurements raise questions about the room temperature perovskite structure of the $CsPbI_{3-x}Br_x$ compositions with small $x$, previously thought to be a cubic perovskite, which is shown in Chapter 6 to be an orthorhombic perovskite polymorph. This finding motivates preliminary work presented in Chapter 7 aimed at chemical stabilisation of this orthorhombic perovskite polymorph. Finally, Chapter 8 summarises the work presented in this thesis, and recommends further research for the development of stable perovskite materials for photovoltaics.

# Acknowledgements

First, I would like to thank God for creating a world in which perovskites exist, and for providing an abundance of solar energy to motivate this research.

My thanks are also due to the Commonwealth Scholarship Commission, for making this opportunity possible.

A huge thank you to Professor Henry Snaith, FRS, for taking me on as a young scientist with no prior experience in photovoltaics. You certainly challenged me with the task of stabilising the inorganic perovskites. Your vision and never-ending enthusiasm are powerful inspiration for scientists both young and old.

To the numerous 'Snaithlings' past and present, I am indebted to you all. Particular thanks go to my key advisors Giles Eperon, Dave Moore, Amir Abbas Haghighirad and Nobuya Sakai. Special thanks to Golnaz Sadoughi, Rui Sheng, Olivia Ashton, Martina Congiu, Nakita Noel, and Alex Ramadan. Your encouragement and friendship countered the toughest of days. Thanks also to my collaborators in the Herz, Johnston, Nicholas, and Riede groups, and to Laura Miranda, Eline Hutter and Tom Savenije, and Paulina Plochocka and team.

Thanks always to my family and friends outside of the perovskite community for your love and care. Special thanks to my parents, for piquing my curiosity from day one, inspiring me to set lofty goals and supporting me to achieve them. To Emily, thanks for always keeping us laughing. You're the best sister ever. To my old friends Michelle, Jessica, and Teresa, what would we do without Skype?! Your stories have always brightened my day. To my new friends and neighbours in Oxford, you've made life in Summertown House such fun.

And last but not least, to my husband, Aaron Hawke, for enabling this journey, for keeping life in perspective, and for making each year more awesome than the last.

# Contents

# List of Abbreviations and Acronyms

| Abbreviation or Acronym | Definition |
|---|---|
| AM1.5G | The spectrum used as a laboratory standard for determining the PCE of a solar cell. This 'global spectrum' represents the incident sunlight expected on a solar cell at ground level. |
| CB | Conduction Band |
| DFT | Density Functional Theory |
| DMF | N,N-dimethylformamide |
| DMSO | Dimethyl sulfoxide |
| EDX | Electron Dispersive X-ray |
| $E_F$ | Fermi level |
| $E_G$ | The bandgap energy of a material (the energy difference between the CB and the VB) |
| EQE | External Quantum Efficiency |
| $E_X$ | Exciton binding energy |
| FA | Formamidinium, $NH_2CHNH_2^+$ |
| FF | Fill Factor |
| FTO | Fluorine-doped Tin Oxide |
| FWHM | Full Width Half Maximum |
| GIWAXS | Grazing-Incidence Wide-Angle X-ray Scattering |
| $GW$ | The $GW$ approximation is so named because the electron self energy is the convolution between the electron Green's function, $G$, and the screened Coulomb interaction, $W$. |
| HI | Hydriodic acid |
| HS | High spin |
| HT | High Temperature (here >300 °C) |
| HTM or HTL | Hole-Transporting Material or Layer |
| $J_{MPP}$ | The current density generated at the maximum power point (See $V_{MPP}$) |
| $J_{SC}$ | Short-circuit current density |
| LDA | Local Density Approximation |

| | |
|---|---|
| LNCMI | Laboratoire National des Champs Magnétiques Intenses |
| LT | Low Temperature (here <150 °C) |
| MA | Methylammonium, $CH_3NH_3^+$ |
| PBE | The generalised gradient approximation |
| PCE | Power Conversion Efficiency (see also $\eta$) |
| PL | Photoluminescence |
| PTFE | Polytetrafluoroethylene |
| PV | Photovoltaic |
| RH | Relative Humidity |
| SEM | Scanning Electron Microscope |
| Spiro-OMeTAD | 2,2′,7,7′-Tetrakis(*N,N*-di-*p*-methoxyphenylamine)-9,9′-spirobifluorene, a small organic molecule commonly used as a HTM |
| Spiro-TFSI | 2,2′,7,7′-tetrakis(*N,N*-di-*p*-methoxyphenylamine)-9,9′-spirobifluorene di[bis(trifluoromethanesulfonyl)imide]; Spiro-OMeTAD oxidised with the TFSI salt |
| SPO | Stabilised Power Output |
| SQUID | Superconducting QUantum Interference Device, a magnetometer used to determine magnetic properties of a material from cryogenic temperatures to room temperature |
| UV | Ultra-Violet |
| VB | Valence Band |
| VESTA | Visualisation for Electronic and STructural Analysis, a 3D visualization program for structural models, volumetric data such as electron/nuclear densities, and crystal morphologies |
| $V_{MPP}$ | The operating voltage of a solar cell at which maximum power output is obtained |
| $V_{OC}$ | Open-circuit voltage |
| XRD | X-ray Diffraction |
| ZFC | Zero-Field-Cooled, i.e. cooled in the absence of a magnetic field |
| $\eta$ | Photovoltaic efficiency (see also PCE) |

# 1 Introduction

## 1.1 Context and motivation

With increasing global demand for energy, dwindling fossil fuel reserves, and an increasingly unpredictable climate, the need for efficient renewable energy sources has become paramount. Global energy consumption has more than doubled over the last forty years, and in 2015 was approximately 18.5 TWy/y (Terawatt years per year).[1] The U.S. Energy Information Administration predicts that global energy demand will increase by nearly 30% between 2015 and 2040.[2]

While coal, natural gas, and oil are convenient and widely used energy sources, their known reserves are finite, and they all produce carbon dioxide ($CO_2$) and other greenhouse gases as by-products of combustion. In 2015, coal, natural gas, and oil provided more than 80% of the world's total primary energy supply, and global $CO_2$ emissions from these fuel sources surpassed 32,000 million tonnes.[3] With the projected increase in global energy demand, world energy-related $CO_2$ emissions are also predicted to grow an average 0.6% per year between 2015 and 2040.[2]

The greenhouse effects of continued $CO_2$ emissions are already evident, with changing weather patterns and an increase in extreme weather events as the average global temperature rises.[4] In an attempt to halt global warming from the

 

greenhouse effect, the Kyoto Protocol and Paris climate agreements demand a reduction of global $CO_2$ emissions.[5]

To meet global energy demands and to reduce energy-related $CO_2$ emissions, sources of energy other than fossil fuels are urgently needed as the main provider of both domestic and industrial power. The available sources of energy are depicted graphically in Figure 1-1, in a three-dimensional rendering. Renewable energy sources, and nuclear energy sources such as uranium, are usually considered low-carbon energy sources.[6] While carbon capture and storage reduces energy-related $CO_2$ emissions from fossil fuel energy generation, this solution is only temporary due to finite fossil fuel reserves.

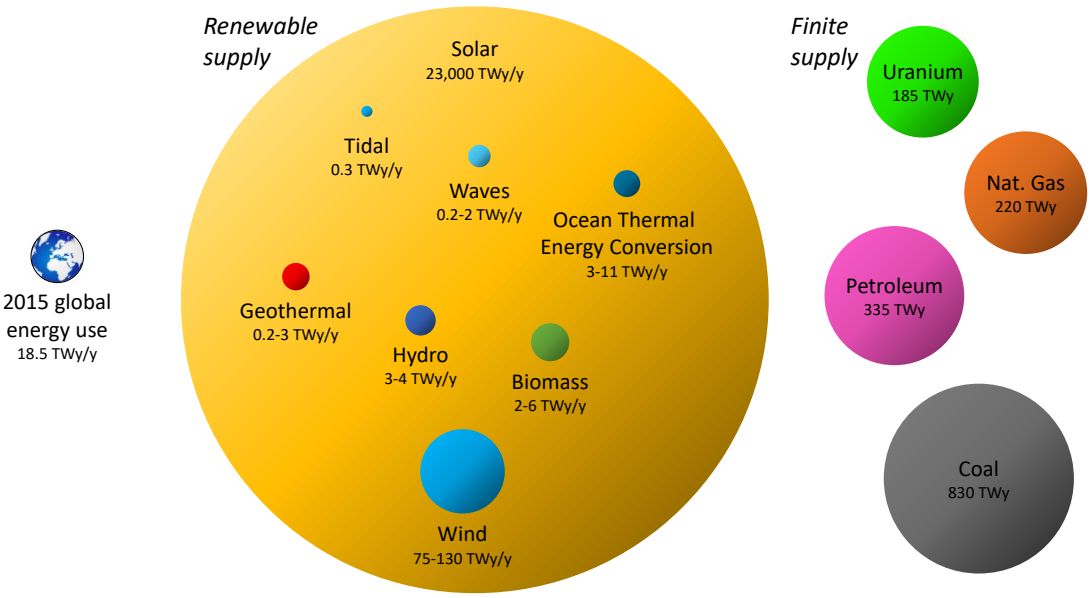


**Figure 1-1. Sources of energy in Terawatt-years (TWy) in comparison to the total energy used globally in 2015, using a three-dimensional rendering. The volume of each sphere represents either the yearly potential energy (renewable energy sources), or the estimated total recoverable energy remaining in 2015 (finite energy sources). Adapted from Perez and Perez, 2015.[1]**

Of the renewable energy sources, the most abundant is solar energy. As can be seen in Figure 1-1, solar energy dwarfs all other sources of energy, with a staggering 23,000 TWy/y incident on land globally.[1]

To harness solar energy in a useable way, we can use photovoltaic (PV) devices such as solar panels (also known as PV modules). Solar panels contain many individual solar cells, each of which converts light from the sun into electricity or heat. Each solar cell contains a sandwich-like junction with at least two layers of different materials, as depicted schematically in Figure 1-2. When illuminated, solar panels can generate enough electricity to power electrical devices from mobile phones to electric cars, and arrays of solar panels can power office buildings and factories.

Present solar panel technology is dominated by silicon photovoltaics, which are becoming increasingly inexpensive to produce and install. In June 2016, the Dubai

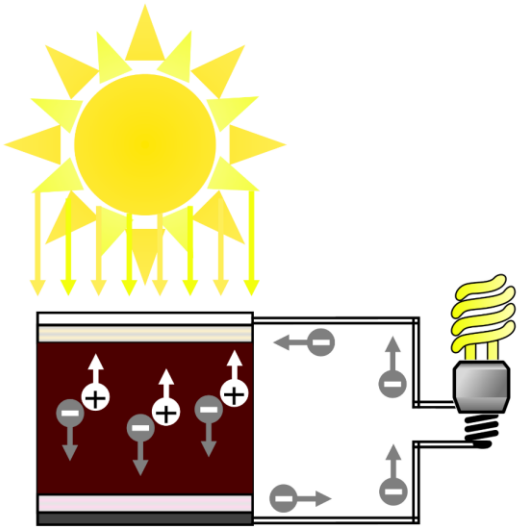

**Figure 1-2. A single junction solar cell. Solar energy is absorbed by a semiconducting material (brown layer), which is sandwiched between layers of other semiconductors (pink and yellow layers). The sunlight creates pairs of free electrons (grey circles) and positive holes (white circles). These charges are collected by the negative (dark grey) or positive (white) electrodes respectively. When an illuminated solar cell is connected to a circuit, current flows which can be used to power devices such as lightbulbs.**

 

Electricity and Water Authority announced plans to build an 800-megawatt solar power plant which would produce electricity at less than 3 U.S. cents per kilowatt hour on average, which is less expensive than coal.[7] With such investment, the World Economic Forum predicts that solar photovoltaic infrastructure will have a lower levelized cost of electricity* than coal or natural gas electricity generation throughout the world by 2020.[8] This cost parity makes solar energy an economically viable option for global energy production.

For solar to supply the global energy demand, there must be enough land available for the solar panels. Based on the U.S. Energy Information Administration's predictions, it has been postulated that solar energy could power the entire world in 2030 with approximately 500,000 $km^2$ of solar panels generating around 200,000 TWh per year.[2,9] This area is calculated assuming each solar panel has an operational solar to electric power conversion efficiency of 20%, and experiences 250 sun days per year with 8 hours of 1000 W $m^{-2}$ irradiation on average. A visualisation of this area of solar panels is provided in Figure 1-3; while this area is roughly the area of Spain, it is only 0.4% of the total global land mass and would include rooftop and building-integrated PV installations.[10] However, this area does not take into account other land area required for installations, for example to avoid shading on a solar farm or for batteries for energy storage.

The required area of solar panels for a given energy generation decreases as the solar to electrical power conversion efficiency (PCE) of the solar panels increases. Most of the cost of solar panels comes from assembly and installation, so a small increase in efficiency leads to a reduced overall cost as well as increasing the potential applications of the solar panels.[11,12]

*The levelized cost of electricity is the total cost of building and operating an energy-generating plant, divided by the total energy output, over the lifetime of the plant.

 

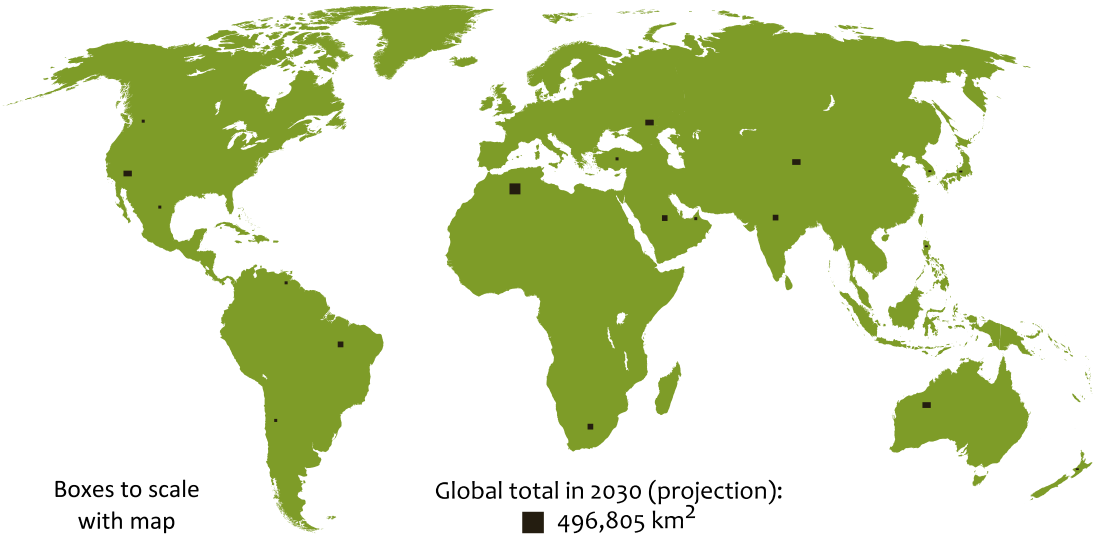


**Figure 1-3. A depiction of the projected surface area of solar panels that would be required to power the world in 2030 using solar energy alone (not including land area for energy storage). Nineteen areas have been distributed across the globe in proportions based on 2009 energy usage, with a total area of 496,805 km$^2$; in practice these areas would be further divided into many installations of various sizes in each country. Adapted from the Land Art Generator Initiative (http://landartgenerator.org).[9]**

While 20% efficiency is a reasonable expectation for a solar panel, and solar panels with efficiencies of ~20% PCE are becoming widespread, there remains much scope for improvement. The efficiency of a single junction solar cell has a theoretical limit of about 33% PCE, known as the Shockley-Queisser limit.[13] Typical silicon solar panels have efficiencies of 20-25%, and the best research-lab silicon solar cells have reached up to 27% power conversion efficiency.[14] However, the single junction silicon solar cell has been intensively developed, and so further improvements in efficiencies of the incumbent technology are limited.

In order to improve the efficiency of solar panels, attention has turned to new materials that are as abundant and as inexpensive as silicon, and work at least as efficiently in solar cells. These new materials may then be used as single junction solar cells to replace silicon, or they can be used in tandem with silicon in multi-junction solar cells.

 

Competitors on efficiency are thin films of inorganic materials such as GaAs, GaInP, GaInAs, and Ge. In early 2018, GaAs holds the record efficiency for a single junction solar cell of about 28%,[15] and multi-junction devices with these materials have reached efficiencies of about 39%.[14] However, the starting materials are expensive and the devices require many processing steps in high vacuum environments which limits their widespread use in solar panels.

Less expensive alternatives include organic small molecules and polymers, and quantum dots of materials such as PbS or PbSe[16,17]. These materials can be easily made into thin films by solution processing methods, such as spin-coating, blade coating or inkjet printing, which allows fast deposition on a large scale for both rigid and flexible substrates. By themselves, these materials yield colourful and light-weight solar panels which are ideal for niche applications where traditional silicon panels are unsuitable. Present efficiencies of these devices are approaching 15%.[14]

Recently another class of solar cells, known as perovskite solar cells, has emerged as an extremely promising competitor to the above technologies, meeting both criteria of low cost and high efficiency. Perovskite solar cells use thin films of metal halide perovskite materials in place of silicon. Perovskite thin films can be made from inexpensive and abundant precursor salts using standard processing techniques such as solution processing or vapour deposition.

As well as being inexpensive to produce, perovskite thin films have many ideal properties for photovoltaics. For example, a thin perovskite film absorbs sunlight strongly, with nearly complete light absorption in films as thin as 300-500 nm in thickness.[18,19] Despite the polycrystalline nature of the films, the absorbed light generates a high proportion of free electrons which are efficiently transported through the film, such that films as thick as 1.2 µm can function in solar cells.[19,20]

 

Perovskite solar cells are now the most efficient thin-film photovoltaic technology. Lead halide perovskites were first reported in solar cells in 2009, at 3.8% power conversion efficiency,[21] and intense research into these materials over the last few years has led to research cell efficiencies as high as 22.7%.[22] Single junction perovskite solar cells are beginning to be commercialised, with 'minimodules' made by Microquanta Semiconductor at 16% efficiency in April 2017.[14,23] Multi-junction solar cells with both perovskite and silicon junctions are also of significant commercial interest, with research-lab efficiencies for perovskite-silicon tandems at 23.6%.[14,23]

Before perovskite solar cells can displace or improve the incumbent silicon solar panels, issues around material stability must be resolved. Commercial solar cells must be stable over 25 years of operation.[19] However, at present there are fundamental limitations on the stability of perovskite solar cells. The instability arises from the perovskite thin films themselves, which contain small organic molecules. When subjected to thermal stresses typical of solar cell operation, these cations can decompose and/or leave the thin films. This chemical instability destroys the perovskite thin film, rendering it unable to function in a solar cell.

## 1.2 Aims of this thesis

The overarching aim of this thesis is to explore whether the chemical stability of perovskite thin films may be improved while retaining the photovoltaic properties necessary for high efficiency solar cells. Chemical stability of the perovskite thin film has been achieved by replacing the small organic cation with the inorganic cation $Cs^+$. This thesis reports on the effects of this modification on properties relevant for solar cell operation.

Perovskites are a vast class of materials which include ferroelectrics, piezoelectrics, thermoelectrics, insulators, semiconductors, conductors, and, perhaps most famously,

 

superconductors.[19] The first perovskite mineral to be discovered was calcium titanate ($CaTiO_3$), which was found by Gustav Rose in 1839 in the Ural mountains and named at his request after Russian war veteran Count Lev A. Perovski.[24] The class of perovskites now includes all other materials with the general formula of $ABX_3$ and a similar crystallographic structure. The perovskite structure will be described in detail in Chapter 2. There are many possible elemental combinations that form perovskites, even with the limitations that the atoms fit together into this crystalline structure, and the charges of the atoms give a neutral overall charge.

Perovskites that have been found to be suitable for photovoltaic applications include those with lead ($Pb^{2+}$) or tin ($Sn^{2+}$) in the 'B' site, and halide ions such as iodide ($I^-$) or bromide ($Br^-$) in the 'X' site. The 'A' site is then required to be a singly-charged cation, which could be inorganic or organic. The first known perovskites of this kind were inorganic lead halide perovskites synthesised by Wells in 1893 with caesium or potassium in the 'A' site.[25–28] 85 years later, it was discovered that small organic cations such as methylammonium ($CH_3NH_3^+$) could also fit into the 'A' site.[29,30] Such 'hybrid' organic-inorganic perovskites were the first perovskites to be explored in solar cells.[21,31] The operating principles of perovskite solar cells will be provided in Chapter 2, along with a brief history of their development.

Replacement of the methylammonium cation with an inorganic cation, to form a fully-inorganic lead halide perovskite, should lead to a material with significantly higher stability. Accordingly, the inorganic perovskite caesium lead bromide ($CsPbBr_3$) has been shown to have higher stability than methylammonium lead bromide, without compromising on photovoltaic performance.[32] It should follow that the inorganic perovskite caesium lead iodide ($CsPbI_3$) would be comparable to the methylammonium equivalent. However, the first report of $CsPbI_3$ as the absorber layer in a solar cell produced solar cells with less than 3% power conversion efficiency, significantly lower than the methylammonium analogue.[33]

 

Rather than a chemical instability, the challenge posed by $CsPbI_3$ is a structural instability. At ambient conditions, $CsPbI_3$ adopts a yellow non-perovskite polymorph with poor photovoltaic properties. The photovoltaic black perovskite polymorph of $CsPbI_3$ is obtained by heating the material above 300 °C followed by rapid cooling to room temperature, or by using a processing aid such as hydriodic acid together with annealing at 100 °C.[33] The fabrication of solar cells with black-phase $CsPbI_3$ then entails all processing steps to be performed either in nitrogen or under vacuum.

The search for a chemically stable perovskite now becomes a quest for structural stabilisation of the inorganic perovskite $CsPbI_3$. While structurally stable, $CsPbBr_3$ is orange and so is better suited to light emission than light absorption. However, perovskites with mixed halides are possible, and so in Chapter 4 $CsPbI_2Br$ is presented as an inorganic perovskite with structural stability in atmospheric conditions better than the neat iodide. As expected, this mixed halide material also has improved chemical stability in comparison with the methylammonium analogue. Additionally, the first $CsPbI_2Br$-based solar cells show better photovoltaic performance than previous inorganic perovskite solar cells.

The realisation of efficient solar cells with inorganic lead halide perovskites raises the question: how does the cation influence the optoelectronic properties of the perovskite? While the inorganic lead halide perovskites have been known since the late $19^{th}$ century, very little is known about their optoelectronic properties and how they compare with the hybrid perovskites. Chapter 5 seeks to remedy this deficit, by presenting relevant optoelectronic properties of $CsPbI_3$, $CsPbBr_3$, and the mixed halide $CsPbI_2Br$. The optoelectronic properties are found to depend more on the halide than the cation, with a higher proportion of the iodide anion necessary for optimal photovoltaic properties. This finding may be understood by considering the contribution of the A, B and X ions to the electronic band structure. For the lead

 

halide perovskites, Filip *et al.* have shown that the atomic/molecular orbitals from the A cation are deep in the valence band of the electronic band structure of the resulting perovskite structure.[34] The nature of the VB and CB edges, and therefore the optoelectronic properties, of the perovskite are then governed by contributions from the B and X ions. In this chapter, the B ion is always occupied by $Pb^{2+}$ and so the measured changes in the optoelectronic properties may be directly attributed to changes in the halide composition.

In order to increase the ambient stability of black $CsPbI_{3-x}Br_x$ thin films, it is important to understand the structural transitions in these materials. $CsPbI_3$ is an anomaly among perovskites in that the only two reported polymorphs are a yellow non-perovskite and a black cubic perovskite, and the transition from non-perovskite to perovskite is direct upon heating to around 300 °C.[35] While most perovskite materials adopt a cubic perovskite structure at high temperatures, their room temperature polymorphs are usually also perovskites, albeit perhaps with some distortions. Chapters 4 and 5 demonstrate that $CsPbI_3$ can exist in black films at room temperature in inert atmosphere, and these films show no phase transitions when further cooled to 2 K under vacuum. These findings suggest that the current understanding of the phase transitions in $CsPbI_3$ is incomplete. Chapter 6 reports on investigations using solid state synthesis and X-ray diffraction into the structure of room temperature black-phase $CsPbI_3$. This material is determined to be an orthorhombic perovskite polymorph of $CsPbI_3$, rather than the high-temperature cubic $CsPbI_3$ polymorph as previously thought. This discovery reconciles $CsPbI_3$ with other perovskite materials and enables a better understanding of the $CsPbI_3$ polymorph that has been studied in films and solar cells. Furthermore, the finding that the black room temperature polymorph of $CsPbI_3$ is already a distorted perovskite is of utmost importance when considering how structural stability of this polymorph may be achieved for the iodide-rich inorganic lead halide perovskites.

 

Finally, Chapter 7 provides some preliminary theoretical and experimental work towards increasing the structural stability of this polymorph for these important materials.

## 1.3 References


1. Perez, R.; Perez, M. "A Fundamental Look At Supply Side Energy Reserves For The Planet". *IEA SHC Sol. Updat.* 2015, *62*, 4–6.
2. U.S. Energy Information Administration. *International Energy Outlook 2017*; 2017.
3. International Energy Agency. *Key World Energy Statistics*; 2017.
4. IPCC 2014 Core Writing Team. *Climate Change 2014: Synthesis Report. Contribution of Working Groups I, II and III to the Fifth Assessment Report of the Intergovernmental Panel on Climate Change*; Pachauri, R. K.; Meyer, L. A., Eds.; Geneva, Switzerland, 2014.
5. United Nations, *Paris Agreement*; http://unfccc.int/essential_background/convention/items/6036.php.
6. Directorate-General for Research and Innovation, E. C.; Joint Research Centre, E. C. *Strategic Energy Technology Plan*; EU Publications, 2017.
7. Mark L. Clifford. *Watch Out, Coal! Dubai Announces Plans For World's Lowest Cost Solar Plant* https://www.forbes.com/sites/mclifford/2016/06/29/cheaper-than-coal-dubai-to-build-worlds-lowest-cost-solar-plant/#54afa8161c81.
8. Samans, R.; Drexler, M. *Renewable Infrastructure Investment Handbook: A Guide for Institutional Investors*; 2016.
9. Land Art Generator Initiative. *Surface Area Required to Power the World with Solar* http://landartgenerator.org.
10. The World Bank Group. *Land area (sq. km) Dataset (Food and Agriculture Organization)* https://data.worldbank.org/indicator/AG.LND.TOTL.K2.
11. Louwen, A.; van Sark, W.; Schropp, R.; Faaij, A. "A Cost Roadmap for Silicon Heterojunction Solar Cells". *Sol. Energy Mater. Sol. Cells* 2016, *147*, 295–314.
12. GTMResearch; SEIA. *Solar Market Insight Report 2017 Q4*; Washington, DC, 2017.
13. Shockley, W.; Queisser, H. J. "Detailed Balance Limit of Efficiency of p-n Junction Solar Cells". *J. Appl. Phys.* 1961, *32*, 510–519.
14. Green, M. A.; Hishikawa, Y.; Warta, W.; Dunlop, E. D.; Levi, D. H.; Hohl-Ebinger, J.; Ho-Baillie, A. W. H. "Solar Cell Efficiency Tables (Version 50)". *Prog. Photovoltaics Res. Appl.* 2017, *25*, 668–676.
15. Kayes, B. M.; Nie, H.; Twist, R.; Spruytte, S. G.; Reinhardt, F.; Kizilyalli, I. C.; Higashi, G. S. "27.6% Conversion Efficiency, a New Record for Single-Junction Solar Cells under 1 Sun Illumination". In 2011 37th IEEE Photovoltaic Specialists Conference; IEEE, 2011; pp. 000004–000008.
16. Chuang, C.-H. M.; Brown, P. R.; Bulović, V.; Bawendi, M. G. "Improved Performance and Stability in Quantum Dot Solar Cells through Band Alignment Engineering". *Nat. Mater.* 2014, *13*, 796–801.


 

17. H. Sargent, E. "Infrared Quantum Dots". *Adv. Mater.* 2005, *17*, 515–522.

18. Ball, J. M.; Petrozza, A. "Defects in Perovskite-Halides and Their Effects in Solar Cells". *Nat. Energy* 2016, *1*, 16149.

19. Snaith, H. J. "Perovskites: The Emergence of a New Era for Low-Cost, High-Efficiency Solar Cells". *J. Phys. Chem. Lett.* 2013, *4*, 3623–3630.

20. Yuan, Z.; Yang, Y.; Wu, Z.; Bai, S.; Xu, W.; Song, T.; Gao, X.; Gao, F.; Sun, B. "Approximately 800-Nm-Thick Pinhole-Free Perovskite Films via Facile Solvent Retarding Process for Efficient Planar Solar Cells". *ACS Appl. Mater. Interfaces* 2016, *8*, 34446–34454.

21. Kojima, A.; Teshima, K.; Shirai, Y.; Miyasaka, T. "Organometal Halide Perovskites as Visible-Light Sensitizers for Photovoltaic Cells". *J. Am. Chem. Soc.* 2009, *131*, 6050–6051.

22. National Renewable Energy Laboratory. *Best Research-Cell Efficiencies* https://www.nrel.gov/pv/assets/images/efficiency-chart.png.

23. Green, M. A.; Hishikawa, Y.; Dunlop, E. D.; Levi, D. H.; Hohl-Ebinger, J.; Ho-Baillie, A. W. Y. "Solar Cell Efficiency Tables (Version 51)". *Prog. Photovoltaics Res. Appl.* 2018, *26*, 3–12.

24. Chakhmouradian, A. R.; Woodward, P. M. "Celebrating 175 Years of Perovskite Research: A Tribute to Roger H. Mitchell". *Phys. Chem. Miner.* 2014, *41*, 387–391.

25. Wells, H. L. "On the Caesium- and the Potassium-Lead Halides". *Am. J. Sci.* 1893, *s3-45*, 121–134.

26. Møller, C. K. "Crystal Structure and Photoconductivity of Cæsium Plumbohalides". *Nature* 1958, *182*, 1436–1436.

27. Møller, C. K. "The Structure of Perovskite-Like Cæsium Plumbo Trihalides". *Mat. Fys. Medd. Dan. Vid. Selsk.* 1959, *32*.

28. Møller, C. K. "The Structure Of Cæsium Plumbo Iodide $CsPbI_3$". *Mat. Fys. Medd. Dan. Vid. Selsk.* 1959, *32*, 1–18.

29. Weber, D. "$CH_3NH_3SnBr_xI_{3x}$ (X=0-3), Ein Sn(II)-System Mit Kubischer Perowskitstruktur". *Zeitschrift für Naturforsch. Tl. b, Anorg. Chemie, Org. Chemie* 1978, *33b*, 862.

30. Weber, D. "$CH_3NH_3PbX_3$, Ein Pb(II)-System Mit Kubischer Perowskitstruktur". *Zeitschrift für Naturforsch. Tl. b, Anorg. Chemie, Org. Chemie* 1978, *33 b*, 1443.

31. Mitzi, D. B.; Feild, C.; Harrison, W.; Guloy, A. "Conducting Tin Halides with a Layered Organic-Based Perovskite Structure". *Nature* 1994, *369*, 467–469.

32. Kulbak, M.; Cahen, D.; Hodes, G. "How Important Is the Organic Part of Lead Halide Perovskite Photovoltaic Cells? Efficient $CsPbBr_3$ Cells". *J. Phys. Chem. Lett.* 2015, *6*, 2452–2456.

33. Eperon, G. E.; Paternò, G. M.; Sutton, R. J.; Zampetti, A.; Haghighirad, A. A.; Cacialli, F.; Snaith, H. J. "Inorganic Caesium Lead Iodide Perovskite Solar Cells". *J. Mater. Chem. A* 2015, *3*, 19688–19695.

34. Filip, M. R.; Eperon, G. E.; Snaith, H. J.; Giustino, F. "Steric Engineering of Metal-Halide Perovskites with Tunable Optical Band Gaps". *Nat. Commun.* 2014, *5*, 5757.

35. Trots, D. M.; Myagkota, S. V. "High-Temperature Structural Evolution of Caesium and Rubidium Triiodoplumbates". *J. Phys. Chem. Solids* 2008, *69*, 2520–2526.

 

# 2 Theory and Background

This chapter provides a general overview of the relevant theory and background knowledge that underpins the work in this thesis. More detailed descriptions may be found in the scientific literature and in textbooks such as those written by Kittel,[1] Harrison,[2] and Nelson.[3]

This chapter presents the structure of the perovskite materials of central importance in this thesis, leading into the optoelectronic properties arising from this structure that are ideal for photovoltaics. The operating principles of solar cells are outlined, and the chapter closes with a brief account of the evolution of perovskite solar cells.

## 2.1 The perovskite structure

The perovskite structure is adopted by a family of compounds commonly found with the general formula $ABX_3$. The basic unit cell of the $ABX_3$ perovskite consists of corner-linked octahedra of X-anions (typically oxygen or halide) with B-cations at their centres (body-centre position) and A-cations between them, as depicted in Figure 2-1.

 

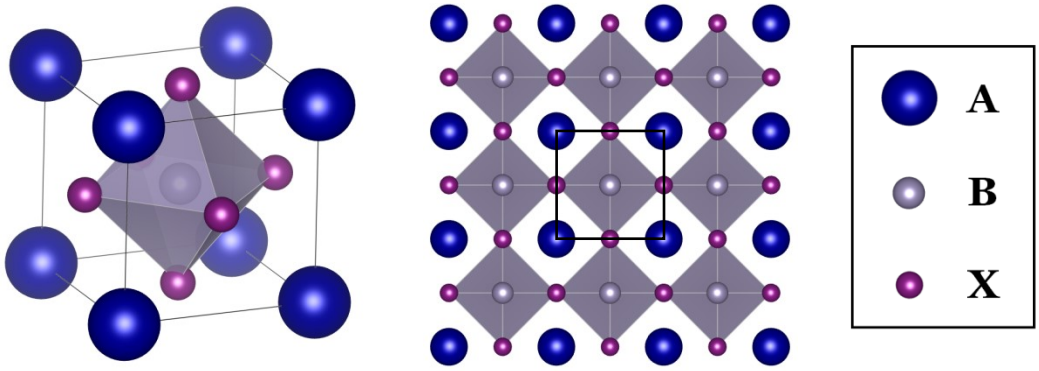


**Figure 2-1. The perovskite structure has a unit cell (left) with a B-cation (in grey) octahedrally coordinated to X-anions (purple) with A-cations (blue) filling the voids between the octahedra. View of the lattice (right) along one crystallographic direction, with a unit cell outlined in black.**

For the perovskites of interest in this thesis, the octahedra are formed by metal 'B' cations such as lead ($Pb^{2+}$) or tin ($Sn^{2+}$), or another metal cation with a charge of +2. These are surrounded by halide 'X' anions, typically iodide ($I^-$), bromide ($Br^-$), chloride ($Cl^-$) or fluoride ($F^-$), or a mix of these. Charge neutrality is obtained by the presence of a singly charged metal 'A' cation, such as caesium ($Cs^+$), or organic cations such as methylammonium ($CH_3NH_3^+$, abbreviated MA) and formamidinium ($H_2NCHNH_2^+$, abbreviated FA), in the void (cubo-octahedral cavity) between the octahedra. These cations are depicted in Figure 2-2(a). Mixes of these cations have recently become popular, with quadruple-cation perovskites in particular reaching high efficiencies in photovoltaic devices.[4,5] Significant research efforts have also been invested in mixed-metal perovskites and lead-free perovskites, with some promising results.[6–8]

Larger organic cations with long organic chains and perhaps with phenyl groups are too large to fit within the cubo-octahedral cavity. Two examples of large cations with relevance for photovoltaics are butylammonium and phenethylammonium, which are shown in Figure 2-2(b). These large cations form fully layered 2D materials, as in Figure 2-2(c), which have excellent material stability but poor

 

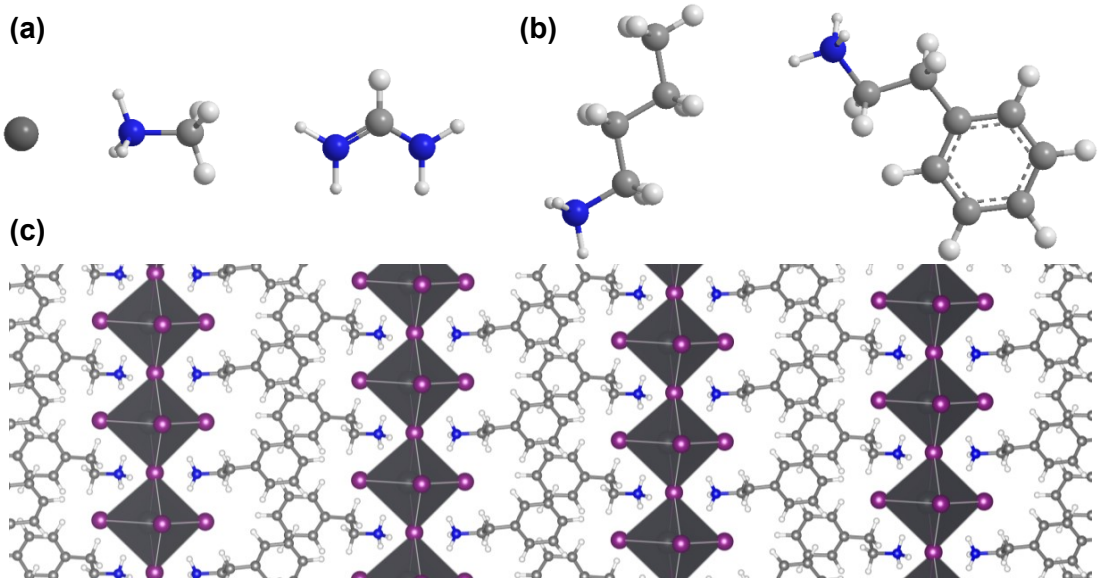


**Figure 2-2. (a) Some of the cations that can occupy the 'A' site are, from left, caesium ($Cs^+$), methylammonium (MA), and formamidinium (FA). (b) Butylammonium (BA) and phenethylammonium (PEA) are too large for the cubo-octahedral cavity. (c) To accommodate large A cations (here PEA), the perovskite structure may separate into two-dimensional layers with overall stoichiometry $A_2PbX_4$.**

optoelectronic properties for photovoltaics.[9] While partial replacement of MA with these large cations in 2D-3D mixed-cation perovskites has been shown to offer some improvement in the chemical stability of the resulting material, this approach has been shown to have an intrinsic compromise between stability and photovoltaic device efficiency.[9,10]

### 2.1.1 Goldschmidt's tolerance factor and octahedral tilting

A geometrical argument for predicting whether a combination of ions will be stable in a perovskite structure is Goldschmidt's tolerance factor, $t$.[11,12] The argument is summarised in the following discussion.

For the ideal cubic perovskite shown in Figure 2-3(a), the bond lengths between the ions may be expressed in terms of the lattice constant $\mathbf{a}$ of the unit cell as follows:

$$\mathbf{2 \times d(B - X) = a}$$
$$\mathbf{2 \times d(A - X) = \sqrt{2}a}$$

Equation 2-1

where $d(B-X)$ is the bond length between B and X ions, and $d(A-X)$ the bond length between A and X ions. For each equivalent pair of ions, the bond length is assumed to be equidistant. Note that the A cation is always larger than the B cation in the perovskite structure.

For packing of rigid spherical ions in the perovskite structure, these bond lengths may be approximated by the ionic (or effective) radii of the A, B and X ions, $r_A$, $r_B$, and $r_X$ respectively, such that Equation 2-1 becomes (with some simplification):

$$\mathbf{2(r_B + r_X) = a}$$
$$\mathbf{\sqrt{2}(r_A + r_X) = a}$$

Equation 2-2

Taking the ratio of these two expressions gives the tolerance factor, t:

$$\mathbf{t = \frac{\sqrt{2}(r_A + r_X)}{2(r_B + r_X)} = \frac{r_A + r_X}{\sqrt{2}(r_B + r_X)}}$$

Equation 2-3

For perfect packing, $t = 1$, and the structure remains as depicted in Figure 2-3(a). However, the perovskite structure can accommodate a wide range of cation and

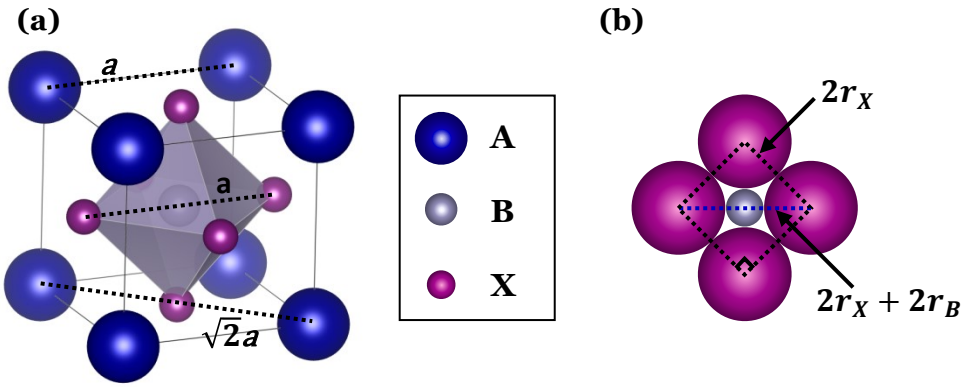


**Figure 2-3. (a) The unit cell of the cubic perovskite $ABX_3$ with bond lengths shown in terms of the lattice constant, $a$. (b) Cross-section through a $BX_6$ octahedron for a minimally-sized B cation.**

anion sizes through tilting or distortions of the octahedra and/or cation displacements. Perovskite structures are found experimentally with tolerance factors of $0.8 \leq t \leq 1$.[12,13] Deviations from the cubic perovskite structure when $t \neq 1$ are highly important, as most perovskite compounds do not have tolerance factors equal to 1.

In order for a perovskite structure to form at all, the B-site cation must be sufficiently large to coordinate octahedrally with the X anions such that the X anions do not contact one another. Figure 2-3(b) illustrates this constraint diagrammatically for octahedra in the cubic perovskite. Basic geometry gives:

$$\boldsymbol{2r_X + 2r_B \geq \sqrt{2} \times 2r_X}$$

which simplifies to

$$\boldsymbol{r_B \geq (\sqrt{2} - 1) r_X \approx 0.41 r_X}$$

This relationship provides the origin of the octahedral factor, $\mu = \frac{r_B}{r_X} > 0.41$, to predict whether a given combination of B and X cations could form stable octahedra.

Even with a sufficiently large B cation, distortions of the octahedra themselves are possible. These distortions tend to arise from electronic instabilities of the B ion.[14] Octahedral distortions include a displacement of the B cation from the centre of the octahedra (e.g. in $BaTiO_3$),[14] and/or elongation of some of the B—X bonds in the octahedra (for example Jahn-Teller distortions of octahedra with B = $Mn^{2+}$ or $Cu^{2+}$).[15]

Given the formation of $BX_6$ octahedra, the formation of a perovskite structure then relies on an appropriately sized A cation. When the A cation is too large for the cubo-octahedral cavity, $t > 1$. In this case, the $BX_6$ octahedra are unable to

 

maintain connectivity of the lattice around the A cation, and the ions adopt lower-dimensional or hexagonal perovskite-like structures as shown in Figure 2-2(c).

When the A cation is only slightly too small for a perfectly cubic corner-sharing octahedral network, such that the tolerance factor becomes smaller than 1, octahedral tilting occurs to stabilise the perovskite structure. Octahedral tilting results in a bending of the soft B—X—B bond angles to retain the connectivity of the octahedral network. This bending shortens some of the A—X bonds without affecting the $BX_6$ octahedral environment, improving the coordination environment and bonding of the A-site cation and stabilising the perovskite structure.[14,15] The many possible combinations of octahedral tilting are well described in Refs. 14 and 16.

A convenient notation for describing octahedral tilting was devised by Glazer in 1972.[16] Here the tilting is described by three letters, one for each axis, such that $a$, $a$, and $c$ would imply tilts of equal magnitude for the $x$ and $y$ axes, but a different magnitude of tilt for the $z$ axis. Lattice connectivity only requires adjacent octahedra to tilt in the plane orthogonal to the tilt axis. A superscript is then used to denote the phase of the tilting for adjacent octahedra along the tilt axis: + for in-phase and − for out-of-phase (0 for no tilting). As examples, the ideal cubic perovskite is $a^0a^0a^0$, the tetragonal perovskite in Figure 2-4(b) is $a^0a^0c^+$, and the orthorhombic perovskite in Figure 2-4(c) is $a^-b^+a^-$.[17]

As the tolerance factor decreases from 1, the degree of octahedral tilting increases in order to maintain the perovskite structure. The most common perovskite structure is orthorhombic with Pnma symmetry and with $a^-b^+a^-$ tilting; this structure is often referred to as the $GdFeO_3$ structure and is shown in Figure 2-4(c).[17] Experimentally, oxide perovskites in the $GdFeO_3$ structure have been observed with tolerance factors from 0.99 to 0.87, where for lower tolerance factors these structures are highly distorted and become increasingly unstable.[17,18] It should also be noted

 

that in this structure, the tilting of octahedra causes shifting in the position of the A-site cation.

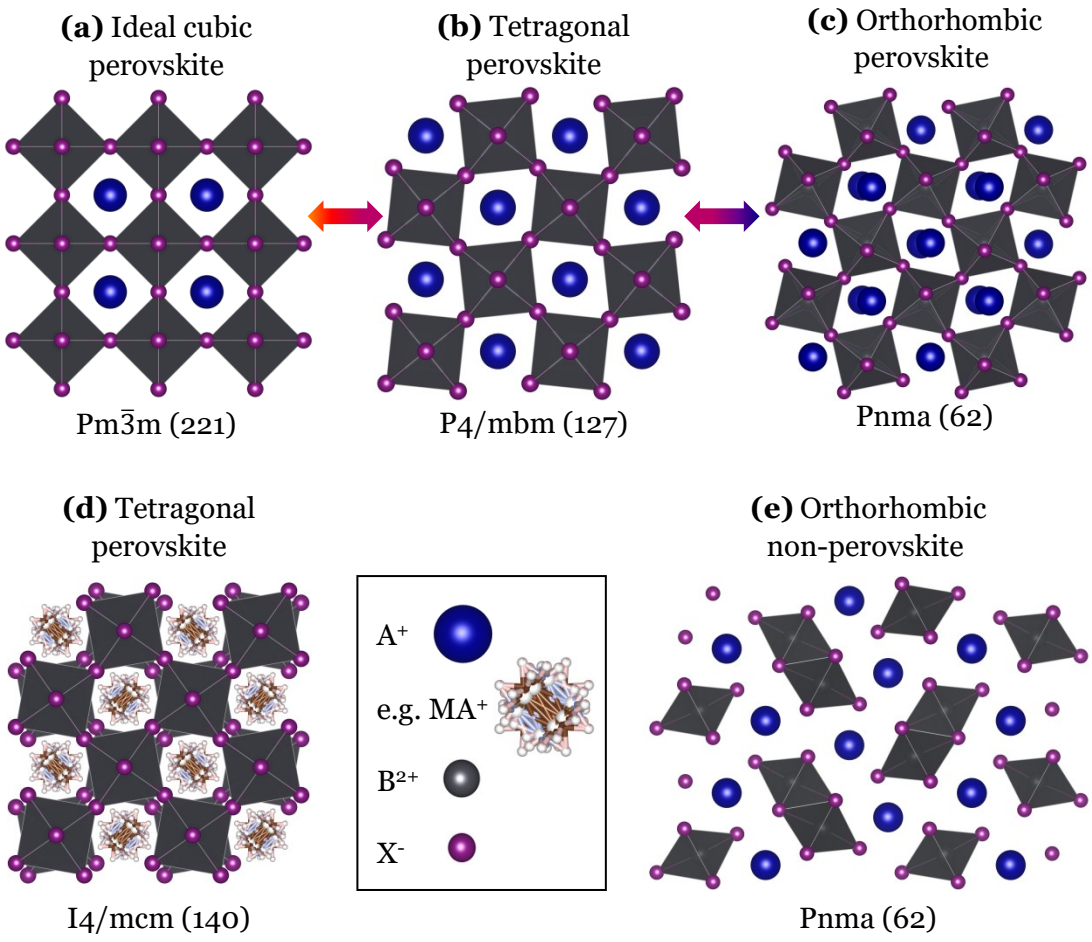


**Figure 2-4. The perovskite structure can accommodate imperfect ionic radii by distorting from the ideal cubic perovskite (a) to a tetragonal perovskite (b) by rotation of alternate octahedra about one axis. (c) Tilting of the octahedra about a second axis and displacement of the A cation lead to orthorhombic perovskites. (d) The structure of $MAPbI_3$ at room temperature is tetragonal. (e) Rotation to edge-sharing of the octahedra leads to a non-perovskite structure. Key: A cation = blue spheres; B cation = at centres of grey octahedra; X anion = purple spheres; The MA cation (pale pink, brown and blue spheres) is shown as a rotational average. Crystallographic space groups are given below the structures. For example, P denotes the primitive Bravais lattice, m denotes a mirror plane, $\bar{3}$ indicates three-fold inversion symmetry, and a, b, c and n denote glide planes.**[19]

When the A cation is much too small, the corner-sharing octahedral network collapses, and again alternative structures are adopted. These structures are typically lower in symmetry, and lack the corner-sharing octahedral network which gives rise to many valuable properties of perovskite materials. As a relevant example of the effect of A cation size, the $Cs_{1-x}Rb_xPbCl_3$ and $Cs_{1-x}Rb_xPbBr_3$ solid solutions convert from the perovskite structure to a non-perovskite structure of edge-sharing octahedra when the A cation becomes too small for the $PbBr_6$ octahedral network ($x > 0.6$).[18]

In the region of perovskite structure formation, the octahedral tilting exhibited by a perovskite with a particular combination of ions usually also depends on the ambient conditions, e.g. temperature and pressure. At high temperature, most perovskites adopt the ideal cubic perovskite structure shown in Figure 2-4(a). Upon cooling, the octahedra may first tilt or rotate about a single axis, giving a tetragonal structure as in Figure 2-4(b). Further cooling may lead to rotation of the octahedra about a second and even a third axis, and/or displacements of the A cation, resulting in orthorhombic polymorphs such as Figure 2-4(c). An increase in pressure can lead to compression of the $BX_6$ octahedra and/or a change in the octahedral tilting.[20] Varying the size of the A-site cation may be considered a form of chemical pressure, and is a common way to tune the octahedral tilting in a perovskite structure.[18]

Octahedral tilting distortions lower the symmetry of the perovskite, reduce the coordination of the A-cation (e.g. from 12 to 8), and change the orbital overlap.[17] The effect of octahedral tilting on the optoelectronic properties of perovskite materials will be discussed later in this chapter.

 

### 2.1.2 Perovskite materials relevant to this thesis

Of the lead-halide perovskites of interest for photovoltaics, the most studied perovskite is the hybrid organic-inorganic perovskite, $MAPbI_3$. Here an effective radius of 217 pm for the MA cation and Shannon ionic radii of 119 pm for $Pb^{2+}$ and 220 pm for $I^-$ give a tolerance factor of 0.912.[21] Although this value is comfortably within the region of perovskite formation, the ideal cubic perovskite structure is only obtained when $MAPbI_3$ is heated above 330 K. At room temperature, the cubic structure is distorted by rotation of adjacent octahedra about one axis to a lower-symmetry tetragonal space group I4/mcm, shown in Figure 2-4(d). At low temperature, around 160 K, the octahedra tilt around additional cubic axes, lowering the symmetry further to the orthorhombic Pnma space group.[22]

In the inorganic perovskites, MA is replaced by the much smaller $Cs^+$ cation (188 pm). Due to the smaller size of the $Cs^+$ cation, the inorganic lead halide perovskites have tolerance factors below 0.9, and so exist in the cubic perovskite structure only at high temperatures. For $CsPbBr_3$ ($t = 0.862$), the high-temperature structure is cubic above about 400 K, and cooling yields a tetragonal (P4/mbm) polymorph around 360 K and an orthorhombic (Pnma) polymorph below this temperature.[23,24] In contrast, for $CsPbI_3$ ($t = 0.851$), the stable polymorph at room temperature is a non-perovskite structure with edge-sharing octahedra, as shown in Figure 2-4(e). On heating, the non-perovskite polymorph transitions to the cubic perovskite polymorph around 590 K with no intermediate polymorphs reported, in contrast to all other perovskites known to the author.[23,25] It will be shown in Chapter 6 that cooling cubic $CsPbI_3$ to room temperature leads to an orthohombic perovskite polymorph similar to that of $CsPbBr_3$. These two perovskites and the mixed-halide compositions are of central importance in this thesis, and will be discussed in detail in the experimental results chapters.

 

## 2.2 Semiconductor bandgaps

### 2.2.1 Energy bands

The individual atoms which make up the structures in the previous section have discrete energy levels that the electrons occupy, which are described by the solutions to Schrödinger's equation for each atom. When atoms come together to form a solid material, the discrete atomic energy levels become bands of allowed energies. Figure 2-5 depicts three of the possible options for how these bands may be populated, in the configurations that we call metals, semiconductors and insulators.

In this picture, electrons typically reside in energy levels within the valence band, leaving the conduction band energy levels mostly empty. The energy bands are populated by electrons according to the Fermi-Dirac distribution, which is given in

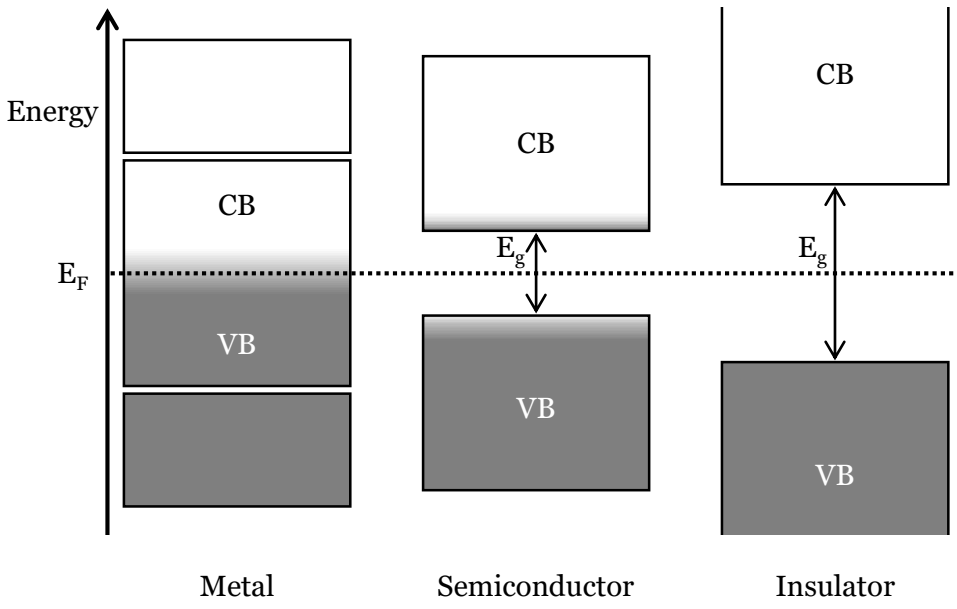


**Figure 2-5. Allowed energy bands with typical electron occupancies (shaded grey) at room temperature for metals, semiconductors and insulators. CB and VB denote the conduction and valence bands respectively, which are separated by the bandgap energy $E_g$. The Fermi level $E_F$ is shown as a dashed line.**

 

Equation 2-4. Here $n(E)$ is the number of electrons at an energy $E$ and temperature $T$, $k_B$ is Boltzman's constant, and $E_F$ is the Fermi level, a hypothetical energy level for which there is 50% probability of occupation at all temperatures.

$$n(E) = \frac{1}{e^{\frac{E-E_F}{k_B T}} + 1} \qquad \text{Equation 2-4}$$

For metals, the valence and conduction bands overlap and the Fermi level lies within the bands, such that the conduction band is always partially filled and conduction is possible at all temperatures. For Fermi levels within the bandgap, the behaviour of the material as a semiconductor or an insulator depends on the temperature. If the thermal energy is sufficient to excite some electrons across the bandgap into the conduction band (e.g. for bandgaps up to approximately 3 eV at room temperature), the material behaves as a semiconductor. Conduction is also possible by holes in the valence band. For larger bandgaps, the probability of thermal excitation of electrons into the conduction band is very low, and so these materials are typically insulators.

### 2.2.2 The nearly-free electron model

How these bands form in crystalline materials with a periodic array of atoms, can be described by the 'nearly-free electron model'. Here consider that a mobile electron in the lattice is like a free electron which is slightly perturbed by the periodic potential from the positive ion cores. These nearly-free electrons propagate as Bloch waves: combinations of a plane wave (for a free electron) and a periodic potential (from the crystal lattice). Energies of the Bloch waves follow a free electron dispersion relation $E(\boldsymbol{k}) = \frac{\hbar^2}{2m}(k_x^2 + k_y^2 + k_z^2)$, shown in Figure 2-6(a), where $\boldsymbol{k} = (k_x, k_y, k_z)$ is the wavevector and $\frac{\hbar^2}{2m}$ is a constant. In a three-dimensional crystal, the wavevector directions are described in relation to the lattice directions in the crystal.

 

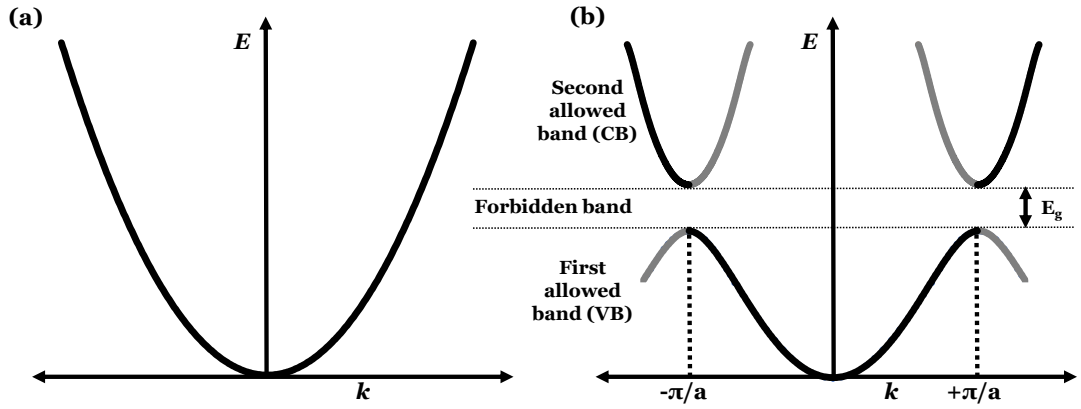


**Figure 2-6. Energy versus wavevector dispersion relations (a) for a free electron, and (b) for an electron in a linear monatomic lattice with lattice constant $a$, where the first energy gap $E_g$ occurs at $k = \pm\pi/a$.**

Like other waves in crystals, these electron waves may also be Bragg reflected from the lattice. Considering only one dimension, in a linear monatomic lattice with a periodic lattice spacing $a$, the reflections occur for waves with wavevectors $k = \pm\frac{n\pi}{a}$, where $n$ is an integer. Figure 2-6(b) shows how these reflections lead to bandgaps in crystalline materials. The symmetry of the crystal means that $E(\boldsymbol{k}) = E(-\boldsymbol{k})$ and $E(\boldsymbol{k}) = E(\boldsymbol{k} + \frac{2\pi}{a})$. The smallest set of $\boldsymbol{k}$'s giving unique Bloch wave solutions forms a region in $\boldsymbol{k}$-space called the 'Brillouin zone', which in Figure 2-6(b) is between $k = \pm\frac{\pi}{a}$. In Figure 2-6(b), the valence band maximum and conduction band minimum are at the same wavevector $\boldsymbol{k}$, which gives a 'direct' bandgap. It is possible for there to be a displacement in $\boldsymbol{k}$, in which case the bandgap is 'indirect'.

## 2.2.3 The tight-binding model

While the nearly-free electron model can explain the origin of a bandgap in a crystalline material, a more accurate model for the electronic structure of perovskite materials is the tight-binding model. The tight-binding model provides a framework

 

in which both the crystal structure and the chemical composition together determine the electronic band structure.

In the tight-binding model, the atoms that make up the structure are treated as a central positive nucleus surrounded by tightly-bound electrons. The electrons occupy well-localised orbitals, which may be atomic orbitals and/or their linear combinations. Figure 2-7 depicts s and p atomic orbitals and an $sp^3$ hybrid orbital.

As atoms come together, their outermost valence orbitals begin to overlap. This overlap interaction results in bonding and anti-bonding orbitals $\varepsilon_b$ and $\varepsilon_a$, as shown in Figure 2-7 for the interaction between neighbouring $sp^3$ orbitals. The strength of the overlap interaction $V$ gives the splitting (or the bond energy) of the bonding and anti-bonding energy levels, and accounts for interactions between all neighbouring

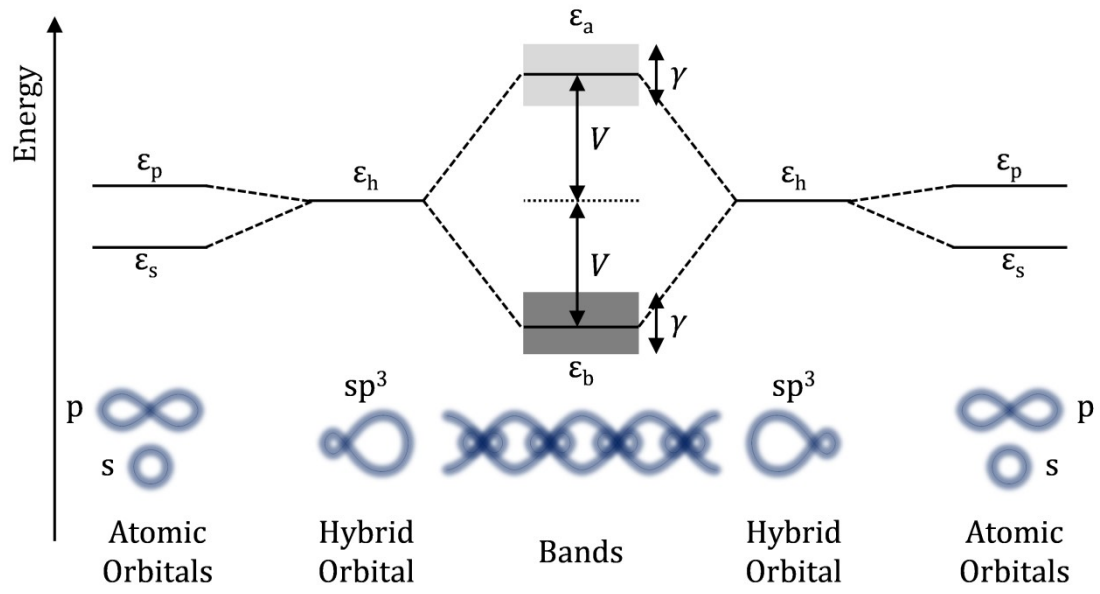


**Figure 2-7. Band formation in non-polar solids in the tight-binding model. Valence electrons in each atom are described as occupying linear combinations of atomic orbitals. Here one s and three p orbitals are combined to form hybridised $sp^3$ orbitals. These orbitals overlap to form bonds, where the bonding and antibonding energy levels $\varepsilon_b$ and $\varepsilon_a$ are split by an energy $2V$. The bonding and antibonding energy levels are broadened into energy bands in the solid. Adapted from Ref. 2.**

 

orbitals. While the orbital overlap is highly dependent on the symmetry of the orbitals and their orientations in the crystal, particularly for interactions between p-, d-, and f-orbitals, in all cases the overlap interaction increases as the interatomic separation decreases.

In a solid, overlap interactions between adjacent bonding (or antibonding) orbitals split each electron energy level into a band of electron states, shown by shaded areas in Figure 2-7. The width $\gamma$ of these bands increases with increasing overlap interaction, for example through decreasing the interatomic separation. The bandgap energy $E_g$ is then given by $2V - \gamma$. Depending on the relative magnitudes of the bonding interaction $V$ and the band width $\gamma$, the conduction and valence energy bands may overlap in energy or may be separated by some band gap $E_g$.

For interactions between atoms with orbitals of different energies, the band formation is slightly modified as depicted in Figure 2-8. Here the bandgap also includes an additional contribution from the energy difference $2\alpha$ between the interacting orbitals, where $\alpha$ is the polar energy, and originates from the difference in electronegativity of the atoms. The bonding energy $\beta$ may then be expressed as $\beta = \sqrt{V^2 + \alpha^2} - \alpha$, for $V$ the orbital overlap interaction as previously.[26] Inclusion of the polar energy here reflects the covalency of the resulting bond. Note that in Figure 2-7, the bonding atoms are non-polar, and so $\alpha = 0$, and $\beta = V$.

The bandgap may then be written as

$$\mathbf{E_g = 2\alpha + 2\beta - \frac{\gamma_{VB} + \gamma_{CB}}{2} = 2\sqrt{V^2 + \alpha^2} - \frac{\gamma_{VB} + \gamma_{CB}}{2}} \qquad \textbf{Equation 2-5}$$

In general, larger differences in electronegativity result in larger bandgaps.[26] Additionally, for increasing polar energy the bandwidth $\gamma$ generally decreases, as the overlap interaction becomes less significant.

 

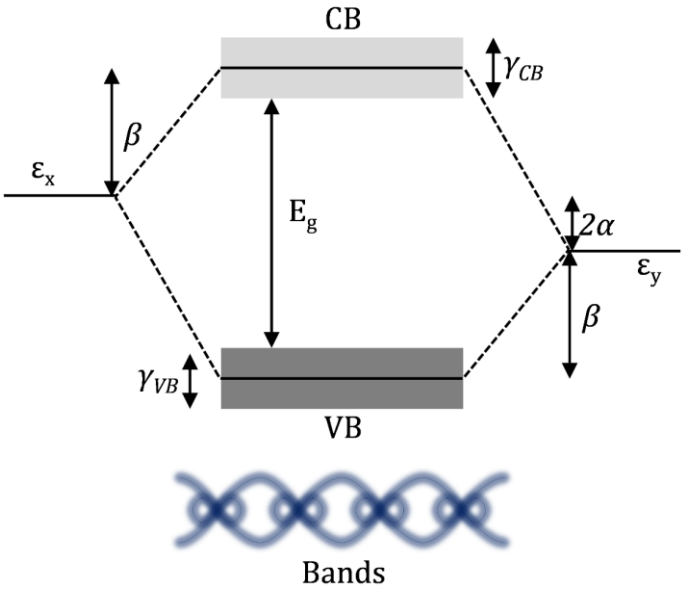


**Figure 2-8. Band formation for two orbitals with an energy difference of $2\alpha$. The splitting $\beta$ is the strength of the bonding interaction. In a solid, the VB and CB broaden into bands with widths $\gamma_{VB}$ and $\gamma_{CB}$, respectively. The band gap energy $E_g$ is between VB and CB edges. Adapted from Ref. 26.**

An important example of the tight-binding model is the electronic band structure of elements in the diamond-structure: C, Si, Ge, and α-Sn. These elements bond tetrahedrally through $sp^3$ hybrid orbitals as in Figure 2-7. As the atomic radii increase, so too does the interatomic separation in the solid. Consequently, the overlap interaction decreases, which reduces the bandgap from insulating (C) to semiconducting (Si, Ge) to metallic (α-Sn).[27] Intriguingly, application of hydrostatic pressure leads to bandgap narrowing in Si. [28] This phenomenon has been attributed to mixing of bonding d-orbitals with anti-bonding s and p states near the (indirect) bandgap, which lowers the energy of the conduction band in that region. A reduction in interatomic separation through the application of pressure reduces the energies of the d-states, and consequently narrows the bandgap.[29]

 

For the lead halide perovskite materials discussed in this thesis, narrowing of the bandgap is seen when the halide radius increases. The primary origin of this bandgap narrowing is the decrease in electronegativity of the halide, which reduces the difference in electronegativity between the halide and lead, and therefore the polar energy contribution ($2\alpha$) to the bandgap. For example, the two perovskites discussed in most depth in this thesis, $CsPbBr_3$ and $CsPbI_3$, have bandgaps of around 2.35 eV and 1.75 eV respectively.[24,30–32] Changes in orbital overlap play a secondary role in the bandgap change here.

In contrast, the A-site cation only indirectly influences the bandgap by virtue of its size, which affects the tilting of the octahedra. For lead halide perovskites with the same halide, the bandgap is significantly affected by changes in orbital overlap due to octahedral tilting. Examination of the orbitals contributing to the bandgap shows that the valence band maximum is mainly formed by halide p-orbitals while the conduction band minimum arises mainly from the lead 6p-orbitals.[20,33] Notably, orbitals from the A cation appear deep in the valence band and so do not directly contribute to the bandgap. Instead, additional contributions to the valence band come from the Pb-6s orbitals, and the halide p-orbitals contribute to the conduction bands.[33] The bandgap is then highly dependent on the B—X 'backbone'. As the octahedra tilt and the B−X−B bonds become increasingly bent, the overlap of the p-p orbitals between neighbouring atoms along the B—X backbone decreases.[33] This decrease in orbital overlap leads to narrower conduction and valence bands, giving an increase in the band gap.[18] This relationship is exemplified by the $Cs_{1-x}Rb_xPbCl_3$ and $Cs_{1-x}Rb_xPbBr_3$ solid solutions, where the band gap increases as the magnitude of the octahedral tilting distortion increases.[18]

Changes in the orbital overlap from octahedral tilting can also significantly affect conduction in the perovskite. In the tight-binding model, conduction may be viewed as electrons 'hopping' from one unoccupied atomic orbital to another. In perovskites,

 

electrons typically hop from one B cation to another.[34] The probability of conduction then depends on the overlap integral between the unoccupied orbitals of the B cations in the perovskite. In some cases, octahedral tilting can reduce or even prevent charge carrier migration via hopping.[35]

## 2.3 Absorption and emission

An important feature of the semiconducting bandgap is that electrons at the top of the valence band may be excited into the conduction band by light irradiation, leaving an electron vacancy (hole) in the valence band. This photoexcitation requires the incident photon energy to be greater than the bandgap, as depicted in Figure 2-9(a). Excess energy is lost as heat to the lattice in a process known as thermalisation. Photoexcited electrons in the conduction band (and holes in the valence band) may propagate through the material as mobile charge, and this 'photoconductivity' is a vital property of photovoltaic materials. Alternatively, excited electrons may recombine with a hole in the valence band and emit the difference in energy as light, another key property known as 'photoluminescence'. These competing processes are depicted in Figure 2-9(b). The recombination time for photoexcited charges is typically much longer than the thermalisation time, and so constant illumination results in steady-state populations of electrons and holes in the conduction and valence bands respectively. These steady-state populations split the Fermi levels for electrons and holes into 'quasi-Fermi levels', as in Figure 2-9(c).

By measuring the light absorption and emission properties of a semiconducting material it is possible to determine information about the bandgap. Typical absorption and photoluminescence spectra for lead halide perovskites are shown in Figure 2-10. The perovskite materials discussed in this thesis are direct bandgap semiconductors with photoluminescence emission close to the absorption onset.

 

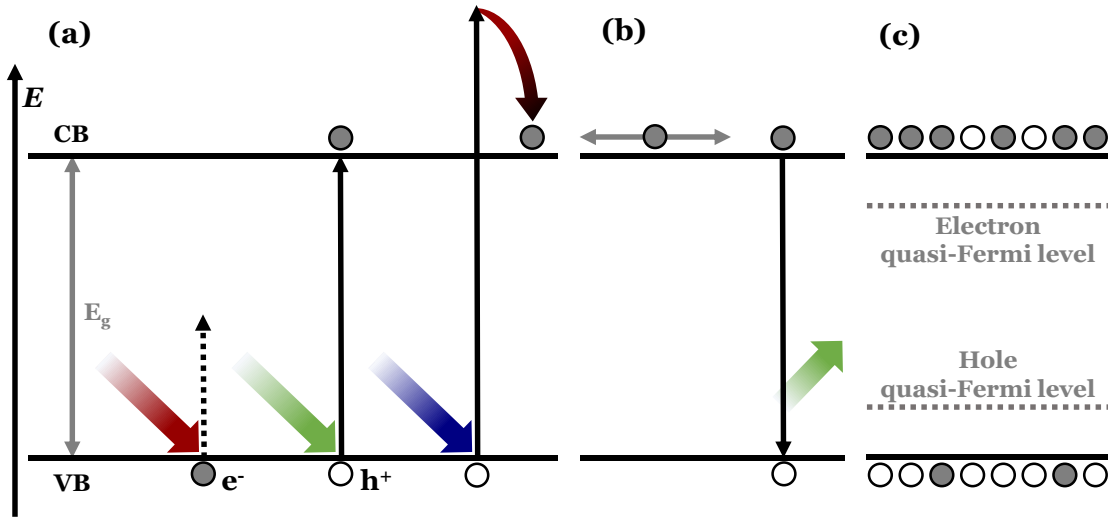


Figure 2-9. (a) Absorption of energy by photoexcitation. Low energy photons (red arrow) cannot excite an electron ($e^-$) from the valence band (VB) across the bandgap ($E_g$) into the conduction band (CB). Photons with at least the bandgap energy (green and blue arrows) excite electrons across the bandgap, with a vacancy ($h^+$) left in the valence band, and any excess energy released as heat (curved arrow). (b) Electrons in the conduction band may conduct electrical charge (grey arrows), or emit the bandgap energy as light (green arrow) by recombining with a hole in the valence band. (c) Constant illumination causes splitting of the Fermi levels for electrons and holes into 'quasi-Fermi levels'.

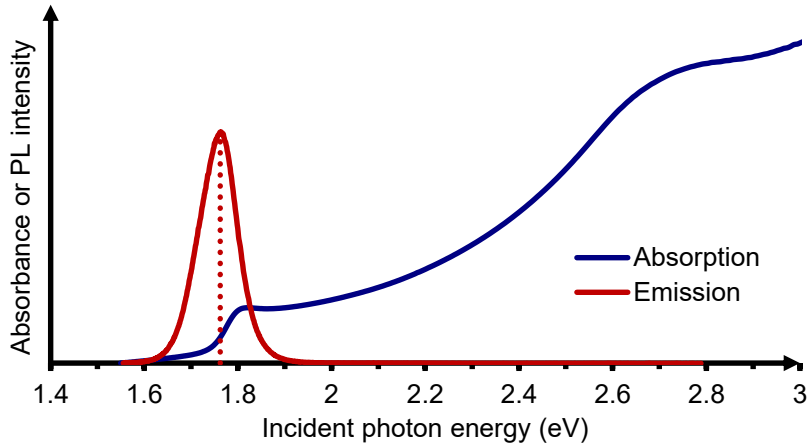


Figure 2-10. Absorption and photoluminescence emission (PL) of a thin film of the inorganic perovskite $CsPbI_3$. The peak of the emission (dashed line) is very near the absorption onset.

## 2.4 Excitons

When photoexcited charges are generated the electron and hole initially form an 'exciton' which is held together by a Coulombic interaction. The strength of this interaction is given by the exciton binding energy.

For the hydrogen atom, the binding energy between electron and proton is known as the Rydberg, $R_0$:

$$\mathbf{R_0 = \frac{m_0 e^4}{2\hbar^2} = 13.6\ eV} \qquad \textbf{Equation 2-6}$$

where $m_0$ is the free electron mass. The most probable distance between the electron and proton in the hydrogen atom is known as the Bohr radius $a_0$, and is approximately 0.5 Å.

In a bulk material, the binding energy $R^*$ of the ground excitonic state may be expressed as:

$$\mathbf{R^* = \frac{\mu e^4}{2\hbar^2 \varepsilon_{eff}^2} = \frac{\mu R_0}{m_0 \varepsilon_{eff}^2}} \qquad \textbf{Equation 2-7}$$

where $\mu$ is the reduced mass ($\mu^{-1} = m_e^{-1} + m_h^{-1}$), and $\varepsilon_{eff}$ is the relative dielectric constant. The separation $r$ of the electron and hole in the exciton is then given by:

$$\mathbf{r = \frac{a_0 \varepsilon_{eff}}{\mu}} \qquad \textbf{Equation 2-8}$$

Exciton binding energies for semiconducting materials are typically about three orders of magnitude smaller than the binding energy of the hydrogen atom due to dielectric screening by the nuclei and electrons in the material. For silicon, the exciton binding energy is about 15 meV,[36] which is sufficiently small that the thermal energy available at room temperature allows separation of the exciton into free charges. In Chapter 5, magneto-transmission measurements are used to determine exciton binding energies of 15-30 meV in $CsPbI_{3-x}Br_x$ perovskites. These small binding energies correspond to weakly bound Wannier excitons with

 

separations of around 50 Å. Large exciton binding energies result in a large proportion of the photoexcited charges recombining radiatively, rather than separating into free charges, resulting in strong photoluminescence, an excitonic peak at the absorption onset in absorption spectra, and short charge-carrier diffusion lengths. These properties make strongly excitonic materials poor photovoltaic absorbers but ideal for light emission applications such as lasers and LEDs.

## 2.5 Defects in semiconductors

Defects in a semiconductor crystal can take the form of a structural discontinuity (crystallographic defect) or a foreign atom in the lattice (impurity). In both cases these imperfections affect the semiconductor properties. Figure 2-11(a) illustrates an impurity defect where an atom with one more electron than needed for bonding is substituted on a lattice site. The extra electron is donated to the lattice, leaving a positive charge on the donor atom. The energy levels of the donor states for such an

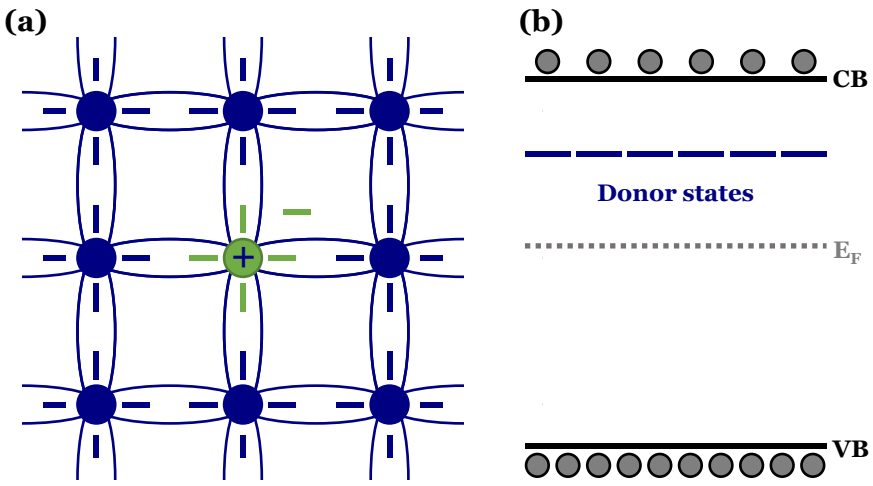


**Figure 2-11. (a) n-type doping of a semiconductor by an impurity atom (green) with one more electron (green dash) than required for bonding. (b) The extra 'donor' electrons have donor energy levels close to the conduction band and may be easily promoted to the conduction band.**

 

impurity are depicted in Figure 2-11(b). Here electrons may be promoted into the conduction band by the ambient temperature, or conduction can occur by electrons hopping between donor states, making the material 'n-type'. Similar conductivity is possible with substitution of an atom with one fewer electron, which becomes an acceptor and the material becomes 'p-type'. In many semiconductors, impurities are added intentionally to 'dope' the material so that conduction is possible at temperatures where there would otherwise be very few mobile charge carriers.

While impurity defects are intentional, crystallographic defects are unintentional and are present in all semiconductors even with the most careful processing conditions. Crystallographic defects include vacancies (or the wrong ion) on a lattice site and ions in interstitial sites within the crystal, illustrated in Figure 2-12(a-c).

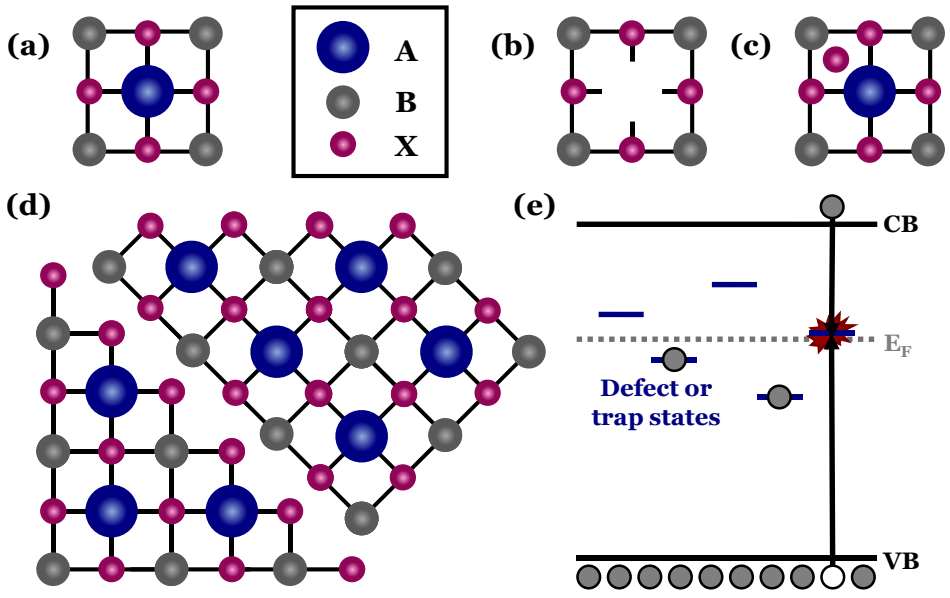


**Figure 2-12. Crystallographic defects in the cubic perovskite lattice of A, B, and X ions: (a) a perfect lattice (b) a vacancy (c) an interstitial (d) a grain boundary. (e) Trap states in the middle of the bandgap. Recombination of an electron from the conduction band and a hole from the valence band can be facilitated by a trap state.**

Larger scale structural defects such as steps and dislocations are also possible. Grain boundaries are prevalent defects in the polycrystalline thin films in this thesis, and are depicted in Figure 2-12(d).

These defects create their own energy levels known as defect or trap states, as illustrated in Figure 2-12(e). Trap states can be detected by measuring absorption below the bandgap energy. If a trap state is 'shallow', then thermal energy is sufficient to promote any trapped charge to the closest band edge, and the trap behaves like a dopant state. On the other hand, 'deep' trap states central in the bandgap usually retain a significant population of electrons. A high density of trapped electrons can pin the Fermi level among the trap states.

As well as trapping otherwise mobile charges, trap states can act as recombination centres for an electron from the conduction band and a hole from the valence band. Trap-mediated recombination is typically non-radiative and reduces the density of photoexcited charge carriers, and therefore the quasi-Fermi level splitting, making these trap states detrimental to the operation of photovoltaic devices.

## 2.6 Operating principles of photovoltaic devices

### 2.6.1 Semiconductor junctions

In order for photoexcited charges to be used as current in a photovoltaic device, they must be fully separated, and collected at opposite contacts. By sandwiching a semiconductor between carefully selected contact materials, it is possible to create a spatial asymmetry in the central semiconductor material which drives the charges away from the point of excitation towards the contacts, where they are collected. Such an 'asymmetric junction' is depicted in Figure 2-13, where the central semiconductor is a perovskite material, and the contact materials are either n- or p-type. The device is completed by metallic contacts to the circuit on either side.

 

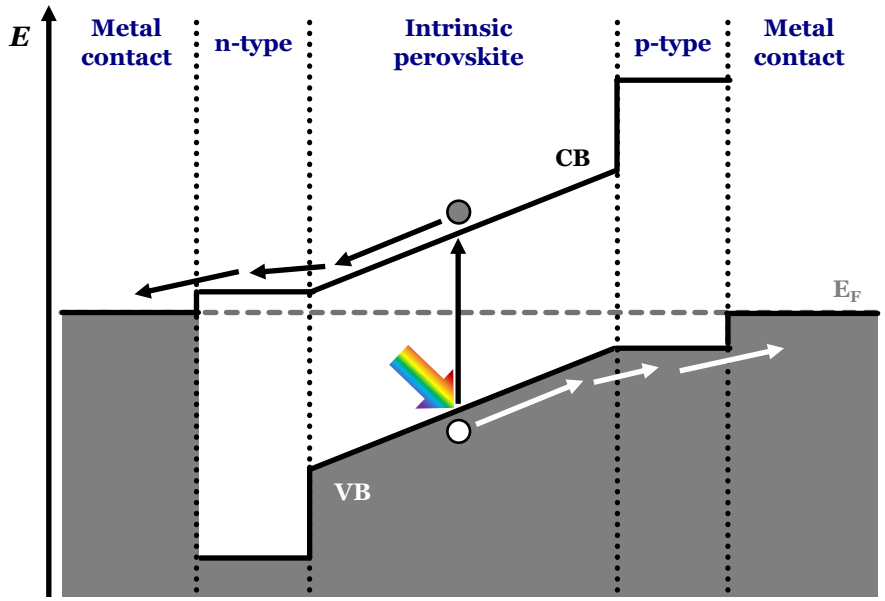


**Figure 2-13. An idealized n-i-p semiconductor junction used in perovskite photovoltaic devices. Charges are generated by sunlight (rainbow arrow), and are pulled to the contacts by the built-in voltage. This diagram shows short-circuit conditions; band bending at the interfaces is omitted for clarity.**

The Fermi levels of the different materials align on contact, leading to an asymmetry or built-in voltage across the device. Under illumination, photoexcited charges are generated in the perovskite layer and are immediately pulled to either the n- or p-type charge extraction layers and metallic contacts by the asymmetry. In Figure 2-13, the metallic contacts are at the same voltage, which is called short-circuit conditions (to be described more fully in the next section). Applying a voltage difference across the device enables power to be generated under illumination.

### 2.6.2 Photovoltaic device characterisation

A photovoltaic device is like a battery which requires light to operate, and so is often called a 'solar cell'. However, unlike the usual battery cell which is a voltage source, an illuminated solar cell behaves like a current source.

 

To characterise a solar cell, a bias voltage sweep is applied to the device while it is illuminated with 1 sun equivalent of light, and the generated current is measured. Such a bias sweep typically results in a current density – voltage (J-V) curve as illustrated in Figure 2-14. There are four key characteristics of a PV device which can be determined from the J-V curve under illumination: the short-circuit current density, $J_{SC}$, the open-circuit voltage, $V_{OC}$, the fill factor, $FF$, and the efficiency, $\eta$. These parameters will be defined and discussed in the following paragraphs along with other important parameters.

The short-circuit current density, $J_{SC}$, is the current per unit area which flows through the device when the terminals of the illuminated device are connected together. The magnitude of the current density depends on the spectrum of the incident light, and on the quantum efficiency of the cell. The quantum efficiency is

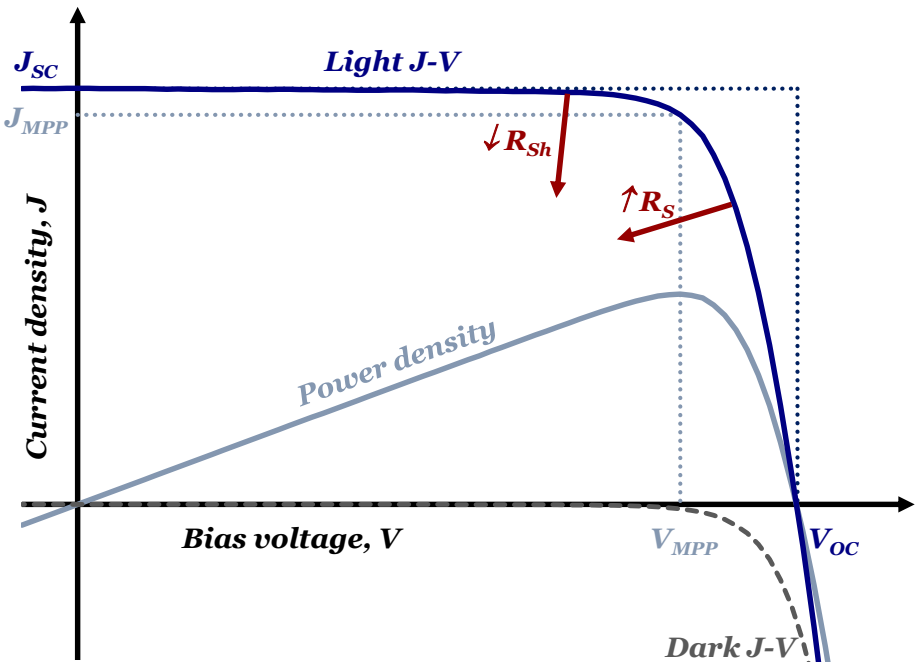


**Figure 2-14. Characteristic current density – voltage (J-V) curves under illumination (Light J-V) and in the dark (Dark J-V), along with the power density calculated from the Light J-V. See text for further definitions.**

a measure of the probability of a photon of a certain wavelength generating an electron which reaches the contacts and is extracted successfully. Recalling Figure 2-9(a), a semiconductor with a small bandgap will absorb more photons and generate a larger current density than a wider-bandgap semiconductor under the same illumination, assuming a similar quantum efficiency.

When a solar cell is under load, a small current flows through the device even in the dark. Because of the asymmetric junction required for charge extraction, a good solar cell is rectifying, and the 'dark current' (*Dark J-V* in Figure 2-14) typically follows diode-like behaviour. The characteristic J-V curve under illumination (*Light J-V* in Figure 2-14) can then be considered an approximate superposition of the short-circuit current density, $J_{SC}$, with the Dark J-V. This is described by Equation 2-9 for an ideal diode, where $J_0$ is some constant, $q$ is the electronic charge, $k_B$ is Boltzmann's constant, and $T$ is the temperature in Kelvin.

$$J(V) = J_{SC} - J_0(e^{qV/mk_BT} - 1) \qquad \textbf{Equation 2-9}$$

In reality, solar cells deviate significantly from ideal diode behaviour due to parasitic series and shunt resistances. Series resistance, $R_S$, originates from low conductivity within the semiconductor materials and at the junctions between them, and ideally should be as small as possible. Shunt resistance, $R_{Sh}$, should be as high as possible but is reduced by pinholes in the semiconductor layers and direct leakage between contacts. These resistances reduce the squareness of the J-V curve as depicted by the red arrows in Figure 2-14.

The open-circuit voltage, $V_{OC}$, is the voltage that develops across an illuminated solar cell when the terminals of the device are isolated. The magnitude of this voltage is set by the difference in quasi-Fermi levels of electrons and holes (recall Figure 2-9(c) and $E = qV$), and is always less than $E_g/q$. In a real perovskite solar cell the loss in open-circuit voltage compared to $E_g/q$ is typically at least 360 mV.[37]

 

A solar cell generates power for positive voltages up to the open-circuit voltage. The power density is then the product of current density and voltage, for which there is a maximum power point ($V_{MPP}$,$J_{MPP}$). A simple measurement of operational stability termed 'stabilised power output' (SPO) is to hold the device at $V_{MPP}$ and monitor any change in $J_{MPP}$.

The fill factor, $FF$, defines the 'squareness' of the J-V curve, and is calculated by:

$$FF = \frac{J_{MPP}V_{MPP}}{J_{SC}V_{OC}} \qquad \text{Equation 2-10}$$

Fill factors are typically around 60-70% for perovskite solar cells,[31,37] although there are a few reports of fill factors over 80%.[38–40]

The efficiency, $\eta$, of the device is then the power delivered at the maximum power point, in comparison with the power, $P_S$, supplied by the light source, according to Equation 2-11.

$$\eta = \frac{J_{MPP}V_{MPP}}{P_S} = \frac{J_{SC}V_{OC}FF}{P_S} \qquad \text{Equation 2-11}$$

Hence these four parameters form the characteristic measurements for solar cells.

In order to compare solar cell performance between different laboratories, standard test conditions have been defined as an incident power density, $P_S$, of 1000 W m$^{-2}$ from a spectrum known as 'AM1.5G', at a temperature of 25 °C. Here AM 1.5 specifies the spectrum of sunlight that has reached Earth's surface after travelling through the air mass, AM, of Earth's atmosphere on a path that is 1.5 times the shortest (normal incidence) path length. This path corresponds to a solar zenith angle of 48.2°. The suffix G for 'Global' radiation specifies that the sunlight collected includes both direct and scattered sunlight, and the current standard for the AM1.5 G spectrum is ASTM G173-03.[41] Solar simulators rarely supply this

 

spectrum and so must be calibrated to account for the mismatch between AM1.5G and the supplied spectrum.

### 2.6.3 Tandem solar cells

From the above discussion it is evident that a solar cell with an absorbing layer from a narrow bandgap semiconductor absorbs many photons and so generates a large current but a low voltage due to the small bandgap. Conversely, a wide bandgap solar cell absorbs fewer photons and generates a smaller current but a larger voltage. In between these extremes there is an optimal bandgap where it is possible to achieve the highest power output from a single semiconductor material, which for the AM1.5G spectrum is around 1.4 eV.[3]

In practice, more power can be generated from the AM1.5G spectrum by using at least two semiconductor materials, in what is called a 'tandem solar cell'. A schematic of a tandem solar cell with three semiconductors is shown in Figure 2-15(a). Here the three semiconductors are each made into individual solar cells in a vertical stack with the widest bandgap on top and the narrowest on the bottom. The high energy sunlight is absorbed by the upper wide-bandgap cell(s), and the lower energy sunlight is transmitted through to the bottom cell(s). The individual cells can be made on separate substrates with two terminals for each cell, or made sequentially on the same substrate (monolithic) with only two terminals for the stack. The 2-terminal configuration is technically more challenging and requires current matching between layers.

Figure 2-15(b) shows the portions of the AM1.5G solar spectrum absorbed by each layer; note that the lowest bandgap cell would also absorb the blue and green photons if they were not absorbed by the layers above, and so generates a smaller current when in the tandem stack. While the voltage of each cell is also slightly lowered by filtering from the cells above, overall the tandem solar cell produces a

 

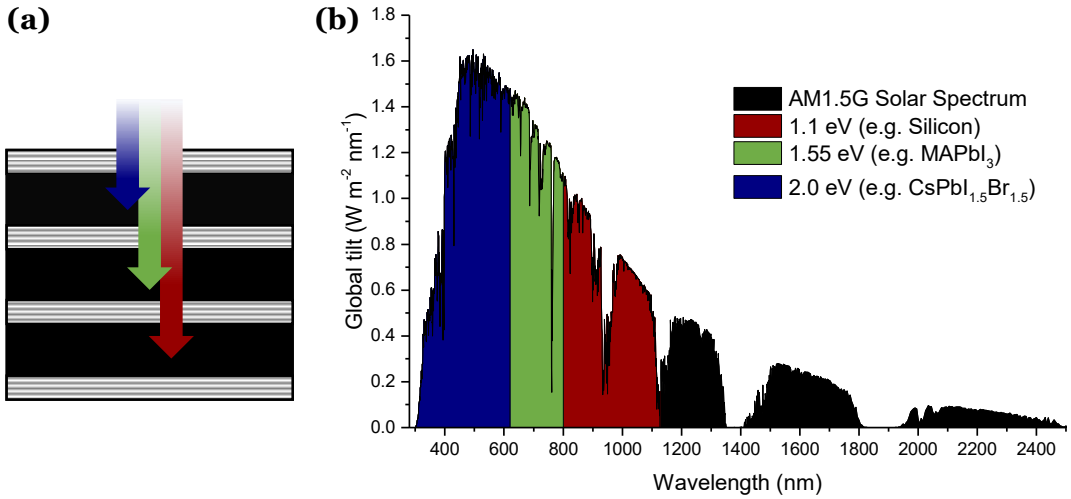


**Figure 2-15. (a) A diagrammatic representation of a triple-junction tandem solar cell with three different semiconductors, which each absorb part of the solar spectrum (coloured arrows), separated by charge transport interlayers. (b) The AM1.5G solar spectrum (black), with shading to show which part is absorbed by each of the semiconductor layers in (a). The bandgaps (and possible materials) for each semiconductor layer are given in the legend.**

voltage near the summation of the voltages of the individual solar cells. As well as increasing the overall power output, this higher voltage is also more useable. In research labs, tandem solar cells with five junctions have achieved efficiencies of nearly 39% and voltages over 4 V.[42]

The perovskite materials discussed in this thesis are semiconductors with bandgaps of 1.7 to 2.3 eV which have great potential for use in the top cell of a tandem solar cell.[43] The optimal bandgaps for each cell are interrelated, and depend on the number of junctions in the tandem solar cell. The maximal PCEs for two junctions have been calculated for a range of bandgaps for top and bottom cells, and are shown diagrammatically in Figure 2-16 for 2-terminal and 4-terminal junctions.[44,45]

Narrow-bandgap materials suitable for use as absorbers in the bottom cell include silicon, copper indium gallium (di)selenide (CIGS), and mixed lead-tin perovskites. These materials have bandgaps from 1.1 to around 1.25 eV, which give optimal

 

bandgaps of 1.7-1.8 eV for the top cell in 2-terminal configuration, and a wider range of possible top cell bandgaps for the 4-terminal configuration.[44,45]

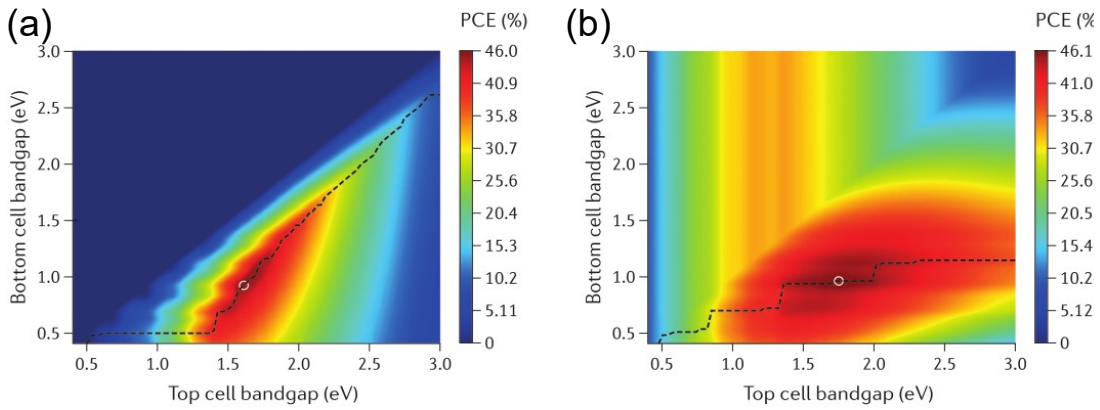


**Figure 2-16. Theoretical maximum PCEs for (a) 2-terminal and (b) 4-terminal tandem solar cells with bandgaps between 0.5 and 3.0 eV for each of the top and bottom cells. The black line indicates the maximum efficiency for a given top cell bandgap, and the white circle shows the overall highest efficiency. Adapted from Ref. 44. © Springer Nature.**

## 2.7 A brief history of perovskite photovoltaics

Perovskite solar cells emerged out of dye-sensitised solar cells by simply replacing the light-absorbing dye with a thin layer of perovskite ($MAPbI_3$ or $MAPbBr_3$), as depicted in Figure 2-17(a).[46] In this configuration, a mesoporous titania ($TiO_2$) layer provides both a physical scaffold for the thin layer of dye or perovskite as well as immediate collection of electrons generated in the light-absorbing layer, and charge balance is provided by a redox couple in the electrolyte. The perovskite layer is deposited from a solution of the precursor salts (methylammonium halide and lead(II) halide), and crystallises as nanocrystals within the pores of the titania scaffold.

Replacing the dye with perovskite was partially successful, and initial efficiencies were over 3%.[46] However, the devices degraded rapidly during operation due to the

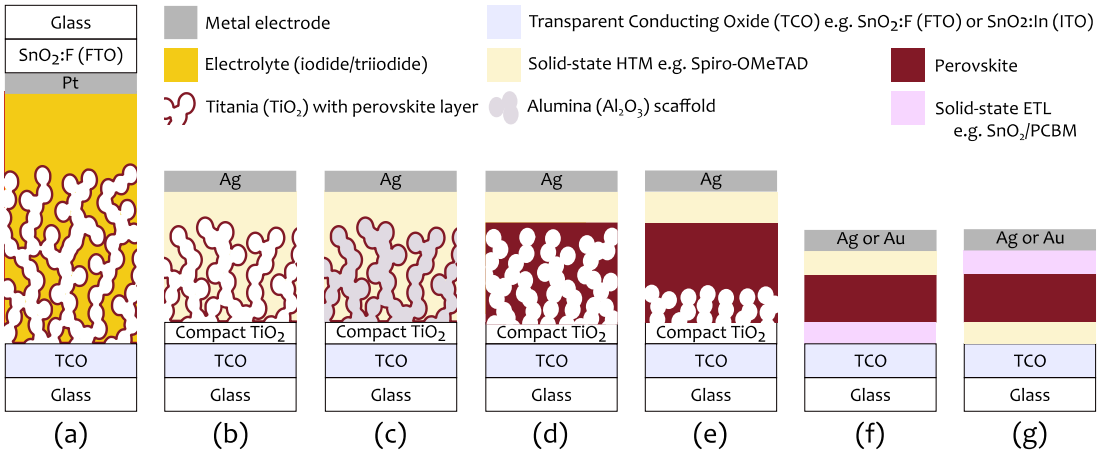


**Figure 2-17. The evolution of the perovskite solar cell, as described in the main text. (a) Perovskite-sensitised solar cell with hole transport provided by an electrolyte. (b) Solid-state perovskite-sensitised solar cell. (c) Meso-superstructured solar cell. (d) Fully-infiltrated mesoporous scaffold. (e) Mesoporous scaffold with thick perovskite capping layer. (f) and (g) Planar solar cells in n-i-p and p-i-n architectures respectively, where the n and p layers can be a variety of materials, both organic and inorganic. Adapted from Ref. 52.**

corrosive electrolyte layer used as a hole transport mechanism in the device architecture.[47] This problem was eventually solved by using a solid-state architecture with doped organic materials such as polypyrrole or 2,2′,7,7′-tetrakis(*N*,*N*-di-*p*-methoxyphenyl-amine)9,9′-spirobifluorene (Spiro-OMeTAD) as a solid hole-transporting layer (HTM).[48,49] In this solid-state configuration, depicted in Figure 2-17(b), perovskite-sensitised devices achieved efficiencies over 9%.[50,51]

Intriguingly, improved performance up to 10.9% was demonstrated for an insulating scaffold made of alumina ($Al_2O_3$) rather than titania, shown in Figure 2-17(c).[53] The alumina-scaffolded devices were termed 'meso-superstructured solar cells' (MSSCs), and the fact that these devices worked at all showed that the perovskite layer has excellent charge transport properties. Indeed, it is perhaps surprising that these perovskite materials achieved such high efficiencies with so little optimisation. In most other polycrystalline semiconductors prepared with such simple processing

 

methods, there is a high density of defects with associated defect energy levels which typically lead to increased non-radiative recombination.[54] However, it was later revealed that while there are intrinsic defects in $MAPbI_3$, these defects form shallow trap states.[55,56] These trap states are predominantly inactive due to the relatively low energy of the longitudinal optical phonons which correspond to Pb-halide modes.[57,58]

From this finding, the amount of expensive solid-state hole transport material needed was minimised by fully infiltrating the mesoporous scaffold with perovskite, as in Figure 2-17(d), which led to progressively thinner mesoporous layers with thick perovskite capping layers, as in Figure 2-17(e). Over time, the need for a mesoporous scaffold has been eliminated, leading to the era of 'planar' thin-film perovskite solar cells. These can take the two configurations shown in Figure 2-17(f) and (g), where electrons are collected either from the bottom or the top of the device respectively.

Although planar thin film solar cells were not a new concept,[59] to make a working planar solar cell with a perovskite layer providing light absorption, charge generation and ambipolar charge transport requires a continuous and high-quality thin film of perovskite. Typically the perovskite layer is deposited by solution processing methods such as spin-coating (see Figure 2-18) for which planar films pose a significant challenge: the mesoporous scaffold enables a continuous film with relative ease, but without a scaffold, dewetting of the film leads to uneven film thickness or island-like growth, especially when forming the film in ambient air.[60,61] While holey films can be useful, for example in semi-transparent solar cells,[62] the operational efficiency is significantly lower than with a continuous film, and initial attempts at removing the scaffold reduced the device efficiency from over 12% to less than 5%.[63]

 

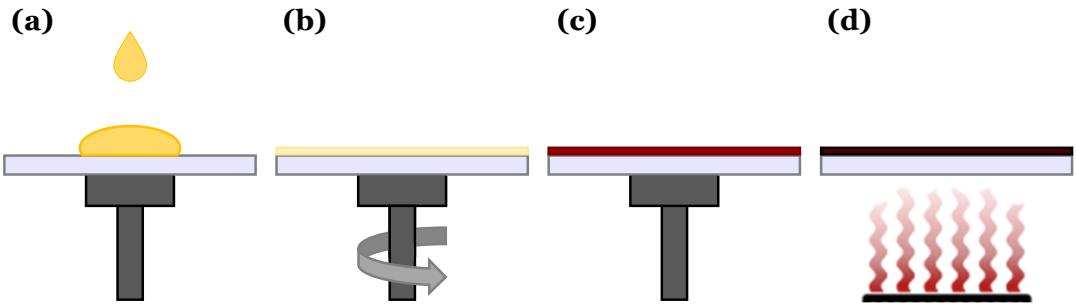


**Figure 2-18. The spin-coating technique for solution-based film deposition. (a) A substrate is secured to a chuck by vacuum, and the solution is dropped onto the centre. (b) The chuck begins to spin, accelerating to at least 2000 rpm, which spreads the solution into a thin wet film. (c) As the film dries, the precursors begin to crystallise. (d) The film is annealed on a hot plate to finish crystallization.**

To circumvent the technical challenge of solution processing a continuous thin film, the first high-efficiency planar perovskite solar cells were fabricated by vapour deposition.[61] In this method, the two precursor salts (e.g. methylammonium halide and lead(II) halide) are deposited from heated crucibles onto the substrate under vacuum, as shown in Figure 2-19. The temperatures of the crucibles are carefully adjusted to control the deposition rates of the precursors, such that the resulting film has the correct stoichiometry. This method produces a perovskite layer with highly uniform and easily tuneable thickness, which in devices gave over 15% efficiency, far outperforming the best solution processed equivalent at the time.[61] These high-efficiency solar cells inspired many researchers around the globe to take on the challenge of fabricating planar perovskite solar cells, leading to further optimisation of both vapour deposition and solution processing methods for perovskite film deposition.

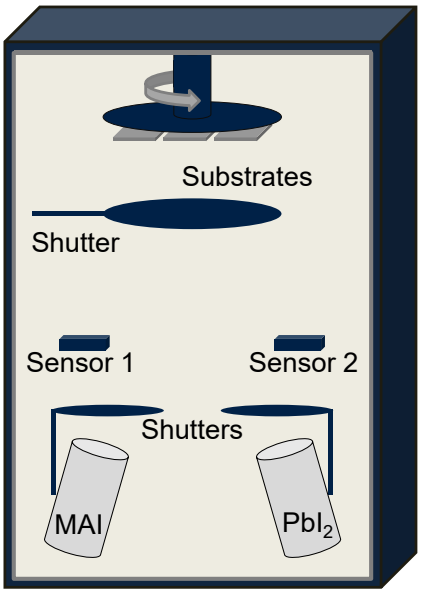


**Figure 2-19. A typical vapour deposition chamber, which is evacuated to pressures around $10^{-5}$ mbar. Crucibles filled with precursor materials such as methylammonium iodide (MAI) and lead iodide ($PbI_2$) are heated and the rate of evaporation monitored by sensors. Deposition of the material onto the substrate is controlled by at least one shutter and may be simultaneous (co-evaporation) or sequential. Substrates are loaded upside-down and may be temperature controlled and/or rotated during deposition.**

Optimisation of the perovskite solar cell also extended to exploration of different device architectures. During the time of this thesis, both 'n-i-p' and 'p-i-n' architectures have been tested, leading to rapid advancements in power conversion efficiency. A wide variety of electron-transport materials (ETMs) and hole-transport materials (HTMs) have been explored, both organic and inorganic. In addition to titania, electron-transport layers now include tin oxide ($SnO_2$), zinc oxide (ZnO), and fullerene-based organic materials such as $C_{60}$ and PCBM (phenyl-$C_{61}$-butyric acid methyl ester).[64–69] Spiro-OMeTAD remains the standard hole-transport material, despite its costly synthesis and poor thermal stability.[70,71] Spiro-OMeTAD also requires careful doping to gain sufficiently conductive layers for solar cell operation that do not react with the perovskite layer.[72,73] Alternative organic HTMs are numerous, and include small molecules and polymers such as PEDOT:PSS (poly(3,4-ethylenedioxythiophene) polystyrene sulfonate) and PTAA (poly(triarylamine)).[7,74] Worth mentioning here is a versatile, stable and low-cost HTM formed of a composite layer of a network of functionalised carbon nanotubes infiltrated with a protective polymer such as polycarbonate (PC) or PMMA

 

(poly(methyl methacrylate)).[71,75] Inorganic hole transport layers include nickel oxide, copper iodide and copper thiocyanate, which all have high thermal stability.[67,70,76,77]

While there are many options for transport materials, the optimal device architecture usually depends on the composition and processing conditions of the perovskite layer. For example, each subsequent layer requires orthogonal solvents to avoid washing away existing layers. In the iodide-based inorganic solar cells discussed in this thesis, high-temperature processing conditions for the perovskite layer limit the underlying charge transport layer to metal oxides with high thermal stability. Sensitivity to air restricts charge transport layers above the perovskite layer to those which do not require exposure to air to achieve full doping. These constraints are significant hurdles to achieving high efficiency devices with iodide-based inorganic perovskites.

During exploration of different device architectures, it was noticed that some perovskite solar cells showed hysteresis.[30,69,78,79] Specifically, the J-V curve would differ depending on the scan direction, scan speed, and the history of the device (pre-biasing/light-soaking), as in Figure 2-20(a). This effect misled researchers into reporting artificially inflated efficiencies when compared with stabilised power output measurements.

The origin of the hysteresis phenomenon is believed to arise from ion migration within perovskite materials, in combination with charge trapping, or surface recombination, at the perovskite interfaces within the device.[78–80] The most likely culprits for ion migration are point defects of halide ions (both vacancies and interstitials).[54] The timescale for hysteresis can be anywhere from seconds to hours, which is compatible with ion migration.[30,81]

 

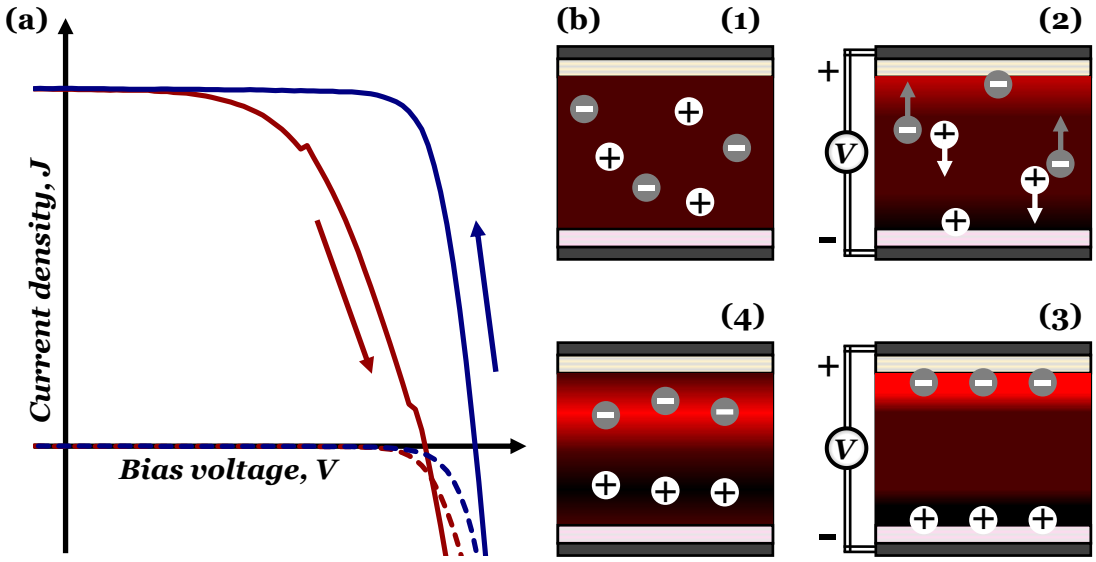


**Figure 2-20. (a) A J-V scan showing hysteresis in a pre-biased n-i-p perovskite solar cell: the reverse scan (blue) is 'better' than the forward scan (red) for both the light J-V (solid lines) and the dark J-V (dashed lines). (b) A possible mechanism for hysteresis in perovskite solar cells is through both ion migration and trap filling: 1. The as-made device has a uniform distribution of mobile ions (+ and −) and trap states (not shown). 2. Applied bias causes movement of ions towards n-type (pink) or p-type (yellow) contacts, accompanied by mobile charge carriers of the opposite charge (red or black shading). 3. Ions and mobile charge carriers build up at the contacts, compensating the applied bias and filling all available trap states. 4. Ions and mobile charges slowly dissipate from the contacts once the applied bias is removed, allowing the trap states to be depopulated and repopulated again.**

A possible mechanism for hysteresis is illustrated in Figure 2-20(b).[79,80] For clarity, only the n-type interface is considered in the following discussion, as it may be assumed that the equivalent process occurs at the p-type interface with mobile ions and charge carriers of opposite sign. Initially there is a uniform distribution of mobile ions and trap states throughout the film. Application of a large positive applied bias voltage causes positively-charged mobile ions to move towards the n-type charge extraction layer (contact). These ions form a layer at the interface between the perovskite layer and the contact. Simultaneously, mobile electrons

 

(either photo-excited or injected from the contacts) are attracted to these positive ions, and holes are repelled, leading to an increased density of electrons at the interface. This effective n-type doping of the interface aids charge extraction at the contact, and the high density of electrons means that all available traps are populated. In the absence of a significant hole density to enable trap-assisted recombination, this region of the perovskite layer acts as if it is trap-free, resulting in ideal diode behaviour when the reverse scan is commenced. As the voltage bias is released during the reverse scan, the ions and mobile charges slowly return to a uniform distribution and trap-assisted recombination recommences. Hysteresis in the forward scan then reveals whether the perovskite layer contains a significant density of trap states. It should be noted that a simpler explanation of ion migration with no trap filling would result in hysteresis in FF but not in voltage.

As well as optimisation of the device architecture and efficiency, considerable research has gone into the perovskite material itself, especially in the last four years. During the time of this thesis, the library of perovskite absorbers for solar cells has been extended significantly. Of particular importance has been the emergence of the inorganic metal halide perovskites as promising candidates for photovoltaic and optoelectronic applications. This thesis presents significant advances in the development of these inorganic metal halide perovskites as stable absorber materials for photovoltaics.

## 2.8 References

1. Kittel, C. *Introduction to Solid State Physics*; 8th ed.; John Wiley & Sons, Inc., 2005.
2. Harrison, W. A. *Electronic Structure and the Properties of Solids*; Dover.; 1989.
3. Nelson, J. *The Physics of Solar Cells*; Imperial College Press: London, 2008.
4. McMeekin, D. P.; Sadoughi, G.; Rehman, W.; Eperon, G. E.; Saliba, M.; Horantner, M. T.; Haghighirad, A.; Sakai, N.; Korte, L.; Rech, B.; Johnston, M. B.; Herz, L. M.; Snaith, H. J. "A Mixed-Cation Lead Mixed-Halide Perovskite Absorber for Tandem Solar Cells". *Science* 2016, *351*, 151–155.
5. Bu, T.; Liu, X.; Zhou, Y.; Yi, J.; Huang, X.; Luo, L.; Xiao, J.; Ku, Z.; Peng, Y.; Huang, F.; Cheng, Y.-B.; Zhong, J. "A Novel Quadruple-Cation Absorber for

 

Universal Hysteresis Elimination for High Efficiency and Stable Perovskite Solar Cells". *Energy Environ. Sci.* 2017, *10*, 2509–2515.

6. Eperon, G. E.; Leijtens, T.; Bush, K. A.; Prasanna, R.; Green, T.; Wang, J. T.-W.; McMeekin, D. P.; Volonakis, G.; Milot, R. L.; May, R.; Palmstrom, A.; Slotcavage, D. J.; Belisle, R. A.; Patel, J. B.; Parrott, E. S.; Sutton, R. J.; Ma, W.; Moghadam, F.; Conings, B.; et al. "Perovskite-Perovskite Tandem Photovoltaics with Optimized Band Gaps". *Science* 2016, *354*, 861–865.
7. Klug, M. T.; Osherov, A.; Haghighirad, A. A.; Stranks, S. D.; Brown, P. R.; Bai, S.; Wang, J. T.-W.; Dang, X.; Bulović, V.; Snaith, H. J.; Belcher, A. M. "Tailoring Metal Halide Perovskites through Metal Substitution: Influence on Photovoltaic and Material Properties". *Energy Environ. Sci.* 2017, *131*, 6050–6051.
8. Volonakis, G.; Filip, M. R.; Haghighirad, A. A.; Sakai, N.; Wenger, B.; Snaith, H. J.; Giustino, F. "Lead-Free Halide Double Perovskites via Heterovalent Substitution of Noble Metals". 2016.
9. Milot, R. L.; Sutton, R. J.; Eperon, G. E.; Haghighirad, A. A.; Martinez Hardigree, J.; Miranda, L.; Snaith, H. J.; Johnston, M. B.; Herz, L. M. "Charge-Carrier Dynamics in 2D Hybrid Metal–Halide Perovskites". *Nano Lett.* 2016, *16*, 7001–7007.
10. Smith, I. C.; Hoke, E. T.; Solis-Ibarra, D.; McGehee, M. D.; Karunadasa, H. I. "A Layered Hybrid Perovskite Solar-Cell Absorber with Enhanced Moisture Stability". *Angew. Chemie* 2014, *126*, 11414–11417.
11. Goldschmidt, V. M. "Die Gesetze Der Krystallochemie". *Naturwissenschaften* 1926, *14*, 477–485.
12. Saparov, B.; Mitzi, D. B. "Organic–Inorganic Perovskites: Structural Versatility for Functional Materials Design". *Chem. Rev.* 2016, *116*, 4558–4596.
13. Travis, W.; Glover, E. N. K.; Bronstein, H.; Scanlon, D. O.; Palgrave, R. G. "On the Application of the Tolerance Factor to Inorganic and Hybrid Halide Perovskites: A Revised System". *Chem. Sci.* 2016, *7*, 4548–4556.
14. Woodward, P. M.; IUCr. "Octahedral Tilting in Perovskites. I. Geometrical Considerations". *Acta Crystallogr. Sect. B Struct. Sci.* 1997, *53*, 32–43.
15. Lufaso, M. W.; Woodward, P. M. "Jahn-Teller Distortions, Cation Ordering and Octahedral Tilting in Perovskites Jahn±Teller Distortions, Cation Ordering and Octahedral Tilting in Perovskites". *Chem. Fac. Publ.* 2004, *3*.
16. Glazer, A. M. "The Classification of Tilted Octahedra in Perovskites". *Acta Crystallogr. Sect. B Struct. Crystallogr. Cryst. Chem.* 1972, *28*, 3384–3392.
17. Lufaso, M. W.; Woodward, P. M. "Prediction of the Crystal Structures of Perovskites Using the Software Program SPuDS". *Acta Crystallogr. Sect. B Struct. Sci.* 2001, *57*, 725–738.
18. Linaburg, M. R.; McClure, E. T.; Majher, J. D.; Woodward, P. M. "$Cs_{1-x}Rb_xPbCl_3$ and $Cs_{1-x}Rb_xPbBr_3$ Solid Solutions: Understanding Octahedral Tilting in Lead Halide Perovskites". *Chem. Mater.* 2017, *29*, 3507–3514.
19. Hammond, C. *Introduction to Crystallography*; Revised.; Oxford University Press: Oxford, UK., 1992.
20. Beimborn, J. C.; Hall, L. M. G.; Tongying, P.; Dukovic, G.; Weber, J. M. "Pressure Response of Photoluminescence in Cesium Lead Iodide Perovskite Nanocrystals". *J. Phys. Chem. C* 2018, *122*, 11024–11030.

 

21. Shannon, R. D. "Revised Effective Ionic Radii and Systematic Studies of Interatomic Distances in Halides and Chalcogenides". *Acta Crystallogr. Sect. A* 1976, *32*, 751–767.

22. Whitfield, P. S.; Herron, N.; Guise, W. E.; Page, K.; Cheng, Y. Q.; Milas, I.; Crawford, M. K. "Structures, Phase Transitions and Tricritical Behavior of the Hybrid Perovskite Methyl Ammonium Lead Iodide". *Sci. Rep.* 2016, *6*, 35685.

23. Sharma, S.; Weiden, N.; Weiss, A. "Phase Diagrams of Quasibinary Systems of the Type: $ABX_3$ — $A'BX_3$; $ABX_3$ — $AB'X_3$, and $ABX_3$ — $ABX'_3$; X = Halogen". *Zeitschrift für Phys. Chemie* 1992, *175*, 63–80.

24. Stoumpos, C. C.; Malliakas, C. D.; Peters, J. A.; Liu, Z.; Sebastian, M.; Im, J.; Chasapis, T. C.; Wibowo, A. C.; Chung, D. Y.; Freeman, A. J.; Wessels, B. W.; Kanatzidis, M. G. "Crystal Growth of the Perovskite Semiconductor $CsPbBr_3$: A New Material for High-Energy Radiation Detection". *Cryst. Growth Des.* 2013, *13*, 2722–2727.

25. Trots, D. M.; Myagkota, S. V. "High-Temperature Structural Evolution of Caesium and Rubidium Triiodoplumbates". *J. Phys. Chem. Solids* 2008, *69*, 2520–2526.

26. Zeier, W. G.; Zevalkink, A.; Gibbs, Z. M.; Hautier, G.; Kanatzidis, M. G.; Snyder, G. J. "Thinking Like a Chemist: Intuition in Thermoelectric Materials". *Angew. Chemie Int. Ed.* 2016, *55*, 6826–6841.

27. Angilella, G. G. N.; March, N. H.; Howard, I. A.; Pucci, R. "Pressure Dependence of the Energy Gaps in Diamond-Type Semiconductors, and Their III-V Analogues such as InSb". *J. Phys. Conf. Ser.* 2008, *121*, 32006.

28. Paul, W. "Band Structure of the Intermetallic Semiconductors from Pressure Experiments". *J. Appl. Phys.* 1961, *32*, 2082–2094.

29. Fahy, S.; Chang, K. J.; Louie, S. G.; Cohen, M. L. "Pressure Coefficients of Band Gaps of Diamond". *Phys. Rev. B* 1987, *35*, 5856–5859.

30. Eperon, G. E.; Paternò, G. M.; Sutton, R. J.; Zampetti, A.; Haghighirad, A. A.; Cacialli, F.; Snaith, H. J. "Inorganic Caesium Lead Iodide Perovskite Solar Cells". *J. Mater. Chem. A* 2015, *3*, 19688–19695.

31. Sutton, R. J.; Eperon, G. E.; Miranda, L.; Parrott, E. S.; Kamino, B. A.; Patel, J. B.; Hörantner, M. T.; Johnston, M. B.; Haghighirad, A. A.; Moore, D. T.; Snaith, H. J. "Bandgap-Tunable Cesium Lead Halide Perovskites with High Thermal Stability for Efficient Solar Cells". *Adv. Energy Mater.* 2016, *6*, 1502458.

32. Kulbak, M.; Cahen, D.; Hodes, G. "How Important Is the Organic Part of Lead Halide Perovskite Photovoltaic Cells? Efficient $CsPbBr_3$ Cells". *J. Phys. Chem. Lett.* 2015, *6*, 2452–2456.

33. Filip, M. R.; Eperon, G. E.; Snaith, H. J.; Giustino, F. "Steric Engineering of Metal-Halide Perovskites with Tunable Optical Band Gaps". *Nat. Commun.* 2014, *5*, 5757.

34. Tilley, R. J. D. *Perovskites: Structure-Property Relationships*; John Wiley & Sons, Incorporated, 2016.

35. Hwang, H. Y.; Cheong, S.-W.; Radaelli, P. G.; Marezio, M.; Batlogg, B. "Lattice Effects on the Magnetoresistance in Doped $LaMnO_3$". *Phys. Rev. Lett.* 1995, *75*, 914–917.

36. Green, M. A. "Improved Value for the Silicon Free Exciton Binding Energy". *AIP Adv.* 2013, *3*, 112104.

37. Noel, N. K.; Congiu, M.; Ramadan, A. J.; Fearn, S.; McMeekin, D. P.; Patel, J. B.;

 

Johnston, M. B.; Wenger, B.; Snaith, H. J. "Unveiling the Influence of pH on the Crystallization of Hybrid Perovskites, Delivering Low Voltage Loss Photovoltaics". *Joule* 2017, *1*, 328–343.

38. Stolterfoht, M.; Wolff, C. M.; Amir, Y.; Paulke, A.; Perdigón-Toro, L.; Caprioglio, P.; Neher, D. "Approaching the Fill Factor Shockley–Queisser Limit in Stable, Dopant-Free Triple Cation Perovskite Solar Cells". *Energy Environ. Sci.* 2017, *10*, 1530–1539.
39. Yang, W. S.; Park, B.-W.; Jung, E. H.; Jeon, N. J.; Kim, Y. C.; Lee, D. U.; Shin, S. S.; Seo, J.; Kim, E. K.; Noh, J. H.; Seok, S. Il. "Iodide Management in Formamidinium-Lead-Halide–based Perovskite Layers for Efficient Solar Cells". *Science* 2017, *356*.
40. Wu, C.-G.; Chiang, C.-H.; Tseng, Z.-L.; Nazeeruddin, M. K.; Hagfeldt, A.; Grätzel, M. "High Efficiency Stable Inverted Perovskite Solar Cells without Current Hysteresis". *Energy Environ. Sci.* 2015, *8*, 2725–2733.
41. A.S.T.M. International. "ASTM G173-03(2012)". *Standard Tables for Reference Solar Spectral Irradiances: Direct Normal and Hemispherical on 37° Tilted Surface*, 2012.
42. Green, M. A.; Hishikawa, Y.; Warta, W.; Dunlop, E. D.; Levi, D. H.; Hohl-Ebinger, J.; Ho-Baillie, A. W. H. "Solar Cell Efficiency Tables (Version 50)". *Prog. Photovoltaics Res. Appl.* 2017, *25*, 668–676.
43. Hörantner, M. T.; Snaith, H. "Predicting and Optimising the Energy Yield of Perovskite-on-Silicon Tandem Solar Cells under Real World Conditions". *Energy Environ. Sci.* 2017.
44. Eperon, G. E.; Hörantner, M. T.; Snaith, H. J. "Metal Halide Perovskite Tandem and Multiple-Junction Photovoltaics". *Nat. Rev. Chem.* 2017, *1*, 95.
45. Hörantner, M. T.; Leijtens, T.; Ziffer, M. E.; Eperon, G. E.; Christoforo, M. G.; McGehee, M. D.; Snaith, H. J. "The Potential of Multijunction Perovskite Solar Cells". *ACS Energy Lett.* 2017, *2*, 2506–2513.
46. Kojima, A.; Teshima, K.; Shirai, Y.; Miyasaka, T. "Organometal Halide Perovskites as Visible-Light Sensitizers for Photovoltaic Cells". *J. Am. Chem. Soc.* 2009, *131*, 6050–6051.
47. Im, J.-H.; Lee, C.-R.; Lee, J.-W.; Park, S.-W.; Park, N.-G. "6.5% Efficient Perovskite Quantum-Dot-Sensitized Solar Cell". *Nanoscale* 2011, *3*, 4088.
48. Bach, U.; Lupo, D.; Comte, P.; Moser, J. E.; Weissörtel, F.; Salbeck, J.; Spreitzer, H.; Grätzel, M. "Solid-State Dye-Sensitized Mesoporous $TiO_2$ Solar Cells with High Photon-to-Electron Conversion Efficiencies". *Nature* 1998, *395*, 583–585.
49. Murakoshi, K.; Kogure, R.; Wada, Y.; Yanagida, S. "Solid State Dye-Sensitized $TiO_2$ Solar Cell with Polypyrrole as Hole Transport Layer". *Chem. Lett.* 1997, *26*, 471–472.
50. Kim, H.-S.; Lee, C.-R.; Im, J.-H.; Lee, K.-B.; Moehl, T.; Marchioro, A.; Moon, S.-J.; Humphry-Baker, R.; Yum, J.-H.; Moser, J. E.; Grätzel, M.; Park, N.-G. "Lead Iodide Perovskite Sensitized All-Solid-State Submicron Thin Film Mesoscopic Solar Cell with Efficiency Exceeding 9%.". *Sci. Rep.* 2012, *2*, 591.
51. Lee, M. M.; Teuscher, J.; Miyasaka, T.; Murakami, T. N.; Snaith, H. J. "Efficient Hybrid Solar Cells Based on Meso-Superstructured Organometal Halide Perovskites.". *Science* 2012, *338*, 643–647.
52. Snaith, H. J. "Perovskites: The Emergence of a New Era for Low-Cost, High-

Efficiency Solar Cells". *J. Phys. Chem. Lett.* 2013, *4*, 3623–3630.

53. Lee, M. M.; Teuscher, J.; Miyasaka, T.; Murakami, T. N.; Snaith, H. J. "Efficient Hybrid Solar Cells Based on Meso-Superstructured Organometal Halide Perovskites". *Science* 2012, *338*, 643–647.

54. Ball, J. M.; Petrozza, A. "Defects in Perovskite-Halides and Their Effects in Solar Cells". *Nat. Energy* 2016, *1*, 16149.

55. Yin, W.-J.; Shi, T.; Yan, Y. "Unique Properties of Halide Perovskites as Possible Origins of the Superior Solar Cell Performance". *Adv. Mater.* 2014, *26*, 4653–4658.

56. Brandt, R. E.; Stevanović, V.; Ginley, D. S.; Buonassisi, T. "Identifying Defect-Tolerant Semiconductors with High Minority-Carrier Lifetimes: Beyond Hybrid Lead Halide Perovskites". *MRS Commun.* 2015, *5*, 265–275.

57. Sendner, M.; Nayak, P. K.; Egger, D. A.; Beck, S.; Müller, C.; Epding, B.; Kowalsky, W.; Kronik, L.; Snaith, H. J.; Pucci, A.; Lovrinčić, R. "Optical Phonons in Methylammonium Lead Halide Perovskites and Implications for Charge Transport". *Mater. Horizons* 2016, *3*, 613–620.

58. Kirchartz, T.; Markvart, T.; Rau, U.; Egger, D. A. "Impact of Small Phonon Energies on the Charge-Carrier Lifetimes in Metal-Halide Perovskites". *J. Phys. Chem. Lett.* 2018, *9*, 939–946.

59. Chopra, K. L.; Paulson, P. D.; Dutta, V. "Thin-Film Solar Cells: An Overview". *Prog. Photovoltaics Res. Appl.* 2004, *12*, 69–92.

60. Eperon, G. E.; Habisreutinger, S. N.; Leijtens, T.; Bruijnaers, B. J.; van Franeker, J. J.; DeQuilettes, D. W.; Pathak, S.; Sutton, R. J.; Grancini, G.; Ginger, D. S.; Janssen, R. A. J.; Petrozza, A.; Snaith, H. J. "The Importance of Moisture in Hybrid Lead Halide Perovskite Thin Film Fabrication". *ACS Nano* 2015, *9*, 9380–9393.

61. Liu, M.; Johnston, M. B.; Snaith, H. J. "Efficient Planar Heterojunction Perovskite Solar Cells by Vapour Deposition.". *Nature* 2013, *501*, 395–398.

62. Eperon, G. E.; Burlakov, V. M.; Goriely, A.; Snaith, H. J. "Neutral Color Semitransparent Microstructured Perovskite Solar Cells". *ACS Nano* 2014, *8*, 591–598.

63. Ball, J. M.; Lee, M. M.; Hey, A.; Snaith, H. J. "Low-Temperature Processed Meso-Superstructured to Thin-Film Perovskite Solar Cells". *Energy Environ. Sci.* 2013, *6*, 1739.

64. Song, J.; Zheng, E.; Bian, J.; Wang, X.-F.; Tian, W.; Sanehira, Y.; Miyasaka, T. "Low-Temperature $SnO_2$-Based Electron Selective Contact for Efficient and Stable Perovskite Solar Cells". *J. Mater. Chem. A* 2015, *3*, 10837–10844.

65. Ke, W.; Fang, G.; Liu, Q.; Xiong, L.; Qin, P.; Tao, H.; Wang, J.; Lei, H.; Li, B.; Wan, J.; Yang, G.; Yan, Y. "Low-Temperature Solution-Processed Tin Oxide as an Alternative Electron Transporting Layer for Efficient Perovskite Solar Cells". *J. Am. Chem. Soc.* 2015, *137*, 6730–6733.

66. Liu, D.; Kelly, T. L. "Perovskite Solar Cells with a Planar Heterojunction Structure Prepared Using Room-Temperature Solution Processing Techniques". *Nat. Photonics* 2013, *8*, 133–138.

67. You, J.; Meng, L.; Song, T.-B.; Guo, T.-F.; Yang, Y. (Michael); Chang, W.-H.; Hong, Z.; Chen, H.; Zhou, H.; Chen, Q.; Liu, Y.; De Marco, N.; Yang, Y. "Improved Air Stability of Perovskite Solar Cells via Solution-Processed Metal Oxide Transport

 

Layers". *Nat. Nanotechnol.* 2015, *11*, 75–81.

68. Hörantner, M. T.; Nayak, P. K.; Mukhopadhyay, S.; Wojciechowski, K.; Beck, C.; McMeekin, D. P.; Kamino, B.; Eperon, G. E.; Snaith, H. J. "Shunt-Blocking Layers for Semitransparent Perovskite Solar Cells". *Adv. Mater. Interfaces* 2016, 1500837.
69. Momblona, C.; Gil-Escrig, L.; Bandiello, E.; Hutter, E. M.; Sessolo, M.; Lederer, K.; Blochwitz-Nimoth, J.; Bolink, H. J. "Efficient Vacuum Deposited P-I-N and N-I-P Perovskite Solar Cells Employing Doped Charge Transport Layers". *Energy Environ. Sci.* 2016, *9*, 3456–3463.
70. Madhavan, V. E.; Zimmermann, I.; Roldán-Carmona, C.; Grancini, G.; Buffiere, M.; Belaidi, A.; Nazeeruddin, M. K. "Copper Thiocyanate Inorganic Hole-Transporting Material for High-Efficiency Perovskite Solar Cells". *ACS Energy Lett.* 2016, *1*, 1112–1117.
71. Habisreutinger, S. N.; Leijtens, T.; Eperon, G. E.; Stranks, S. D.; Nicholas, R. J.; Snaith, H. J. "Carbon Nanotube/polymer Composites as a Highly Stable Hole Collection Layer in Perovskite Solar Cells". *Nano Lett.* 2014, *14*, 5561–5568.
72. Nguyen, W. H.; Bailie, C. D.; Unger, E. L.; McGehee, M. D. "Enhancing the Hole-Conductivity of Spiro-OMeTAD without Oxygen or Lithium Salts by Using Spiro(TFSI)$_2$ in Perovskite and Dye-Sensitized Solar Cells". *J. Am. Chem. Soc.* 2014, *136*, 10996–11001.
73. Pellaroque, A.; Noel, N. K.; Habisreutinger, S. N.; Zhang, Y.; Barlow, S.; Marder, S. R.; Snaith, H. J. "Efficient and Stable Perovskite Solar Cells Using Molybdenum Tris(dithiolene)s as P-Dopants for Spiro-OMeTAD". *ACS Energy Lett.* 2017, 2044–2050.
74. Shin, S. S.; Yeom, E. J.; Yang, W. S.; Hur, S.; Kim, M. G.; Im, J.; Seo, J.; Noh, J. H.; Seok, S. Il. "Colloidally Prepared La-Doped $BaSnO_3$ Electrodes for Efficient, Photostable Perovskite Solar Cells". *Science* 2017, *356*, 167–171.
75. Habisreutinger, S. N.; Leijtens, T.; Eperon, G. E.; Stranks, S. D.; Nicholas, R. J.; Snaith, H. J. "Enhanced Hole Extraction in Perovskite Solar Cells Through Carbon Nanotubes". *J. Phys. Chem. Lett.* 2014, *5*, 4207–4212.
76. Christians, J. A.; Fung, R. C. M.; Kamat, P. V. "An Inorganic Hole Conductor for Organo-Lead Halide Perovskite Solar Cells. Improved Hole Conductivity with Copper Iodide". *J. Am. Chem. Soc.* 2014, *136*, 758–764.
77. Arora, N.; Dar, M. I.; Hinderhofer, A.; Pellet, N.; Schreiber, F.; Zakeeruddin, S. M.; Grätzel, M. "Perovskite Solar Cells with CuSCN Hole Extraction Layers Yield Stabilized Efficiencies Greater than 20.". *Science* 2017, *358*, 768–771.
78. Snaith, H. J.; Abate, A.; Ball, J. M.; Eperon, G. E.; Leijtens, T.; Noel, N. K.; Stranks, S. D.; Wang, J. T.; Wojciechowski, K.; Zhang, W. "Anomalous Hysteresis in Perovskite Solar Cells". *J. Phys. Chem. Lett.* 2014, 1511–1515.
79. Tress, W.; Marinova, N.; Moehl, T.; Zakeeruddin, S. M.; Mohammad K., N.; Grätzel, M. "Understanding the Rate-Dependent J-V Hysteresis, Slow Time Component, and Aging in $CH_3NH_3PbI_3$ Perovskite Solar Cells: The Role of a Compensated Electric Field". *Energy Environ. Sci.* 2015.
80. van Reenen, S.; Kemerink, M.; Snaith, H. J. "Modeling Anomalous Hysteresis in Perovskite Solar Cells". *J. Phys. Chem. Lett.* 2015, *6*, 3808–3814.
81. Saliba, M. "Perovskite Solar Cells Must Come of Age". *Science* 2018, *359*, 388–389.

 

# 3 Experimental Methods

This chapter outlines the synthetic procedures for perovskite thin-film, powder, and device preparation pertinent to the chapters in this thesis containing experimental results. Deviations from these procedures not stated here are described in the relevant results chapter.

## 3.1 Materials

All materials were purchased from Sigma-Aldrich, Alfa Aesar or DyeSol (Greatcell Solar) and used as received unless stated otherwise. Pre-oxidised Spiro (Spiro-TFSI) was synthesised in-house by Martina Congiu, from Spiro-OMeTAD from Borun Chemicals or Lumtec, following a literature procedure.[1] In brief, SpiroOMeTAD was stirred at room temperature for 24 h in degased dichloromethane under nitrogen atmosphere, with an excess of silver bis(trifluoromethanesulfonyl)imide (at least 1:2 ratio by mol). The reaction product was dissolved in methylene chloride, filtered, and dried using rotary evaporation. The dark green solid was purified by dissolution in a minimal amount of dichloromethane followed by precipitation in dry diethyl ether. The resulting powder was collected using a filter and purified twice more, followed by vacuum drying before use.

 

## 3.2 Preparation of perovskite thin films

### 3.2.1 $CsPb(I_xBr_{1-x})_3$ and $MAPb(I_xBr_{1-x})_3$ single step solution process

$PbI_2$, $PbBr_2$, MAI, and/or CsI were dissolved in DMF in the appropriate molar ratios to give a 0.43 M precursor solution of $CsPb(I_xBr_{1-x})_3$ or $MAPb(I_xBr_{1-x})_3$. The precursor solution was prepared and used in a nitrogen-filled dry glovebox ($H_2O$ < 0.1 ppm). To form perovskite films, the precursors were spin-coated at 1500 rpm for 45 seconds. The films were then annealed at 330-350 °C (100 °C for $MAPbI_2Br$) for 10 minutes.

### 3.2.2 $CsPb(I_xBr_{1-x})_3$ two-step dip conversion

Lead bromide was prepared as a concentrated solution in DMF (1.6 g $PbBr_2$ in 4.4 mL DMF stirred at 70 °C for 30 mins then filtered with a 0.2 um PTFE filter), and deposited by spin-coating at 2500 rpm for 60 s onto FTO substrates with both compact and mesoporous $TiO_2$ layers (see Section 3.4.2). The $PbBr_2$ layer was dried at 70 °C, dipped into a solution of CsI and/or CsBr in methanol (on hotplate at 70 °C) for ten minutes, and then washed with isopropanol and dried with nitrogen. The films were annealed at 250 °C for 10 minutes, with an additional 3 minutes at 350 °C for the iodide-rich films, and cooled to room temperature in a controlled humidity atmospheric chamber at 20-25% RH.

### 3.2.3 $CsPbBr_3$ two-step vapour deposition

The precursor salts, $PbBr_2$ and CsBr, were loaded into separate baffle boxes (rectangular deep tungsten boats with holey lids) in a BOC Edwards Auto 306 evaporator, along with clean glass microscope slides as substrates. The evaporator was evacuated to a pressure below $6 \times 10^{-6}$ mbar before beginning deposition. Sequential layers of $PbBr_2$ (107 nm) and CsBr (93 nm) were each deposited at 1-

 

2 Å/s onto the room-temperature substrates, with either two or four layers in total, to give 200 nm or 400 nm thick films. The $CsPbBr_3$ perovskite was formed by annealing the films at 250 °C on a hotplate in air for 10 minutes.[2]

### 3.2.4 $CsPbI_3$ for structure determination

*HT:* CsI and $PbI_2$ were dissolved at 0.8 M in DMF:DMSO 2:1 by volume, where DMSO is dimethyl sulfoxide. Films were spincoated at 500 rpm for 10 s with a 10 s ramp, followed by 20 s at 1500 rpm, with nitrogen quenching and chlorobenzene drench during the second step. The black phase was formed by a 1 minute anneal at 350 °C followed by rapid cooling to room temperature.

*LT:* CsI and $PbI_2$ were dissolved at 0.5 M in N,N-dimethylformamide (DMF), and 33 µL hydriodic acid (57% w/w Sigma Aldrich) per mL solution was added immediately before spincoating. To gain films that were sufficiently thick but still fully converted to black, films were spincoated at 500 rpm for 10 s with a 10 s ramp, followed by 20 s at 1500 rpm with nitrogen quenching to dry the film. The black phase was formed by a 1 minute anneal at 105 °C.

All processes were performed in a glovebox filled with nitrogen gas. Films for optical characterisation were spincoated with a higher spin speed of 2000 rpm for the second step to obtain a higher optical clarity of the resulting films. To obtain scratched powders, the films were scratched from glass substrates using razor blades.

### 3.2.5 $Cs(Pb,Mg)I_3$ single step solution process

$CsPbI_3$ and $CsMgI_3$ were dissolved separately at 0.3 M in DMF, and hydriodic acid (21 µL/mL) was added to the two stock solutions. Mixed solutions were prepared immediately before spin-coating; the solutions with 10-25% Mg were found to precipitate colourless crystals after ~1 month. Films were spin-coated at 1500 rpm for 45 s in nitrogen atmosphere and annealed at 100 °C for 10 mins.

 

## 3.3 Preparation of perovskite materials by solid state synthesis

High-purity precursor salts were weighed into a mortar in stoichiometric amounts, and ground together with a pestle for 25-30 minutes by hand. The ground powder was transferred to a quartz ampoule and evacuated, ensuring a good vacuum before the ampoule was sealed. The sealed ampoule was sintered and/or melted in a furnace at least once, and cooled slowly in the furnace as it cooled or removed from the furnace and cooled rapidly by splashing small amounts of water on the ampoule. The heat treatment process is depicted in Figure 3-1.

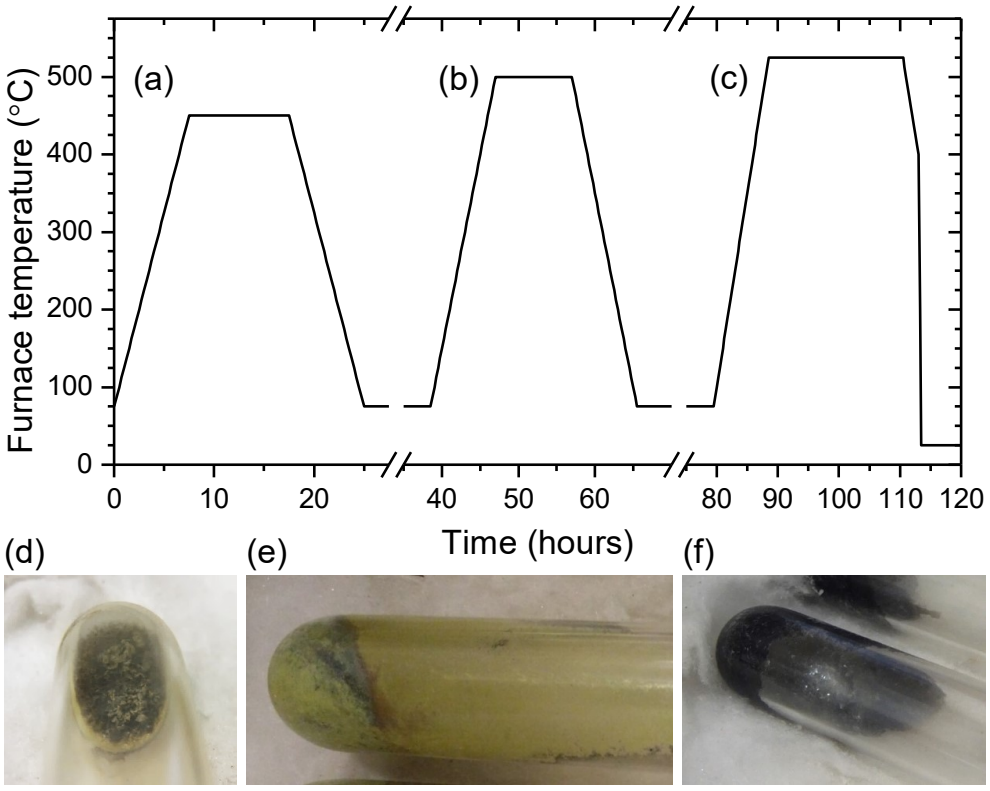


**Figure 3-1. Temperature profiles for solid state synthesis by (a) sintering and slow cooling, (b) melting and slow cooling, or (c) melting and rapid cooling. Photographs of the ampoules resulting from (d) sintering, (e) slow cooling from the melt, (f) rapid cooling from the melt.**

For XRD analysis, each solid mass was ground into powder and reheated at 400 °C in batches, for approximately 20 s per batch (until black to the eye), before being transferred to a piece of room temperature aluminium foil to cool quickly. Figure 3-2 illustrates the preparation of a powder sample in the black perovskite polymorph.

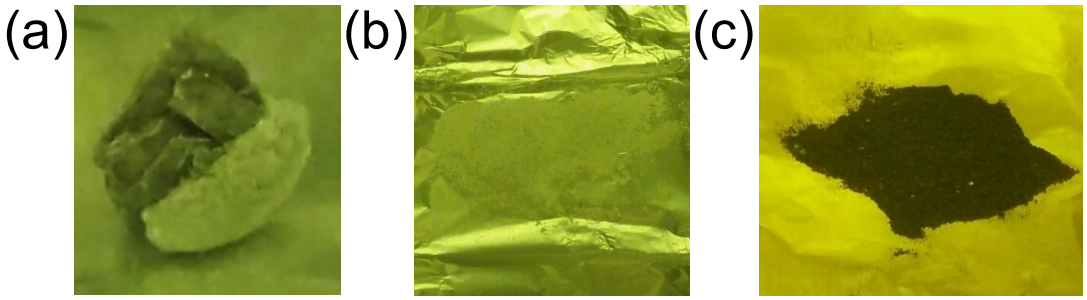


**Figure 3-2. Preparation of a powder sample from solid state synthesis for XRD. (a) A two-phase ingot resulting from slow cooling from the melt. (b) Powder ground from the yellow crystalline $CsPbI_3$ part of the ingot. (c) The black $CsPbI_3$ powder produced by heating the yellow powder to 400 °C briefly before rapid cooling.**

## 3.4 Photovoltaic device fabrication

### 3.4.1 Substrate preparation

Fluorine doped tin oxide (FTO)-coated glass substrates (Pilkington, 7 Ω $\square^{-1}$) were patterned using HCl and zinc powder to etch the FTO, with scotch tape masking. The etched substrates were cleaned sequentially with detergent, de-ionized water, acetone and isopropanol, followed by oxygen plasma treatment for 5-10 minutes immediately before deposition of the next layer.

### 3.4.2 Inorganic compact and mesoporous layer deposition

The compact (c-) $TiO_2$ layer was spin-coated (2000 rpm for 60 s) from a mildly acidic solution of titanium isopropoxide in anhydrous ethanol with 12 mM HCl

 

added, and sintered at 500 °C for 45 minutes. For the best $TiO_2$-based devices, the spin-coated and sintered c-$TiO_2$ layer was immersed in a 15 mM aqueous solution of $TiCl_4$ for 60 minutes at 70 °C and sintered again at 500 °C. For mesoporous (m-) devices, 230 nm or 400 nm mesoporous $TiO_2$ was deposited on the sintered spincoated $TiO_2$ layer by spin-coating at 2000 rpm a 1:4 or 1:3 dilution (by weight) of Dyesol 18NR-T paste:ethanol. This was then annealed by heating slowly to 500 °C then holding for 30 mins.

### 3.4.3 Perovskite layer deposition

The various methods of deposition of the perovskite thin films were described in Section 3.2.

### 3.4.4 Organic charge transport layer deposition

Pre-oxidised Spiro-OMeTAD (Spiro) layers were spincoated at 2000 rpm from a 0.08 M solution of SpiroOMeTAD: Spiro-TFSI 9:1 in chlorobenzene, with tert-butylpyridine (10 mL/mL).

### 3.4.5 Electrode deposition

The devices were completed by deposition of the electrodes through a shadow mask, in a Kurt J. Lesker NANO36 thermal evaporator. Typically these electrodes would consist of 80 to 120 nm of silver, or 20 nm of gold followed by 120 nm of silver.

## 3.5 Photovoltaic device characterisation

### 3.5.1 Current density-voltage (J-V) measurements

The solar cells were masked with a metal aperture to define the active area of 0.092 $cm^2$ and measured in a light-tight sample holder to minimize any edge effects and to ensure that the reference cell and test cell are located during measurement in the same spot under the solar simulator. The current density–voltage ($J$-$V$) curves

 

were measured (2400 Series SourceMeter, Keithley Instruments) under simulated AM 1.5 sunlight at 100 mW $cm^{-2}$ irradiance generated by an Abet Class AAB Sun 2000 simulator, with the intensity calibrated with an NREL calibrated KG5 filtered Si reference cell. The mismatch factor was calculated to be 1.04% over the response range of these materials. For the fast *J-V* scans, cells were scanned from forward bias to short-circuit at a rate of 0.38 V/s after holding under illumination at 1.2 V for 5 seconds. The maximum power point was determined from these fast *J-V* scans and current measured holding at this voltage for the stabilised power output SPO holding scans. All J-V curves and SPOs were measured in air.

### 3.5.2 External Quantum Efficiency (EQE) measurements

External quantum efficiency (EQE) was measured by Prof. Michael Johnston at the University of Oxford via custom-build Fourier-transform photocurrent spectrometry based on a Bruker Vertex 80v Fourier Transform Interferometer. The solar cells were illuminated with simulated sunlight (AM 1.5 sunlight, ~100 mW $cm^{-2}$) and calibrated to a Newport-calibrated reference silicon solar cell with a known external quantum efficiency. EQE was measured under nitrogen.

## 3.6 Optical characterisation

### 3.6.1 Substrate preparation

Glass slides and quartz optical discs (Spectrosil) were cleaned sequentially in acetone and isopropanol, and then treated with oxygen plasma for 5 or 10 minutes immediately before film deposition.

### 3.6.2 Absorbance measurements

Unless otherwise stated, a Varian Cary 300 UV-Vis spectrophotometer with either a nitrogen-filled optical cell or an internally-coupled integrating sphere were used to

 

acquire absorbance spectra. Samples were mounted at the entrance of the integrating sphere and a diffuse reflector was mounted at the exit port. A diagram of the integrating sphere used for the measurements in this thesis is provided in Figure 3-3.

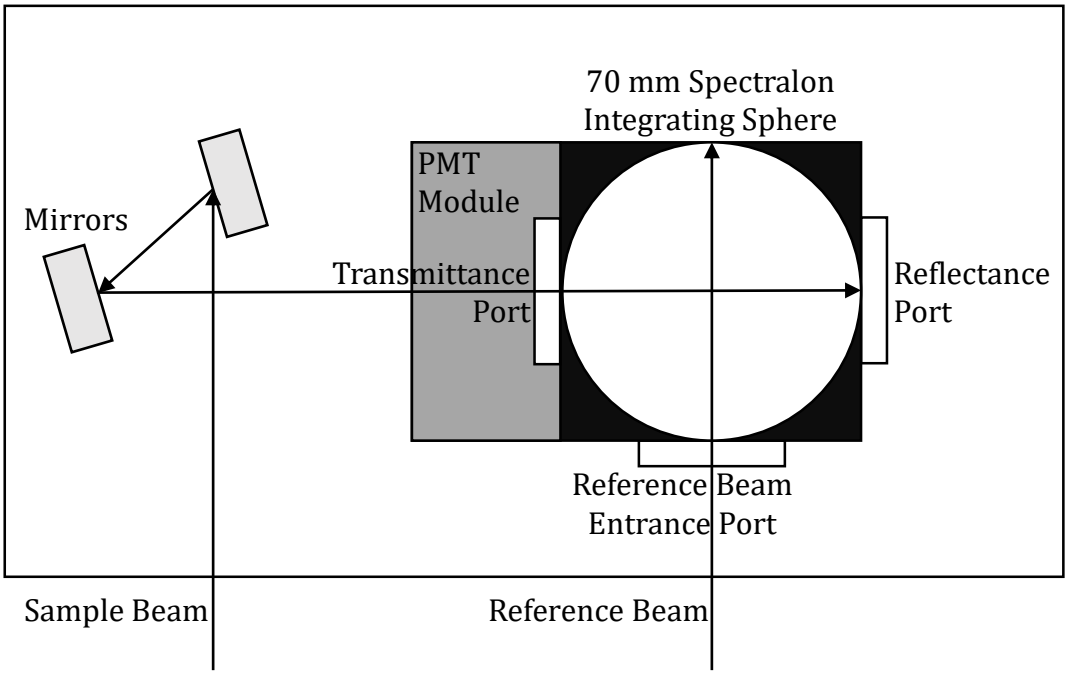


**Figure 3-3. The integrating sphere set-up used for absorption measurements of perovskite thin films. The sample is placed at the transmittance port with the perovskite film facing into the sphere, and the reflectance port is covered with a white Spectralon standard. The transmitted light is collected at the base of the sphere and detected by a photomultiplier tube (PMT) module.**

In Chapter 6, temperature-dependent absorption spectra were measured using a Perkin-Elmer Lambda 1050 UV/Vis/NIR spectrophotometer. For temperature-dependent measurements, the quartz disc with $CsPbI_3$ film was placed on a glass cover slip (with the $CsPbI_3$ thin-film in contact with the cover slip) in a temperature-controlled optical stage (Linkam THMS 600). The optical stage was purged with nitrogen and sealed before measurement.

 

### 3.6.3 Bandgap determination

Optical bandgaps $E_g$ were estimated from absorbance spectra collected with an integrating sphere via a Tauc plot. This method assumes the material is a semiconductor with a distribution of electrons which follows the Fermi-Dirac distribution. The absorption coefficient $\alpha$ then follows the relation:

$$\boldsymbol{\alpha(E) \propto (E - E_g)^{1/2}} \qquad \textbf{Equation 3-1}$$

where $E = h\nu$ is the energy of the absorbed photons in eV, and $\alpha = 10^4 \ln(10^A)$ for the measured absorbance $A$. The exponent of ½ assumes the material has a direct, allowed optical transition.

Plotting $(\alpha h\nu)^2$ against the energy in eV reveals a linear region for which extrapolation to the $x$-axis gives an estimation of the optical bandgap $E_g$. An example of this method is illustrated in Figure 3-4.

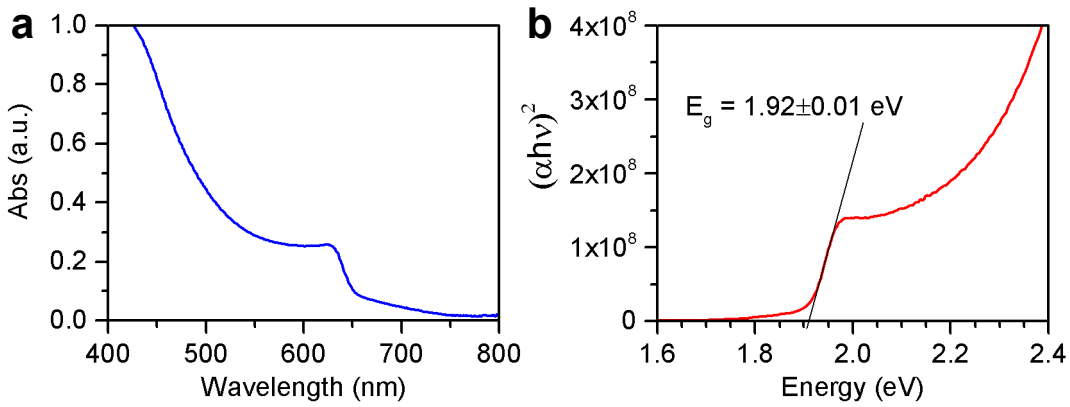


**Figure 3-4. (a) Absorbance measurement of a film of $CsPbI_2Br$, taken using an integrating sphere. (b) Corresponding Tauc plot assuming direct bandgap, showing the linear region extrapolated to intercept the energy axis to give the bandgap estimation. Errors are estimated by the sensitivity of the fitted line.**

 

Other methods of determining a bandgap include finding the steepest part of the absorption onset, by normalisation or by calculating the gradient of the absorption onset. These methods are useful as a relative measure for comparing similar films, for example if the direct or indirect nature of the bandgap is uncertain.

In Chapter 6, the onset of absorption was determined by fitting the experimental absorption spectrum with a model based on Elliott's theory.[3] This model considers both excitonic and continuum absorption. The fitting followed the formulation reported recently by Davies et al.[4] The transitions were broadened with a Gaussian function. Good agreement is obtained near the band edge. However, similar to $MAPbI_3$, the absorption spectrum strongly deviates for higher wavelength due to the presence of a higher energy transition which is not taken into account in this simplified model.

### 3.6.4 Photoluminescence measurements

Unless otherwise stated, steady-state photoluminescence (PL) measurements were collected with a Jobin-Yvon Fluorolog spectrofluorimeter with a monochromated Xenon light source, or with a Fluorescence Lifetime Spectrophotometer (Fluo Time 300, PicoQuant GmbH) with laser excitation at 405 nm.

For Chapter 4, PL measurements were made by Elizabeth Parrott at the University of Oxford where the samples were mounted in a vacuum cell with fused silica windows, maintaining a pressure of $1.2 \times 10^{-4}$ mbar, to prevent changes in the samples during measurement. The samples were excited using a tunable Ti:Sapphire pulsed laser (Mai Tai, Spectra-Physics) with a repetition rate of 80 MHz and a wavelength of 820 nm, which was frequency doubled to 410 nm using a BBO crystal. The excitation power was (290±5) µW over a spot size of approximately 0.2 $mm^2$. Further details are provided in the published manuscript.[5] These PL measurements are also shown in Chapter 5 for the $CsPbI_3$ and $CsPbI_2Br$ films.

 

### 3.6.5 Magneto-optical measurements

Magneto-optical measurements were made on thin films of the inorganic perovskites prepared at the University of Oxford. The measurements were conducted by Zhuo Yang, Krzysztof Galkowski, Alessandro Surrente, and Atsuhiko Miyata at the Laboratoire National des Champs Magnétiques Intenses (LNCMI) in Toulouse, France. For full experimental details please see the published manuscript.[2] Due to changes in the films during transit between Oxford and Toulouse, some of the films were re-annealed before being subjected to these magneto-optical measurements. $CsPbI_3$ films were annealed at 350 °C for 10 minutes, and $CsPbI_2Br$ and $CsPbBr_3$ films were annealed at 250 °C for 5 − 7 minutes using an oven (ambient atmosphere).

## 3.7 Material characterisation

### 3.7.1 Substrate preparation

Glass slides, coverslips, and FTO slides were cleaned sequentially in acetone and isopropanol, and then treated with oxygen plasma for 5 or 10 minutes immediately before film deposition.

### 3.7.2 Film surface and composition characterisation

A Hitachi S-4300 field emission scanning electron microscope was used to acquire scanning electron microscope (SEM) images. SEM with electron dispersive x-ray (EDX) analysis was performed by Dr Jason Brown using a FEI Quanta 600 FEG scanning electron microscope with an Oxford Instruments INCA Energy detector.

### 3.7.3 Film thicknesses

Sample thicknesses were measured using a Veeco Dektak 150 surface profilometer.

 

### 3.7.4 X-Ray Diffraction (XRD)

A Panalytical X'pert powder diffractometer with Cu anode X-ray source (Cu $K_{\alpha 1}$, 1.54060 Å) was used for XRD characterisation measurements of both films and powders unless otherwise stated. Anton Paar Domed Sample Holders were used for room-temperature XRD of air-sensitive films and powders in nitrogen atmosphere, as illustrated in Figure 3-5. Measurements made by Dr Laura Miranda (Oxford PV, Begbroke) used a PANalytical Empyrean PIXcel$^{1D}$ diffractometer with Cu anode, with an Anton Parr TTK450 heating stage for temperature-dependent measurements in nitrogen atmosphere.

Structural parameters were obtained by Dr Amir Abbas Haghighirad by Rietveld refinement using General Structural Analysis Software.[6,7] Single crystal data were collected for $CsPbI_3$ (non-perovskite yellow phase) at 293 K using an Agilent Supernova diffractometer that uses Mo $K_a$ beam with $\lambda = 0.71073$ Å and is fitted with an Atlas detector. Data integration and cell refinement was performed using CrysAlis Pro Software.[8] The structure was analysed by Patterson and Direct

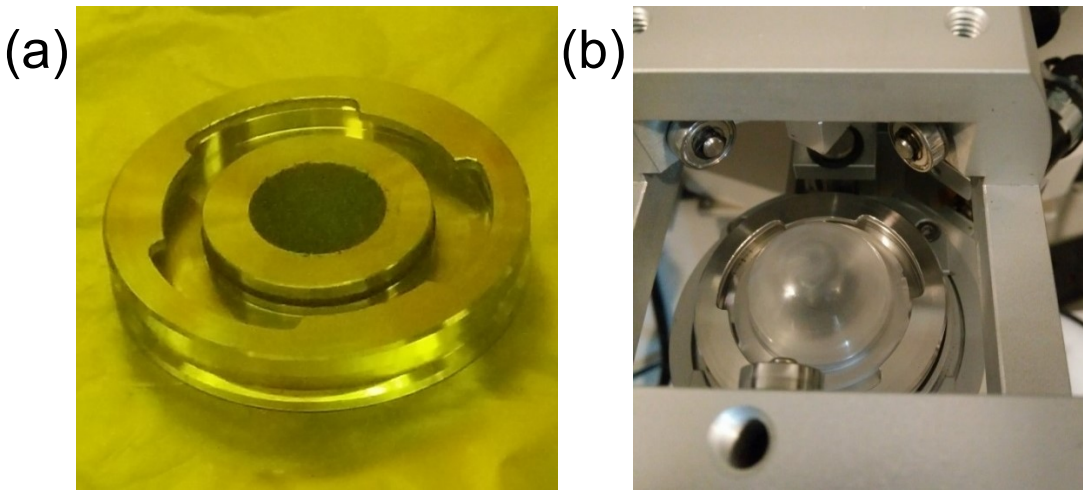


**Figure 3-5. (a) Preparation of an air-sensitive powder as a packed powder sample in an Anton Paar Domed Sample Holder for XRD. (b) The sample with transparent polycarbonate dome being loaded into the diffractometer.**

 

methods and refined using the SHELXL 2014 software package.[9]

Crystal structures were visualised and XRD patterns simulated using the 3D visualization program VESTA.[10]

### 3.7.5 Magnetic measurements

Magnetic measurements were made by Dr Dharmalingam Prabhakaran at the University of Oxford. A commercial Quantum Designs 7T MPMS SQUID (Superconducting quantum interference device magnetometer) was used to measure the magnetisation of the powder samples. Temperature dependent magnetisations were measured in the zero-field-cooled (ZFC) condition.

## 3.8 Electronic structure calculations

Electronic band structures and formation energies were calculated by Dr Marina Filip using methods as for previous calculations for $MAPbI_3$.[4] Band gap calculations, within the *GW* approximation,[11,12] include spin-orbit coupling and eigenvalue self-consistency.[13–15] The procedure used for interpolation and calculation of effective masses is described in detail in Ref. 15. All band structures and formation energies were calculated at 0 K and 0 GPa, without taking into account the effect of lattice vibrations.

## 3.9 References

1. Nguyen, W. H.; Bailie, C. D.; Unger, E. L.; McGehee, M. D. "Enhancing the Hole-Conductivity of Spiro-OMeTAD without Oxygen or Lithium Salts by Using Spiro(TFSI)$_2$ in Perovskite and Dye-Sensitized Solar Cells". *J. Am. Chem. Soc.* 2014, *136*, 10996–11001.
2. Yang, Z.; Surrente, A.; Galkowski, K.; Miyata, A.; Portugall, O.; Sutton, R. J.; Haghighirad, A. A.; Snaith, H. J.; Maude, D. K.; Plochocka, P.; Nicholas, R. J. "Impact of the Halide Cage on the Electronic Properties of Fully Inorganic Cesium Lead Halide Perovskites". *ACS Energy Lett.* 2017, *2*, 1621–1627.
3. Elliott, R. J. "Intensity of Optical Absorption by Excitons". *Phys. Rev.* 1957, *108*, 1384–1389.
4. Davies, C. L.; Filip, M. R.; Patel, J. B.; Crothers, T. W.; Verdi, C.; Wright, A. D.;

Milot, R. L.; Giustino, F.; Johnston, M. B.; Herz, L. M. "Bimolecular Recombination in Methylammonium Lead Triiodide Perovskite Is an Inverse Absorption Process". *Nat. Commun.* 2018, *9*, 293.

5. Sutton, R. J.; Eperon, G. E.; Miranda, L.; Parrott, E. S.; Kamino, B. A.; Patel, J. B.; Hörantner, M. T.; Johnston, M. B.; Haghighirad, A. A.; Moore, D. T.; Snaith, H. J. "Bandgap-Tunable Cesium Lead Halide Perovskites with High Thermal Stability for Efficient Solar Cells". *Adv. Energy Mater.* 2016, *6*, 1502458.
6. Larson, A. C.; Dreele, R. B. Von. *General Structure Analysis System (GSAS)*; Los Alamos, New Mexico, 2000.
7. Toby, B. H. "EXPGUI, a Graphical User Interface for GSAS". *J. Appl. Crystallogr.* 2001, *34*, 210–213.
8. Agilent. *CrysAlis PRO*; Agilent Technologies Ltd, Yarnton, Oxfordshire, England, 2014.
9. Sheldrick, G. M. "Crystal Structure Refinement with SHELXL". *Acta Crystallogr. Sect. C Struct. Chem.* 2015, *71*, 3–8.
10. Momma, K.; Izumi, F. "VESTA: A Three-Dimensional Visualization System for Electronic and Structural Analysis". *J. Appl. Crystallogr.* 2008, *41*, 653–658.
11. Hedin, L. "New Method for Calculating the One-Particle Green's Function with Application to the Electron-Gas Problem". *Phys. Rev.* 1965, *139*, A796–A823.
12. Hybertsen, M. S.; Louie, S. G. "Electron Correlation in Semiconductors and Insulators: Band Gaps and Quasiparticle Energies". *Phys. Rev. B* 1986, *34*, 5390–5413.
13. Marini, A.; Hogan, C.; Grüning, M.; Varsano, D. "Yambo: An Ab Initio Tool for Excited State Calculations". *Comput. Phys. Commun.* 2009, *180*, 1392–1403.
14. Filip, M. R.; Giustino, F. "GW Quasiparticle Band Gap of the Hybrid Organic-Inorganic Perovskite $CH_3NH_3PbI_3$: Effect of Spin-Orbit Interaction, Semicore Electrons, and Self-Consistency". *Phys. Rev. B* 2014, *90*, 245145.
15. Filip, M. R.; Verdi, C.; Giustino, F. "GW Band Structures and Carrier Effective Masses of $CH_3NH_3PbI_3$ and Hypothetical Perovskites of the Type $APbI_3$: A = $NH_4$, $PH_4$, $AsH_4$, and $SbH_4$". *J. Phys. Chem. C* 2015, *119*, 25209–25219.

 

# 4 Caesium Lead Halide Perovskites as Stable Materials for Perovskite Solar Cells

The work presented in this chapter has been published in:

R. J. Sutton, G. E. Eperon, L. Miranda, E. S. Parrott, B. A. Kamino, J. B. Patel, M. T. Hörantner, M. B. Johnston, A. A. Haghighirad, D. T. Moore, and H. J. Snaith, 'Bandgap-Tunable Cesium Lead Halide Perovskites with High Thermal Stability for Efficient Solar Cells', *Adv. Energy Mater.* 6, 1502458 (2016).

DOI: 10.1002/aenm.201502458

Direct link: http://doi.wiley.com/10.1002/aenm.201502458

## 4.1 Wider context and summary

Most of the research into perovskite solar cells has focussed on hybrid organic-inorganic perovskites. However, the stability of these hybrid perovskites is limited by the small organic cation required for the formation of the 3D perovskite structure. While the amount of small organic cation can be reduced and the stability increased by incorporating a large hydrophobic cation, a fundamental chemical instability remains in these materials.

To overcome the chemical instability, here the inorganic lead halide perovskites are considered. Specifically, the organic cation is fully replaced by the largest non-radioactive singly-charged alkali metal cation, caesium. However, the $Cs^+$ cation is not large enough to maintain the perovskite structure with lead and iodide at ambient conditions. In contrast, the bromide equivalent, caesium lead tribromide, has a stable perovskite structure at ambient conditions.

This chapter builds on early work on caesium lead iodide by manipulating the chemical composition to increase the stability of the resulting perovskite material. Some of the iodide ions are substituted by bromide ions, and the bandgap of the resulting solid solutions is shown to shift linearly to higher energies. This substitution lowers the energy required to form the perovskite structure and so increases the ambient stability with respect to the neat iodide. For a specific mixed halide composition, better stability is found than for the methylammonium equivalent when subjected to thermal stressing. For this optimal composition photovoltaic devices are fabricated with higher efficiency than the neat $CsPbI_3$ inorganic perovskite.

In summary, this chapter represents pioneering work in the now-blossoming field of inorganic perovskite photovoltaics.

 

## 4.2 Introduction

Hybrid organic-inorganic halide perovskite materials have been well-studied in the past few years, and solar cells using these materials have seen a rapid rise in efficiency from 3.8% to over 20% in less than 5 years.[1–4] These materials typically comprise organic cations, such as methylammonium (MA) and/or formamidinium (FA), in a lead halide framework.[5] Although these hybrid perovskite solar cells exhibit high efficiencies, the thin-film perovskite absorber layers are subject to compositional degradation due to both heat and humidity,[6] therefore, addressing the long term stability is a primary concern for the community.[7] Compositional stability under thermal stressing is particularly important for solar cell operation; for certification solar modules must be able to operate successfully between temperatures of -40 °C and +85 °C, and in some geographic locations of high solar irradiance these upper operating temperatures can be regularly reached.[8]

Although bulk powders and single crystals of $MAPbI_3$ do not undergo thermal decomposition until temperatures in excess of 200 °C,[9,10] achieving such thermal stability in thin films of the hybrid perovskites is challenging due to the high surface to volume ratio as well as the inherent instability of the organic cation. Specifically, thin films of methylammonium lead iodide thermally degrade to lead iodide at temperatures above 85 °C.[6] Formamidinium perovskites are much more thermally stable than methylammonium perovskites,[5] and it has recently been shown that thin films of mixtures of organic formamidinium and inorganic caesium (Cs) cations can be both structurally and thermally stable above 100 °C.[11,12] However, the ultimate avenue for improving the thermal compositional stability is to replace the organic component entirely with an inorganic cation such as caesium. The fully inorganic caesium lead halides have been known since their first synthesis in 1893.[13] Since the initial report, there have been many studies of the properties of caesium lead halides,[14–21] and these materials are now garnering interest from both the

 

photovoltaic and light emission communities with a few recent reports of them being used in solar cells and as emissive nanocrystals.[22–27]

These previous reports provide much insight into the compositional and structural phase stability of these inorganic perovskites. Here the phase diagram of caesium lead bromide ($CsPbBr_3$) and caesium lead iodide ($CsPbI_3$) is shown in Figure 4-1. Both of these compounds are compositionally stable up to their melting points which are in excess of 460 °C.[16] $CsPbBr_3$ crystallizes in an orthorhombic phase at room temperature, and transitions to a tetragonal perovskite phase at 88 °C and to the "orange" cubic perovskite phase at 130 °C.[21,22] In contrast, $CsPbI_3$ is stable in an orthorhombic non-perovskite structure (yellow phase) at room temperature, and changes to the cubic perovskite (black phase) when heated above ~300 °C.[14,16] Unfortunately, $CsPbI_3$ is unstable in the black perovskite phase in ambient atmosphere and rapidly converts to the non-perovskite yellow phase.[14,23]

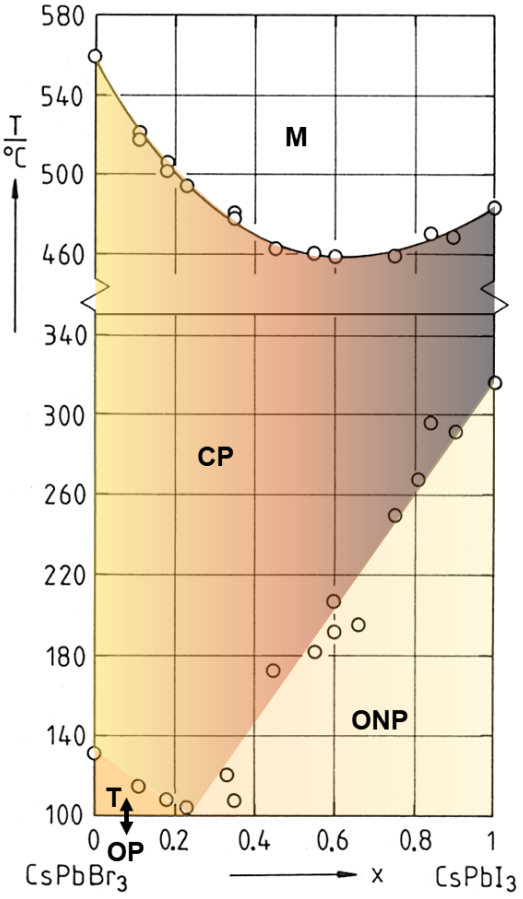


**Figure 4-1. Phase diagram of the $CsPbBr_3$ and $CsPbI_3$ solid solutions, where shading is added to represent the approximate colours of the most stable compounds at these temperatures. Key (from top): M = melt, CP = cubic perovskite, ONP = orthorhombic non-perovskite, T = tetragonal, OP = orthorhombic perovskite. Adapted from Sharma et al.[16]**

For nanocrystals on the order of 5 nm in size, these phase transitions appear to be altered such that nanocrystals of $CsPbI_3$ are more stable in the cubic phase at room temperature than bulk $CsPbI_3$, although both revert to the non-perovskite phase over time.[25] It is expected that the phase transitions in the polycrystalline films will be similar to those in the bulk. Hence, for these materials, it is apparent that the structural stability is the important parameter to resolve, rather than the compositional stability, under terrestrial solar cell operating temperatures.

In the mixed-halide region between $CsPbBr_3$ and $CsPbI_3$, solid solutions form in the bulk material, as illustrated in Figure 4-1.[16] However, for thin films, solution processing is difficult for the bromide-rich compositions, due to solubility limitations of the bromide ion. This problem was recently overcome by using a two-step method to make films of neat $CsPbBr_3$, and subsequent solar cells using $CsPbBr_3$ as the light absorbing material.[22]

Here, this two-step method is used to form the full series of caesium lead halide perovskite thin films from $CsPbBr_3$ to $CsPbI_3$. However, uniform film deposition is challenging. In contrast, a one-step solution processing route is demonstrated to create uniform thin films of caesium perovskites with high iodide content. Based on these results an appropriate mixed-halide composition with increased structural stability in ambient atmosphere is selected. With this 1.92 eV band gap material solar cells are obtained which operate in air at room temperature with close to 10% power conversion efficiency.

## 4.3 Two-step deposition of $CsPbI_{3-x}Br_x$

Initially, an adaptation of the two-step method reported by Kulbak *et al.* is demonstrated to form the full series of caesium lead halide perovskites.[22] The first step is to spin-coat lead bromide in dimethylformamide (DMF) onto a mesoporous $TiO_2$ scaffold, and dry at 70 °C. When dry, these lead bromide films are dipped for

 

ten minutes in a heated solution of the caesium halide salt(s) in methanol. These films are subsequently annealed at high temperature (250 – 350 °C), to form the cubic perovskite. Here, various ratios of CsI and CsBr are mixed in the dipping solution to obtain perovskite films with varying halide composition. The films change visibly in appearance, from orange $CsPbBr_3$ to dark brown for $CsPbI_{3-x}Br_x$ as in the photographs in Figure 4-2(a). Figure 4-2(b) shows tunable absorbance onsets of these films from 530 nm to 700 nm, consistent with solid solutions of iodide and bromide mixtures forming.

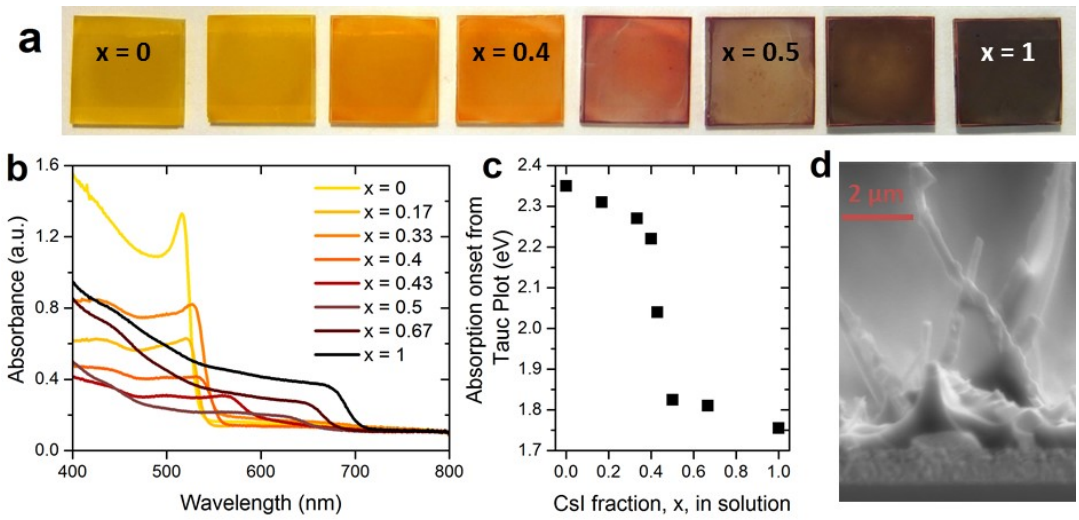


**Figure 4-2. (a) Photographs and (b) absorbance spectra for caesium lead halide perovskite films prepared by dipping lead iodide in a solution of CsBr and/or CsI in methanol, such that 'x' is the fraction of CsI in solution. (c) Absorption onsets as determined from (b) by Tauc analysis as a function of halide fraction in the dipping solution. (d) SEM image of nanowires formed when a lead bromide film is dipped into a solution of caesium iodide (x = 1).**

Intriguingly, the composition of the perovskite film is skewed towards the dominant halide in solution, as shown by the non-linear relationship in Figure 4-2(c) between absorption onset and CsI fraction 'x' in solution. All films were dipped for an equal time (10 minutes), and prior literature suggests that the possibility of ion exchange may mean that the composition is additionally dependent on dipping time.[28–30]

Although the absorbance and color of such films appears promising, Figure 4-2(d) shows scanning electron micrographs of the cross-section of the films where there is a prevalence of protruding wire-shaped crystals. This non-optimal morphology is reflected in the poor photovoltaic device efficiencies in Figure 4-3, where the best-performing devices (x=0.67 and x=1) have stable power outputs below 2%.

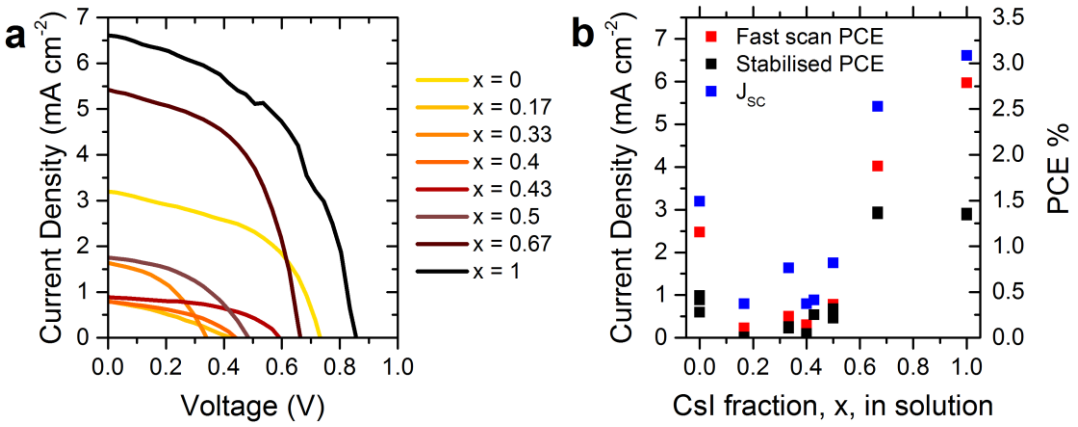


**Figure 4-3. (a) Current density-voltage (J-V) characteristics and (b) J-V (red) and stabilised (black) power conversion efficiencies, and short-circuit current density ($J_{SC}$) parameters (blue) for devices fabricated by the two-step dip-conversion method illustrated in Figure 4-2.**

## 4.4 One-step deposition of $CsPbI_{3-x}Br_x$

The device performance in Figure 4-3 is promising but severely limited by the morphology of the films produced by the two-step method. In order to obtain much smoother films, instead a one-step solution processing method is pursued. For $CsPbI_3$ the precursors are readily soluble in DMF, and subsequent spin-coating yields smooth and uniform thin films, especially with the addition of hydriodic acid (HI) which allows formation of the black phase at 100 °C.[23]

This one-step solution process may be used to form useable films with up to one third of the total halide content as bromide (denoted here as $CsPbI_2Br$); above this

 

bromide content the solubility of the bromide ion is limiting in DMF. These films were annealed at high temperature since attempts to use hydriodic and/or hydrobromic acid to lower the crystallization temperature were unsuccessful for the mixed halide compositions. Figure 4-4(a) and (b) shows absorption and luminescence (PL) spectra respectively for films of iodide/bromide mixtures from $CsPbI_3$ to $CsPbI_2Br$. A shift to shorter wavelengths is observed in the absorption onset and photoluminescence peak with increasing bromide concentration. Figure 4-4(c) plots these energies as a function of iodide content, 'x' in $CsPb(I_xBr_{1-x})_3$; the linear trend observed for the absorbance follows Vegard's law, indicating that solid solutions of the iodide-bromide mixtures are formed throughout this series. This hypothesis is supported by observations by Sharma *et al.* that the cubic lattice parameter varies linearly and the solid to liquid phase transition is continuous from caesium lead bromide to caesium lead iodide.[16] Note that for only a small amount of bromide, the photoluminescence peak is nearer the neat iodide than expected, suggesting there may be microscopic regions of inhomogeneity for this composition. To see if the iodide-bromide mixture in solution gives a film of the same composition, energy-dispersive X-ray (EDX) analysis is used to determine the iodide to bromide ratio of the composition $CsPbI_2Br$. The scanning electron microscopy (SEM) image of the film is shown in Figure 4-5, for which the EDX analysis for several spots gave the ratios Cs:Pb:I:Br = $(0.96 \pm 0.09):(1.00):(1.9 \pm 0.3):(0.95 \pm 0.13)$, normalised to the lead content.

 

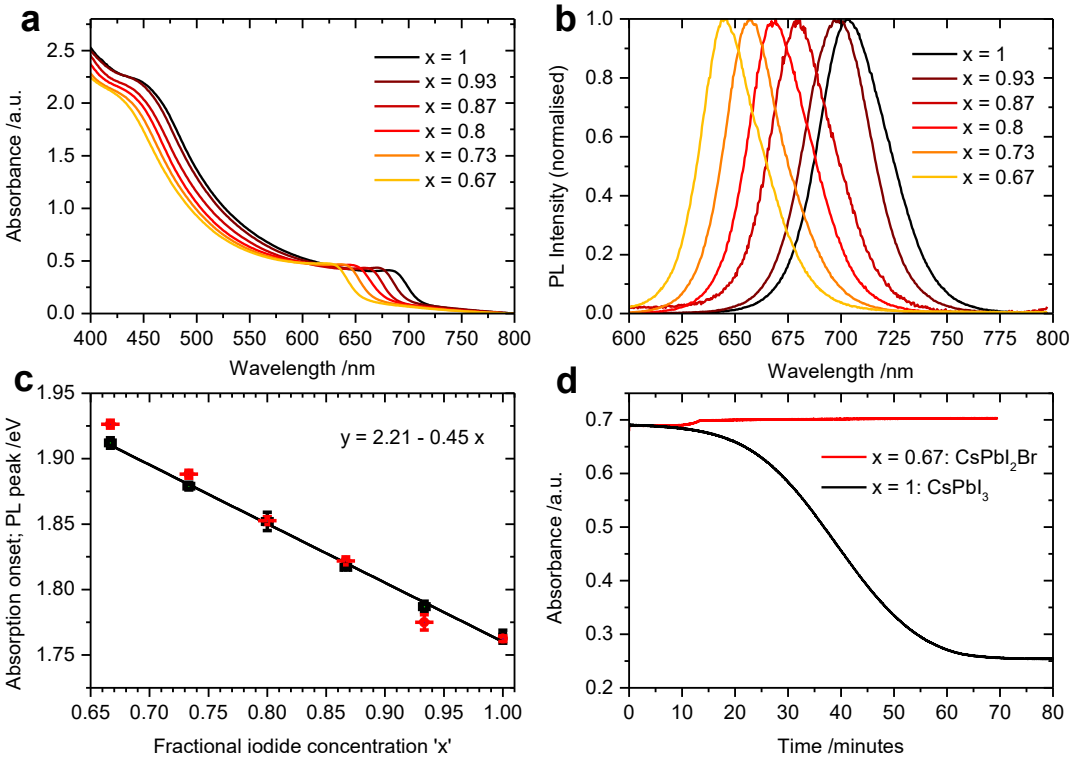


**Figure 4-4. (a) Absorbance spectra and (b) photoluminescence (PL) spectra for mixed halide $CsPb(I_xBr_{1-x})_3$ films with varying iodide concentration 'x'. These films were annealed at 330-350 °C and measured in nitrogen or under vacuum respectively. PL spectra were measured by Elizabeth Parrott at the University of Oxford, using a tunable pulsed laser at 410 nm with a spot size of ~0.2 $mm^2$. (c) Absorbance onsets (black squares), determined by Tauc plots of absorbance spectra taken with an integrating sphere, and PL peak positions (red circles); solid line is the linear fit to the absorbance. Error bars indicate the range of values obtained. (d) Absorbance over time of thin films of $CsPbI_3$ and $CsPbI_2Br$, measured at 675 and 625 nm respectively, when exposed to a slow flow of air at 50% RH. The slight increase in the absorbance of the $CsPbI_2Br$ film is not yet fully understood.**

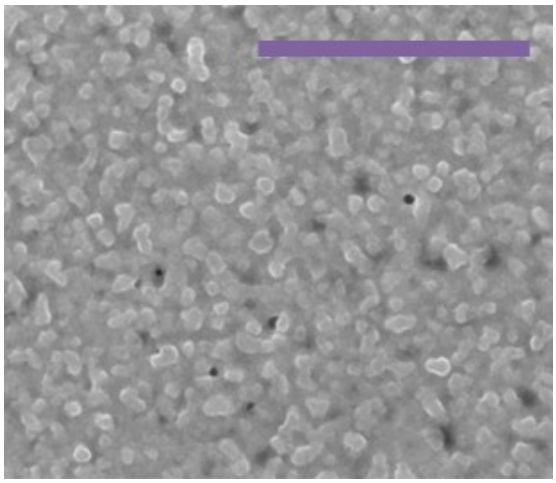

**Figure 4-5. SEM image of a $CsPbI_2Br$ film spincoated from DMF onto a silicon substrate for EDX analysis. The scale bar is 2 μm. Image and analysis in collaboration with Dr Jason Brown at the University of Oxford.**

Despite being able to form the black phase of $CsPbI_3$ at low temperatures in an inert environment, once exposed to air these films rapidly undergo a phase transition to the thermodynamically stable yellow phase. This rapid change in air is due to a catalytic effect of moisture on the kinetics of the conversion.[31] Figure 4-4(d) shows the relative instability of $CsPbI_3$ compared with $CsPbI_2Br$. For a thin film enclosed in a nitrogen chamber with a low flow of air (50% RH), $CsPbI_3$ reverts to the low temperature yellow phase in about an hour, while $CsPbI_2Br$ is stable under the same conditions. It is known that the phase transition temperature for the orthorhombic to cubic perovskite transition reduces with increasing bromide content.[16] The lower phase transition temperature is expected to be the predominant reason for the enhanced stability of the $CsPbI_2Br$ under ambient conditions. $CsPbI_2Br$ is therefore a promising material which appears to combine ambient stability and suitable bandgap and thus warrants further investigation for solar cell applications. In particular, its bandgap of 1.92 eV makes it promising as an option for inclusion in tandem devices with c-Si and copper indium gallium (di)selenide solar cells.[32]

 

## 4.5 Temperature-dependent XRD

To demonstrate that the addition of bromide reduces the transition temperature for thin films, and to prove the inherent thermal stability of these material at elevated temperatures, Figure 4-6 shows in-situ X-ray diffraction (XRD) patterns while heating films of $CsPbI_3$ and $CsPbI_2Br$ at temperatures up to 400 °C. The appearance of the perovskite structure is seen around 350 °C for $CsPbI_3$ and around 230 °C for $CsPbI_2Br$, which is a reduction of over 100 °C in the transition temperature with the addition of bromide.[16,19] For $CsPbI_2Br$ the XRD peaks for this perovskite structure appear at higher angles than those of the high temperature black phase of $CsPbI_3$ due to the bromide content which is expected to contract the lattice.

To verify that the perovskite structure remains when the film is annealed and rapidly cooled, Figure 4-7 shows photographs, absorbance spectra and XRD patterns taken at room temperature for separate $CsPbI_2Br$ films annealed for 20 minutes at a single temperature. In Figure 4-7(b), the absorption spectrum of the yellow polymorph is visible for annealing temperatures up to and including 200 °C. The perovskite structure is formed from 250 °C, with the optimal crystallinity and absorbance found when annealing closer to 350 °C.

Remarkably, it is well-known that at such high temperatures thin films of the hybrid organic-inorganic perovskites such as methylammonium (MA) and formamidinium (FA) lead iodide degrade very rapidly.[5,6] Specifically, $MAPbI_3$ thin films will start to thermally degrade at temperatures above 85 °C, and $FAPbI_3$ thin films at temperatures above 150 °C.

 

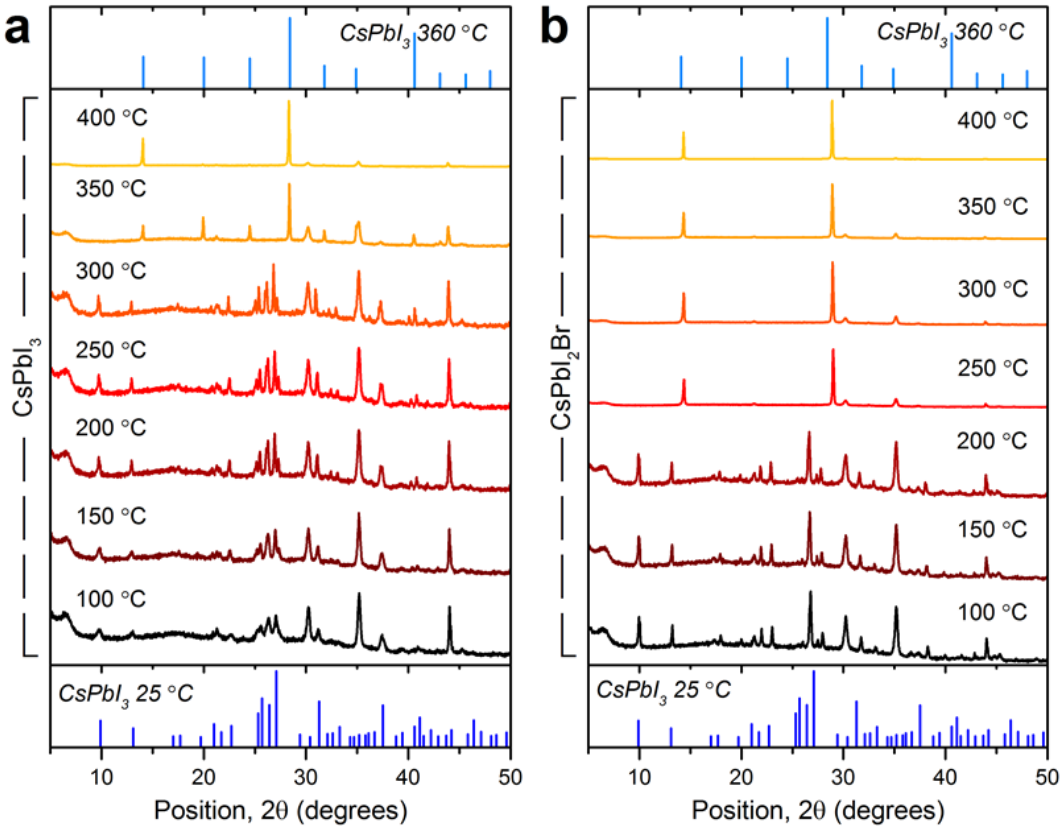


**Figure 4-6. 'In-situ annealing' X-ray diffraction patterns from films of (a) $CsPbI_3$ and (b) $CsPbI_2Br$ on glass, measured during a slow temperature ramp in a sealed chamber under a flow of nitrogen. X-ray scattering due to the Kapton film is seen below $2\theta = 10°$. $CsPbI_3$ powder XRD patterns at room temperature (dark blue) and at high temperature (light blue) are shown for reference.[19] These patterns were measured by Dr Laura Miranda at Oxford PV, Begbroke.**

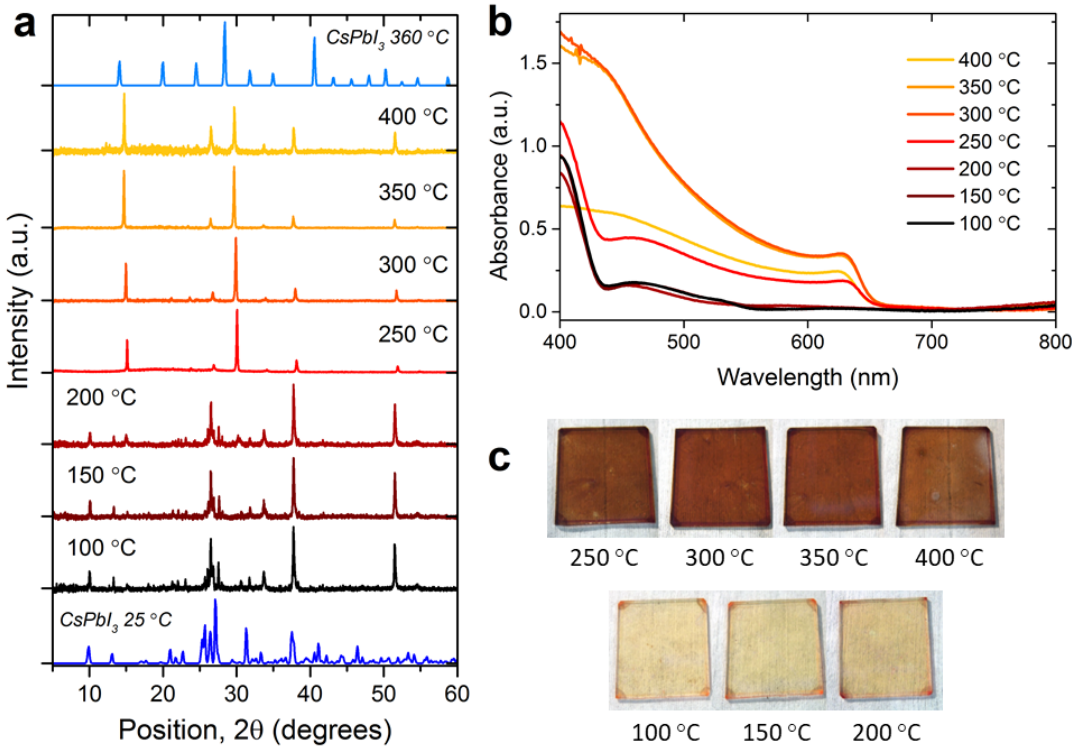


**Figure 4-7. (a) XRD patterns, (b) absorbance spectra and (c) photographs of $CsPbI_2Br$ films annealed for 20 minutes at the specified temperature then cooled rapidly to room temperature for measurement. $CsPbI_3$ powder XRD patterns at room temperature (dark blue) and at high temperature (light blue) are shown for reference.[19]**

## 4.6 Stability testing of $CsPbI_2Br$ and $MAPbI_2Br$

To further illustrate the thermal and atmospheric stability of $CsPbI_2Br$ under conditions more similar to solar cell operating conditions, $CsPbI_2Br$ is compared to thin films of the organic methylammonium equivalent, $MAPbI_2Br$ perovskite, at 85 °C in air. Figure 4-8 presents absorbance spectra and XRD patterns for films of $CsPbI_2Br$ and $MAPbI_2Br$ heated on a hotplate at 85 °C in air in a controlled humidity environment of between 20 and 25% RH. For $CsPbI_2Br$, Figure 4-8(a) shows that after 270 minutes of heating the absorbance remains approximately constant (within the spot to spot measurement accuracy) with the initial absorbance at 627 nm.

 

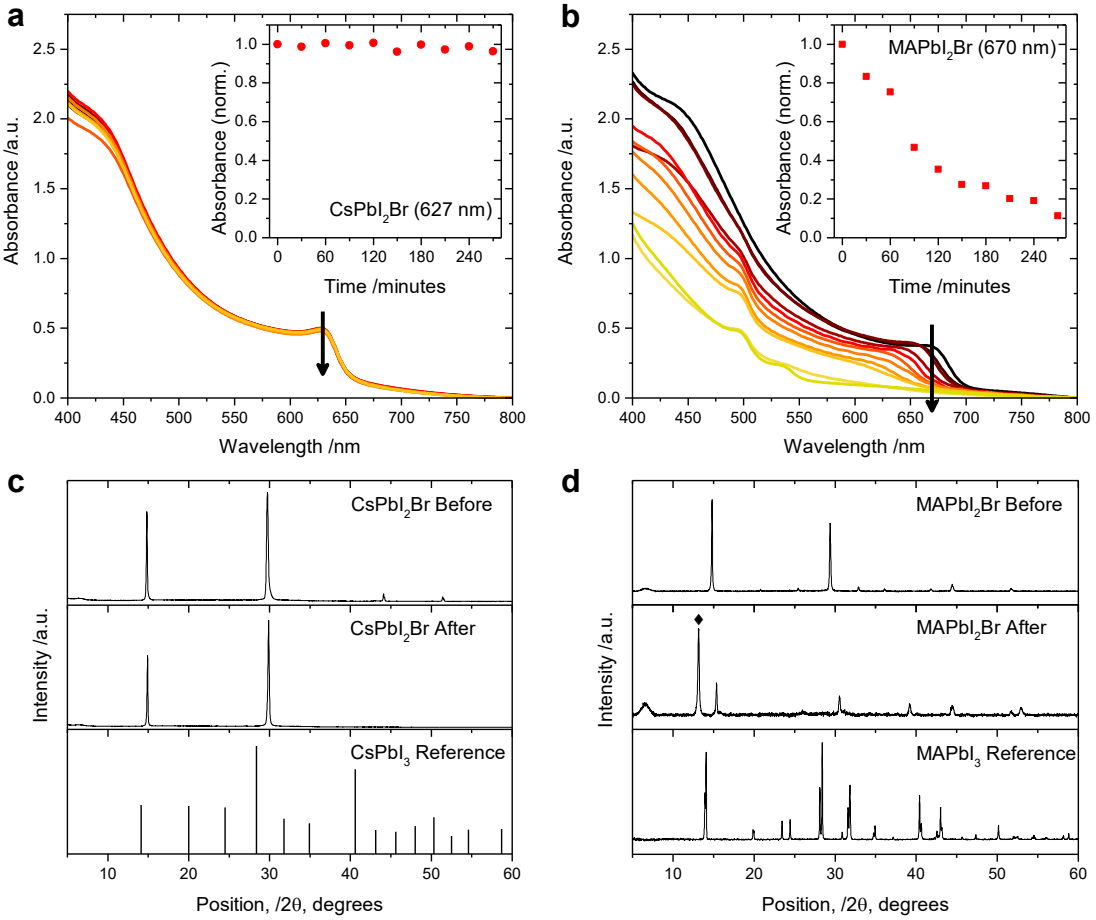


**Figure 4-8. Absorbance spectra for films of (a) $CsPbI_2Br$ and (b) $MAPbI_2Br$ for different times of heating at 85 °C in 20-25% RH. Arrows indicate direction of increasing time of heating. Insets: absorption intensity over time at peak of onset (627 nm and 670 nm respectively; arrow positions in main plot). XRD patterns before and after 270 minutes of heating at 85 °C in 20-25% RH for (c) $CsPbI_2Br$ and (d) $MAPbI_2Br$, measured by Dr Laura Miranda at Oxford PV, Begbroke. X-ray scattering due to the Kapton film is seen below $2\theta = 10°$; the $PbI_{2-x}Br_x$ peak position is indicated by a diamond. The reference powder pattern for $CsPbI_3$ (cubic phase) is from Trots and Myagkota;[19] the $MAPbI_3$ (tetragonal phase) powder pattern was provided by Amir Abbas Haghighirad at the University of Oxford and is from a crushed single crystal.**

In the XRD patterns in Figure 4-8(c) peaks characteristic of the $CsPbI_2Br$ perovskite phase are seen both before and after heating, and no peaks indicating other material compositions or degradation. In contrast, for $MAPbI_2Br$ in Figure 4-8(b) a continuous decrease in the perovskite absorbance at 670 nm is observed

 

over 270 minutes of heating, such that after heating the film appears visibly yellow. The XRD patterns in Figure 4-8(d) show perovskite peaks for $MAPbI_2Br$ before heating; after heating new peaks appear, including a $PbI_{2-x}Br_x$ peak near 13° which indicates that MABr and/or MAI have been removed. This figure shows that $CsPbI_2Br$ exhibits both phase and compositional stability when heated at 85 °C in 20-25% RH, while $MAPbI_2Br$ shows compositional instability under the same conditions.

## 4.7 Photovoltaic devices with $CsPbI_2Br$

For this mixed-halide composition, $CsPbI_2Br$, the ambient stability is greatly increased such that it should now be possible to make solar cells with this material and test them under ambient conditions. To empirically verify that the carrier diffusion length is sufficient in this material, devices were prepared with the two different architectures shown in Figure 4-9: a planar architecture with only compact $TiO_2$ (c-$TiO_2$) as the n-type charge collection layer, which requires a material with sufficient charge mobility and carrier lifetime for extraction of charges; and a mesoporous architecture, where the inclusion of a mesoporous $TiO_2$ (m-$TiO_2$) layer allows electrons to be extracted from the perovskite much closer to the site of generation. The final device configuration is then glass/FTO/c-$TiO_2$/m-$TiO_2$ (optional)/perovskite (~150 nm)/Spiro-OMeTAD/Ag, where the hole-transporting Spiro-OMeTAD layer is already oxidized. Further details regarding device preparation are provided in the Experimental Methods chapter. Functioning devices were obtained with stabilized power outputs (SPOs) of over 4% in both configurations, with an average power conversion efficiency (PCE) of 2.5-3% (see Figure 4-9 and Table 4-1).

 

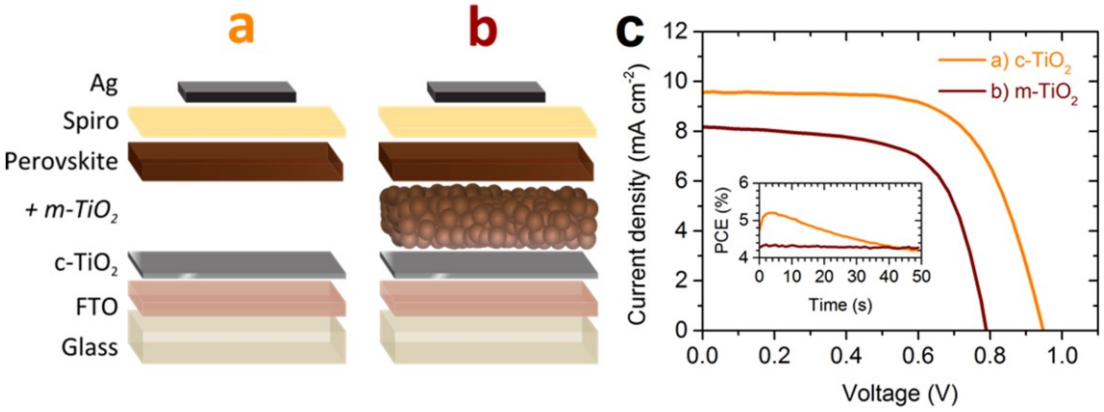


**Figure 4-9 Schematic of device architectures tested: (a) compact $TiO_2$ (c-$TiO_2$), and (b) both compact and mesoporous $TiO_2$ (m-$TiO_2$). (c) J-V curves for the best-performing devices of each configuration. Inset: Stabilised power output (SPO) measurements for these devices.**

**Table 4-1 Average (best) device parameters extracted from current density-voltage characteristics measured under AM1.5 100 mW $cm^{-2}$ illumination for the devices in Figure 4-9. Averages are from at least 10 devices per architecture, where ± values denote the standard deviation for the dataset.**

| Device architecture | $J_{SC}$ (mA $cm^{-2}$) | PCE from J-V (%) | $V_{OC}$ (V) | FF |
|---|---|---|---|---|
| (a) c-TiO2 | 7.9 ± 1.9 (9.6) | 2.5 ± 2.3 (5.9) | 0.5 ± 0.4 (0.95) | 0.4 ± 0.2 (0.71) |
| (b) m-TiO2 | 7.0 ± 2.1 (8.3) | 2.9 ± 1.5 (4.3) | 0.7 ± 0.1 (0.80) | 0.5 ± 0.2 (0.67) |

Importantly, these working planar devices (architecture (b)) show that $CsPbI_2Br$ is capable of generating and transporting charges over hundreds of nanometres without the requirement for distributed heterojunctions, consistent with previous findings for $CsPbI_3$.[23]

Focusing on the planar c-$TiO_2$ structure, by optimizing the deposition process several devices were fabricated with over 6% PCE, including a champion device with 9.8% current density-voltage (*J-V*) scan efficiency which delivered 5.6% SPO (Figure 4-10(a) and (b)). Figure 4-10(c-g) shows histograms of the *J-V* scan parameters for a batch of 32 solar cells and SPOs for the best 16 solar cells. Figure

4-10(h) tabulates these parameters for the device in (a) and (b), and for the batch average. There is significant variation within a batch, with an average PCE of 6% and two exceptional devices yielding PCEs above 9%. All devices were measured in ambient atmosphere without any encapsulation. At the time of this study, these were the most efficient inorganic perovskite solar cells reported, and a considerable improvement on the first neat $CsPbI_3$ solar cells.[23]

The external quantum efficiency for a typical device is provided in Figure 4-11. The onset of charge generation matches well with the absorption onset near 650 nm, and integration of the measured EQE spectrum over the solar spectrum estimates a short-circuit current density of 10.6 mA $cm^{-2}$, slightly lower than the average $J_{SC}$.

To put these values into context, the Shockley–Queisser limit for a bandgap of 1.92 eV gives a maximum possible short-circuit current density ($J_{SC}$) of 16.3 mA $cm^{-2}$, and a maximum open-circuit voltage ($V_{OC}$) of 1.63 V.[33,34] Hence, although these results are very encouraging, there remains much scope for improvement, particularly in the open-circuit voltage which is 0.52 V short of the Shockley–Queisser limit and shows a voltage deficit (difference between band gap and open-circuit voltage) of at least 0.8 eV. This voltage deficit is likely due to the presence of defects, both within the bulk perovskite crystal and at the surfaces and grain boundaries. For example, the voltage deficit has been reduced to less than 0.4 eV in hybrid organic-inorganic perovskite solar cells by careful control of the crystallisation to reduce the density of defects.[35] Additionally, surface passivation by organic ligands such as amine groups is known to increase the luminescence efficiency of lead halide perovskites, particularly in nanocrystals.[25] Consequently, surface passivation by the amine groups inherently present in hybrid organic-inorganic perovskite solar cells may be a reason for the higher $V_{OC}$s (typically ~0.1V higher on average) observed for $MAPbBr_3$ cells compared with $CsPbBr_3$ cells.[36] Recently, the voltage deficit for subsequent $CsPbI_2Br$ perovskite solar cells has been

 

reduced by passivation of the surfaces and grain boundaries of the inorganic perovskite, combined with improvements to the synthetic procedure to optimize crystal quality. For example, $V_{OC}$s up to 1.32 V and device efficiencies over 14% have been reported for $CsPbI_{3-x}Br_x$ perovskite solar cells where organic moieties such as polythiophene and FAI respectively have been used to passivate the surface of the inorganic perovskite.[37,38]

Figure 4-10(a) also shows that there is significant hysteresis present in the *J-V* scan measurements for these devices, similar to previously reported $CsPbI_3$ solar cells,[23] which may be due in part to the choice of charge extraction layers. For example, swapping $TiO_2$ for $C_{60}$ as the electron collection layer,[39] or the use of $MoO_3$ as a hole extracting layer have been shown to achieve high PCE and hysteresis suppression with hybrid perovskites and caesium lead iodide devices respectively.[24]

In addition, despite increased stability when compared with neat $CsPbI_3$, exposed thin films of $CsPbI_2Br$ still revert to the yellow phase in air over prolonged exposure to ambient atmosphere (hours or days depending upon the ambient humidity). Hence additional tuning of the crystal may be required to form an appropriately phase-stable inorganic perovskite.

 

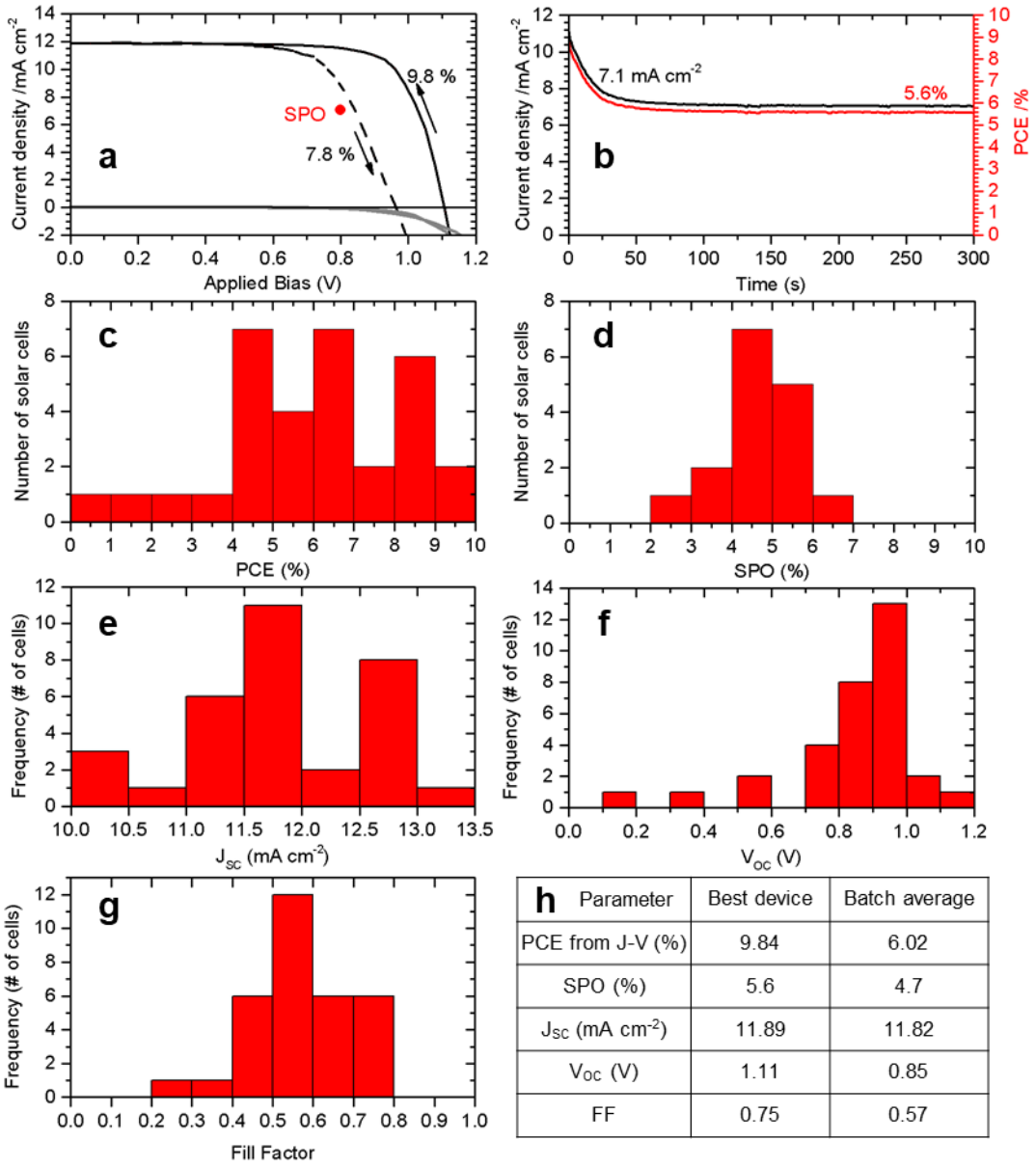


| h Parameter | Best device | Batch average |
|---|---|---|
| PCE from J-V (%) | 9.84 | 6.02 |
| SPO (%) | 5.6 | 4.7 |
| $J_{SC}$ (mA cm$^{-2}$) | 11.89 | 11.82 |
| $V_{OC}$ (V) | 1.11 | 0.85 |
| FF | 0.75 | 0.57 |

**Figure 4-10. (a) Champion device current density-voltage (J-V) scan under illumination (black lines) and in the dark (grey lines) from forward bias to short-circuit (solid lines) and from short-circuit to forward bias (dashed lines). (b) Champion device SPO measurement (PCE in red; current density in black). Average values over the last 200 seconds are shown in the figure and the stabilized 'SPO' J-V point is shown in (a) by a solid red circle. Histograms for a batch of 32 devices for (c) J-V scan efficiencies (PCE), (d) stabilized power output measurements (SPO, for the best 16 devices in the batch), (e) short-circuit current density ($J_{SC}$), (f) open-circuit voltage ($V_{OC}$), and (g) fill factor. (h) Device parameters from the J-V scans for the champion device in (a-b) and for the batch average of the devices in (c-g).**

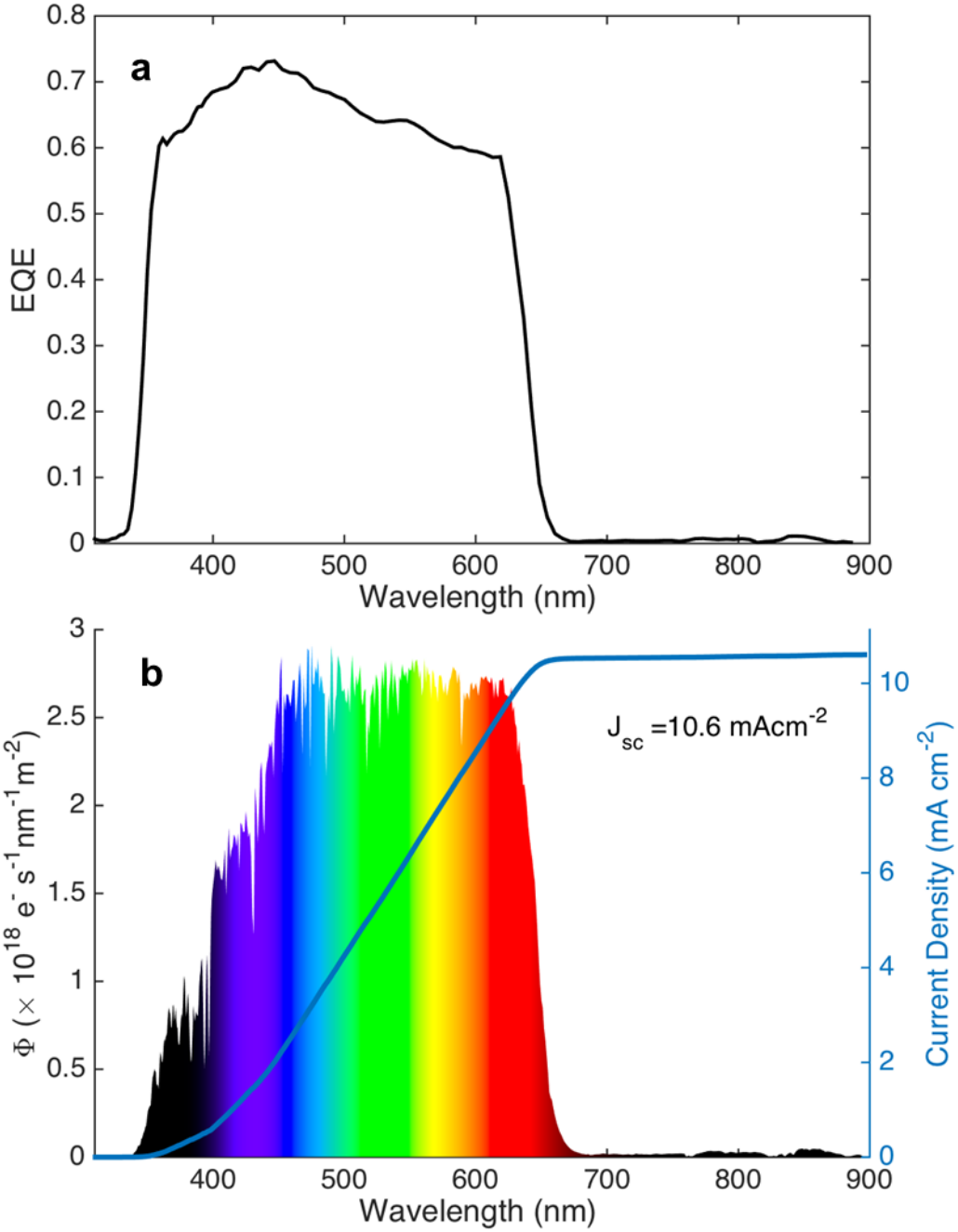


**Figure 4-11. (a) External Quantum Efficiency (EQE) spectrum for a typical CsPbI2Br solar cell, measured under nitrogen. (b) Photo-generated device current per unit wavelength per unit area calculated from the EQE data in (a) using the ASTM G173-03 Global Tilt reference spectrum. The coloured spectrum in (b) is the ASTM G173-03 spectral flux integrated with the EQE spectrum from (a). EQE was measured in collaboration with Prof. Michael Johnston at the University of Oxford.**

## 4.8 Conclusion and outlook

In this chapter, fully-inorganic perovskites have been explored as thermally stable alternatives to organic-inorganic perovskites for photovoltaic devices. In particular, $CsPbI_2Br$ has been used to make solar cells with 5.6% stabilized power output and with *J-V* scan efficiencies up to 9.8%, representing the highest efficiency achieved for the fully inorganic lead halide perovskites at the time of publication. Also, the potential for these materials to yield even higher efficiencies with further optimization was discussed.

The improved stability of this particular inorganic perovskite has also been displayed in this chapter. By substituting one third of the iodide for bromide, the ambient stability has been significantly improved, as compared to $CsPbI_3$, while still retaining a usefully low bandgap of 1.92 eV suitable for tandem solar cell applications. This increased stability and lower transition temperature to the perovskite structure also render the material much more 'user-friendly' than $CsPbI_3$, enabling the preparation of photovoltaic devices with some processing steps in ambient atmosphere.

In general, these fully inorganic materials show high thermal stability in comparison to their hybrid counterparts, making them superior candidates for long-term operation under thermally stressful conditions. However, there is still a need for further understanding of the structural stability at ambient temperatures of caesium lead halide perovskites, especially given the rapid conversion to non-perovskite structures in iodide-rich compositions when exposed to ambient atmosphere. As well as being of scientific interest, this knowledge is required to assess the full applicability of these inorganic perovskites to solar power generation where stability is required on timescales of years. Importantly, the results in this chapter present inorganic halide perovskites as compositionally-stable materials for photovoltaics.

 

## 4.9 References


1. Kojima, A.; Teshima, K.; Shirai, Y.; Miyasaka, T. "Organometal Halide Perovskites as Visible-Light Sensitizers for Photovoltaic Cells". *J. Am. Chem. Soc.* 2009, *131*, 6050–6051.
2. Zhou, H.; Chen, Q.; Li, G.; Luo, S.; Song, T. -b.; Duan, H.-S.; Hong, Z.; You, J.; Liu, Y.; Yang, Y. "Interface Engineering of Highly Efficient Perovskite Solar Cells". *Science* 2014, *345*, 542–546.
3. Jeon, N. J.; Noh, J. H.; Yang, W. S.; Kim, Y. C.; Ryu, S.; Seo, J.; Seok, S. Il. "Compositional Engineering of Perovskite Materials for High-Performance Solar Cells". *Nature* 2015, *517*, 476–480.
4. Roldán-Carmona, C.; Gratia, P.; Zimmermann, I.; Grancini, G.; Gao, P.; Graetzel, M.; Nazeeruddin, M. K. "High Efficiency Methylammonium Lead Triiodide Perovskite Solar Cells: The Relevance of Non-Stoichiometric Precursors". *Energy Environ. Sci.* 2015, *8*, 3550–3556.
5. Eperon, G. E.; Stranks, S. D.; Menelaou, C.; Johnston, M. B.; Herz, L. M.; Snaith, H. J. "Formamidinium Lead Trihalide: A Broadly Tunable Perovskite for Efficient Planar Heterojunction Solar Cells". *Energy Environ. Sci.* 2014, *7*, 982.
6. Conings, B.; Drijkoningen, J.; Gauquelin, N.; Babayigit, A.; D'Haen, J.; D'Olieslaeger, L.; Ethirajan, A.; Verbeeck, J.; Manca, J.; Mosconi, E.; Angelis, F. De; Boyen, H.-G. "Intrinsic Thermal Instability of Methylammonium Lead Trihalide Perovskite". *Adv. Energy Mater.* 2015, *5*, 1500477.
7. Leijtens, T.; Eperon, G. E.; Noel, N. K.; Habisreutinger, S. N.; Petrozza, A.; Snaith, H. J. "Stability of Metal Halide Perovskite Solar Cells". *Adv. Energy Mater.* 2015, *5*, 1500963.
8. Osterwald, C. R.; McMahon, T. J. "History of Accelerated and Qualification Testing of Terrestrial Photovoltaic Modules: A Literature Review". *Prog. Photovoltaics Res. Appl.* 2009, *17*, 11–33.
9. Baikie, T.; Fang, Y.; Kadro, J. M.; Schreyer, M.; Wei, F.; Mhaisalkar, S. G.; Graetzel, M.; White, T. J. "Synthesis and Crystal Chemistry of the Hybrid Perovskite $(CH_3NH_3)PbI_3$ for Solid-State Sensitised Solar Cell Applications". *J. Mater. Chem. A* 2013, *1*, 5628.
10. Liu, Y.; Yang, Z.; Cui, D.; Ren, X.; Sun, J.; Liu, X.; Zhang, J.; Wei, Q.; Fan, H.; Yu, F.; Zhang, X.; Zhao, C.; Liu, S. F. "Two-Inch-Sized Perovskite $CH_3NH_3PbX_3$ (X = Cl, Br, I) Crystals: Growth and Characterization". *Adv. Mater.* 2015, *27*, 5176–5183.
11. Lee, J.-W.; Kim, D.-H.; Kim, H.-S.; Seo, S.-W.; Cho, S. M.; Park, N.-G. "Formamidinium and Cesium Hybridization for Photo- and Moisture-Stable Perovskite Solar Cell". *Adv. Energy Mater.* 2015, *5*, 1501310.
12. McMeekin, D. P.; Sadoughi, G.; Rehman, W.; Eperon, G. E.; Saliba, M.; Horantner, M. T.; Haghighirad, A.; Sakai, N.; Korte, L.; Rech, B.; Johnston, M. B.; Herz, L. M.; Snaith, H. J. "A Mixed-Cation Lead Mixed-Halide Perovskite Absorber for Tandem Solar Cells". *Science* 2016, *351*, 151–155.
13. Wells, H. L. "On the Caesium- and the Potassium-Lead Halides". *Am. J. Sci.* 1893, *s3-45*, 121–134.
14. Møller, C. K. "Crystal Structure and Photoconductivity of Cæsium Plumbohalides".


 

*Nature* 1958, *182*, 1436–1436.

15. Fröhlich, D.; Heidrich, K.; Künzel, H.; Trendel, G.; Treusch, J. "Cesium-Trihalogen-Plumbates a New Class of Ionic Semiconductors". *J. Lumin.* 1979, *18–19*, 385–388.
16. Sharma, S.; Weiden, N.; Weiss, A. "Phase Diagrams of Quasibinary Systems of the Type: $ABX_3$ — $A'BX_3$; $ABX_3$ — $AB'X_3$, and $ABX_3$ — $ABX'_3$; X = Halogen". *Zeitschrift für Phys. Chemie* 1992, *175*, 63–80.
17. Kondo, S.; Sakai, T.; Tanaka, H.; Saito, T. "Amorphization-Induced Strong Localization of Electronic States in $CsPbBr_3$ and $CsPbCl_3$ Studied by Optical Absorption Measurements". *Phys. Rev. B* 1998, *58*, 11401–11407.
18. Rodová, M.; Brožek, J.; Knížek, K.; Nitsch, K. "Phase Transitions in Ternary Caesium Lead Bromide". *J. Therm. Anal. Calorim.* 2003, *71*, 667–673.
19. Trots, D. M.; Myagkota, S. V. "High-Temperature Structural Evolution of Caesium and Rubidium Triiodoplumbates". *J. Phys. Chem. Solids* 2008, *69*, 2520–2526.
20. Murtaza, G.; Ahmad, I. "First Principle Study of the Structural and Optoelectronic Properties of Cubic Perovskites $CsPbM_3$ (M=Cl, Br, I)". *Phys. B Condens. Matter* 2011, *406*, 3222–3229.
21. Stoumpos, C. C.; Malliakas, C. D.; Peters, J. A.; Liu, Z.; Sebastian, M.; Im, J.; Chasapis, T. C.; Wibowo, A. C.; Chung, D. Y.; Freeman, A. J.; Wessels, B. W.; Kanatzidis, M. G. "Crystal Growth of the Perovskite Semiconductor $CsPbBr_3$: A New Material for High-Energy Radiation Detection". *Cryst. Growth Des.* 2013, *13*, 2722–2727.
22. Kulbak, M.; Cahen, D.; Hodes, G. "How Important Is the Organic Part of Lead Halide Perovskite Photovoltaic Cells? Efficient $CsPbBr_3$ Cells". *J. Phys. Chem. Lett.* 2015, *6*, 2452–2456.
23. Eperon, G. E.; Paternò, G. M.; Sutton, R. J.; Zampetti, A.; Haghighirad, A. A.; Cacialli, F.; Snaith, H. J. "Inorganic Caesium Lead Iodide Perovskite Solar Cells". *J. Mater. Chem. A* 2015, *3*, 19688–19695.
24. Ripolles, T. S.; Nishinaka, K.; Ogomi, Y.; Miyata, Y.; Hayase, S. "Efficiency Enhancement by Changing Perovskite Crystal Phase and Adding a Charge Extraction Interlayer in Organic Amine Free-Perovskite Solar Cells Based on Cesium". *Sol. Energy Mater. Sol. Cells* 2016, *144*, 532–536.
25. Protesescu, L.; Yakunin, S.; Bodnarchuk, M. I.; Krieg, F.; Caputo, R.; Hendon, C. H.; Yang, R. X.; Walsh, A.; Kovalenko, M. V. "Nanocrystals of Cesium Lead Halide Perovskites ($CsPbX_3$ , X = Cl, Br, and I): Novel Optoelectronic Materials Showing Bright Emission with Wide Color Gamut". *Nano Lett.* 2015, *15*, 3692–3696.
26. Zhang, D.; Eaton, S. W.; Yu, Y.; Dou, L.; Yang, P. "Solution-Phase Synthesis of Cesium Lead Halide Perovskite Nanowires". *J. Am. Chem. Soc.* 2015, *137*, 9230–9233.
27. Song, J.; Li, J.; Li, X.; Xu, L.; Dong, Y.; Zeng, H. "Quantum Dot Light-Emitting Diodes Based on Inorganic Perovskite Cesium Lead Halides ($CsPbX_3$)". *Adv. Mater.* 2015, *27*, 7162–7167.
28. Moore, D. T.; Sai, H.; Wee Tan, K.; Estroff, L. A.; Wiesner, U. "Impact of the Organic Halide Salt on Final Perovskite Composition for Photovoltaic Applications". *APL Mater.* 2014, *2*, 81802.
29. Nedelcu, G.; Protesescu, L.; Yakunin, S.; Bodnarchuk, M. I.; Grotevent, M. J.;

Kovalenko, M. V. "Fast Anion-Exchange in Highly Luminescent Nanocrystals of Cesium Lead Halide Perovskites ($CsPbX_3$ , X = Cl, Br, I)". *Nano Lett.* 2015, *15*, 5635–5640.

30. Jang, D. M.; Park, K.; Kim, D. H.; Park, J.; Shojaei, F.; Kang, H. S.; Ahn, J.-P.; Lee, J. W.; Song, J. K. "Reversible Halide Exchange Reaction of Organometal Trihalide Perovskite Colloidal Nanocrystals for Full-Range Band Gap Tuning". *Nano Lett.* 2015, *15*, 5191–5199.
31. Dastidar, S.; Hawley, C. J.; Dillon, A. D.; Gutierrez-Perez, A. D.; Spanier, J. E.; Fafarman, A. T. "Quantitative Phase-Change Thermodynamics and Metastability of Perovskite-Phase Cesium Lead Iodide". *J. Phys. Chem. Lett.* 2017, *8*, 1278–1282.
32. Bremner, S. P.; Levy, M. Y.; Honsberg, C. B. "Analysis of Tandem Solar Cell Efficiencies under AM1.5G Spectrum Using a Rapid Flux Calculation Method". *Prog. Photovoltaics Res. Appl.* 2008, *16*, 225–233.
33. Shockley, W.; Queisser, H. J. "Detailed Balance Limit of Efficiency of p-n Junction Solar Cells". *J. Appl. Phys.* 1961, *32*, 510–519.
34. Tress, W.; Marinova, N.; Inganäs, O.; Nazeeruddin, M. K.; Zakeeruddin, S. M.; Graetzel, M. "Predicting the Open-Circuit Voltage of $CH_3NH_3PbI_3$ Perovskite Solar Cells Using Electroluminescence and Photovoltaic Quantum Efficiency Spectra: The Role of Radiative and Non-Radiative Recombination". *Adv. Energy Mater.* 2015, *5*, 1400812.
35. Noel, N. K.; Congiu, M.; Ramadan, A. J.; Fearn, S.; McMeekin, D. P.; Patel, J. B.; Johnston, M. B.; Wenger, B.; Snaith, H. J. "Unveiling the Influence of pH on the Crystallization of Hybrid Perovskites, Delivering Low Voltage Loss Photovoltaics". *Joule* 2017, *1*, 328–343.
36. Egger, D. A.; Bera, A.; Cahen, D.; Hodes, G.; Kirchartz, T.; Kronik, L.; Lovrincic, R.; Rappe, A. M.; Reichman, D. R.; Yaffe, O. "What Remains Unexplained about the Properties of Halide Perovskites?". *Adv. Mater.* 2018, 1800691.
37. Zeng, Q.; Zhang, X.; Feng, X.; Lu, S.; Chen, Z.; Yong, X.; Redfern, S. A. T.; Wei, H.; Wang, H.; Shen, H.; Zhang, W.; Zheng, W.; Zhang, H.; Tse, J. S.; Yang, B. "Polymer-Passivated Inorganic Cesium Lead Mixed-Halide Perovskites for Stable and Efficient Solar Cells with High Open-Circuit Voltage over 1.3 V". *Adv. Mater.* 2018, *30*, 1705393.
38. Bian, H.; Bai, D.; Jin, Z.; Wang, K.; Liang, L.; Wang, H.; Zhang, J.; Wang, Q.; Liu, S. (Frank). "Graded Bandgap $CsPbI_{2+x}Br_{1-x}$ Perovskite Solar Cells with a Stabilized Efficiency of 14.4%". *Joule* 2018, *0*.
39. Wojciechowski, K.; Leijtens, T.; Siprova, S.; Schlueter, C.; Hörantner, M. T.; Wang, J. T.-W.; Li, C.-Z.; Jen, A. K.-Y.; Lee, T.-L.; Snaith, H. J. "$C_{60}$ as an Efficient n-Type Compact Layer in Perovskite Solar Cells". *J. Phys. Chem. Lett.* 2015, *6*, 2399–2405.

 

# 5 Optoelectronic Properties of Caesium Lead Halide Perovskites

The work presented in this chapter is based on the following publication:

Yang, Z.; Surrente, A.; Galkowski, K.; Miyata, A.; Portugall, O.; Sutton, R. J.; Haghighirad, A. A.; Snaith, H. J.; Maude, D. K.; Plochocka, P.; Nicholas, R. J. 'Impact of the Halide Cage on the Electronic Properties of Fully Inorganic Cesium Lead Halide Perovskites', *ACS Energy Lett.* 2, 1621–1627 (2017).

DOI: 10.1021/acsenergylett.7b00416

Direct link: https://pubs.acs.org/doi/10.1021/acsenergylett.7b00416

## 5.1 Wider context and summary

At the time of this study, interest was growing in inorganic perovskites due to their significantly greater chemical stability than the hybrid organic-inorganic perovskites. A number of groups had demonstrated operational solar cells with inorganic perovskites, but very little was known about their electronic properties. In contrast, the optoelectronic properties of the hybrid lead halide perovskites with methylammonium or formamidinium cations were well-known.

The main barrier to gaining a thorough understanding of the electronic properties of the inorganic lead halide perovskites was the difficulty in fabricating and handling thin films of these materials. Fabrication of thin films of the iodide-rich compositions was possible with solution-processing, but the films rapidly return to the yellow non-perovskite polymorph at ambient conditions. Fabrication of continuous and thick films of bromide-rich compositions by solution processing was challenging without a mesoporous scaffold due to the low solubility of the precursors in common spin-coating solvents. To overcome this limitation, here a preparation route using vapour deposition is developed for thick planar films of $CsPbBr_3$.

Successful preparation of planar $CsPbBr_3$ films with no scaffold enabled the detailed study in this chapter, which investigates fundamental electronic properties of the inorganic lead halide perovskites. Specifically, this work determines the exciton binding energies, effective masses, and dielectric constants of three inorganic perovskites: $CsPbI_3$, $CsPbI_2Br$ and $CsPbBr_3$, and finds that the halide significantly affects these electronic properties.

As well as being a useful comparison between the halides, this work also allows a comparison between the inorganic and hybrid perovskites. Here, the dielectric constants are found to be similar to their hybrid counterparts, and the exciton binding energies and effective masses are as expected for the material bandgaps. The similarity between the inorganic and hybrid perovskites for these key electronic

 

properties demonstrates that their origin is related to the lead halide cage rather than the cation.

This chapter represents a significant step in understanding the possibilities and limitations of the inorganic perovskites in photovoltaic applications.

## 5.2 Introduction

Organic-inorganic methylammonium lead halide perovskites have proven high efficiencies,[1,2] but, as has been demonstrated in the previous chapter, the stability of the perovskite is hindered by the volatility of the methylammonium cation.[3,4] Although using a larger, less volatile cation such as formamidinium (FA), in $FAPbI_3$, initially looks promising because $FAPbI_3$ has a low bandgap of ~1.5 eV, this compound exists in a yellow hexagonal polymorph at ambient conditions due to the large size of the FA cation.[5] In contrast, the inorganic perovskite $CsPbI_3$ has a desirable bandgap for tandem applications (~1.75 eV) but exists in a yellow non-perovskite polymorph at ambient conditions due to the small size of the Cs cation.[6,7] Consequently, employing a combination of FA and Cs has been shown to stabilize the perovskite structure, and devices with mixed FA, MA and Cs cations have reached efficiencies over 21%.[8–11] However, despite the remarkable climb in efficiency of perovskite solar cells with mixed organic and inorganic cations in the perovskite absorbers, very little is known about the electronic properties of the inorganic perovskites.

This chapter sets out to provide experimentally determined results for the electronic properties relevant for photovoltaic applications, specifically exciton binding energy, effective mass, and dielectric screening, for the inorganic perovskites caesium lead bromide ($CsPbBr_3$), caesium lead iodide ($CsPbI_3$), and the mixed halide composition $CsPbI_2Br$. The cubic polymorphs of these perovskites are formed by heating to temperatures above 150 °C and 300 °C respectively.[12,13] The films used in solar cells

 

are formed by quench cooling the cubic polymorph to room temperature.[6,7] Interestingly, unlike in the hybrid perovskites, no further phase transitions are detected on lowering the temperature from room temperature to 4.2 K. Here, magneto-transmission spectroscopy measurements on these perovskites show that the exciton binding energy (R*) and reduced mass ($\mu$) scale with the bandgap, as was found for the hybrid perovskites.[14,15] Specifically, the exciton binding energy of $CsPbI_3$ is sufficiently low for charge separation and free-carrier-like behaviour at room temperature. The dielectric constant ($\varepsilon_{eff}$) is calculated from the above two parameters and found to be comparable to the hybrid perovskites, with significant changes due to the bromide.[14,15] At low temperature, thermal motion of the organic cations is not possible,[16] and so the similarity of the dielectric screening suggests that the screening mechanism is determined only by the halide in the lead halide octahedra.

## 5.3 Fabrication of planar $CsPbBr_3$ thin films

This section outlines the development of a procedure for the deposition of planar thin films of $CsPbBr_3$.

Solution-processed planar films were in all cases not of a sufficient quality for magneto-transmission measurements. Various solution-process methods were tested, including one-step and two-step methods. One-step spin-coating produced very thin films with *N,N*-dimethylformamide (DMF) as the solvent due to the low solubility of caesium bromide (CsBr) and lead bromide ($PbBr_2$) when in solution together. The solubility of these precursors in dimethyl sulfoxide is higher, but the films were poorly covered. Sequential spin-coating is a popular method for the hybrid perovskites, as the stoichiometry can be controlled by annealing excess organic cation out of the film. This method proved ineffective for $CsPbBr_3$ in part due to the high thermal stability of the inorganic cation, which requires exact stoichiometry

 

of the as-spun layers. Further limiting this method was the low solubility of CsBr in isopropanol; instead CsBr was spin-coated from methanol which led to uneven film coverage. Dip-coating yields high-quality films of $CsPbBr_3$ when using a mesoporous $TiO_2$ scaffold.[7,17] However, dip-conversion of a planar $PbBr_2$ film in a solution of CsBr in methanol is very slow and tends to result in destruction of the film by the dipping solvent.

To overcome these limitations, vapour deposition was explored as a preparation route for thick planar films of $CsPbBr_3$. While vapour deposition is a well-known technique for producing continuous and uniform films,[18] prior to this study evaporated films of $CsPbBr_3$ had been deposited only when starting from a powder of $CsPbBr_3$ prepared by solid state synthesis.[19–21] These reports commented that even when beginning from a powdered $CsPbBr_3$ crystal, the temperature of the substrate during deposition and the annealing post-deposition significantly affected the crystallinity of the resulting vapour-deposited film.[19,21]

Sequential evaporation has been demonstrated for hybrid perovskite films, in which the lead halide layer is usually deposited first, followed by the organic salt. Here the $CsPbBr_3$ perovskite was deposited by sequential evaporation of layers of $PbBr_2$ (107 nm) and CsBr (93 nm), and both deposition orders were tested to see if the order affects the final film quality. Full experimental details may be found in the Experimental Methods chapter.

The films were annealed after deposition to ensure thorough inter-diffusion of the adjacent precursor salts and the formation of $CsPbBr_3$ in the perovskite structure. The absorption of the films before and after annealing is shown in Figure 5-1 for both deposition orders. Although deposited onto room temperature substrates, very little inter-diffusion occurred during deposition for an initial layer of $PbBr_2$, resulting in a microcrystalline film.[21] Annealing of this film gives a well-defined 1s exciton absorption peak around 520 nm (2.38 eV). A higher initial absorbance is

 

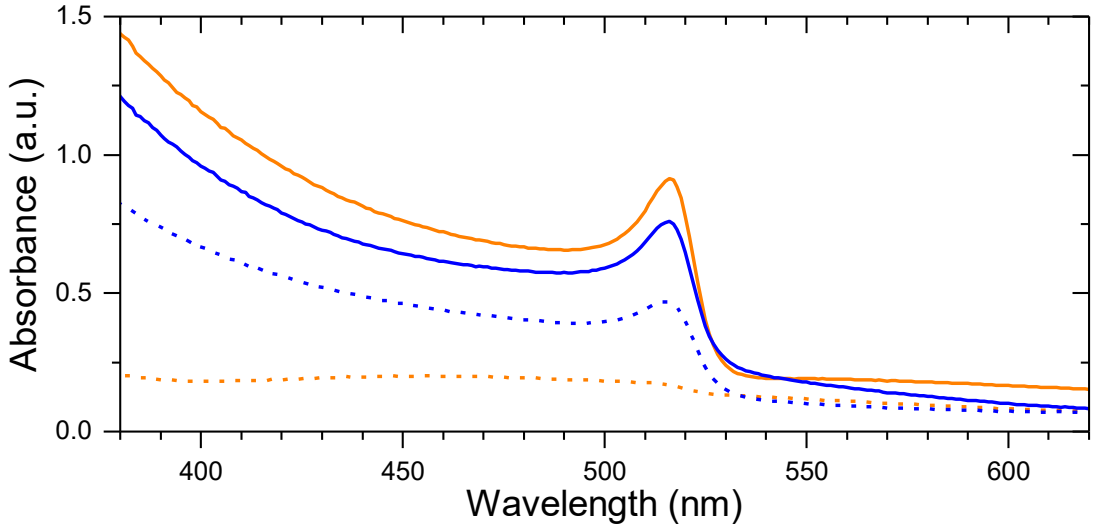


**Figure 5-1. Absorbance of as-deposited (dashed lines) and annealed (solid lines) $CsPbBr_3$ films, for deposition orders of $PbBr_2$/CsBr (orange) and CsBr/$PbBr_2$ (blue).**

seen for an initial layer of CsBr, although the final absorbance is lower than for an initial layer of $PbBr_2$.

The photoluminescence (PL) for a $PbBr_2$/CsBr thin film is shown in Figure 5-2 for a variety of annealing parameters. The photoluminescence peak is centred around 524 nm (2.37 eV), which is consistent with previous observations of polycrystalline films of $CsPbBr_3$.[21] The optimal annealing times and temperatures were determined by the time required to reach maximum absorbance at each temperature. These parameters are shown in the inset of Figure 5-2. A minimum temperature of 100 °C is required to enable inter-diffusion of the two layers. With increasing annealing temperature there is a slight peak shift of ~2 nm to longer wavelength, most likely due to an increase in size of the polycrystalline domains.

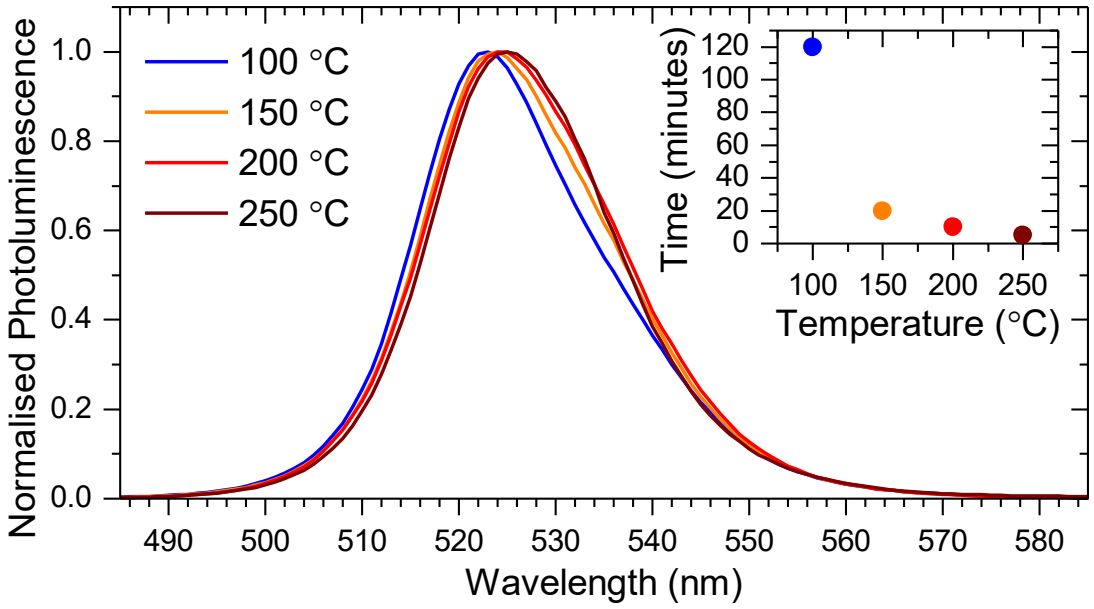


**Figure 5-2. Normalised photoluminescence (PL) of $CsPbBr_3$ thin films ($PbBr_2$/CsBr), with annealing as per the times and temperatures in the inset.**

To verify the phase purity of the annealed $CsPbBr_3$ layers, X-ray diffraction patterns were collected for both deposition orders. These patterns are shown in Figure 5-3 along with a reference powder pattern for $CsPbBr_3$. Sharp peaks in the films are shown to match in position with the powder diffraction reference with the aid of vertical lines. Deviations in intensity suggest some orientation of the polycrystalline domains in the films. In particular, the $0k0$ peaks are very small or absent. Importantly there are no peaks evident from crystalline domains of compounds other than $CsPbBr_3$ and the quartz substrate. No peaks are seen at 12.8° in Figure 5-3(a) or Figure 5-3(b) from excess unreacted lead bromide in the vapour-deposited films. Other mixed compounds of lead bromide and caesium bromide are possible with slight deviations in stoichiometry, such as $CsPb_2Br_5$ and/or $Cs_4PbBr_6$.[22,23] However, in Figure 5-3(a) or Figure 5-3(b), there are no peaks visible from these compounds or from CsBr, indicating that the films are stoichiometric.

 

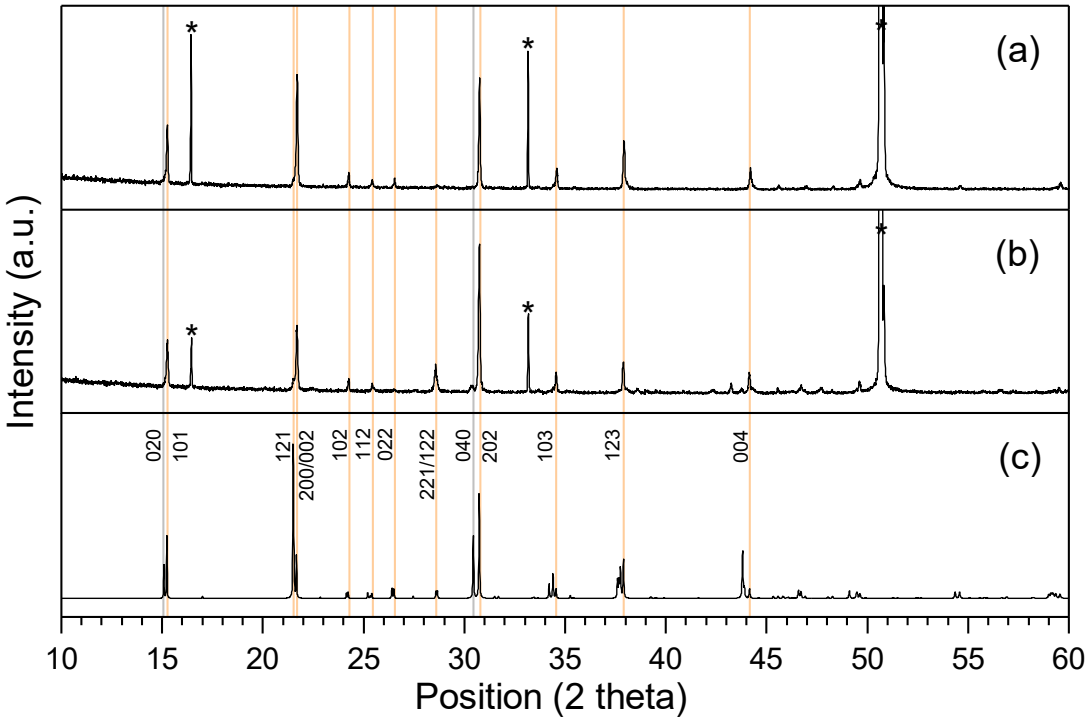


**Figure 5-3. X-ray diffraction (XRD) patterns for annealed $CsPbBr_3$ films with layers deposited as (a) $PbBr_2$/CsBr and (b) CsBr/$PbBr_2$. These patterns were measured at room temperature with a Panalytical X'pert powder diffractometer with Cu $K_{\alpha 1}$ radiation. * denotes peaks from the z-cut quartz substrate. (c) Reference pattern simulated in VESTA for a Cu anode for a powder of $CsPbBr_3$ at 298 K at ambient conditions (orthorhombic perovskite, space group Pbnm(62), cif from Stoumpos et al.[24]).[25] Orange lines show matching of peaks with reference pattern; grey lines show suppressed peaks.**

## 5.4 Temperature-dependent optical measurements

For temperature-dependent optical measurements, thin films of $CsPbBr_3$ were prepared as described in the previous section, using sequential deposition of $PbBr_2$ (107 nm) followed by CsBr (93 nm). $CsPbI_3$ and $CsPbI_2Br$ perovskite layers were deposited as for the thin films in Chapter 4. Although black after preparation in Oxford, the iodide-rich films arrived in France in the yellow non-perovskite polymorph. To prepare the $CsPbI_3$ and $CsPbI_2Br$ films for measurement, they were briefly annealed above their respective transition temperatures of 350 °C and 250 °C until visibly black, and then immediately transferred to the cryostat and put under

 

vacuum. The retention of the black phase after annealing is evidenced by the transmission of these films, shown in Figure 5-4(c) and (b) respectively, where the absorption onsets are below 2 eV for all temperatures from room temperature down to 4.2 K. Although the $CsPbBr_3$ films retained their orange-yellow appearance during transit, these films were measured with and without re-annealing at 250 °C (above the transition to the cubic polymorph) to check for structural transitions. Figure 5-4(a) shows no significant difference between the as-made and re-annealed films, indicating that the films adopt the orthorhombic perovskite polymorph when quench cooled from the cubic polymorph.

Interestingly, a linear dependence of the bandgap with temperature is seen in Figure 5-4(d) for all three perovskites. The absence of any discontinuities from room temperature down to 4.2 K suggests that no phase transitions occur below room temperature, unlike for the hybrid perovskites.[14,15] The absence of any phase transitions for the neat bromide compound is consistent with the film beginning in the orthorhombic perovskite polymorph at room temperature and remaining in this polymorph as the temperature decreases.[12,13,24] However, for the iodide-rich compositions, which are thought to be in the high-temperature cubic perovskite polymorph at room temperature, the absence of any structural transitions to lower symmetry perovskites is unusual.[6,7] This discrepancy is investigated further in Chapter 6.

 

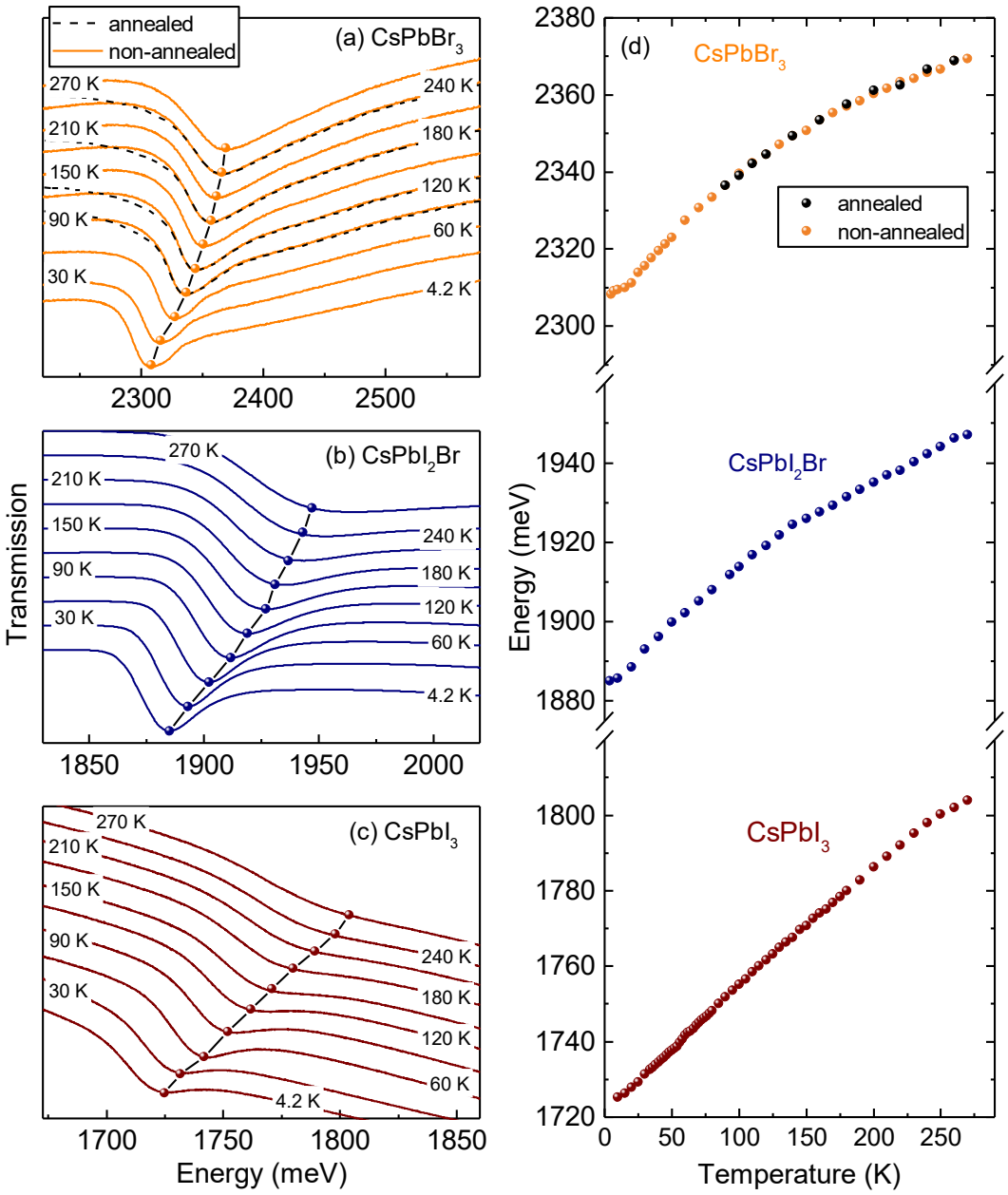


**Figure 5-4. Temperature-dependent transmission spectra for (a) $CsPbBr_3$, (b) $CsPbI_2Br$, and (c) $CsPbI_3$ from room temperature down to 4.2 K. Symbols mark the shift of the 1s absorption onset with temperature, which are the points plotted in (d). For $CsPbBr_3$, samples were measured with (dashed lines) and without (solid lines) re-annealing. These measurements were made by Zhuo Yang and Krzysztof Galkowski at the Laboratoire National des Champs Magnétiques Intenses (LNCMI).**

## 5.5 Low-temperature magneto-transmission spectroscopy

Because the photoactive polymorphs of all three perovskites are retained from room temperature to cryogenic temperatures, it was possible to further investigate the optical properties of these films in high magnetic fields.

Magneto-transmission spectroscopy is a powerful experimental technique which can probe the band structure of a semiconductor, and which has already been used to determine the binding energy and reduced mass of the exciton in organic–inorganic perovskites.[14,15,26] The theory behind this technique will be briefly outlined here before the presentation of the results.

A charged particle, of mass $m$, velocity $v$, and charge $q$, undergoes cyclotron motion perpendicular to the magnetic field with a radius $r$ in a magnetic field $B$, where the centripetal force is provided by the magnetic Lorentz force:

$$\frac{mv^2}{r} = qBv \qquad \text{Equation 5-1}$$

For charge carriers (including excitons) in a material, the reduced mass $\mu$ may be used, where $\mu^{-1} = m_e^{-1} + m_h^{-1}$. The cyclotron frequency $\omega_c$ of the charge carriers is then given by Equation 5-2.

$$\omega_c = \frac{v}{r} = \frac{eB}{\mu} \qquad \text{Equation 5-2}$$

Note that $\omega_c$ is independent of the cyclotron radius for a fixed ratio of $e{:}\mu$, and instead depends only on the applied magnetic field.

The cyclotron motion is quantised, with allowed Landau levels $E_L = \left(n + \frac{1}{2}\right)\hbar\omega_c$ for $n = 0, 1, 2, \ldots$ For a material with bandgap $E_g$, separate 'ladders' of Landau levels for electrons and for holes are present within each of the conduction and valence bands, as depicted in Figure 5-5. For optical excitation, dipole-allowed transitions between Landau levels in the valence band to Landau levels in the conduction band are possible when $\Delta n = 0$.

 

The excitation energy $E$ for the transition is then given by Equation 5-3:

$$\boldsymbol{E = E_g + \left(n + \frac{1}{2}\right)\frac{\hbar eB}{\mu}}, \text{ for } \boldsymbol{n = 0, 1, 2, \ldots}$$

**Equation 5-3**

The Landau levels are easily broadened by scattering of charge carriers. For Landau levels to be observed, the lifetime $\tau$ of the charge carriers must be long enough to complete at least one full oscillation, i.e. $\omega_c\tau > 1$. In practice, observation of Landau levels requires low temperatures to reduce scattering, and large magnetic fields to gain sufficient separation of the Landau levels.

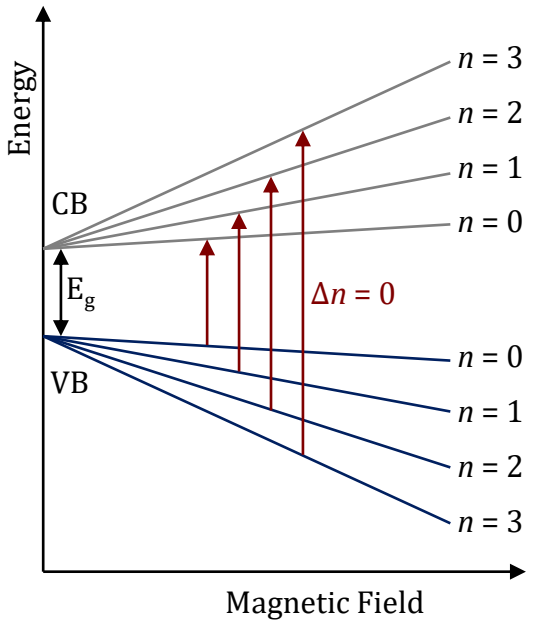


**Figure 5-5. Landau levels in the conduction (CB) and valence (VB) bands for both electrons and holes. Dipole-allowed transitions where $\Delta n = 0$ are indicated by red arrows.**

In the low-temperature magneto-transmission spectroscopy here, transitions between Landau levels are seen as local minima in the optical transmission spectra using two complementary techniques. In the long pulse technique, a sample is illuminated with white light, and the absorption spectrum measured in the presence of an applied magnetic field (typically up to ~70 T). In the short pulse (single turn coil) technique, the sample is illuminated with monochromatic laser light and the magnetic field scanned, which allows measurements up to 150 T.

The energies for which local absorption maxima (transmission minima) occur may be plotted against the magnetic field and fitted using Equation 5-3 in order to determine the reduced mass $\mu$. This method is quite effective in the high magnetic

field limit, where the magnetic force is much greater than the Coulomb force: the electron is then comparatively weakly bound in the field direction and so behaves more like a free charge carrier.[27]

Closer to the band edge, the transitions are exciton-like and are more accurately described by a hydrogen-like model in high magnetic field.[28] For an excitonic system in zero field, the eigenenergies $E_N$ of the $N^{\text{th}}$ excitonic level are given by Equation 5-4. Numerical solutions for the variation of these eigenenergies in a magnetic field have been calculated by Makado and McGill.[27]

$$E_N = E_g - \frac{R^*}{N^2}, \text{ for } N = 1, 2, 3, \ldots \qquad \text{Equation 5-4}$$

Here the exciton binding energy $R^* = \frac{R_0 \mu}{m_0 \varepsilon_{eff}{}^2}$, where $R_0$ is the atomic Rydberg, $m_0$ is the free electron mass and $\varepsilon_{eff}$ is the relative dielectric constant. It should be noted that $\varepsilon_{eff} = \frac{e^2}{\hbar}\sqrt{\frac{\mu}{2R^*}}$ is the relative dielectric constant (relative to $\varepsilon_0$). $\varepsilon_{eff}$ is neither the static nor the high frequency dielectric constant, but rather $\varepsilon$ at an intermediate frequency given by the exciton binding energy, and reflects the frequency with which the electron and hole rotate around each other in the exciton.

Of the parameters in Equation 5-4, only $\mu$ and $\varepsilon_{eff}$ are free variables. With the accurate estimation of $\mu$ from fitting of the inter-Landau level transitions, $\varepsilon_{eff}$ and $R^*$ may then be determined by fitting the remaining local absorption maxima with Equation 5-4.

Figure 5-6(a)-(c) show how the transmission spectra at 2 K change in the presence of intense magnetic fields for each of the inorganic perovskites. To clearly see the effect of the magnetic field on the optical transmission, spectra are shown divided by the zero-field spectrum. Minima in the differential transmission are marked by downward arrows. The first of these minima, for example at ~2313 meV in Figure 5-6(c) for $CsPbBr_3$, is attributed to the 1s excitonic state, and shows a blue shift and an increase in absorption with applied magnetic field.

 

For the neat halides, the 2s excitonic transition is also visible as a slight dip on the higher energy side of the 1s absorption. Further higher energy minima from free carrier transitions between Landau levels in the valence and conduction bands are visible with high magnetic fields, particularly for $CsPbI_3$. These free carrier transitions are better resolved with the short pulse technique, as shown in Figure 5-6(d)-(f) for each of the perovskites. Here high magnetic fields ($B > 70$ T) are generated as a short pulse by a single turn coil while the transmission of monochromatic laser light through the sample is measured.

Fits to these minima using Equation 5-3 and Equation 5-4 give the values in Table 5-1 for the three perovskites, which are compared graphically with the respective values from the hybrid perovskites in Figure 5-7. Landau fan charts illustrating the fittings may be found in the published manuscript.[28]

**Table 5-1. Experimentally-determined parameters for caesium-based perovskite compounds at 2 K.**

| Compound | $E_g$ (meV) | $\mu$ ($m_0$) | R* (meV) | $\varepsilon_{eff}$ |
|---|---|---|---|---|
| $CsPbI_3$ | 1723 | 0.114 ± 0.01 | 15 ± 1 | 10.0 |
| $CsPbI_2Br$ | 1906 | 0.124 ± 0.02 | 22 ± 3 | 8.6 |
| $CsPbBr_3$ | 2342 | 0.126 ± 0.01 | 33 ± 1 | 7.3 |

 

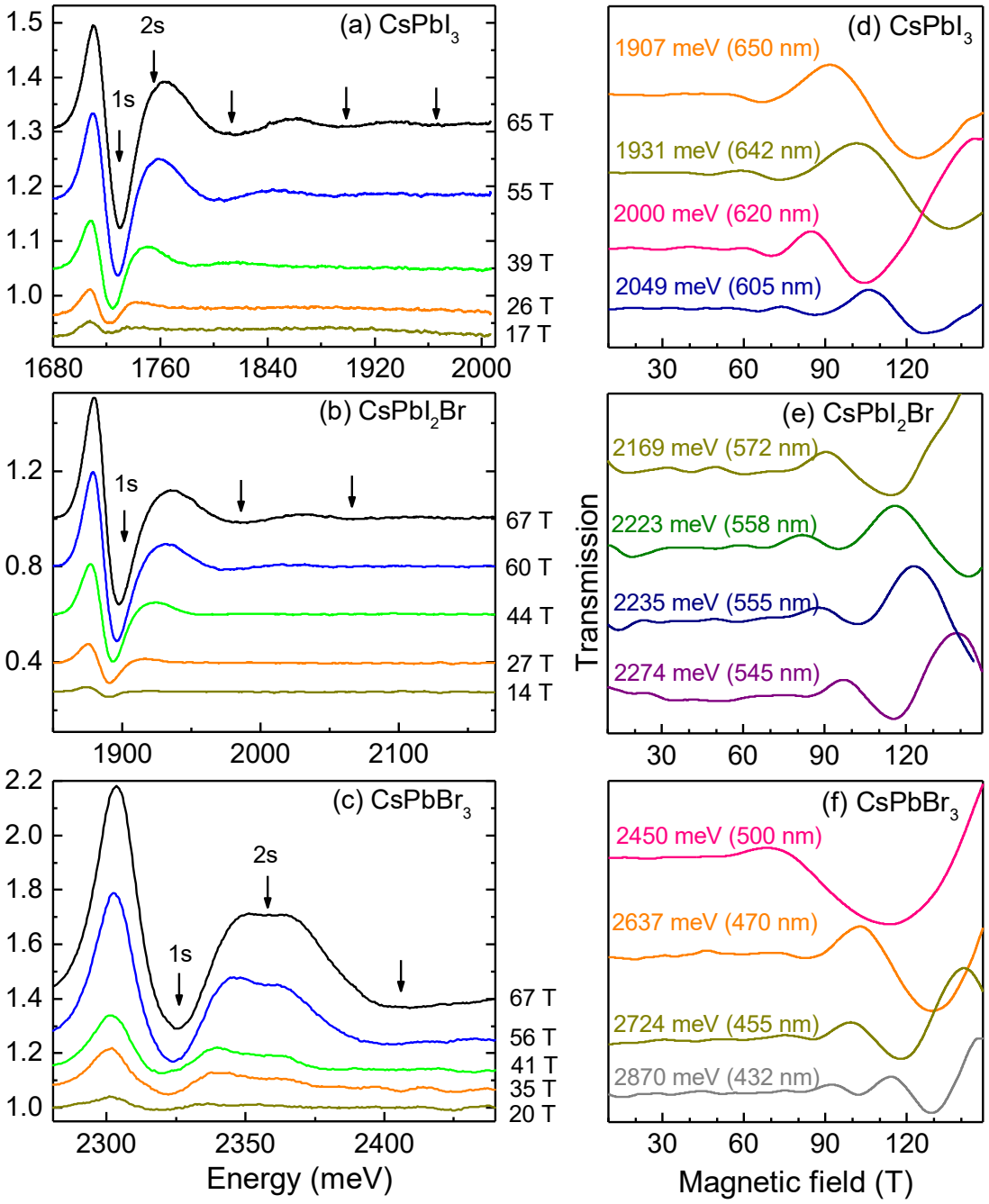


**Figure 5-6. Measurements of the optical transmission at 2 K under high magnetic fields for each of the three perovskites. (a)-(c) show differential transmission spectra, where the transmission spectrum at the specified magnetic field is divided by the zero-field spectrum, for long pulse magnetic fields. Downward arrows mark local minima. (d)-(f) show transmission at the specified wavelength as a function of magnetic field, obtained by the short pulse technique. These measurements were made by Zhuo Yang, Krzysztof Galkowski, Alessandro Surrente, and Atsuhiko Miyata at the LNCMI.**

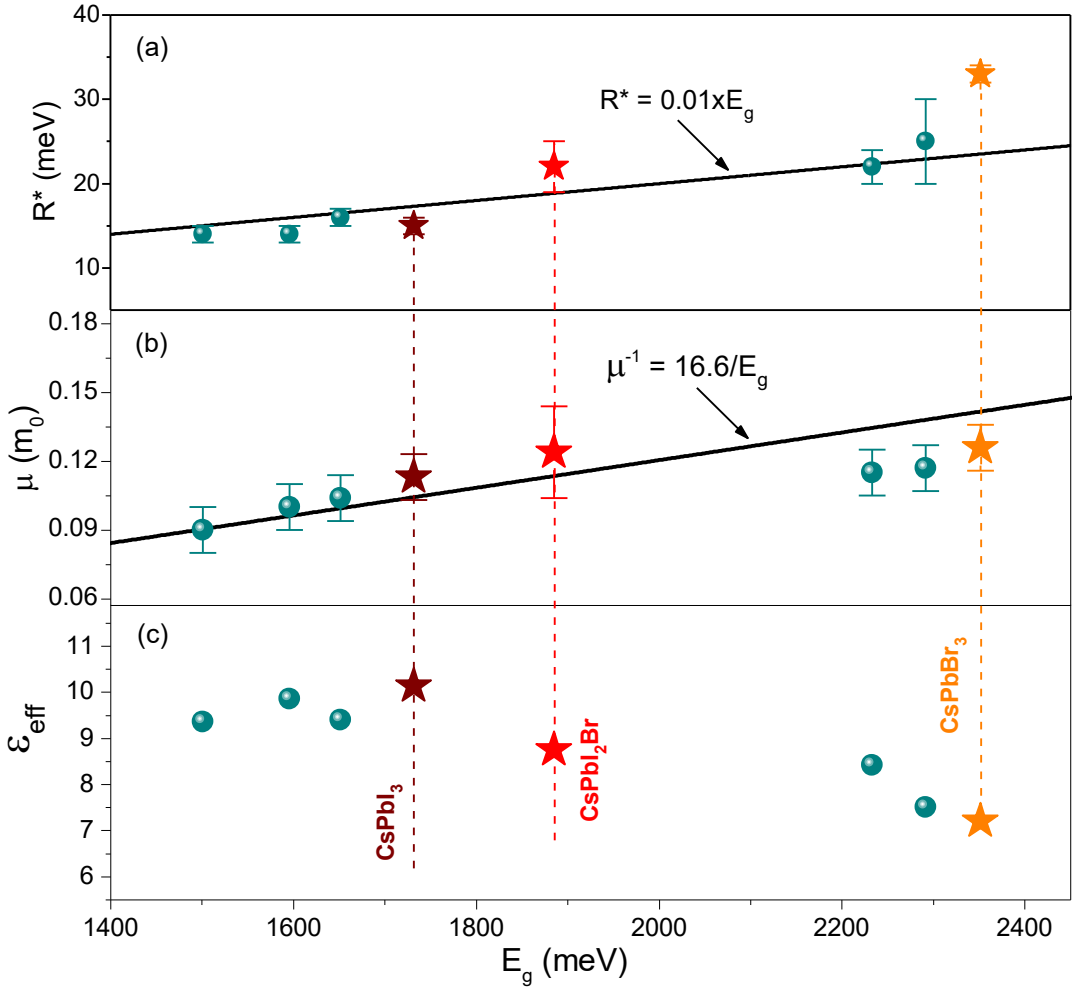


**Figure 5-7. (a) Exciton binding energy, R*, (b) reduced mass, μ, and (c) dielectric constant, $\varepsilon_{eff}$, determined from the data in Figure 5-6 for the three inorganic perovskites (stars), compared with the respective values for the hybrid perovskites (teal circles).[15] These values were determined by Zhuo Yang and Krzysztof Galkowski at the LNCMI.**

These experimentally-determined parameters are in excellent agreement with density functional theory of the hybrid perovskites, taking into account the experimental band gap.[29] In particular, the exciton reduced masses are similar to previously determined values for the hybrid perovskites shown in Figure 5-7(b).[15] The reduced mass of $CsPbI_3$ is also within theoretical predictions for the cubic polymorph, which range between from ~0.07 $m_0$[30,31] and ~0.18 $m_0$.[32]

The exciton binding energies of the inorganic lead halide perovskites are comparable to those of the hybrid perovskites, as shown in Figure 5-7(a), with a similar increase in binding energy with bandgap energy. Given that no phase transition is observed for these three perovskites from room temperature to 2 K, the exciton binding energies are unlikely to vary significantly with temperature over this region. The similarity of magnetic-field dependent behaviour between 2 K and 170 K is shown for $CsPbBr_3$ in the published manuscript.[28] It follows that at room temperature, or even at solar cell operating temperatures, it is highly likely that the photogenerated charge carriers in all three perovskites behave like free carriers.

A comparison of the dielectric constants, $\varepsilon_{eff}$, of the inorganic and hybrid perovskites in Figure 5-7(c) shows that the dielectric constant decreases as the halide mass decreases. As the organic cation motion is frozen at low temperatures, this trend implies that the dielectric screening depends more strongly on the halide than on the cation. This trend is consistent with theoretical calculations and with Raman spectroscopy of the hybrid perovskites which showed that the main contributions to the dielectric permittivity of lead halide perovskites are stretching modes of the Pb–X bond and rocking modes of the Pb–X–Pb backbone.[33,34]

## 5.6 Conclusion and outlook

In this chapter, a method was developed for fabricating thin films of $CsPbBr_3$, which enabled a comprehensive experimental study of the electronic properties of the inorganic perovskites. Specifically, thin films of $CsPbBr_3$ were prepared by sequential evaporation of $PbBr_2$ and CsBr followed by annealing. This method is a highly controlled, reproducible alternative to solution processing for depositing planar films of $CsPbBr_3$.

This study highlighted the huge influence of the halide on the optoelectronic properties of lead halide perovskites. Most research on perovskite solar cells involves

 

iodide-rich perovskites. However, the highest efficiency solar cells have a small amount of bromide. The amount of bromide has usually been limited due to issues with halide segregation, but here the decrease in dielectric constant with bromide indicates that limiting the bromide content is also important to ensure efficient charge separation. Rather, $CsPbBr_3$ has a bright future in light emission applications.

A secondary finding, which is highly important for this thesis, is the absence of any phase transitions observed in the inorganic perovskite thin films, unlike for the hybrid perovskites. While no phase transitions would be expected for the orthorhombic $CsPbBr_3$, the iodide-rich perovskites are thought to be trapped in a cubic phase when black. The cubic phase is usually the high temperature polymorph of a perovskite material, and typically would transition to orthorhombic (or at least tetragonal) as the temperature is lowered. Additionally, $CsPbI_3$ is known to be unstable in the black polymorph at ambient conditions. The absence of phase transitions in the iodide-rich perovskites is inconsistent with the preparation of these films in a cubic phase, and so further investigation of these quench-cooled films is needed. Fortunately, the absence of phase transitions in these materials means that the determined parameters are representative of the thin films used in inorganic perovskite solar cells.

The electronic properties determined in this study for the inorganic lead halide perovskites are on par with their hybrid counterparts, which is promising for the future of inorganic perovskite solar cells. The similarity between inorganic and hybrid perovskites also fits with the improvements in device performance when mixing caesium and organic cations. However, despite the similarity of electronic properties, solar cells with inorganic lead halide perovskites lag behind their hybrid counterparts. The highest power conversion efficiency of a perovskite solar cell with an inorganic perovskite absorber is around 14%,[35–37] while mixed cation perovskite

 

solar cells with a similar bandgap are over 22%.[8–11] The findings in this chapter show no reason for this efficiency gap other than a scarcity of research effort on developing inorganic perovskite solar cells, along with the difficulty in maintaining the black phase of the iodide-rich perovskites.

## 5.7 References


1. Shin, S. S.; Yeom, E. J.; Yang, W. S.; Hur, S.; Kim, M. G.; Im, J.; Seo, J.; Noh, J. H.; Seok, S. Il. "Colloidally Prepared La-Doped $BaSnO_3$ Electrodes for Efficient, Photostable Perovskite Solar Cells". *Science* 2017, *356*, 167–171.
2. National Renewable Energy Laboratory. Best Research-Cell Efficiencies https://www.nrel.gov/pv/assets/images/efficiency-chart.png.
3. Niu, G.; Guo, X.; Wang, L. "Review of Recent Progress in Chemical Stability of Perovskite Solar Cells". *J. Mater. Chem. A* 2015, *3*, 8970–8980.
4. Patel, J. B.; Milot, R. L.; Wright, A. D.; Herz, L. M.; Johnston, M. B. "Formation Dynamics of $CH_3NH_3PbI_3$ Perovskite Following Two-Step Layer Deposition". *J. Phys. Chem. Lett.* 2015, *7*, acs.jpclett.5b02495.
5. Eperon, G. E.; Stranks, S. D.; Menelaou, C.; Johnston, M. B.; Herz, L. M.; Snaith, H. J. "Formamidinium Lead Trihalide: A Broadly Tunable Perovskite for Efficient Planar Heterojunction Solar Cells". *Energy Environ. Sci.* 2014, *7*, 982.
6. Eperon, G. E.; Paternò, G. M.; Sutton, R. J.; Zampetti, A.; Haghighirad, A. A.; Cacialli, F.; Snaith, H. J. "Inorganic Caesium Lead Iodide Perovskite Solar Cells". *J. Mater. Chem. A* 2015, *3*, 19688–19695.
7. Sutton, R. J.; Eperon, G. E.; Miranda, L.; Parrott, E. S.; Kamino, B. A.; Patel, J. B.; Hörantner, M. T.; Johnston, M. B.; Haghighirad, A. A.; Moore, D. T.; Snaith, H. J. "Bandgap-Tunable Cesium Lead Halide Perovskites with High Thermal Stability for Efficient Solar Cells". *Adv. Energy Mater.* 2016, *6*, 1502458.
8. McMeekin, D. P.; Sadoughi, G.; Rehman, W.; Eperon, G. E.; Saliba, M.; Horantner, M. T.; Haghighirad, A.; Sakai, N.; Korte, L.; Rech, B.; Johnston, M. B.; Herz, L. M.; Snaith, H. J. "A Mixed-Cation Lead Mixed-Halide Perovskite Absorber for Tandem Solar Cells". *Science* 2016, *351*, 151–155.
9. Bu, T.; Liu, X.; Zhou, Y.; Yi, J.; Huang, X.; Luo, L.; Xiao, J.; Ku, Z.; Peng, Y.; Huang, F.; Cheng, Y.-B.; Zhong, J. "A Novel Quadruple-Cation Absorber for Universal Hysteresis Elimination for High Efficiency and Stable Perovskite Solar Cells". *Energy Environ. Sci.* 2017, *10*, 2509–2515.
10. Wang, Z.; McMeekin, D. P.; Sakai, N.; van Reenen, S.; Wojciechowski, K.; Patel, J. B.; Johnston, M. B.; Snaith, H. J. "Efficient and Air-Stable Mixed-Cation Lead Mixed-Halide Perovskite Solar Cells with n-Doped Organic Electron Extraction Layers". *Adv. Mater.* 2017, *29*, 1604186.
11. Saliba, M.; Matsui, T.; Seo, J.-Y.; Domanski, K.; Correa-Baena, J.-P.; Mohammad K., N.; Zakeeruddin, S. M.; Tress, W.; Abate, A.; Hagfeldt, A.; Grätzel, M. "Cesium-Containing Triple Cation Perovskite Solar Cells: Improved Stability, Reproducibility and High Efficiency". *Energy Environ. Sci.* 2016.


 

12. Sharma, S.; Weiden, N.; Weiss, A. "Phase Diagrams of Quasibinary Systems of the Type: $ABX_3$ — $A'BX_3$; $ABX_3$ — $AB'X_3$, and $ABX_3$ — $ABX'_3$; X = Halogen". *Zeitschrift für Phys. Chemie* 1992, *175*, 63–80.

13. Rodová, M.; Brožek, J.; Knížek, K.; Nitsch, K. "Phase Transitions in Ternary Caesium Lead Bromide". *J. Therm. Anal. Calorim.* 2003, *71*, 667–673.

14. Miyata, A.; Mitioglu, A.; Plochocka, P.; Portugall, O.; Wang, J. T.-W.; Stranks, S. D.; Snaith, H. J.; Nicholas, R. J. "Direct Measurement of the Exciton Binding Energy and Effective Masses for Charge Carriers in Organic–inorganic Tri-Halide Perovskites". *Nat. Phys.* 2015, *11*, 582–587.

15. Galkowski, K.; Mitioglu, A.; Miyata, A.; Plochocka, P.; Portugall, O.; Eperon, G. E.; Wang, J. T.-W.; Stergiopoulos, T.; Stranks, S. D.; Snaith, H. J.; Nicholas, R. J. "Determination of the Exciton Binding Energy and Effective Masses for Methylammonium and Formamidinium Lead Tri-Halide Perovskite Semiconductors". *Energy Environ. Sci.* 2016, *9*, 962–970.

16. Poglitsch, A.; Weber, D. "Dynamic Disorder in Methylammonium-trihalogenoplumbates (II) Observed by Millimeter-Wave Spectroscopy". *J. Chem. Phys.* 1987, *87*, 6373–6378.

17. Kulbak, M.; Cahen, D.; Hodes, G. "How Important Is the Organic Part of Lead Halide Perovskite Photovoltaic Cells? Efficient $CsPbBr_3$ Cells". *J. Phys. Chem. Lett.* 2015, *6*, 2452–2456.

18. Liu, M.; Johnston, M. B.; Snaith, H. J. "Efficient Planar Heterojunction Perovskite Solar Cells by Vapour Deposition.". *Nature* 2013, *501*, 395–398.

19. Kondo, S.; Sakai, T.; Tanaka, H.; Saito, T. "Amorphization-Induced Strong Localization of Electronic States in $CsPbBr_3$ and $CsPbCl_3$ Studied by Optical Absorption Measurements". *Phys. Rev. B* 1998, *58*, 11401–11407.

20. Heidrich, K.; Künzel, H.; Treusch, J. "Optical Properties and Electronic Structure of $CsPbCl_3$ and $CsPbBr_3$". *Solid State Commun.* 1978, *25*, 887–889.

21. Kondo, S.; Kakuchi, M.; Masaki, A.; Saito, T. "Strongly Enhanced Free-Exciton Luminescence in Microcrystalline $CsPbBr_3$ Films". *J. Phys. Soc. Japan* 2003, *72*, 1789–1791.

22. Wells, H. L. "On the Caesium- and the Potassium-Lead Halides". *Am. J. Sci.* 1893, *s3-45*, 121–134.

23. Møller, C. K. "Crystal Structure and Photoconductivity of Cæsium Plumbohalides". *Nature* 1958, *182*, 1436–1436.

24. Stoumpos, C. C.; Malliakas, C. D.; Peters, J. A.; Liu, Z.; Sebastian, M.; Im, J.; Chasapis, T. C.; Wibowo, A. C.; Chung, D. Y.; Freeman, A. J.; Wessels, B. W.; Kanatzidis, M. G. "Crystal Growth of the Perovskite Semiconductor $CsPbBr_3$: A New Material for High-Energy Radiation Detection". *Cryst. Growth Des.* 2013, *13*, 2722–2727.

25. Momma, K.; Izumi, F. "VESTA: A Three-Dimensional Visualization System for Electronic and Structural Analysis". *J. Appl. Crystallogr.* 2008, *41*, 653–658.

26. Yang, Z.; Surrente, A.; Galkowski, K.; Bruyant, N.; Maude, D. K.; Haghighirad, A. A.; Snaith, H. J.; Plochocka, P.; Nicholas, R. J. "Unraveling the Exciton Binding Energy and the Dielectric Constant in Single-Crystal Methylammonium Lead Triiodide Perovskite". *J. Phys. Chem. Lett.* 2017, *8*, 1851–1855.

 

27. Makado, P. C.; McGill, N. C. "Energy Levels of a Neutral Hydrogen-like System in a Constant Magnetic Field of Arbitrary Strength". *J. Phys. C Solid State Phys.* 1986, *19*, 873–885.

28. Yang, Z.; Surrente, A.; Galkowski, K.; Miyata, A.; Portugall, O.; Sutton, R. J.; Haghighirad, A. A.; Snaith, H. J.; Maude, D. K.; Plochocka, P.; Nicholas, R. J. "Impact of the Halide Cage on the Electronic Properties of Fully Inorganic Cesium Lead Halide Perovskites". *ACS Energy Lett.* 2017, *2*, 1621–1627.

29. Umari, P.; Mosconi, E.; De Angelis, F. "Relativistic GW Calculations on $CH_3NH_3PbI_3$ and $CH_3NH_3SnI_3$ Perovskites for Solar Cell Applications". *Sci. Rep.* 2015, *4*, 4467.

30. Amat, A.; Mosconi, E.; Ronca, E.; Quarti, C.; Umari, P.; Nazeeruddin, M. K.; Grätzel, M.; De Angelis, F. "Cation-Induced Band-Gap Tuning in Organohalide Perovskites: Interplay of Spin-Orbit Coupling and Octahedra Tilting". *Nano Lett.* 2014, *14*, 3608–3616.

31. Chang, Y. H.; Park, C. H.; Matsuishi, K. "First-Principles Study of the Structural and the Electronic Properties of the Lead-Halide-Based Inorganic-Organic Perovskites $(CH_3NH_3)PbX_3$ and $CsPbX_3$ (X = Cl, Br, I)". *J. Korean Phys. Soc.* 2004, *41*.

32. Giorgi, G.; Fujisawa, J.-I.; Segawa, H.; Yamashita, K. "Cation Role in Structural and Electronic Properties of 3D Organic–Inorganic Halide Perovskites: A DFT Analysis". *J. Phys. Chem. C* 2014, *118*, 12176–12183.

33. Sendner, M.; Nayak, P. K.; Egger, D. A.; Beck, S.; Müller, C.; Epding, B.; Kowalsky, W.; Kronik, L.; Snaith, H. J.; Pucci, A.; Lovrinčić, R. "Optical Phonons in Methylammonium Lead Halide Perovskites and Implications for Charge Transport". *Mater. Horizons* 2016, *3*, 613–620.

34. Pérez-Osorio, M. A.; Milot, R. L.; Filip, M. R.; Patel, J. B.; Herz, L. M.; Johnston, M. B.; Giustino, F. "Vibrational Properties of the Organic–Inorganic Halide Perovskite $CH_3NH_3PbI_3$ from Theory and Experiment: Factor Group Analysis, First-Principles Calculations, and Low-Temperature Infrared Spectra". *J. Phys. Chem. C* 2015, *119*, 25703–25718.

35. Hu, Y.; Bai, F.; Liu, X.; Ji, Q.; Miao, X.; Qiu, T.; Zhang, S. "Bismuth Incorporation Stabilized α-$CsPbI_3$ for Fully Inorganic Perovskite Solar Cells". *ACS Energy Lett.* 2017, *2*, 2219–2227.

36. Lau, C. F. J.; Deng, X.; Zheng, J.; Kim, J.; Zhang, Z.; Zhang, M.; Bing, J.; Wilkinson, B.; Hu, L.; Patterson, R.; Huang, S.; Ho-Baillie, A. "Enhanced Performance via Partial Lead Replacement with Calcium for a $CsPbI_3$ Perovskite Solar Cell Exceeding 13% Power Conversion Efficiency". *J. Mater. Chem. A* 2018, *6*, 5580–5586.

37. Bian, H.; Bai, D.; Jin, Z.; Wang, K.; Liang, L.; Wang, H.; Zhang, J.; Wang, Q.; Liu, S. (Frank). "Graded Bandgap $CsPbI_{2+x}Br_{1-x}$ Perovskite Solar Cells with a Stabilized Efficiency of 14.4%". *Joule* 2018, *0*.

 

# 6 The Crystal Structure of Black-Phase Caesium Lead Iodide

The work presented in this chapter has been published as:

R. J. Sutton, M. R. Filip A. A. Haghighirad, N. Sakai, B. Wenger, F. Giustino, and H. J. Snaith, 'Cubic or Orthorhombic? Revealing the Crystal Structure of Metastable Black-Phase $CsPbI_3$ by Theory and Experiment', *ACS Energy Lett.* 3, 1787–1794 (2018).

DOI: 10.1021/acsenergylett.8b00672

Direct link: http://pubs.acs.org/doi/10.1021/acsenergylett.8b00672

## 6.1 Wider context and summary

In order to design a structurally-stable inorganic perovskite related to $CsPbI_3$, it is vital to have a thorough understanding of the crystal structure of black-phase $CsPbI_3$. Room-temperature films of black-phase $CsPbI_3$ are widely thought to be trapped in a cubic perovskite polymorph. In this chapter, this assumption is challenged. Full structural refinement of room temperature black-phase $CsPbI_3$ in an orthorhombic polymorph is presented. It is demonstrated that this polymorph is adopted by both powders and by thin-films of black-phase $CsPbI_3$, fabricated either by high- or low-temperature processes. We perform electronic band structure calculations for the orthorhombic polymorph and find excellent agreement with experimental data and close similarities with methylammonium lead iodide. We investigate the structural transitions and thermodynamic stability of the various polymorphs of $CsPbI_3$, and show that the orthorhombic polymorph is the most stable among its other perovskite polymorphs, but it remains less stable than the yellow non-perovskite polymorph. In summary, this chapter represents a step change in thinking for the $CsPbI_3$ perovskite system.

## 6.2 Introduction

Recently there has been significant interest in the iodide-rich inorganic lead halide perovskites for optoelectronic applications. This is due to the high thermal stability of perovskites comprising an inorganic cation, in comparison to the hybrid lead-halide perovskites which comprise organic ammonium cations.[1] In particular, caesium lead iodide ($CsPbI_3$) has gained popularity due to its useful band gap of ~1.72 eV, along with the mixed halide composition $CsPbI_2Br$ which exhibits increased stability with only a small increase in band gap to ~1.92 eV.[1,2] Current best research-cell efficiencies for inorganic perovskite absorbers are around 14%, with multiple reproduced efficiencies of around 11%.[3–7]

 

While the inorganic perovskites are thermally stable, structurally there are significant instabilities for the iodide-rich compositions. The main hindrance to research efforts on these materials is that they readily undergo structural transitions between the desired perovskite material, thought to be a cubic perovskite, and an undesired yellow non-perovskite.[8,1] As well as being inconvenient, it is unusual for a cubic perovskite polymorph to transition directly to a non-perovskite polymorph. Additionally, measurements of the perovskite polymorph reveal no structural transitions from room temperature to 2 K for films under vacuum.[2] The absence of any structural transitions questions the widely-held assumption that this polymorph adopts the high-temperature cubic perovskite structure.[6,9–12]

In order to overcome the structural instabilities of the iodide-rich inorganic perovskites, an accurate understanding of the structure of the perovskite polymorph is required, particularly for $CsPbI_3$. Early reports of $CsPbI_3$ proposed a 'monoclinically distorted perovskite structure', with lattice constants $a = b = 6.15$ Å, $c = 6.23$ Å, $\beta = 88.15°$, or possibly a superstructure similar to that of $CsPbBr_3$.[13,14] More recently, Stoumpos and Kanatzidis have presented tetragonal and orthorhombic structures as determined from temperature-dependent X-ray diffraction (XRD) patterns of powdered $CsPbI_3$ when slowly cooled from the cubic polymorph.[15,16] There have also been a few reports of orthorhombic structures for nanocrystals, nanowires and thin-films.[17–21]

In this chapter, the structure of the black room-temperature polymorph of $CsPbI_3$ is investigated. $CsPbI_3$ powder is isolated in a black polymorph at room temperature, for which high-quality XRD patterns are obtained. Using full refinement of these patterns, it is shown that black $CsPbI_3$ adopts an orthorhombic perovskite polymorph at room temperature which is similar to that of $CsSnI_3$. These XRD patterns of thin-films of $CsPbI_3$ are then indexed with the orthorhombic structure, revealing strong texture in films prepared using high-temperature annealing, and

 

weak texture for films prepared from low-temperature processing routes. To support the claim that these films adopt an orthorhombic perovskite, *GW* band structures are calculated using the refined structure. Very similar properties to the hybrid perovskites are found, as well as to the experimental data, confirming that the well-studied manifestation of $CsPbI_3$ is indeed an orthorhombic perovskite. The chapter concludes with an investigation of the structural transitions and relative stabilities by comparing the formation energies of the various polymorphs of $CsPbI_3$.

## 6.3 Crystal structure determination

To solve the structure of room-temperature black phase $CsPbI_3$, first a powder of $CsPbI_3$ is prepared in the yellow non-perovskite δ-$CsPbI_3$ polymorph using solid state synthesis. The ingot was ground into a powder, and measured with powder X-ray diffraction (XRD). Comparison with the known crystal structure (see Figure 6-1 and Table 6-A1) verifies the product as $CsPbI_3$. Further experimental details are provided in the Experimental Methods chapter.

To gain 'black phase $CsPbI_3$' powder, the yellow δ-$CsPbI_3$ powder was annealed for approximately 20 s at 673 K until fully black, and then rapidly cooled to room temperature. The black powder was kept in inert atmosphere (nitrogen gas) for repeated XRD measurements, in a sample holder with polycarbonate dome, and the measurement was concluded when diffraction peaks from yellow δ-$CsPbI_3$ were visible in the XRD pattern.

 

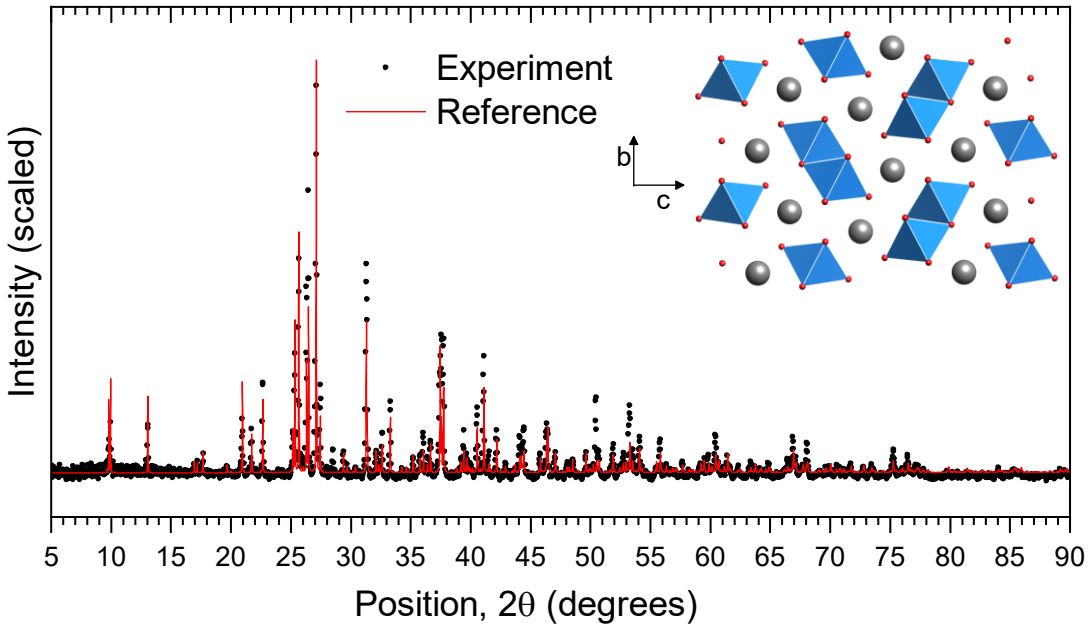


**Figure 6-1. (black dots) XRD pattern for the yellow powder of δ-$CsPbI_3$ prepared by solid state synthesis and measured with Cu $K_{\alpha 1}$ radiation. (red line) Reference powder pattern of non-perovskite δ-$CsPbI_3$ at room temperature, simulated from structural data from a single crystal (see Table 6-A1 in the Appendix to this chapter). (Inset) Polyhedral model where grey spheres represent $Cs^+$ cations, $Pb^{2+}$ cations are at the centres of the blue octahedra, and red spheres represent I- anions.**

Figure 6-2 shows the XRD pattern of the black powder at room temperature. In this XRD pattern, peak splitting is evident in the three characteristic perovskite peaks near 15°, 20° and 30° 2ϑ. This splitting indicates symmetry lowering from the cubic polymorph.[22] The additional reflection peaks, particularly between 20° and 30° 2ϑ, are suggestive of an orthorhombic structure similar to the room temperature orthorhombic $CsSnI_3$ polymorph.[23,24]

The data in Figure 6-2 were refined using Rietveld refinement. The particular orthorhombic structure used for Rietveld refinement was derived from the cubic polymorph by a sequence of tilting known as #10,[25] or $a^+b^-b^-$ in Glazer notation.[26] A polyhedral model of the refined structure is shown in Figure 6-2 and Table 6-1 provides structural parameters from the refinement.

 

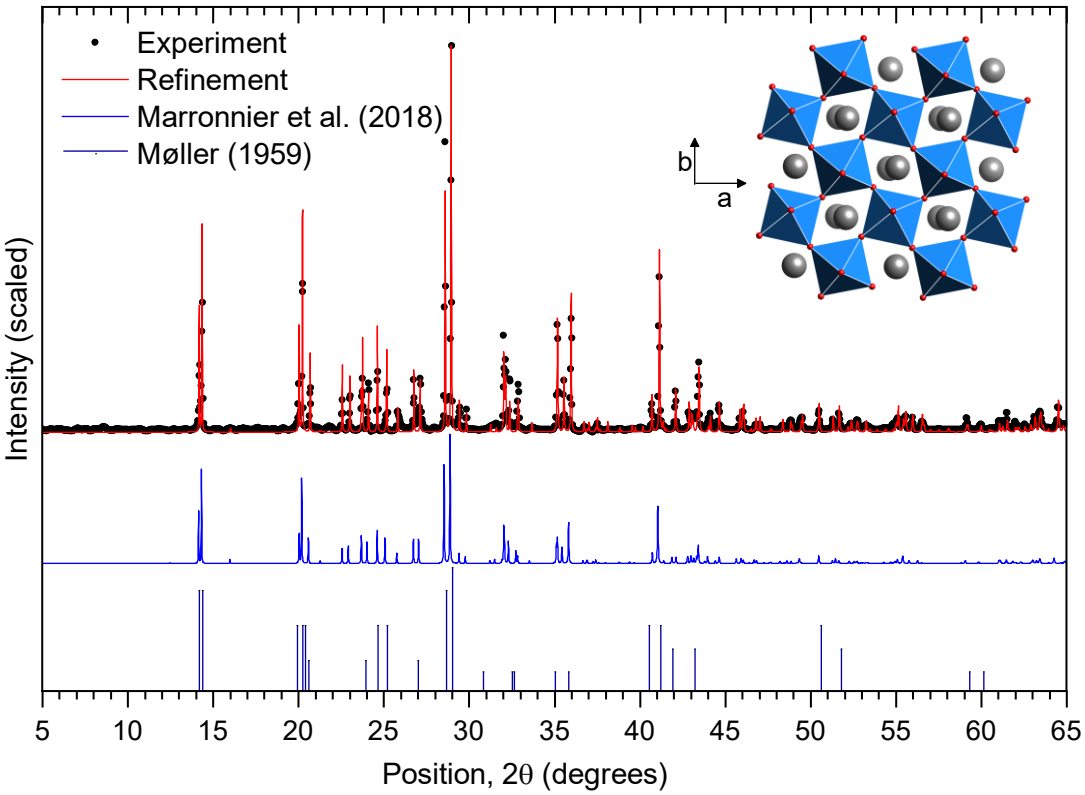


**Figure 6-2. (black dots) XRD pattern for the black powder of γ-$CsPbI_3$ prepared by solid state synthesis, and measured with Cu $K_{\alpha 1}$ radiation at 293 K. (red line) Rietveld refinement of orthorhombic perovskite γ-$CsPbI_3$ at room temperature, with polyhedral model in inset; Structural parameters for the refinement are provided in Table 6-1 and a standard Rietveld plot is provided in Figure 6-A1. The orthorhombic structure was refined by Dr Amir Abbas Haghighirad at the Karlsruhe Institute of Technology. (blue line) XRD pattern calculated for Cu $K_{\alpha 1}$ radiation for the orthorhombic perovskite structure determined by Marronnier et al. at 325 K.[16] (dark blue droplines) Re-creation of the XRD pattern measured by Møller in 1959.[13]**

Recently, Marronnier *et* al. have also reported an orthorhombic polymorph of $CsPbI_3$ at 325 K.[16] In comparison, the orthorhombic structure determined here exhibits subtle differences in the distortion of the octahedra which have significant implications on the physical properties determined later in this chapter. Specifically, the octahedra in the structure here are more elongated, with Pb–I bond lengths ranging from 3.15 to 3.22 Å (compared with 3.17 to 3.18 Å). Additionally,

 

the octahedral tilting is greater, with $\beta = 14.75°$ and $\delta = 9.682°$ (compared with 11.5° and 9.9° respectively), and the overall structure has a smaller unit cell of 947.2 $Å^3$ (compared to 953.9 $Å^3$). These structural differences are likely a result of different sample preparation methods and measurement temperature.

Originally, Møller proposed a monoclinic structure for this black polymorph.[13] The stick pattern is recreated in Figure 6-2. While the strongest lines of Møller's pattern match the experimental data here, many weaker peaks are missing. This comparison supports the legitimacy of refinement in an orthorhombic perovskite structure.

**Table 6-1. Summary of refined structural parameters for quench-cooled black-phase γ-$CsPbI_3$ obtained from the Rietveld refinement in Figure 6-A1. The refined parameters were determined by Dr Amir Abbas Haghighirad at the Karlsruhe Institute of Technology.**

| **Compound** | **$CsPbI_3$** |
|---|---|
| Colour of powder | Black |
| Measurement temperature | 293 K |
| Crystal system | Orthorhombic |
| Space group | *P n a m* |
| Unit cell dimensions | a = 8.8561±0.0004 Å, b = 8.5766±0.0003 Å, c = 12.4722±0.0006 Å,, α = β = γ = 90° |
| Volume | 947.33±0.05 $Å^3$ |
| Z | 4 |
| Density (calculated) | 5.054 g/$cm^3$ |
| Number of data | 2414 |
| $R_{wp}$ | 0.07747 |
| $R_p$ | 0.04908 |
| Goodness of fit | 1.256 |
| Wavelength | Cu $K_{\alpha 1}$, 1.540500 Å |

Atomic positions

| **Atom** | **Wyckoff Position** | **x** | **y** | **z** | **Occupancy** |
|---|---|---|---|---|---|
| Cs | 4c | 0.45995 | 0.50509 | ¼ | 1 |
| Pb | 4a | 0 | ½ | 0 | 1 |
| I | 4c | 0.00113 | 0.56202 | ¼ | 1 |
| I | 8d | 0.30538 | 0.69731 | -0.035771 | |

| | |
|---|---|
| Isotropic temperature factors, $U_{iso}$ ($Å^2$) | (Cs) 0.0394 ± 0.0003, (Pb) 0.0327 ± 0.0003, (I1) 0.0385 ± 0.0004, (I2) 0.0368 ± 0.0004 |

## 6.4 Crystal structure in thin films of black-phase $CsPbI_3$

For application in optoelectronic devices, it is important to determine whether the orthorhombic perovskite polymorph is also adopted by thin-films of $CsPbI_3$. Close investigation of the various reports of thin-films of $CsPbI_3$ in the literature reveals that the reported XRD patterns of black-phase $CsPbI_3$ thin-films differ between different preparation methods. Of the reports of $CsPbI_3$ thin-films in the literature, there are two contrasting preparation routes which can be grouped into high-temperature (HT) and low-temperature (LT). In the HT route, yellow non-perovskite δ-$CsPbI_3$ films are heated above the transition temperature into the black cubic α-$CsPbI_3$ perovskite polymorph and rapidly cooled. In the LT route, an additive, typically hydriodic acid (HI), is used to facilitate formation of black thin-films at temperatures below 423 K. Here black $CsPbI_3$ thin-films and their scratched powders were prepared for analysis by XRD by both HT and LT preparation routes.

In the HT route, yellow δ-$CsPbI_3$ films were prepared by spin-coating a solution of CsI and $PbI_2$ in a mixed solvent containing both *N,N*-dimethylformamide (DMF) and dimethyl sulfoxide (DMSO).[27] To gain black films, the yellow films were heated briefly at ~620 K for approximately 2 minutes until visibly black, and then quickly cooled to room temperature in nitrogen gas. Typical XRD patterns for these films are presented in Figure 6-3(a). The peaks are sharp and well defined, and match well to similar XRD patterns in the literature for films prepared from vapour deposition,[27,28] or by solution-processing from DMF,[8,27,29] DMSO,[30] mixes of DMF and DMSO,[27] or even DMF with HI,[31] provided that the resulting films are annealed at temperatures above the transition to the cubic polymorph and quickly cooled. The formation of black-phase $CsPbI_3$ was confirmed by absorption and steady-state photoluminescence (PL) of the film which are shown in Figure 6-4(a). The absorption onset occurs near 700 nm and the PL peak near 720 nm as expected.[1]

 

The high temperature annealing leads to micron-sized domains (see Scanning Electron Microscope (SEM) images in Figure 6-4(b)), as found previously by Atomic Force Microscopy (AFM) measurements.[27]

In the LT process, HI was used as an additive in a precursor solution of CsI and $PbI_2$ in DMF to facilitate the formation of a black $CsPbI_3$ film at 373 K.[8] The XRD patterns of these films are shown in Figure 6-3(c). Here splitting of the characteristic perovskite peaks is evident as a shoulder at 14.2° 2ϑ, two peaks near 20° 2ϑ, and a small peak at 28.6° 2ϑ. This peak splitting is consistent with previous literature

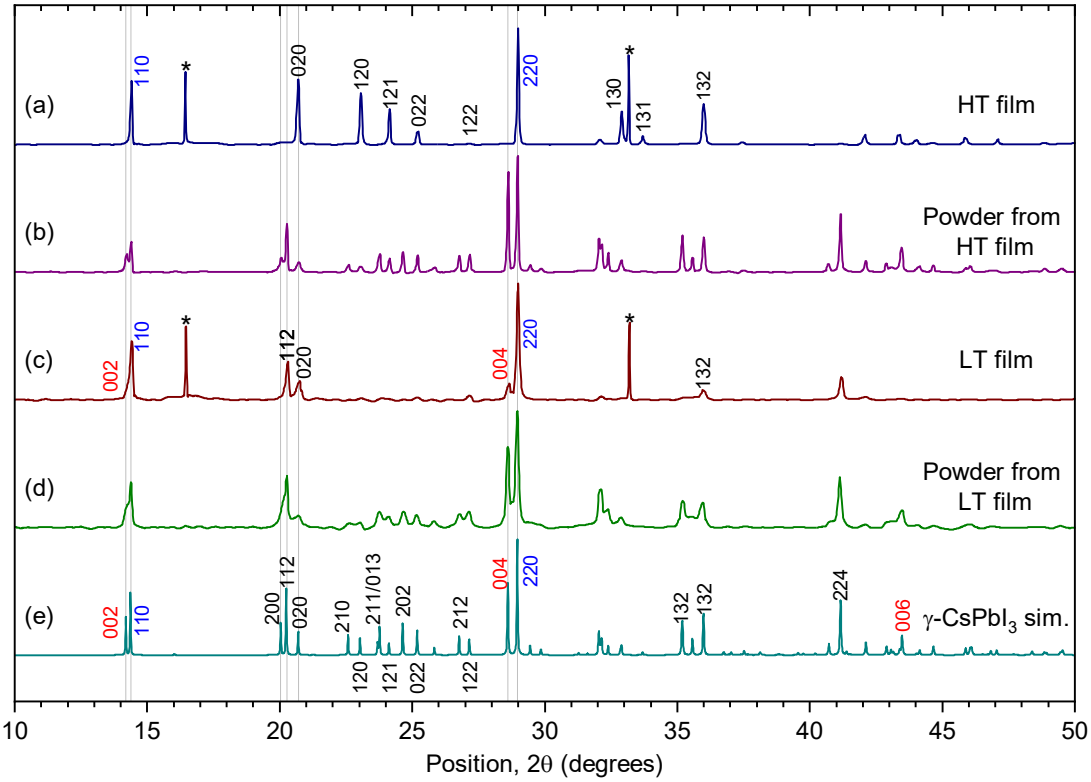


**Figure 6-3. XRD patterns from black γ-$CsPbI_3$ films, and powders obtained from such films, at room temperature. (a) Black films prepared by a HT route (DMF:DMSO); (b) powder scratched from the HT films. (c) Black films prepared by a LT route (DMF+HI); (d) powder scratched from the LT films. * denotes peaks from the underlying z-cut quartz substrate. All samples were prepared in nitrogen-filled domed sample holders. XRD was measured with Cu $K_{\alpha 1}$ radiation. (e) XRD pattern for the refined γ-$CsPbI_3$ orthorhombic structure in Figure 6-2, simulated and indexed using VESTA.[32] Miller indices are assigned for the films based on the refined pattern.**

 

reports on $CsPbI_3$ prepared with HI in the precursor solution.[8,33] It should be noted that similar diffraction patterns have also been found by adding $BiI_3$, or amines such as phenethylamine (PEA), to the precursor solution.[3,20] The absorption and PL of the LT-processed films are shown in Figure 6-4(c). Again, the absorption onset is near 700 nm and the PL peak near 720 nm. In Figure 6-4(d), polycrystalline domains of a few hundred nm across are visible in the SEM images of the LT films, which is consistent with previous SEM and AFM measurements.[8,27]

The XRD patterns of these two films have fewer strong peaks when compared to the refined γ-$CsPbI_3$ orthorhombic structure presented in the previous section. It is possible either that the films adopt a less distorted polymorph than the synthesised

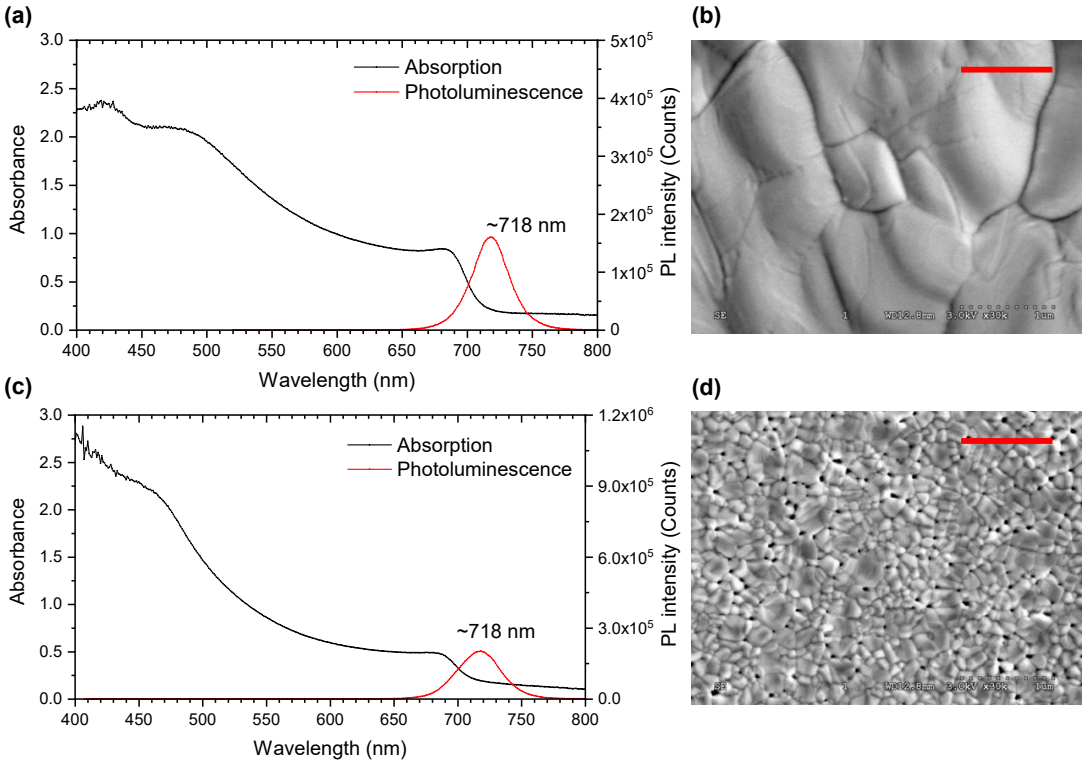


**Figure 6-4. Absorption (black) and PL (red) of $CsPbI_3$ films spin-coated from (a) DMF:DMSO mixed solvent and (c) DMF with HI additive. Films were approximately 700 nm and 250 nm respectively in thickness. Scanning electron microscope (SEM) images of $CsPbI_3$ films spin-coated on FTO/$TiO_2$ substrates, from (b) DMF:DMSO mixed solvent and (d) DMF with HI additive. Scale bar = 1 μm.**

powder, or that some peaks are missing due to preferential orientation within the films.

To determine which of these possibilities is more likely, randomly oriented powders were obtained by scratching the films off the substrate. Figure 6-3(b) and (d) show XRD patterns for the scratched powders from the HT and LT films respectively. In both cases the peak positions align well between the films and their powders, and several additional peaks are visible in comparison to the films. Furthermore, the scratched powders both exhibit peak splitting in the three characteristic perovskite peaks near 15°, 20° and 30° 2$\vartheta$. The reference pattern in Figure 6-3(e) is the refinement of the γ-$CsPbI_3$ orthorhombic polymorph, simulated and indexed in the 3D visualization program, VESTA.[32]

*Via* comparison of the XRD patterns of the films and their scratched powders with the γ-$CsPbI_3$ orthorhombic polymorph, it is determined that the films adopt this same orthorhombic polymorph at room temperature, but preferred orientation is observed in the films. Specifically, the HT films are strongly textured, whereas the LT films are weakly textured. In Figure 6-3(a) and (c), Miller indices are assigned to the peaks in these films based on the refined γ-$CsPbI_3$ orthorhombic structure. The strongest peaks in the diffraction patterns from the films arise primarily from diffraction from the [*hk*0] family of planes. This preferential orientation in γ-$CsPbI_3$ films from the HT route is consistent with previous reports of XRD patterns from films of cubic $CsPbI_3$. In a study using Grazing-Incidence Wide-Angle X-ray Scattering (GIWAXS) analysis of a $CsPbI_3$ film at 593 K, it was determined that crystallites within the film were oriented with the $[100]_{cubic}$ direction normal to the substrate,[34] which is further supported by Figure 4-6, for example, where only the $[100]_{cubic}$ and $[200]_{cubic}$ diffraction peaks were visible when the film was heated to 673 K. In the γ-$CsPbI_3$ films from the HT route seen in Figure 6-3(a), this orientation is preserved as the film is quickly cooled, such that the strong $[100]_{cubic}$

 

diffraction peak becomes a strong $[110]_{\text{orthorhombic}}$ diffraction peak, and peaks from the $[00l]$ family of planes are absent.

In Figure 6-3(c), the XRD pattern from the LT films fabricated with HI as an additive is closer to a powder pattern but still exhibits some preferential orientation. Here, peaks from the $[00l]$ family of planes are present, but are weaker than the 1:2 ratio expected for the [002] and [110] peaks in the γ-$CsPbI_3$ powder pattern. Intriguingly, dominant peaks from the $[00l]$ family of planes are evident for LT films made using PEA as an additive where the 3D perovskite structure is retained.[20] These observations indicate that LT additive-assisted crystallisation is able to access a different preferred orientation of the orthorhombic $CsPbI_3$ crystallites with a significant proportion of crystallites perpendicularly rotated through 90° in comparison with the HT processing route. Figure 6-5 provides an illustration of the two possible predominant crystallite orientations within the films.

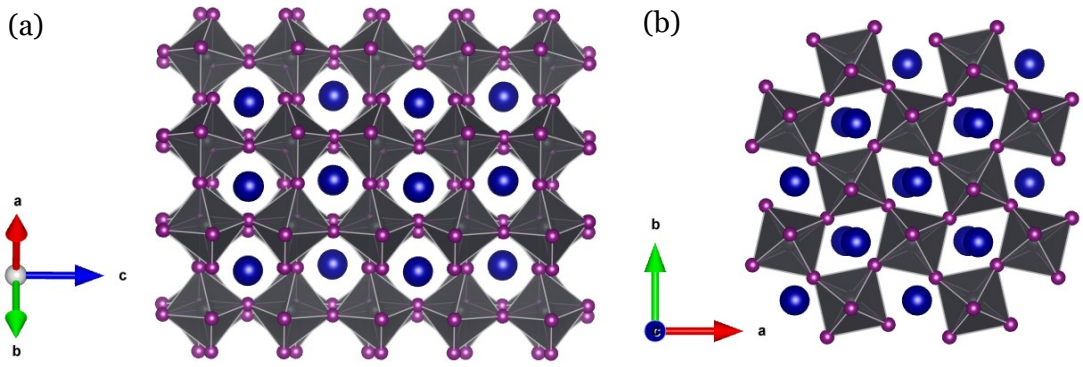


**Figure 6-5. (a) Plan view of possible preferential orientation of crystallites in films from high-temperature processing routes, where the c-axis is parallel with the substrate. (b) Plan view of possible preferential orientation of crystallites in films from low-temperature processing routes, where the c-axis is perpendicular to the substrate. In both cases the page represents the substrate on which the film is prepared.**

 

## 6.5 Electronic band structure calculations

It is now possible to investigate the different polymorphs of $CsPbI_3$ from *ab initio* electronic structure calculations. Figure 6-6 shows the electronic band structure of γ-$CsPbI_3$ calculated within the local density approximation to density functional theory (DFT/LDA),[35,36] and the *GW* approximation,[37] including spin-orbit coupling, using the refined experimental crystal structure. The *GW* approximation both increases the dispersion in the valence band and shifts the conduction band rigidly when compared to the DFT/LDA eigenvalues, in close resemblance to the case of orthorhombic methylammonium lead iodide ($MAPbI_3$).[38]

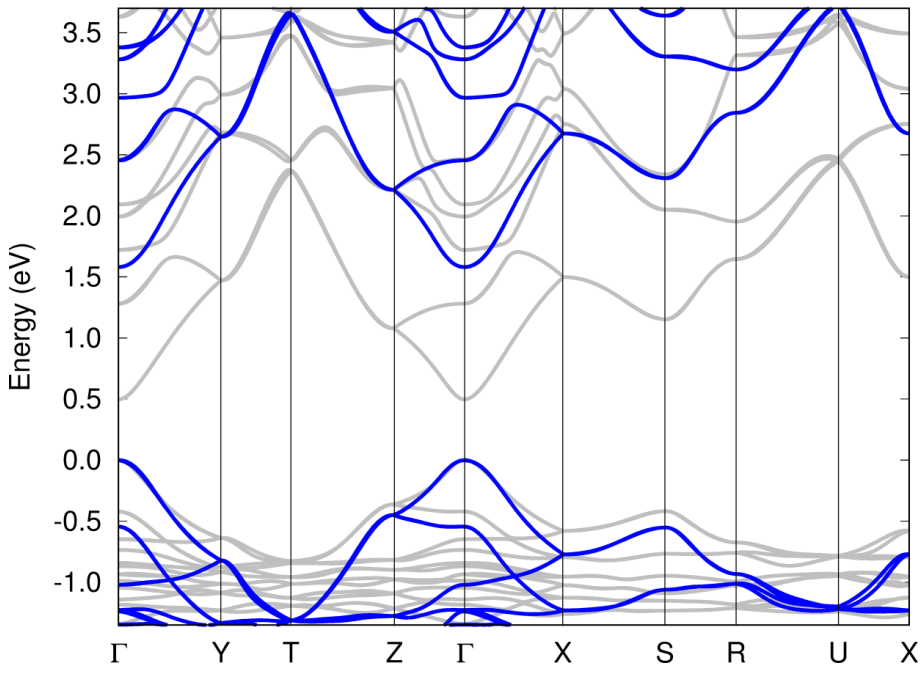


**Figure 6-6. Comparison between the DFT/LDA (grey) and the GW (blue) band structure of the orthorhombic perovskite γ-$CsPbI_3$. The band structure is calculated on the high-symmetry path Γ [0, 0, 0] - Y [0, π/b, 0] - T [0, π/b, π/c], Z [0, 0, π/c] - Γ - X [π/a, 0, 0] - S [π/a, π/b, 0] - R [π/a, π/b, π/c] - U [π/a, 0, π/c] - X [π/a, 0, 0], where a, b and c are the lattice parameters determined experimentally in this work. The band structure was calculated by Dr Marina Filip at the University of Oxford.**

Table 6-2 summarises the band gaps calculated for γ-$CsPbI_3$ from DFT/LDA and *GW*. As expected, the DFT/LDA band gap is underestimated with respect to experiment by 1.2 eV. Using the *GW* approximation, this discrepancy is resolved to obtain a band gap of 1.57 eV, 0.15 eV smaller than the experimental optical band gap of 1.72 eV at 2 K,[2] and with an expected error bar of 0.1 eV. Interestingly, the band gap of γ-$CsPbI_3$ is the same as previously obtained in the case of orthorhombic $MAPbI_3$ (1.57 eV).[39] This similarity may be rationalised from structural considerations. Both the experimental orthorhombic structures of $CsPbI_3$ (293 K, this work) and $MAPbI_3$ (100 K, ref [40]) exhibit very similar structural features, with an average Pb-I bond length of 3.18 Å and equatorial Pb-I-Pb bond angles of 151° in the unit cell in both cases. The only difference in the structure appears for the apical bond angles of 161° and 163°, for $CsPbI_3$ and $MAPbI_3$ respectively. Given this small difference in their structural features, the close similarity in the calculated *GW* band gaps of $CsPbI_3$ and $MAPbI_3$ is consistent with previous DFT predictions.[41]

It should be noted that the orthorhombic polymorph of $MAPbI_3$ is experimentally observed at temperatures lower than 170 K, above which there is a structural transition to the tetragonal polymorph with a corresponding change in optical band gap of at least 110 meV, when determined by the onset for the continuum in the Elliot model.[39] This difference in band gap at the structural transition is similar to

**Table 6-2. Band gap and effective masses calculated for orthorhombic γ-$CsPbI_3$ within DFT/LDA and GW, including spin-orbit coupling. These values were calculated by Dr Marina Filip at the University of Oxford.**

| Method | Band gap (eV) | Electron effective mass ($m_e$) | Hole effective mass ($m_e$) | Reduced effective mass ($m_e$) |
|---|---|---|---|---|
| DFT | 0.49 | 0.14 | 0.12 | 0.07 |
| *GW* | 1.57 | 0.23 | 0.24 | 0.12 |
| Exp. | 1.72 [2,42] | N/A | N/A | 0.114±0.01 [2] |

 

the ~170 meV difference between the continuum onsets at room temperature of tetragonal $MAPbI_3$ (1.64 eV, ref 39) and orthorhombic $CsPbI_3$ (1.81 eV, Figure 6-7). These observations emphasise that the bandgap in lead halide perovskites is determined primarily by the degree of octahedral tilting, rather than the A-site cation. A similar increase in the bandgap with increased octahedral tilting is seen in the $Cs_{1-x}Rb_xPbCl_3$ and $Cs_{1-x}Rb_xPbBr_3$ solid solutions.[22] This trend has previously been rationalised by considering the decrease in orbital overlap as the octahedra tilt and the B–X–B bonds become increasingly bent.[41] This decrease in orbital overlap leads to narrower conduction and valence bands, giving an increase in the band gap.[22] The A-site cation then only indirectly affects the opto-electronic properties of the lead halide perovskites through octahedral tilting.[2,41]

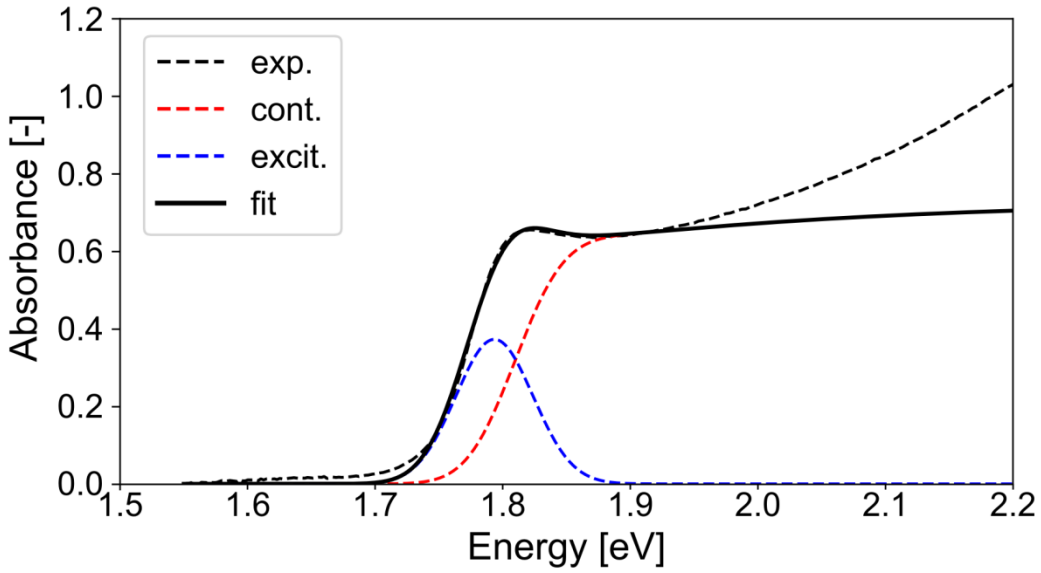


**Figure 6-7. Experimental absorption spectrum from Figure 6-4(a) of a thin-film of $CsPbI_3$ (black dashed line) taken at room temperature, fitted using Elliott's model (black line) by Dr Bernard Wenger at the University of Oxford. The excitonic contribution (blue dashed line) and the continuum contribution (red dashed line) are plotted separately. Both excitonic and continuum transitions are broadened with a Gaussian function of width $\sigma$ = 30 meV. Fit parameters: $E_X$ = 18.3 meV, $E_G$ = 1.810 eV.**

 

In addition, Table 6-2 shows the electron and hole effective masses calculated for the orthorhombic γ-$CsPbI_3$ perovskite. As in the case of $MAPbI_3$,[38,39] the electron, hole, and reduced effective masses are underestimated within DFT/LDA by almost a factor of 2, as compared to the *GW* effective masses and magneto-absorption measurements.[2] By contrast, the *GW* reduced effective mass is in excellent agreement with experiment.[2] In addition, the *GW* effective masses are very close in value for electrons and holes. This is very similar to the case of $MAPbI_3$, and consistent with experimental observation that both electrons and holes can be efficiently transported through the perovskite layer.[43]

## 6.6 The cubic polymorph of $CsPbI_3$

Figure 6-8 shows the *GW* band structure calculated at 0 K for the cubic perovskite polymorph of $CsPbI_3$, for which the band gap is 1.14 eV. From previous work, *GW* band gaps are expected to agree well with experiment for halide perovskites.[38,39,44]

To experimentally investigate the band gap of cubic α-$CsPbI_3$, temperature-dependent absorption measurements were made on thin-films of $CsPbI_3$ (see Figure 6-9 and Figure 6-10). As the PL was found to be unmeasurable above ~180 °C, it was not possible to use this as a second estimate of the bandgap. The bandgap is found to be (1.78±0.01) eV at 623 K (350 °C), which is much higher than the calculated band gap at 0 K. This difference is consistent with previous studies of the cubic phase of $MAPbI_3$, and has been associated with temperature-induced structural fluctuations of perovskites.[45–48] Both experimental and theoretical crystal structure studies concluded that the cubic structure of $MAPbI_3$ at high temperature consists of an ensemble of randomly distorted $PbI_6$ octahedra, and is not strictly cubic.[45–47] In a comprehensive molecular dynamics study, Ref. 49 showed that while the ensemble of these distorted structures amounts to an average cubic symmetry, at any single moment in time the average band gap of the ensemble is a larger value

 

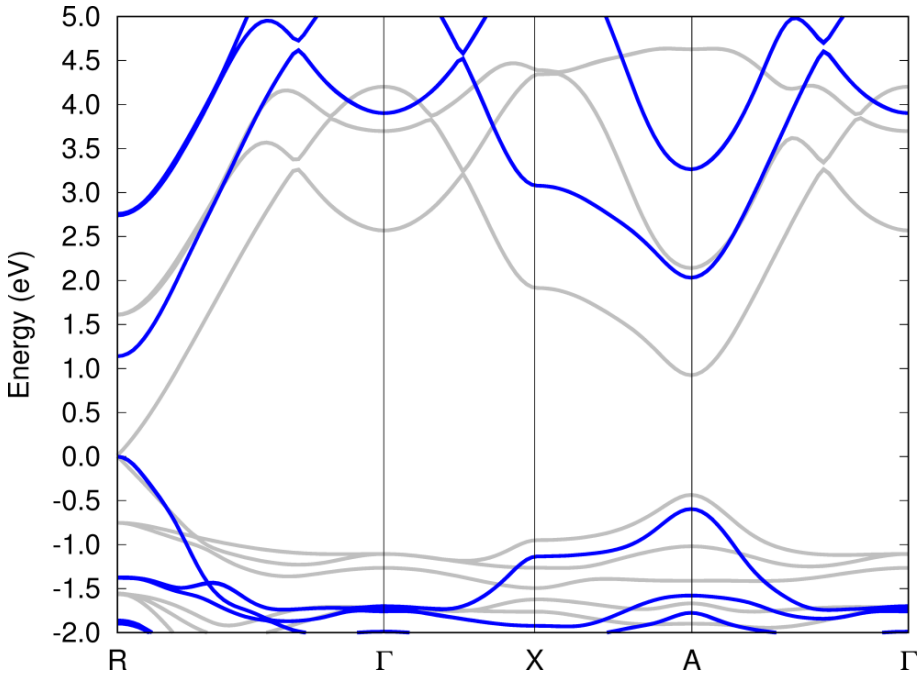


**Figure 6-8. Comparison between the DFT/LDA (grey) and the GW (blue) band structure of the cubic perovskite α-$CsPbI_3$. The band structure is calculated on the high-symmetry path Γ [0, 0, 0] - X [π/a, 0, 0] - S [π/a, π/a, 0] - R [π/a, π/a, π/a] - Γ, where a is the lattice parameter determined experimentally in Ref. 50. The band structure was calculated by Dr Marina Filip at the University of Oxford.**

than that calculated for a static cubic perovskite. A similar effect is expected to take place in the case of cubic $CsPbI_3$.

A recent X-ray diffraction study identified phase transitions upon slow cooling of $CsPbI_3$ from the cubic polymorph to a tetragonal polymorph at 539 K, and to the orthorhombic polymorph at 425 K.[16] Here optical methods were used to see if it is possible to detect associated changes in the band gap at these phase transitions. In Figure 6-9, a continuous red-shift in the absorption onset is observed for the $CsPbI_3$ films slowly cooled from 623 K, before conversion to the yellow δ-$CsPbI_3$ polymorph below 553 K. The inset in Figure 6-10 reveals that the red-shift is linear above 583 K (310 °C). In this temperature range, the linear red-shift is consistent with the

 

film remaining in the cubic α-$CsPbI_3$ polymorph.[50] Below 543 K the film converts to the yellow polymorph due to the slow rate of cooling. In the intermediate region it is not possible to confidently assign a phase as both the continuation of a linear trend and a very slight deviation to a higher bandgap lie within experimental uncertainty. However, there is no abrupt change in band gap evident for the black polymorph over this temperature range to indicate a discontinuous phase transition. Furthermore, it should be noted that in previous work the black phase of $CsPbI_3$ has been realised at temperatures as low as 2 K.[2] The main difference here is that the perovskite film has been cooled so slowly that the transition from the black to yellow polymorph is allowed, rather than being kinetically frozen in the black phase.

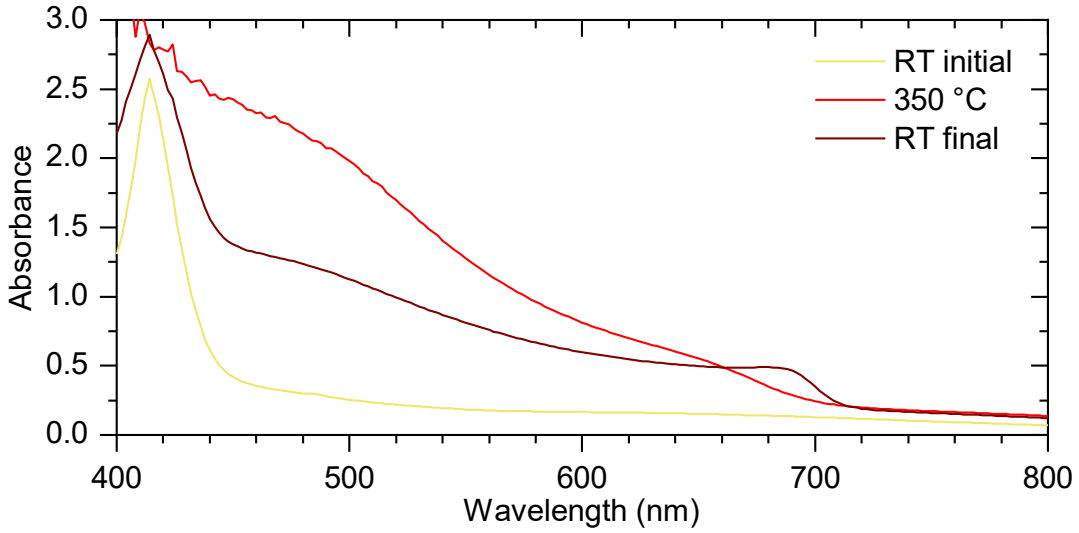


**Figure 6-9. Temperature-dependent absorption of a $CsPbI_3$ film which was initially in the yellow polymorph at room temperature. The film was heated at 150 °C/minute to 350 °C (623 K), where it converted to the cubic polymorph. The film was then cooled as fast as possible using water cooling (>150 °C/minute) and the absorption measured when the film reached room temperature again. Tauc analysis of the black-phase films gives bandgaps of 1.78 eV and 1.74 eV for the 623 K and RT measurements respectively.**

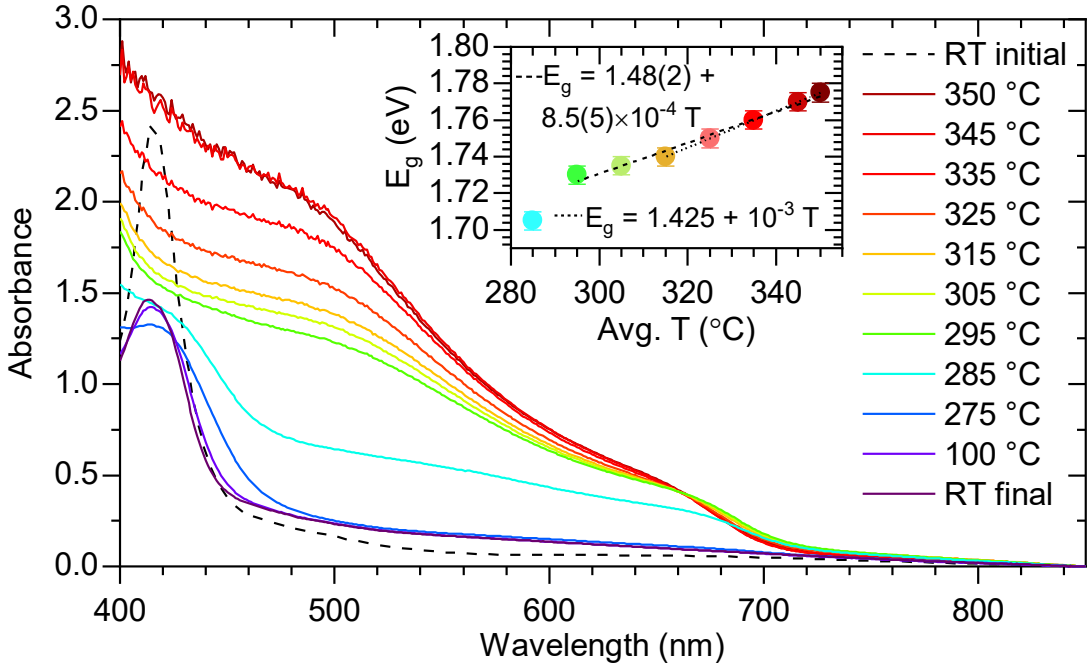


**Figure 6-10. Temperature-dependent absorption of a $CsPbI_3$ film which was initially in the yellow polymorph. The film was heated at 50 °C/minute to 350 °C (623 K), where it converted to the cubic polymorph. The film was then cooled at 2 °C/minute while measuring the absorption. The traces are labelled by the temperature at the midpoint of each 5-minute measurement. The yellow polymorph is regained upon reaching 275 °C (543 K) with this cooling rate. (inset) Estimates of the optical bandgap $E_g$ from Tauc analysis which give a red shift with decreasing temperature of 0.85-1.00 meV/K.**

## 6.7 Polymorphism and structural transitions in $CsPbI_3$

Figure 6-11(a) now summarises diagrammatically the polymorphs of $CsPbI_3$ and their structural transitions. As previously described, the cubic polymorph α-$CsPbI_3$ has been observed by XRD to occur at high temperature, typically above 583 K and irrespective of sample history, and below the melting point above 753 K.[50,51] Slow cooling from α-$CsPbI_3$ and/or exposure to ambient moisture yields the non-perovskite δ-$CsPbI_3$,[50,51] which may also be obtained by crystal growth at room temperature.[13,14,52] This yellow polymorph differs completely from the black polymorphs in both structure and optoelectronic properties.[8]

 

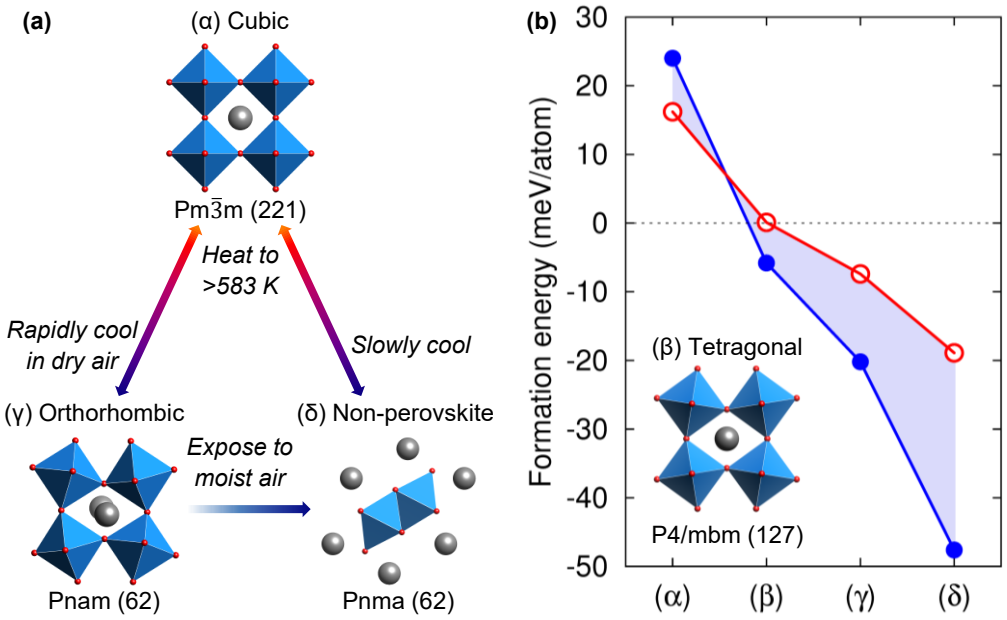


**Figure 6-11. (a) Polyhedral models of the different polymorphs of $CsPbI_3$ and their structural transitions. Cubic α-$CsPbI_3$ occurs at temperatures above 583 K.[50,51] Rapid cooling of α-$CsPbI_3$ in inert atmosphere yields the orthorhombic polymorph γ-$CsPbI_3$ with the structure determined in this work. δ-$CsPbI_3$ is the stable polymorph under ambient conditions.[13,14,50,52] (b) Formation energies calculated for the polymorphs in (a) as well as for a tetragonal β-$CsPbI_3$ polymorph simulated from β-$CsSnI_3$.[23] The formation energies are calculated with respect to the precursors CsI and $PbI_2$ as $E_f$ = E[$CsPbI_3$] − E[CsI] − E[$PbI_2$], where E is the total energy. Calculations are performed at 0 K and 0 GPa, without taking into account the effect of zero-point motion. The red circles and lines correspond to DFT/PBE calculations, while the blue dots and lines correspond to DFT/LDA calculations. The region filled in light blue highlights the difference in the formation energies calculated via the two methods. Formation energies were calculated by Dr Marina Filip at the University of Oxford.**

To this picture is added the orthorhombic perovskite polymorph γ-$CsPbI_3$, formed by rapid cooling of α-$CsPbI_3$ to room temperature in the absence of ambient moisture. Previously reported temperature-dependent synchrotron XRD measurements have shown that the octahedral tilting continuously increases as α-$CsPbI_3$ is cooled, such that the structure appears to proceed through a tetragonal β-

$CsPbI_3$ polymorph before reaching the γ-$CsPbI_3$ polymorph.[16] However, on heating δ-$CsPbI_3$ to the α-$CsPbI_3$ polymorph, the two polymorphs have been observed to coexist during the transition, with no orthorhombic or tetragonal polymorphs evident.[15,16,50] This coexistence means that full conversion to the α-$CsPbI_3$ polymorph, followed by rapid cooling, is always required to obtain the orthorhombic γ-$CsPbI_3$ polymorph at room temperature when starting from non-perovskite δ-$CsPbI_3$.

The thermodynamic stability of the various polymorphs of $CsPbI_3$ is of vital importance for the commercial application of this material. The relative stabilities of the polymorphs may be evaluated by calculating their formation energies. Figure 6-11(b) shows a comparison of the formation energies of the cubic, tetragonal and orthorhombic perovskite polymorphs, along with the non-perovskite polymorph. Structural information for the four polymorphs is provided in Table 6-3.

The formation energies were calculated within the LDA, as well as with the generalised gradient approximation (PBE) to DFT.[35] The formation energies are sensitive to the choice of exchange-correlation functional, and can differ by up to 25 meV per atom. Here consistent trends are seen from each functional, and so the true formation energy may be considered bracketed by the LDA and PBE values.[53]

**Table 6-3. Structural information for formation energy calculations for each of the four polymorphs of $CsPbI_3$. All polymorphs have $\alpha = \beta = \gamma = 90°$.**

| Polymorph | Space group | a (Å) | b (Å) | c (Å) | Source |
|---|---|---|---|---|---|
| Cubic | $Pm\bar{3}m$ (221) | 6.289 | | | Ref. 50 (at 634 K) |
| Tetragonal | P4/mbm (127) | 8.772 | 6.261 | | Ref. 23 (for $CsSnI_3$) |
| Orthorhombic | Pnam (62) | 8.8561 ±0.0004 | 8.5766 ±0.0003 | 12.4722 ±0.0006 | This work (Table 6-1) |
| Non-perovskite | Pnma (62) | 10.462 ±0.005 | 4.799 ±0.005 | 17.765 ±0.005 | This work (Table 6-A1) |

 

In agreement with experiment, these calculations show that the yellow polymorph is the most stable. Of the perovskite polymorphs, the most stable is the orthorhombic structure. This finding agrees with previous studies,[54] and lends weight to the argument here for the adoption of the orthorhombic polymorph by black-phase $CsPbI_3$ at room temperature. Stabilisation of the orthorhombic polymorph with respect to the cubic and tetragonal polymorphs also fits well with the relatively small tolerance factor for $CsPbI_3$, which falls between 0.81 and 0.85 (for Shannon radii) depending on Cs coordination. In this range of tolerance factors, tilted perovskites such as the orthorhombic perovskite identified here are found to be the most stable.[55]

Notably, these experimental and theoretical investigations reveal that the instability of the black $CsPbI_3$ polymorphs with respect to the yellow polymorph constitutes an intrinsic thermodynamic property of the pure $CsPbI_3$ crystal. In addition, it is proposed that a robust stabilisation of all-inorganic lead-halide perovskites can be achieved by developing rational design routes to tune the total energy landscape and energy barrier for the transition between the black and yellow polymorphs through chemical substitution. The work in this chapter demonstrates that by exploring experimental investigations and predictive electronic structure calculations it may be possible to both rationalize observed stability improvements and discover candidate solutions for fully stable black inorganic lead halide perovskite polymorphs.

## 6.8 Conclusion and outlook

This chapter showed that the room temperature black polymorph of $CsPbI_3$ that is being widely investigated for photovoltaic applications is an orthorhombic perovskite, rather than a cubic perovskite. The structure was determined through full refinement of XRD patterns, and a stronger similarity was found with $CsSnI_3$ than with $CsPbBr_3$. In particular, the indexation of thin-films of the orthorhombic

 

polymorph was demonstrated, enabling a better understanding of how crystallite orientation within the films depends on the processing route. From the experimental structural data for the orthorhombic perovskite, the electronic band structure was calculated. The band gap and reduced effective mass show excellent agreement with experimental data, further confirming that the most commonly reported form of $CsPbI_3$ is the orthorhombic perovskite. Additionally, the respective formation energies of the perovskite and non-perovskite polymorphs were calculated. These energies showed that the orthorhombic polymorph is the most stable of the perovskite polymorphs, and the non-perovskite polymorph is the most stable overall. These findings are in agreement with experimental data and with structural transitions in other known perovskites, and highlight the importance of octahedral tilting and distortions on the bandgap and structural stability of lead halide perovskites. These results are vital for all researchers working with thin-films and powders of black $CsPbI_3$ at room temperature, and will greatly assist in the development of a structurally stable inorganic perovskite with excellent photovoltaic properties.

## 6.9 References

1. Sutton, R. J.; Eperon, G. E.; Miranda, L.; Parrott, E. S.; Kamino, B. A.; Patel, J. B.; Hörantner, M. T.; Johnston, M. B.; Haghighirad, A. A.; Moore, D. T.; Snaith, H. J. "Bandgap-Tunable Cesium Lead Halide Perovskites with High Thermal Stability for Efficient Solar Cells". *Adv. Energy Mater.* 2016, *6*, 1502458.
2. Yang, Z.; Surrente, A.; Galkowski, K.; Miyata, A.; Portugall, O.; Sutton, R. J.; Haghighirad, A. A.; Snaith, H. J.; Maude, D. K.; Plochocka, P.; Nicholas, R. J. "Impact of the Halide Cage on the Electronic Properties of Fully Inorganic Cesium Lead Halide Perovskites". *ACS Energy Lett.* 2017, *2*, 1621–1627.
3. Hu, Y.; Bai, F.; Liu, X.; Ji, Q.; Miao, X.; Qiu, T.; Zhang, S. "Bismuth Incorporation Stabilized α-$CsPbI_3$ for Fully Inorganic Perovskite Solar Cells". *ACS Energy Lett.* 2017, *2*, 2219–2227.
4. Nam, J. K.; Chai, S. U.; Cha, W.; Choi, Y. J.; Kim, W.; Jung, M. S.; Kwon, J.; Kim, D.; Park, J. H. "Potassium Incorporation for Enhanced Performance and Stability of Fully Inorganic Cesium Lead Halide Perovskite Solar Cells". *Nano Lett.* 2017, *17*, 2028–2033.
5. Bansal, S.; Chiu, M. "Atmospherically Processed and Stable Cs-Pb Based Perovskite

 

Solar Cells". *MRS Adv.* 2017, 1–8.

6. Swarnkar, A.; Marshall, A. R.; Sanehira, E. M.; Chernomordik, B. D.; Moore, D. T.; Christians, J. A.; Chakrabarti, T.; Luther, J. M. "Quantum Dot-Induced Phase Stabilization of α-$CsPbI_3$ Perovskite for High-Efficiency Photovoltaics". *Science* 2016, *354*, 92–95.
7. Bian, H.; Bai, D.; Jin, Z.; Wang, K.; Liang, L.; Wang, H.; Zhang, J.; Wang, Q.; Liu, S. (Frank). "Graded Bandgap $CsPbI_{2+x}Br_{1-x}$ Perovskite Solar Cells with a Stabilized Efficiency of 14.4%". *Joule* 2018, *0*.
8. Eperon, G. E.; Paternò, G. M.; Sutton, R. J.; Zampetti, A.; Haghighirad, A. A.; Cacialli, F.; Snaith, H. J. "Inorganic Caesium Lead Iodide Perovskite Solar Cells". *J. Mater. Chem. A* 2015, *3*, 19688–19695.
9. Swarnkar, A.; Mir, W. J.; Nag, A. "Can B-Site Doping or Alloying Improve Thermal- and Phase-Stability of All-Inorganic $CsPbX_3$ (X = Cl, Br, I) Perovskites?". *ACS Energy Lett.* 2018, 286–289.
10. Lau, C. F. J.; Deng, X.; Zheng, J.; Kim, J.; Zhang, Z.; Zhang, M.; Bing, J.; Wilkinson, B.; Hu, L.; Patterson, R.; Huang, S.; Ho-Baillie, A. "Enhanced Performance via Partial Lead Replacement with Calcium for a $CsPbI_3$ Perovskite Solar Cell Exceeding 13% Power Conversion Efficiency". *J. Mater. Chem. A* 2018, *6*, 5580–5586.
11. Li, B.; Zhang, Y.; Fu, L.; Yu, T.; Zhou, S.; Zhang, L.; Yin, L. "Surface Passivation Engineering Strategy to Fully-Inorganic Cubic $CsPbI_3$ Perovskites for High-Performance Solar Cells". *Nat. Commun.* 2018, *9*, 1076.
12. Lin, J.; Lai, M.; Dou, L.; Kley, C. S.; Chen, H.; Peng, F.; Sun, J.; Lu, D.; Hawks, S. A.; Xie, C.; Cui, F.; Alivisatos, A. P.; Limmer, D. T.; Yang, P. "Thermochromic Halide Perovskite Solar Cells". *Nat. Mater.* 2018, 1.
13. Møller, C. K. "Crystal Structure and Photoconductivity of Cæsium Plumbohalides". *Nature* 1958, *182*, 1436–1436.
14. Møller, C. K. "The Structure Of Cæsium Plumbo Iodide $CsPbI_3$". *Mat. Fys. Medd. Dan. Vid. Selsk.* 1959, *32*, 1–18.
15. Stoumpos, C. C.; Kanatzidis, M. G. "The Renaissance of Halide Perovskites and Their Evolution as Emerging Semiconductors". *Acc. Chem. Res.* 2015, *48*, 2791–2802.
16. Marronnier, A.; Roma, G.; Boyer-Richard, S.; Pedesseau, L.; Jancu, J.-M.; Bonnassieux, Y.; Katan, C.; Stoumpos, C. C.; Kanatzidis, M. G.; Even, J. "Anharmonicity and Disorder in the Black Phases of Cesium Lead Iodide Used for Stable Inorganic Perovskite Solar Cells". *ACS Nano* 2018, *12*, 3477–3486.
17. Fu, Y.; Zhu, H.; Stoumpos, C. C.; Ding, Q.; Wang, J.; Kanatzidis, M. G.; Zhu, X.; Jin, S. "Broad Wavelength Tunable Robust Lasing from Single-Crystal Nanowires of Cesium Lead Halide Perovskites ($CsPbX_3$, X = Cl, Br, I)". *ACS Nano* 2016, *10*, 7963–7972.
18. Lai, M.; Kong, Q.; Bischak, C. G.; Yu, Y.; Dou, L.; Eaton, S. W.; Ginsberg, N. S.; Yang, P. "Structural, Optical, and Electrical Properties of Phase-Controlled Cesium Lead Iodide Nanowires". *Nano Res.* 2017, *10*, 1107–1114.
19. Paul, T.; Chatterjee, B. K.; Maiti, S.; Sarkar, S.; Besra, N.; Das, B. K.; Panigrahi, K. J.; Thakur, S.; Ghorai, U. K.; Chattopadhyay, K. K. "Tunable Cathodoluminescence over the Entire Visible Window from All-Inorganic Perovskite $CsPbX_3$ 1D

 

Architecture". *J. Mater. Chem. C* 2018, *6*, 3322–3333.

20. Fu, Y.; Rea, M. T.; Chen, J.; Morrow, D. J.; Hautzinger, M. P.; Zhao, Y.; Pan, D.; Manger, L. H.; Wright, J. C.; Goldsmith, R. H.; Jin, S. "Selective Stabilization and Photophysical Properties of Metastable Perovskite Polymorphs of $CsPbI_3$ in Thin Films". *Chem. Mater.* 2017, *29*, 8385–8394.
21. Bertolotti, F.; Protesescu, L.; Kovalenko, M. V.; Yakunin, S.; Cervellino, A.; Billinge, S. J. L.; Terban, M. W.; Pedersen, J. S.; Masciocchi, N.; Guagliardi, A. "Coherent Nanotwins and Dynamic Disorder in Cesium Lead Halide Perovskite Nanocrystals". *ACS Nano* 2017, *11*, 3819–3831.
22. Linaburg, M. R.; McClure, E. T.; Majher, J. D.; Woodward, P. M. "$Cs_{1-x}Rb_xPbCl_3$ and $Cs_{1-x}Rb_xPbBr_3$ Solid Solutions: Understanding Octahedral Tilting in Lead Halide Perovskites". *Chem. Mater.* 2017, *29*, 3507–3514.
23. Yamada, K.; Funabiki, S.; Horimoto, H.; Matsui, T.; Okuda, T.; Ichiba, S. "Structural Phase Transitions of the Polymorphs of $CsSnI_3$ by Means of Rietveld Analysis of the X-Ray Diffraction". *Chem. Lett.* 1991, *20*, 801–804.
24. Chung, I.; Song, J.-H.; Im, J.; Androulakis, J.; Malliakas, C. D.; Li, H.; Freeman, A. J.; Kenney, J. T.; Kanatzidis, M. G. "$CsSnI_3$: Semiconductor or Metal? High Electrical Conductivity and Strong Near-Infrared Photoluminescence from a Single Material. High Hole Mobility and Phase-Transitions". *J. Am. Chem. Soc.* 2012, *134*, 8579–8587.
25. Woodward, P. M.; IUCr. "Octahedral Tilting in Perovskites. I. Geometrical Considerations". *Acta Crystallogr. Sect. B Struct. Sci.* 1997, *53*, 32–43.
26. Glazer, A. M. "The Classification of Tilted Octahedra in Perovskites". *Acta Crystallogr. Sect. B Struct. Crystallogr. Cryst. Chem.* 1972, *28*, 3384–3392.
27. Hutter, E. M.; Sutton, R. J.; Chandrashekar, S.; Abdi-Jalebi, M.; Stranks, S. D.; Snaith, H. J.; Savenije, T. J. "Vapour-Deposited Cesium Lead Iodide Perovskites: Microsecond Charge Carrier Lifetimes and Enhanced Photovoltaic Performance". *ACS Energy Lett.* 2017, *2*, 1901–1908.
28. Shahiduzzaman, M.; Yonezawa, K.; Yamamoto, K.; Ripolles, T. S.; Karakawa, M.; Kuwabara, T.; Takahashi, K.; Hayase, S.; Taima, T. "Improved Reproducibility and Intercalation Control of Efficient Planar Inorganic Perovskite Solar Cells by Simple Alternate Vacuum Deposition of $PbI_2$ and CsI". *ACS Omega* 2017, *2*, 4464–4469.
29. Nam, J. K.; Jung, M. S.; Chai, S. U.; Choi, Y. J.; Kim, D.; Park, J. H. "Unveiling the Crystal Formation of Cesium Lead Mixed-Halide Perovskites for Efficient and Stable Solar Cells". *J. Phys. Chem. Lett.* 2017, 2936–2940.
30. Ripolles, T. S.; Nishinaka, K.; Ogomi, Y.; Miyata, Y.; Hayase, S. "Efficiency Enhancement by Changing Perovskite Crystal Phase and Adding a Charge Extraction Interlayer in Organic Amine Free-Perovskite Solar Cells Based on Cesium". *Sol. Energy Mater. Sol. Cells* 2016, *144*, 532–536.
31. Dastidar, S.; Hawley, C. J.; Dillon, A. D.; Gutierrez-Perez, A. D.; Spanier, J. E.; Fafarman, A. T. "Quantitative Phase-Change Thermodynamics and Metastability of Perovskite-Phase Cesium Lead Iodide". *J. Phys. Chem. Lett.* 2017, *8*, 1278–1282.
32. Momma, K.; Izumi, F. "VESTA: A Three-Dimensional Visualization System for Electronic and Structural Analysis". *J. Appl. Crystallogr.* 2008, *41*, 653–658.
33. Luo, P.; Xia, W.; Zhou, S.; Sun, L.; Cheng, J.; Xu, C.; Lu, Y. "Solvent Engineering

for Ambient-Air-Processed, Phase-Stable $CsPbI_3$ in Perovskite Solar Cells". *J. Phys. Chem. Lett.* 2016, *7*, 3603–3608.

34. Frolova, L. A.; Anokhin, D. V.; Piryazev, A. A.; Luchkin, S. Y.; Dremova, N. N.; Stevenson, K. J.; Troshin, P. A. "Highly Efficient All-Inorganic Planar Heterojunction Perovskite Solar Cells Produced by Thermal Coevaporation of CsI and $PbI_2$". *J. Phys. Chem. Lett.* 2017, *8*, 67–72.

35. Hohenberg, P.; Kohn, W. "Inhomogeneous Electron Gas". *Phys. Rev.* 1964, *136*, B864–B871.

36. Perdew, J. P.; Zunger, A. "Self-Interaction Correction to Density-Functional Approximations for Many-Electron Systems". *Phys. Rev. B* 1981, *23*, 5048–5079.

37. Hybertsen, M. S.; Louie, S. G. "Electron Correlation in Semiconductors and Insulators: Band Gaps and Quasiparticle Energies". *Phys. Rev. B* 1986, *34*, 5390–5413.

38. Filip, M. R.; Verdi, C.; Giustino, F. "GW Band Structures and Carrier Effective Masses of $CH_3NH_3PbI_3$ and Hypothetical Perovskites of the Type $APbI_3$: A = $NH_4$, $PH_4$, AsH4, and $SbH_4$". *J. Phys. Chem. C* 2015, *119*, 25209–25219.

39. Davies, C. L.; Filip, M. R.; Patel, J. B.; Crothers, T. W.; Verdi, C.; Wright, A. D.; Milot, R. L.; Giustino, F.; Johnston, M. B.; Herz, L. M. "Bimolecular Recombination in Methylammonium Lead Triiodide Perovskite Is an Inverse Absorption Process". *Nat. Commun.* 2018, *9*, 293.

40. Baikie, T.; Fang, Y.; Kadro, J. M.; Schreyer, M.; Wei, F.; Mhaisalkar, S. G.; Graetzel, M.; White, T. J. "Synthesis and Crystal Chemistry of the Hybrid Perovskite $(CH_3NH_3)PbI_3$ for Solid-State Sensitised Solar Cell Applications". *J. Mater. Chem. A* 2013, *1*, 5628.

41. Filip, M. R.; Eperon, G. E.; Snaith, H. J.; Giustino, F. "Steric Engineering of Metal-Halide Perovskites with Tunable Optical Band Gaps". *Nat. Commun.* 2014, *5*, 5757.

42. Eperon, G. E.; Stranks, S. D.; Menelaou, C.; Johnston, M. B.; Herz, L. M.; Snaith, H. J. "Formamidinium Lead Trihalide: A Broadly Tunable Perovskite for Efficient Planar Heterojunction Solar Cells". *Energy Environ. Sci.* 2014, *7*, 982.

43. Li, F.; Ma, C.; Wang, H.; Hu, W.; Yu, W.; Sheikh, A. D.; Wu, T. "Ambipolar Solution-Processed Hybrid Perovskite Phototransistors". *Nat. Commun.* 2015, *6*, 8238.

44. Filip, M. R.; Giustino, F. "GW Quasiparticle Band Gap of the Hybrid Organic-Inorganic Perovskite $CH_3NH_3PbI_3$: Effect of Spin-Orbit Interaction, Semicore Electrons, and Self-Consistency". *Phys. Rev. B* 2014, *90*, 245145.

45. Worhatch, R. J.; Kim, H.; Swainson, I. P.; Yonkeu, A. L.; Billinge, S. J. L. "Study of Local Structure in Selected Organic–Inorganic Perovskites in the $Pm\bar{3}M$ Phase". *Chem. Mater.* 2008, *20*, 1272–1277.

46. Choi, J. J.; Yang, X.; Norman, Z. M.; Billinge, S. J. L.; Owen, J. S. "Structure of Methylammonium Lead Iodide within Mesoporous Titanium Dioxide: Active Material in High-Performance Perovskite Solar Cells". *Nano Lett.* 2013, *14*, 127–133.

47. Weller, M. T.; Weber, O. J.; Henry, P. F.; Di Pumpo, A. M.; Hansen, T. C. "Complete Structure and Cation Orientation in the Perovskite Photovoltaic Methylammonium Lead Iodide between 100 and 352 K". *Chem. Commun.* 2015, *51*, 4180–4183.

 

48. Zhang, Q.; Cagin, T.; Goddard, W. A. "The Ferroelectric and Cubic Phases in BaTiO3 Ferroelectrics Are Also Antiferroelectric.". *Proc. Natl. Acad. Sci. U. S. A.* 2006, *103*, 14695–14700.

49. Quarti, C.; Mosconi, E.; Ball, J. M.; D'Innocenzo, V.; Tao, C.; Pathak, S.; Snaith, H. J.; Petrozza, A.; De Angelis, F. "Structural and Optical Properties of Methylammonium Lead Iodide across the Tetragonal to Cubic Phase Transition: Implications for Perovskite Solar Cells". *Energy Environ. Sci.* 2016, *9*, 155–163.

50. Trots, D. M.; Myagkota, S. V. "High-Temperature Structural Evolution of Caesium and Rubidium Triiodoplumbates". *J. Phys. Chem. Solids* 2008, *69*, 2520–2526.

51. Sharma, S.; Weiden, N.; Weiss, A. "Phase Diagrams of Quasibinary Systems of the Type: $ABX_3$ — $A'BX_3$; $ABX_3$ — $AB'X_3$, and $ABX_3$ — $ABX'_3$; X = Halogen". *Zeitschrift für Phys. Chemie* 1992, *175*, 63–80.

52. Wells, H. L. "On the Caesium- and the Potassium-Lead Halides". *Am. J. Sci.* 1893, *s3-45*, 121–134.

53. Filip, M. R.; Liu, X.; Miglio, A.; Hautier, G.; Giustino, F. "Phase Diagrams and Stability of Lead-Free Halide Double Perovskites $Cs_2BB'X_6$: B = Sb and Bi, B′ = Cu, Ag, and Au, and X = Cl, Br, and I". *J. Phys. Chem. C* 2018, *122*, 158–170.

54. Marronnier, A.; Lee, H.; Geffroy, B.; Even, J.; Bonnassieux, Y.; Roma, G. "Structural Instabilities Related to Highly Anharmonic Phonons in Halide Perovskites". *J. Phys. Chem. Lett.* 2017, 2659–2665.

55. Woodward, P. M. "Octahedral Tilting in Perovskites. II. Structure Stabilizing Forces". *Acta Crystallogr. Sect. B Struct. Sci.* 1997, *53*, 44–66.

 

## 6.10 Appendix

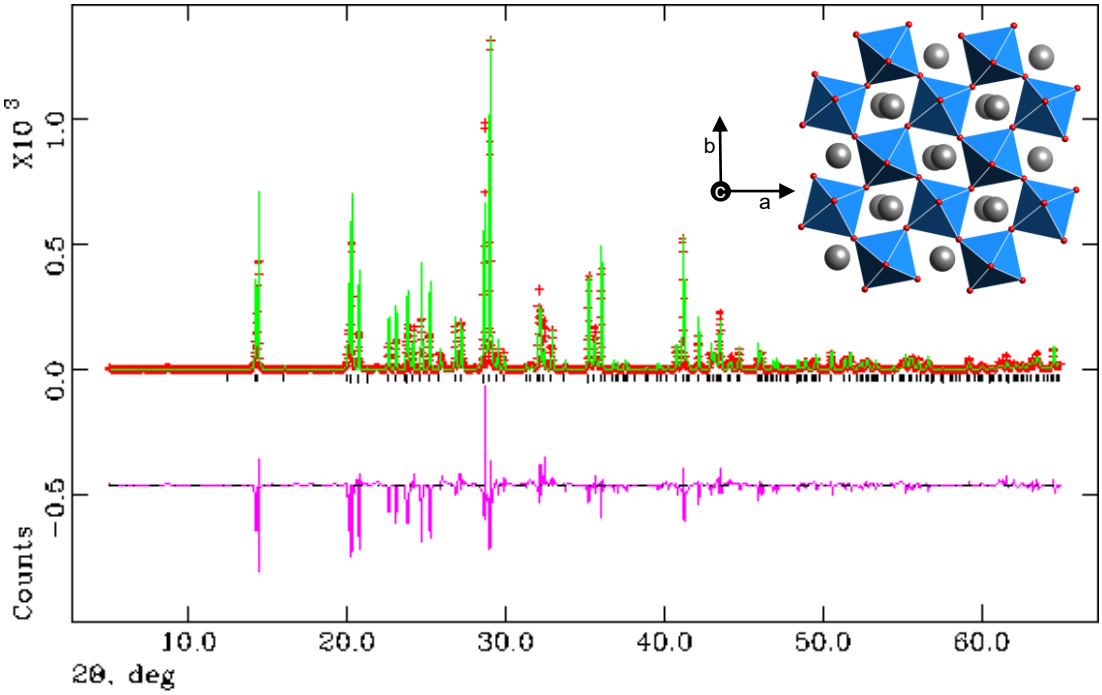


**Figure 6-A1. Rietveld refinement for γ-$CsPbI_3$. (red dots) XRD pattern for the black powder of γ-$CsPbI_3$ prepared by solid state synthesis, and measured with Cu $K_{\alpha 1}$ radiation at 293 K. (green line) Rietveld refinement of orthorhombic perovskite γ-$CsPbI_3$ at room temperature, with tick marks (black lines) and difference curve (pink lines, observed minus calculated). Polyhedral model in inset; Structural parameters of refinement provided in Table 6-1. The orthorhombic structure was refined by Dr Amir Abbas Haghighirad at the Karlsruhe Institute of Technology.**

**Table 6-A1. Crystallographic data for a $CsPbI_3$ single crystal (yellow phase).**

| **Compound** | **$CsPbI_3$** |
|---|---|
| Colour of crystal | Yellow |
| Measurement temperature | 293 K |
| Crystal system | Orthorhombic |
| Space group | *P n m a* (no.62) |
| Unit cell dimensions | a = 10.462 ± 0.005 Å, b= 4.799 ± 0.005 Å, c = 17.765 ± 0.005 Å, $\alpha = \beta = \gamma = 90°$ |
| Volume | 891.93±0.05 $Å^3$ |
| Z | 4 |
| Density (calculated) | 5368 $g/cm^3$ |
| Reflections collected | 17444 |
| Unique reflections | 896 from which none suppressed |
| R(int) | 0.1014 |
| R (sigma) | 0.0318 |
| Goodness-of-fit | 0.782 |
| Final R indices ($R_{all}$) | 0.0389 |
| $wR_{obs}$ | 0.1015 |
| Wavelength | 0.71073 Å |
| Weight scheme for the refinement | Weight = 1 / [ $sigma^2(Fo^2)$ + ( 0.0824 * P )$^2$ + 0.00 * P ] where P = ( Max ( $Fo^2$, 0 ) + 2 * $Fc^2$ ) / 3 |
| Atomic Wyckoff-positions | **Atom** / **Site** / **x** / **y** / **z** / **Occupancy**<br>Pb / 4c / 0.16036 / 0.2500 / 0.06209 / 1<br>Cs / 4c / 0.41584 / 0.2500 / 0.82910 / 1<br>I / 4c / 0.3367 / 0.7500 / 0.99840 / 1<br>I / 4c / 0.2988 / 0.2500 / 0.21286 / 1<br>I / 4c / 0.0321 / 0.2500 / 0.88563 / 1 |
| Isotropic temperature factors, $U_{iso}$ ($Å^2$) | (Cs) 0.0406 ± 0.0004, (Pb) 0.0335 ± 0.0003, (I1) 0.0369 ± 0.0004, (I2) 0.0386 ± 0.0004, (I3) 0.0347 ± 0.0004 |
| Anisotropic temperature factors ($Å^2$) | $U_{11}(Cs)$ = 0.0408 ± 0.0007, $U_{11}(Pb)$ = 0.0338 ± 0.0005, $U_{11}(I1)$ = 0.0340 ± 0.0007, $U_{11}(I2)$ = 0.0374 ± 0.0007, $U_{11}(I3)$ = 0.0291 ± 0.0006<br>$U_{22}$(Cs) = 0.0442 ± 0.0007, $U_{22}(Pb)$ = 0.0367 ± 0.0005, $U_{22}(I1)$ = 0.0378 ± 0.0007, $U_{22}(I2)$ = 0.0473 ± 0.0007, $U_{22}(I3)$ = 0.0456 ± 0.0007, $U_{33}(Cs)$ = 0.0367 ± 0.0006, $U_{33}(Pb)$ = 0.0299 ± 0.0004, $U_{33}(I1)$ = 0.0387 ± 0.0007, $U_{33}(I2)$ = 0.0313 ± 0.0006, $U_{33}(I3)$ = 0.0295 ± 0.0006 |

# 7 Designing Stable Inorganic Perovskite Absorbers for Photovoltaics

## 7.1 Wider context and summary

The previous chapters have shown that the iodide-rich compositions of the caesium lead halide perovskites are promising candidates for photovoltaics, with excellent opt-electronic properties, and proven efficiency in devices. However, the preferential formation of a non-perovskite structure is a serious impediment to the future of these materials in commercial applications. This chapter briefly outlines recent literature reports which claim stabilisation of the perovskite polymorph of $CsPbI_3$, before presenting a rationale behind metal substitution as a means to fully stabilise this material. Some early attempts at experimentally verifying this strategy are shown, and the feasibility of this approach is discussed.

In summary, this chapter provides direction towards realising stable inorganic metal halide absorbers for solar cell applications.

 

## 7.2 Introduction

Hybrid organic-inorganic lead halide perovskites have been intensely investigated in photovoltaics over the last ten years, resulting in power conversion efficiencies well above 20%.[1] Despite this remarkable achievement, there remains a need for perovskite absorbers with bandgaps from 1.8 to 2 eV, for both tandem photovoltaics and light emission.[2,3] These bandgaps are difficult to obtain with the hybrid perovskites. Given the inherent volatility and reactivity of organic cations, the ideal materials to meet this need should be the inorganic lead halide perovskites, which have bandgaps above 1.7 eV and very similar optoelectronic properties to the hybrid lead-halide perovskites.[4] These materials are also easily produced by well-known fabrication techniques for mass production of optoelectronic devices, for example vapour deposition.[4,5] These features make the inorganic lead halide perovskites desirable for a variety of optoelectronic applications.

However, solar cells with inorganic lead halide perovskites lag behind their hybrid counterparts, with power conversion efficiencies reaching around 13%.[6,7] A main contributing factor to this lag is that research efforts are hampered by an undesirable structural transition in the iodide-rich lead halide perovskites. As described in Chapter 6, the yellow non-perovskite polymorph is the most thermodynamically stable of the $CsPbI_3$ polymorphs. The photoactive black phase is a metastable orthorhombic perovskite that rapidly converts to the yellow polymorph in the presence of moisture. This structural instability increases the challenge of working with these materials, as all processing must take place in a dry atmosphere.

Stabilisation of the photoactive black phase is vital in order for these materials to be used in solar panels and other optoelectronic devices. Currently, approaches to stabilisation may be grouped into the three broad categories of processing, inorganic modifications, and organic modifications. This chapter includes a brief review of the

 

published literature for each of these three approaches. In all cases the orthorhombic perovskite polymorph is only kinetically trapped, and the presence of water catalyses the transition to the non-perovskite phase.[8]

Complete structural stability of the inorganic lead halide perovskites requires the most thermodynamically stable phase to be a perovskite phase. In the family of lead halide perovskites with caesium as the cation, the thermodynamically stable phases at room temperature are orthorhombic perovskites for both $CsPbBr_3$ and $CsPbCl_3$,[9–12] and cubic perovskite for the fluoride compound $CsPbF_3$.[13] In this family of compounds it is only the iodide perovskite $CsPbI_3$, and mixed halide compositions such as $CsPbI_2Br$ and $CsPbIBr_2$, for which the thermodynamically stable phase is a non-perovskite.[14–17]

In these inorganic perovskites, halide mixing alone is not enough to obtain a thermodynamically stable orthorhombic perovskite at room temperature with a bandgap below 2 eV. While mixed halide compounds with bandgaps below 2 eV have been shown to have improved ambient stability compared to neat $CsPbI_3$,[15,17] the non-perovskite phase is thermodynamically stable. This is the case even for $CsPbIBr_2$, where the bandgap is ~2.05 eV.[17,18] The orthorhombic perovskite does not become the thermodynamically stable phase until the compound contains more than 80% bromide content,[17] at which point the bandgap is close to 2.2 eV.[16]

In contrast, it is possible to obtain a stable perovskite by mixing $CsPbI_3$ with the hybrid organic-inorganic perovskite formamidinium lead iodide, $FAPbI_3$.[19] $FAPbI_3$ also has a non-perovskite polymorph which is thermodynamically preferred over the perovskite polymorphs. This polymorph is hexagonal due to the large effective size of the FA cation which gives a tolerance factor of 1.04.[20–22] Mixing Cs and FA then brings the tolerance factor within the region of formation of a perovskite structure.[23] Free energy calculations confirm the experimental finding that mixing $CsPbI_3$ and

 

$FAPbI_3$ leads to a perovskite polymorph that is both entropically and thermodynamically favourable.[24]

Similarly, it should be possible to structurally stabilise a perovskite polymorph of $CsPbI_3$ by replacing some or all of the lead cation with a different metal ion, while retaining the advantage of a fully-inorganic perovskite. Substitution of the lead cation with a smaller metal(II) cation could improve the material stability by reducing the effective size of the B-site cation and thus contracting the metal halide network.[25] This approach is not unreasonable, as mixed-metal perovskites are well-known in the literature for the oxide perovskites.[26] In the hybrid lead halide perovskites, a small amount of metal doping has been shown to improve $MAPbI_3$ devices, with a wide range of cations available.[27,28] In the mixed-cation perovskite $FA_{0.75}Cs_{0.25}Pb_{0.5}Sn_{0.5}I_3$, alloying of lead and tin produced a low-bandgap material with high photovoltaic efficiency.[29] In inorganic lead halide perovskites, small amounts of $Ca^{2+}$ in $CsPbI_3$ have been shown to increase photovoltaic efficiency.[6] Manganese ($Mn^{2+}$) substitution has been claimed in $CsPbI_3$ nanocrystals,[30–32] with reports of improved structural stability. However, the mechanism of stabilization is not well understood, and a recent report suggests that $Mn^{2+}$ occupies interstitial lattice sites rather than the B-site in $CsPbI_2Br$.[33]

In this chapter, structural stabilisation of $CsPbI_3$ by metal substitution is discussed as a theoretical approach, and some work towards experimentally verifying this method is presented. Divalent cations with suitable size for inclusion in the perovskite structure are selected using a tolerance factor argument, where minimum substitution fractions are determined for each of these cations. Three cations, namely $Ca^{2+}$, $Mn^{2+}$, and $Mg^{2+}$, are each tested for integration into $CsPbI_3$ using various synthetic methods. Although some increases in stability are found, none of these cations is able to fully stabilize $CsPbI_3$ in a perovskite structure.

 

## 7.3 Previous stabilisation of $CsPbI_3$

Figure 7-1 summarises the methods used so far in the scientific literature where 'increased stability' in the perovskite structure is claimed for $CsPbI_3$. Here increased stability is typically with respect to bulk $CsPbI_3$ or to $CsPbI_3$ without the specified modification. However, with the exception of altered composition, all of these methods stabilise the kinetically-trapped orthorhombic γ-$CsPbI_3$ perovskite by protecting the perovskite from external catalysts (such as ambient moisture)[8] for the transition to the thermodynamically-favourable non-perovskite polymorph.

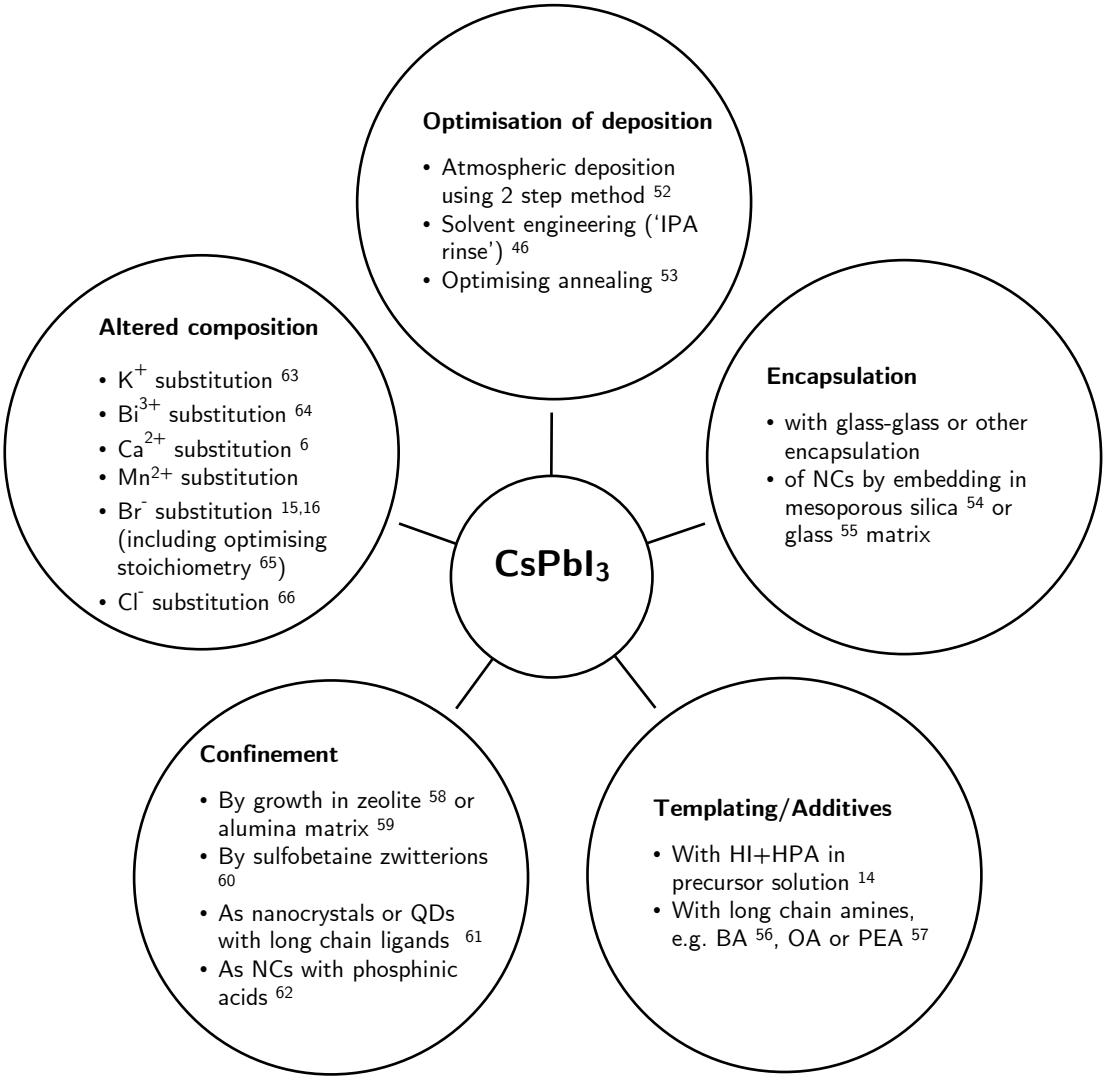


**Figure 7-1. Routes reported in the literature that claim to stabilise a perovskite polymorph of $CsPbI_3$ with respect to the non-perovskite polymorph.**

 

## 7.4 Tuning the tolerance factor by metal substitution

This section presents a mathematical analysis of how the stability of $CsPbI_3$ in the perovskite structure could be increased by partial substitution of lead with a different metal. Here the argument is based on the geometric constraints of packing spheres into the perovskite structure, taking into account the more covalent nature of metal—iodide bonding in comparison to metals bonding with oxide and fluoride anions. It is important to note that this analysis cannot predict whether a particular metal 2+ ion will incorporate into the lattice. Here these calculations are used merely as a guide to predict how much of a given metal ion would be needed for stabilisation assuming substitution onto the $Pb^{2+}$ lattice site.

The Goldschmidt tolerance factor, $t$, may be used to ascertain whether a given elemental composition could be stable in a perovskite structure.[34] The tolerance factor was introduced in Section 2.1.1, and is reproduced in Equation 7-1.

$$t = \frac{r_A + r_I}{\sqrt{2}(r_B + r_I)} \qquad \text{Equation 7-1}$$

Here $r_A$ is the radius of the caesium ion, $r_I = 2.2$ Å is the radius of the iodide ion, and $r_B$ is the radius of the metal ion in octahedral (6-fold) coordination.

In general, for a stable perovskite structure to exist in ambient conditions, a tolerance factor in the range $0.8 \leq t \leq 1$ is required.[21,34] The tolerance factor is typically calculated assuming a cubic perovskite, where the A-site cation is in 12-fold coordination. However, at the lower end of this range, considerable octahedral tilting is required to maintain a perovskite structure. As the octahedra tilt, the A-site cation is displaced from the centre of the cubo-octahedral cavity. This displacement reduces the coordination of the A-site cation from 12-fold to 8-fold, or even 7-fold in some cases.[26] The effective size of the A-site cation depends on the coordination and is typically smaller for lower coordination, which further lowers the

 

tolerance factor of the tilted perovskite.[35] In this discussion, the perovskite structures are orthorhombic, for which the Cs cation is in 8-fold coordination with an ionic radius of 1.74 Å.[35]

Shannon's ionic radii are typically used in tolerance factor calculations, giving good agreement with experimental structures for fluoride and oxide perovskites. However, due to the covalent nature of metal-iodide bonds, the typical Shannon radii do not accurately represent the bonding in these salts. Revised ionic radii for metal ions bonding with iodide anions have been calculated from experimental data, and so these revised radii are used for the present discussion.[21]

Tolerance factors of some $CsMI_3$ compounds, for various metals M, are given in Table 7-1 for the revised ionic radii for metals determined by Travis et al,[21] and in Table 7-2 in Section 7.9 for the Shannon ionic radii. Of particular note are the tolerance factors for $CsPbI_3$ and for $CsSnI_3$ of 0.86 and 0.88 respectively using revised radii for metal-iodide bonds.[21] Both of these compounds can exist in highly tilted metastable orthorhombic perovskite polymorphs at room temperature, but the stable structure at ambient conditions is non-perovskite ($NH_4CdCl_3$-type).[36] Similarly $CsTmI_3$, $CsYbI_3$, and $CsCaI_3$ are known to adopt orthorhombic perovskite polymorphs.[37] However, these materials are highly air-sensitive,[37] and $CsCaI_3$ has been reported to also exist in a non-perovskite structure.[38]

In comparison, the bromide compound $CsPbBr_3$ is stable in an orthorhombic perovskite polymorph at ambient conditions.[39] Using revised radii for lead-bromide bonding gives a tolerance factor of 0.89 for $CsPbBr_3$. The formation of a stable perovskite structure in these known compounds suggests a tolerance factor of at least 0.89 is required for suppression of a 'yellow phase' non-perovskite. To further this point, $CsGeI_3$ has a tolerance factor of 0.938 by these calculations, and experimentally adopts a trigonal perovskite structure, with rhombohedral symmetry ($a$ = 5.98 Å and $\alpha$ = 88.6°).[40,41] While this material is not stable at ambient

 

conditions with respect to oxidation,[40,41] it does indicate that a high-symmetry perovskite structure is possible with caesium and iodide.

With the aim of retaining the optoelectronic properties of $CsPbI_3$ and increasing stability in the perovskite structure, here partial substitution of a different 2+ metal ion into $CsPbI_3$ is considered. For a substitution fraction, $x$, of metal M into $CsPbI_3$,

**Table 7-1. Tolerance factors calculated using revised ionic radii from ref 21 for metals 'M' occupying the B-site in $CsMI_3$. Metals in italics are too large to form stable perovskites with $Cs^+$. Metals in bold italics are considered experimentally in this chapter. Substitution percentages of $CsMI_3$ into $CsPbI_3$ are given for the overall tolerance factor of $CsPbBr_3$ of 0.892. * denotes metal ionic radii from Shannon.[35]**

| B-site Metal | Revised ionic radii for iodide compounds | $R_{Pb} - R_M$ | Tolerance factor for $CsMI_3$ | x (%) for t = 0.892 |
|---|---|---|---|---|
| Ni | 0.57 | 0.46 | 1.006 | 23.2 |
| Hg | 0.61 | 0.42 | 0.991 | 25.4 |
| Ti | 0.66 | 0.37 | 0.974 | 28.8 |
| V | 0.68 | 0.35 | 0.967 | 30.5 |
| Cr | 0.68 | 0.35 | 0.967 | 30.5 |
| Fe | 0.68 | 0.35 | 0.967 | 30.5 |
| ***Mn*** | ***0.72*** | ***0.31*** | ***0.954*** | ***34.4*** |
| Cu* | 0.73 | 0.30 | 0.951 | 35.5 |
| Zn* | 0.74 | 0.29 | 0.948 | 36.8 |
| Co | 0.745 | 0.285 | 0.946 | 37.4 |
| ***Mg*** | ***0.75*** | ***0.28*** | ***0.944*** | ***38.1*** |
| Ge | 0.77 | 0.26 | 0.938 | 41.0 |
| Cd | 0.81 | 0.22 | 0.926 | 48.4 |
| ***Ca*** | ***0.92*** | ***0.11*** | ***0.893*** | ***96.9*** |
| Yb | 0.93 | 0.10 | 0.890 | — |
| Tm | 0.95 | 0.08 | 0.884 | — |
| Sn | 0.97 | 0.06 | 0.879 | — |
| Dy | 0.97 | 0.06 | 0.879 | — |
| Pb | 1.03 | 0 | 0.863 | — |
| Sm | 1.11 | -0.08 | 0.842 | — |
| Eu* | 1.17 | -0.14 | 0.827 | — |
| Sr | 1.18 | -0.15 | 0.824 | — |

 

the effective metal ion radius, $r_B$, is approximated according to Equation 7-2.

$$r_B = x\, r_M + (1 - x)\, r_{Pb} \qquad \text{Equation 7-2}$$

This effective metal radius may be directly substituted into Equation 7-1, to give a linear dependence of the tolerance factor on substitution fraction, as shown in Figure 7-2. Alternately, the required substitution fraction for a desired tolerance factor may be calculated using Equation 7-3, which derives from substitution of Equation 7-2 into Equation 7-1.

$$x = \frac{1}{r_{Pb} - r_M}\left(r_{Pb} + r_I - \frac{r_A + r_I}{\sqrt{2}t}\right) \qquad \text{Equation 7-3}$$

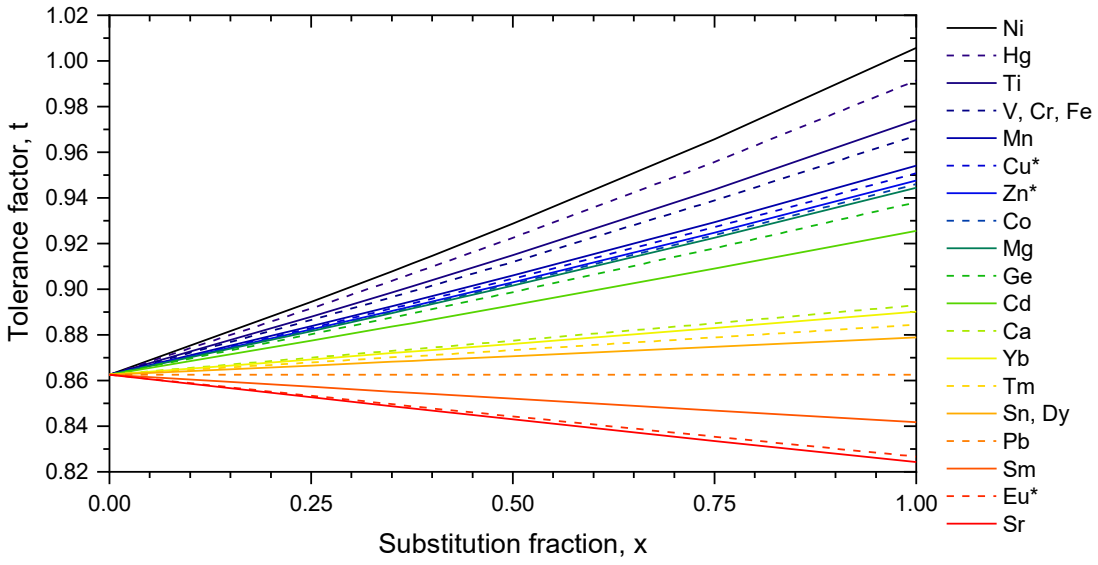


**Figure 7-2. Graphical representation of the dependence of the tolerance factor for a given substitution fraction of $CsMI_3$ into $CsPbI_3$. Exact values of the substitution fraction required for a tolerance factor of ~0.89 are provided in Table 7-1. * denotes metal ionic radii from Shannon.[35]**

In order to select appropriate metal ions for experimental tests, the first consideration is stability of the metal ion in the 2+ oxidation state. Germanium is a promising candidate, but, like $Sn^{2+}$, may be oxidised to the 4+ oxidation state.[29,40,41]

 

Similarly the lanthanides prefer the 3+ oxidation state, so they too are omitted from experimental exploration.

The next consideration is which metal ions are known to form octahedra with iodide. Usually this question is answered through the use of the octahedral factor, $\mu = \frac{r_B}{r_I}$. However, this equation is not valid for the effective metal ion radii used for tolerance calculations above, as these radii are determined by using a fixed iodide radius for the metal-iodide bond length. Instead, a search of the literature reveals that, in addition to the perovskite compounds discussed above, $Mg^{2+}$ and $Mn^{2+}$ coordinate octahedrally with iodide in the hexagonal compounds $CsMgI_3$ and $CsMnI_3$.[42,43] In contrast, $Co^{2+}$ forms tetrahedra with iodide in the orthorhombic non-perovskite compound $Cs_2CoI_4$ and so is not an ideal candidate here.[44]

From Figure 7-2 it is evident that there is a trade-off between the size of the metal ion, and the likelihood of the ion integrating into the lattice. A small substitution percentage is preferable in order to maintain the optoelectronic properties of $CsPbI_3$. In this case, structural stability would require a very small metal to achieve an average metal radius of ~0.93. However, if the metal is too small to form octahedra with iodide independently, it may not integrate into the lattice. On the other hand, structural stability can be ensured with a large substitution percentage of a metal that could form a perovskite by itself, as $CsMI_3$. This large substitution percentage would significantly alter the chemical composition and hence the final material is likely to have very different optoelectronic properties when compared with $CsPbI_3$.

 

## 7.5 Experimental feasibility of metal substitution

This section discusses attempts at experimentally stabilising $CsPbI_3$ by partial substitution of lead with calcium ($Ca^{2+}$), manganese ($Mn^{2+}$), or magnesium ($Mg^{2+}$). These three metals were chosen as representative examples of: a metal that is likely to form octahedra with iodide but requires large substitution to enable stabilisation ($Ca^{2+}$), a metal that has been shown to increase stability but is unlikely to form octahedra with iodide ($Mn^{2+}$), or a metal of similar effective size to germanium but for which a perovskite structure as $CsMI_3$ has not yet been demonstrated ($Mg^{2+}$).

### 7.5.1 Calcium substitution into $CsPbI_3$

To test the validity of the solid state approach for mixing other metals onto the lead site, the first metal discussed is calcium. $Ca^{2+}$ substitution has recently been shown to increase the stability of thin films of $CsPbI_3$, although the increase in stability was attributed to formation of an oxide layer.[6]

Solid state synthesis was used to prepare mixed-metal samples for two substitution fractions, 25% and 50% $Ca^{2+}$ substitution. The unsubstituted γ-$CsPbI_3$ sample prepared by solid state synthesis was previously described in Chapter 6. Appropriate amounts of CsI (Alfa Aesar, 5N), $PbI_2$ (Sigma Aldrich, 5N) and $CaI_2$ (Alfa Aesar, 5N) were ground for 25-30 minutes in a mortar and pestle in a nitrogen-filled glovebox, before being transferred to a quartz ampoule and sealed under vacuum. The precursor salts were melted together in a furnace, at 575 °C for compounds containing $Ca^{2+}$, and at 525 °C for the control. The sample with 25% $Ca^{2+}$ substitution was cooled at 50 °C/hour to 380 °C and then removed from the furnace and cooled in air. The sample with 50% $Ca^{2+}$ substitution and the control were cooled at 50 °C/hour. Powders were prepared in the black polymorph for XRD as described in the Experimental Methods chapter.

 

To determine whether $Ca^{2+}$ substitutes onto the B-site, XRD patterns were measured in nitrogen gas for each sample. These patterns are shown in Figure 7-3. Figure 7-3(a) shows very similar patterns for 0% and 25% $Ca^{2+}$ substitution, but a different pattern for 50% $Ca^{2+}$ substitution. The overall diffraction peak intensities decrease with increasing substitution. Figure 7-3(b) shows a broadening of the 220 reflection with increasing $Ca^{2+}$ substitution. Closer examination of this peak reveals that there may be a slight shift to higher angles. Rietveld refinement of the XRD pattern for 25% $Ca^{2+}$ substitution in the orthorhombic perovskite structure (Pnam) yields lattice parameters of a = 8.8349 Å, b = 8.5702 Å, c = 12.4584 Å, $\alpha = \beta = \gamma = 90°$, which are slightly smaller than the parameters determined for γ-$CsPbI_3$ in Chapter 6 (a = 8.8560 Å, b = 8.5766 Å, c = 12.4722 Å, $\alpha = \beta = \gamma = 90°$). Smaller lattice parameters are expected for substitution with a smaller cation, assuming the structure is retained. In this refinement, it was possible to replace some of the $Pb^{2+}$ by $Ca^{2+}$, which further supports $Ca^{2+}$ substitution onto the $Pb^{2+}$ site in γ-$CsPbI_3$. For 50% $Ca^{2+}$ substitution, while peaks corresponding to the γ-$CsPbI_3$ perovskite are visible, the XRD pattern is not of sufficient quality to extract structural information.

Optical data may also provide further evidence for or against incorporation of $Ca^{2+}$ into the γ-$CsPbI_3$ lattice. To this end, photoluminescence (PL) was measured before the ampoules were broken, which gives a margin of error of approximately 10 nm in the PL peak position due to scattering and alignment effects. Figure 7-4 shows that, unlike in Chapter 6, the PL of γ-$CsPbI_3$ is seen nearer to 700 nm than 720 nm when measured through the ampoule. For the $Ca^{2+}$-substituted samples there is a shift to higher energy with increased substitution. Intriguingly, for 50% $Ca^{2+}$ substitution, Figure 7-4(c) reveals that many colours are present when the sample is illuminated with UV light, indicating compositional variation within the sample. Of particular interest is the blue region, for which the photoluminescence is shown in Figure

 

7-4(d). However, preparation of a phase-pure sample is necessary to determine the origin of the mixed blue and red emission.

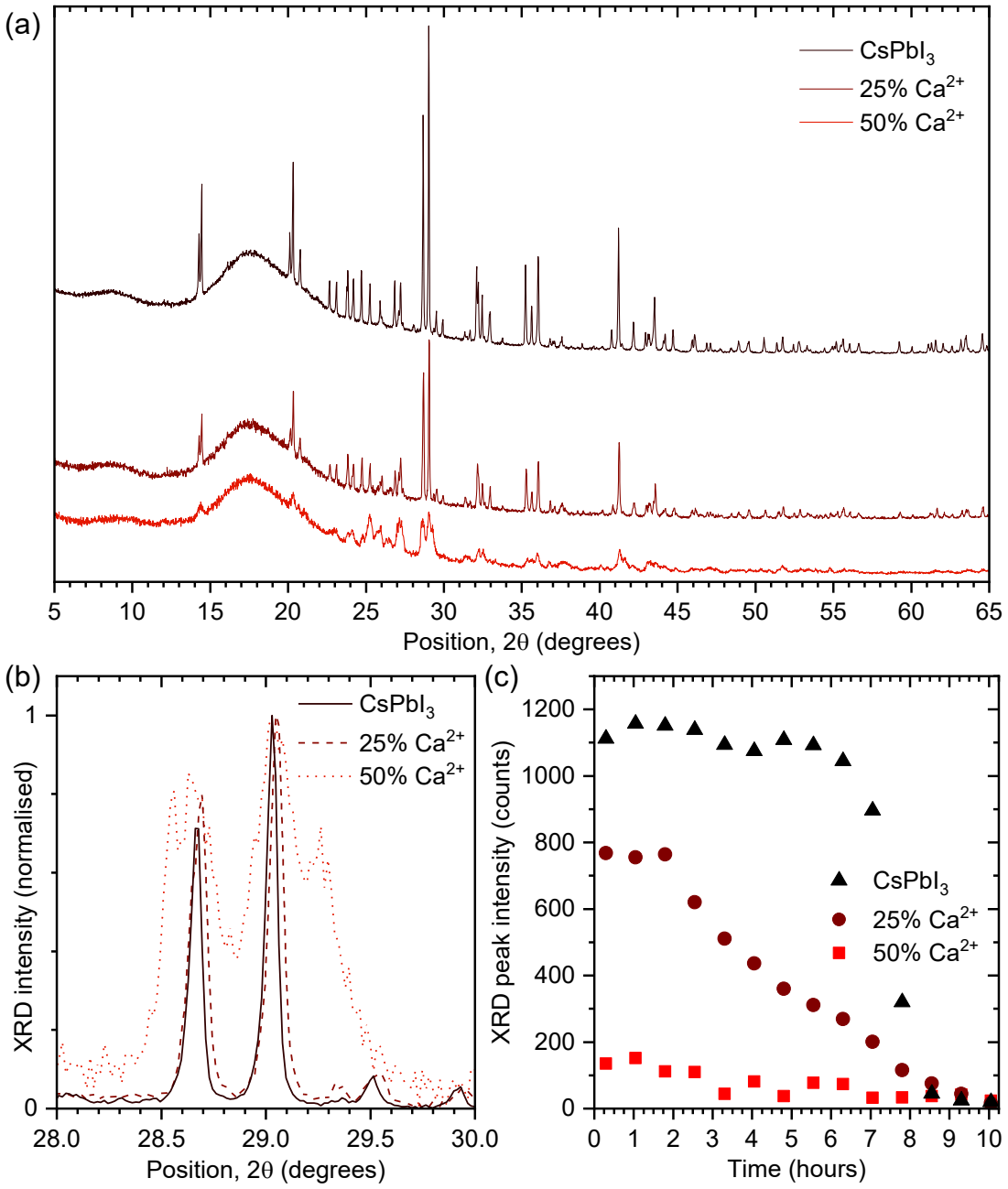


**Figure 7-3. (a) XRD patterns from the neat and $Ca^{2+}$-substituted samples, prepared by solid state synthesis and measured with Cu $K_{\alpha 1}$ radiation at 20 °C. (b) Normalised XRD patterns from (a), highlighting changes in the 220 reflection of the orthorhombic structure (near 29° 2θ). (c) XRD intensity over time for the 220 reflection.**

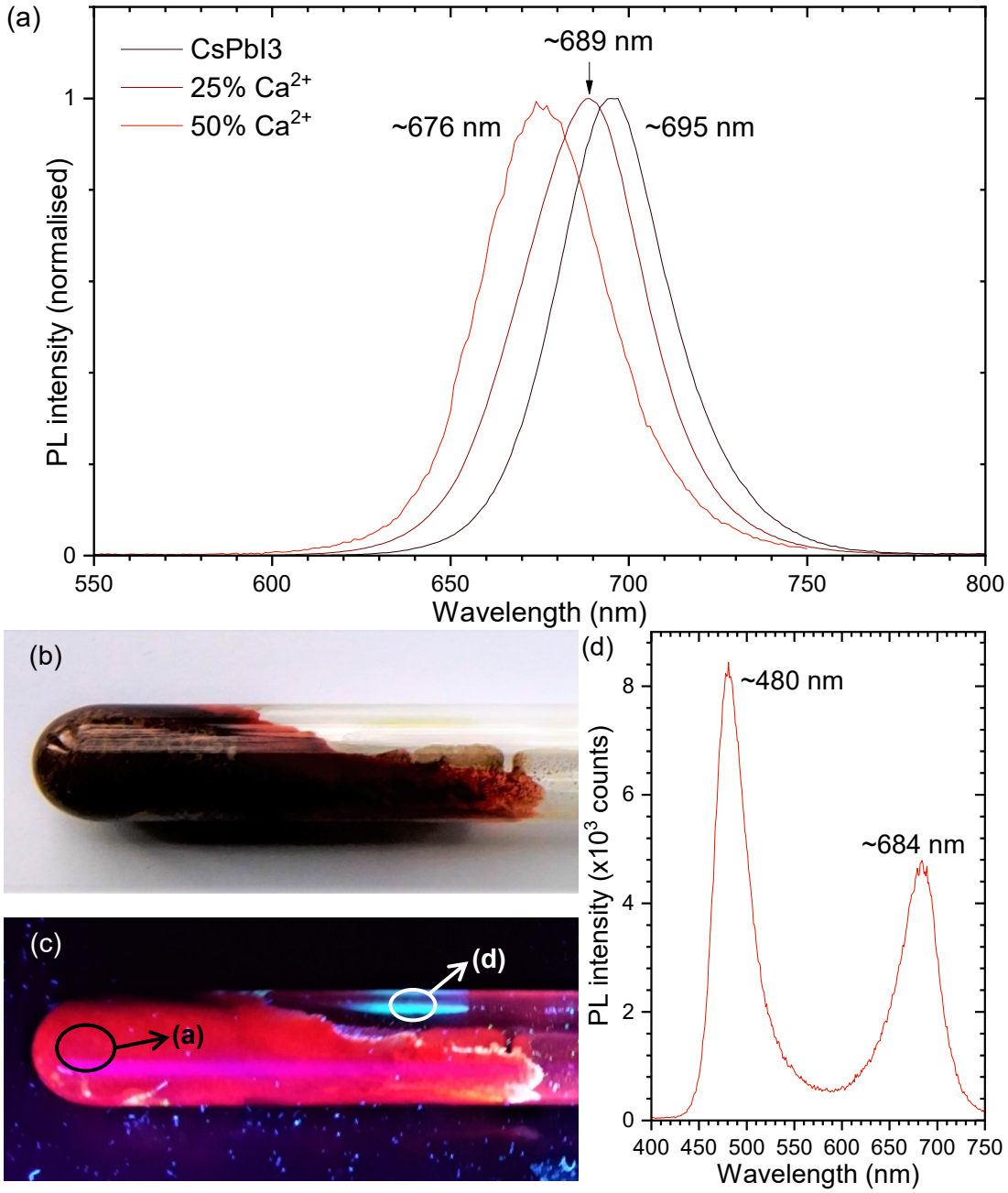


**Figure 7-4. (a) PL through the ampoule for the neat and $Ca^{2+}$-substituted samples. (b) Photograph under room lights of the ampoule containing the dark red ingot with 50% $Ca^{2+}$ substitution. (c) Photograph under 365 nm UV illumination of the ampoule in (b), indicating the regions from which PL was measured. (d) Dual emission measured when exciting the blue region in (c).**

While it is evident that $Ca^{2+}$ is indeed able to integrate into the lattice in place of $Pb^{2+}$, no advantage is gained in terms of structural stability. The $Ca^{2+}$-containing samples visibly show a faster colour change from brown to yellow, and this observation is supported by Figure 7-3(c) which shows a steady decline in XRD intensity for $Ca^{2+}$-containing samples. The lower ambient stability of the $Ca^{2+}$-containing samples is likely to be due to the hygroscopic nature of $CsCaI_3$.[45] Overall these experiments have shown that $Ca^{2+}$ substitution into $CsPbI_3$ is unlikely to result in a stable perovskite structure. As $CsCaBr_3$ is similarly hygroscopic,[45] the prospects for stabilising the mixed-halide perovskite $CsPbI_2Br$ in this way are also limited.

### 7.5.2 Manganese substitution into $CsPbI_3$

The smallest metal tested for stabilisation of $CsPbI_3$ in this work is manganese in its 2+ oxidation state. There are many possible oxidation states of manganese, both higher and lower. To avoid oxidation of $Mn^{2+}$, again solid state synthesis is used to assess whether $Mn^{2+}$ is able to incorporate into the $CsPbI_3$ lattice. As for the $Ca^{2+}$-substituted samples, the appropriate amounts of CsI, $PbI_2$ and $MnI_2$ were ground together in a mortar and pestle for 30 minutes, inside a glovebox filled with nitrogen gas, to form a yellow powder which was transferred to a quartz ampoule, evacuated, and sealed. Here the precursor salts were reacted together by melting at 500 °C. Figure 7-5(a) shows that the melt is a dark red liquid. Quench cooling from 500 °C as in Figure 7-5(b) and (c) yields a dark ingot which is stable under vacuum for over 24 hours before showing signs of yellowing. However, it should be noted that slow cooling from the melt yields a yellow-green solid for all prepared compositions (up to 50% $Mn^{2+}$ substitution). Black powders were prepared for XRD as described in the Experimental Methods chapter.

 


**Figure 7-5. Photographs of the ampoule (a) when removed from the furnace at 500 °C, (b) while cooling, and (c) when rapidly cooled to room temperature.**

XRD patterns for the control, 10% and 25% $Mn^{2+}$ substitution are shown in Figure 7-6(a), with normalised patterns shown in Figure 7-6(b) for the 220 reflection of the orthorhombic perovskite polymorph γ-$CsPbI_3$ determined in Chapter 6. Here increasing $Mn^{2+}$ substitution leads to a slight shift to lower angle of the main perovskite peaks (from 29.03° to 29.01° to 28.98° 2ϑ respectively, for the 220 reflection). As $Mn^{2+}$ is smaller than $Pb^{2+}$, this is shift is not consistent with partial replacement of $Mn^{2+}$ onto the $Pb^{2+}$ site. Rather, this shift is consistent with interstitial incorporation of $Mn^{2+}$ in the $CsPbI_3$ lattice. However, Rietveld refinement of these patterns is necessary to be confident of this conclusion. Figure 7-6(b) and (c) also show an increase in peak width (from 0.066° to 0.075° to 0.084° 2ϑ) together with a reduction in peak intensity for increasing $Mn^{2+}$ substitution. These observations may indicate a reduction in crystallite size and/or an increase in the fraction of amorphous material present in the sample.

In contrast to $Ca^{2+}$ substitution, Figure 7-6(c) shows that the intensity of the 220 perovskite peak is retained for an extended period of time with $Mn^{2+}$ substitution, which indicates an increase in structural stability. This increased stability was also observed as the retention of dark colouration of the powders for weeks when stored in a glovebox filled with nitrogen gas.

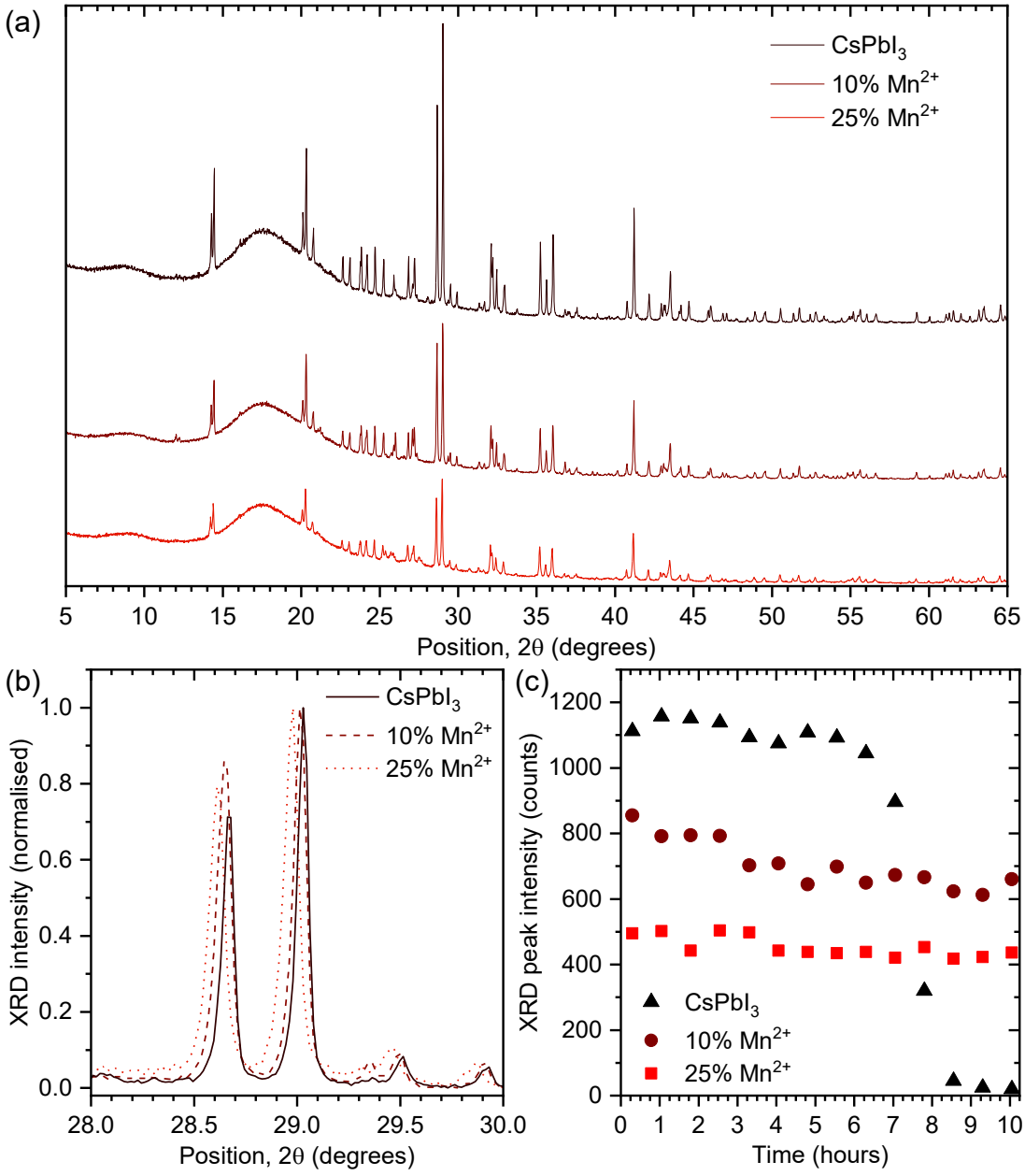


**Figure 7-6. (a) XRD patterns from the neat and $Mn^{2+}$-substituted samples, prepared by solid state synthesis and measured with Cu $K_{\alpha 1}$ radiation at 20 °C. (b) Normalised XRD patterns from (a), highlighting changes in the 220 reflection of the orthorhombic structure (near 29° 2θ). (c) XRD intensity over time for the 220 reflection.**

To determine whether the increase in structural stability is associated with formation of a protective manganese oxide layer, magnetic measurements were made on the samples prepared with $MnI_2$ and also on the $CsPbI_3$ control. These

measurements are shown in Figure 7-7. Figure 7-7(a) shows that at low temperature, magnetisation increases with increasing $MnI_2$ content, and no transitions are detected to indicate manganese oxide in any of the samples. Rather, the small discontinuity in Figure 7-7(b) around 4K for an applied magnetic field of 0.01 T indicates a weak magnetic transition which corresponds to unreacted $MnI_2$. An additional strong transition at 7 K could originate from doping of the perovskite structure with $Mn^{2+}$, for example from interstitial incorporation as indicated by the XRD data above. While it is not possible to conclusively show that $MnI_2$ has integrated into the structure in this way by these measurements, it is possible to conclude that the increase in structural stability is not due to the formation of manganese oxides.

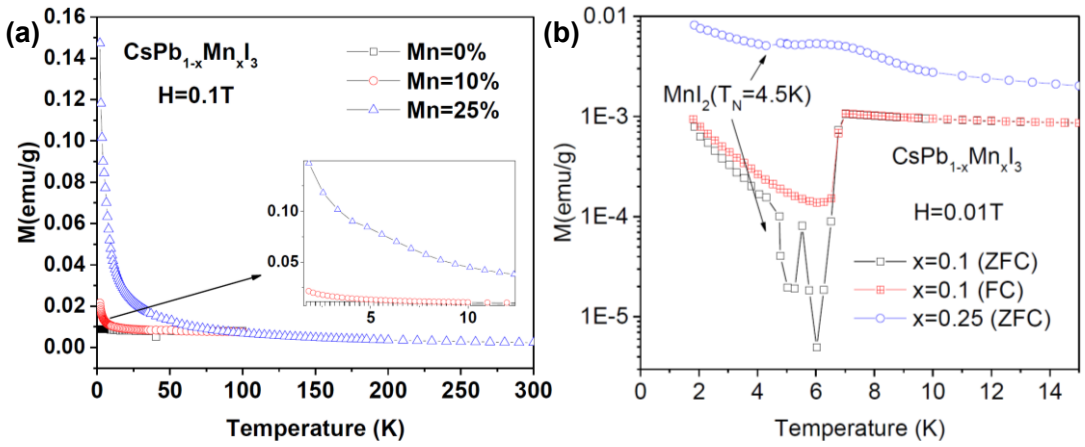


**Figure 7-7. (a) Magnetisation in a magnetic field of 0.1 T for the Mn-containing samples from room temperature to 2 K, in comparison with the control. (b) Magnetisation in a magnetic field of 0.01 T for the Mn-containing samples at cryogenic temperatures. These measurements were made by Dr Dharmalingam Prabhakaran at the University of Oxford.**

Together, these results support previous findings that $Mn^{2+}$ substitution results in interstitial incorporation of $Mn^{2+}$ in the lattice, rather than onto the B-site. The resulting increase in structural stability is then due to the increase in lattice defects, which are expected to slow the propagation of structural transitions in the crystal.

### 7.5.3 Magnesium substitution into $CsPbI_3$

For the preliminary investigation into substitution with $Mg^{2+}$ reported in this section, mixed-metal thin-films were prepared using the low-temperature route described in Chapter 6. Solution processing was possible here because Mg is stable in the desired 2+ oxidation state, and $MgI_2$ is sufficiently soluble in typical spincoating solvents, such as *N,N*-dimethylformamide (DMF).

To determine whether $Mg^{2+}$ substitution promotes major structural changes, XRD patterns for the mixed-metal films were measured while keeping the films in nitrogen atmosphere. These patterns are shown in full in Figure 7-8(a). Films with at most 10% $Mg^{2+}$ substitution show similar XRD patterns to the $CsPbI_3$ control. No change is observed in the position or FWHM of the 220 reflection up to and including 10% $Mg^{2+}$ substitution. For this reflection, maximum intensity is obtained for 5% $Mg^{2+}$ substitution. Further investigation is needed to fully understand whether this increase in peak intensity is due to increased orientation of crystallites in the film, and whether it is accompanied by changes in the film morphology.

Films with 25% and 50% $Mg^{2+}$ substitution show a different XRD pattern with significantly reduced perovskite peaks. In these patterns there are additional peaks, particularly at lower angles, which are shown in more detail in Figure 7-8(b). These low-angle peaks can be assigned to the non-perovskite polymorph δ-$CsPbI_3$, and to other stoichiometries, such as $Cs_4PbI_6$.[46] It has not been determined whether these other phases contain $Mg^{2+}$. It is also evident that there is a small amount of δ-$CsPbI_3$ present in the control sample which is not seen for 2.5-10% $Mg^{2+}$ substitution.

 

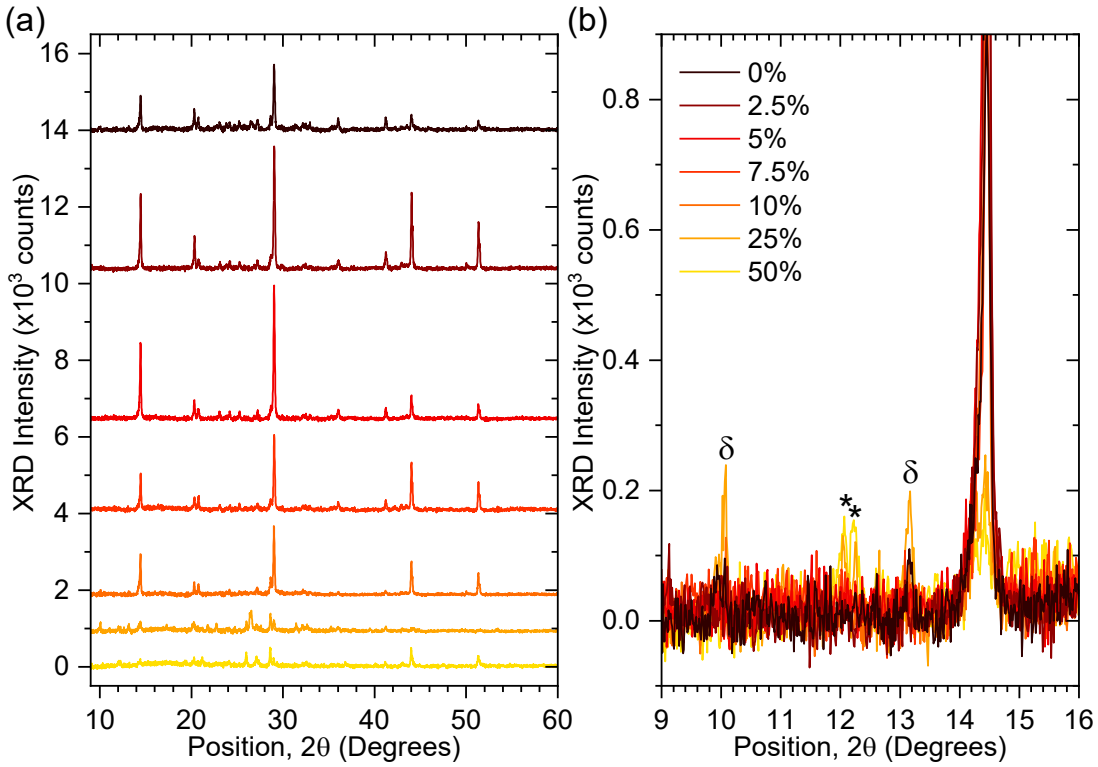


**Figure 7-8. (a) XRD patterns from thin-films of $CsPbI_3$ with various % of $Mg^{2+}$ substitution, measured and measured with Cu $K_{\alpha 1}$ radiation at 20 °C in nitrogen atmosphere by Dr Laura Miranda at Oxford PV. (b) Overlaid XRD patterns from (a), where * denotes peaks from $Cs_4PbI_6$,[46] and δ denotes peaks from a non-perovskite polymorph.**

Detection of other phases is also possible by optical methods. Figure 7-9 shows the absorption of these films, where the absorption onset of γ-$CsPbI_3$ is visible near 700 nm for all compositions. Of particular note is the peak near 375 nm which is visible for higher percentages of $Mg^{2+}$ substitution. This peak is not due to δ-$CsPbI_3$, which has an absorption peak at 415 nm (see Chapter 6 and Ref. 14). Instead, the peak at 375 nm is likely to be absorption from $Cs_4PbI_6$,[46,47] possibly with some $Mg^{2+}$ incorporated.

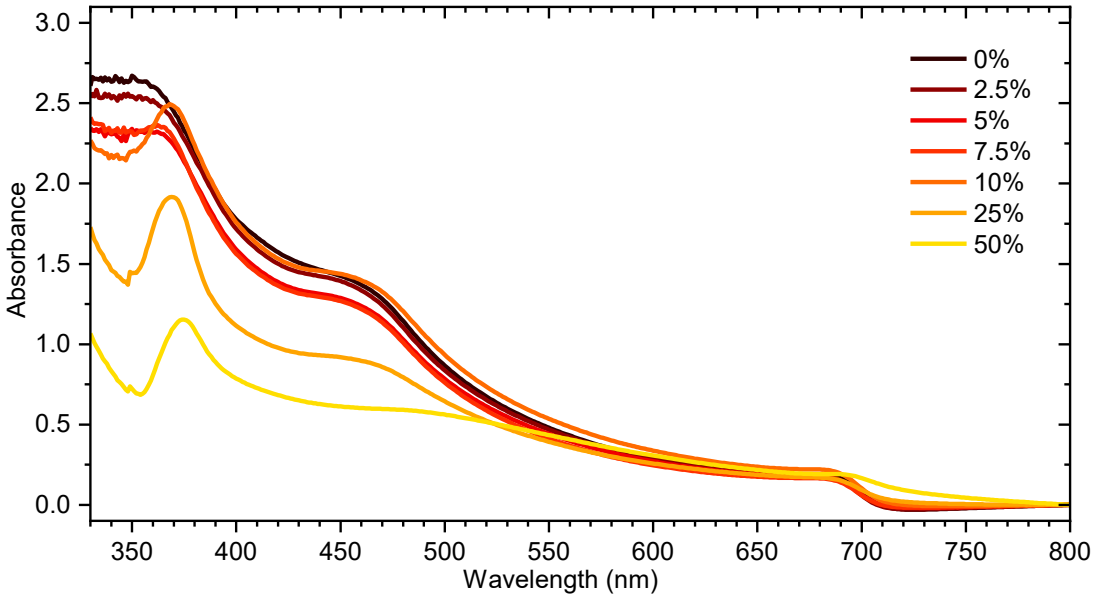


**Figure 7-9. Absorbance spectra of thin-films of $CsPbI_3$ with $Mg^{2+}$ substitution, measured in dual-beam mode, with the sample in a sealed optical cell filled with nitrogen gas.**

Further investigation is necessary to fully understand the effect of $Mg^{2+}$ substitution in $CsPbI_3$ in order to determine whether incorporation is possible through other synthetic routes. The data in this section provide no evidence to suggest that $Mg^{2+}$ incorporates into the film either on the B-site or interstitially. Instead, it seems that substitution with at least 25% $Mg^{2+}$ negates the effect of using HI as an additive to facilitate conversion to the perovskite structure. However, small amounts of $Mg^{2+}$ substitution seem beneficial for the crystallinity of the resulting film, which may lead to improved photovoltaic device performance.

Regarding the structural stability of these films, it was observed by eye that films with higher $Mg^{2+}$ content converted more rapidly to the non-perovskite polymorph when exposed to ambient humidity. However, these films already contained significant amounts of the non-perovskite polymorph. It remains to be seen whether an increase in structural stability may be possible when $Mg^{2+}$ substitution is tested by another synthetic route, such as solid state synthesis.

 

## 7.6 Feasibility of structural stabilisation by metal substitution

The experimental results in this chapter emphasise that calculating an effective value which satisfies the empirical conditions for a perovskite structure according to the Goldschmidt tolerance factor does not guarantee the formation of a stable perovskite structure, even when taking into account the covalent nature of metal-iodide bonds.[21] Several other factors must be taken into account, most importantly the ability of a given metal to form independent octahedra (e.g. not face- or edge-sharing) with the relevant halide. However, the calculations in this chapter were unable to determine whether a given metal would form octahedra with the iodide anion. It is possible that an adapted tolerance factor equation may be necessary for predicting formation of halide perovskites.[48]

Structural information from synthesised compounds may be more useful than the above calculations when considering formation of octahedra, and therefore the formation of a stable orthorhombic perovskite. It was already known that $CsCaI_3$ forms octahedra with the iodide anion in an orthorhombic perovskite polymorph (as well as a non-perovskite polymorph),[37,38] and that $CsMnI_3$ and $CsMgI_3$ form hexagonal non-perovskite structures where the octahedra are not independent.[42,43] The experimental results in this chapter are consistent with the preferences of these metals when bonding with the iodide anion. From this knowledge, it would be sensible to instead look for compounds that are known to form stable perovskite structures, preferably tetragonal or cubic. However, there are no reported perovskites with $Cs^+$ and $I^-$ where the perovskite structure is stable at ambient conditions.

Given the considerations above, it is proposed that future efforts should focus on metal substitution into mixed halide perovskites, such as $CsPbI_2Br$. As shown in this thesis, these mixed halide perovskites exhibit increased structural stability with

 

respect to the neat iodide perovskite. While the addition of bromide has been shown to increase the bandgap of the resulting perovskite, it would be possible to replace up to 50% of the iodide with bromide and retain a bandgap suitable for optoelectronic applications. Additionally, it is possible that metal substitution may lead to a reduction in octahedral tilting, with an associated reduction in bandgap, in which case the inclusion of bromide would be an advantage. As bromide is a smaller anion, the required substitution to obtain a stable perovskite structure should also be reduced compared to the neat iodide perovskite (see Figure 7-10 and Table 7-3 in the Appendix).

Of the experimental routes used in this chapter, solid state synthesis has been demonstrated to be an effective way to determine structural properties. A significant advantage of this technique, especially for these materials, is that slow cooling of the compound from the melt enables instant determination of the thermodynamically preferred polymorph: if the solid is yellow, it is likely to be a non-perovskite, but if it is dark, it is likely to be a perovskite. Subsequent XRD measurements on the resulting powder are typically of sufficient quality to obtain structural information, in contrast to XRD of thin-films where orientation effects or low sample yield from scratched powder result in lower quality data.

## 7.7 Conclusion and outlook

Stabilising the orthorhombic perovskite structure of $CsPbI_3$ and related perovskites is of central importance. In this chapter, previous approaches to stabilisation of the orthorhombic polymorph of $CsPbI_3$ were reviewed, and a rationale motivating stabilisation by metal substitution was presented. $Ca^{2+}$, $Mn^{2+}$ and $Mg^{2+}$ were evaluated experimentally for substitution onto the lead site in $CsPbI_3$ with the aim of finding a substitution that increased the atmospheric stability of the orthorhombic polymorph.

 

For substitution with $Ca^{2+}$ onto the B-site, the structural stability of the orthorhombic polymorph decreased. Increased stability with $Mn^{2+}$ substitution was observed, and attributed to interstitial incorporation of $Mn^{2+}$ into the $CsPbI_3$ lattice. $Mg^{2+}$ substitution was shown to increase the crystallinity of the perovskite thin-film, although the mechanism for this increase was not determined. Overall, this chapter has shown that structural stability of the orthorhombic polymorph of $CsPbI_3$ is very difficult to achieve by metal substitution. None of the mixed-metal compositions prepared in this study was a fully stable orthorhombic perovskite.

The results in this chapter have shown that both metal and halide substitution will be necessary to obtain a stable inorganic perovskite with bandgap between 1.8-2 eV, if this is indeed possible. Additionally, the solid state synthesis technique has been demonstrated to be an effective method for determining whether a given metal integrates into the perovskite structure, and, if so, if this incorporation results in increased stability.

In summary, this chapter provides direction towards realising a stable inorganic absorber for optoelectronic applications.

## 7.8 References


1. NREL. Best Research-Cell Efficiencies https://www.nrel.gov/pv/assets/images/efficiency-chart.png.
2. Hörantner, M. T.; Snaith, H. "Predicting and Optimising the Energy Yield of Perovskite-on-Silicon Tandem Solar Cells under Real World Conditions". *Energy Environ. Sci.* 2017.
3. Eperon, G. E.; Hörantner, M. T.; Snaith, H. J. "Metal Halide Perovskite Tandem and Multiple-Junction Photovoltaics". *Nat. Rev. Chem.* 2017, *1*, 0095.
4. Yang, Z.; Surrente, A.; Galkowski, K.; Miyata, A.; Portugall, O.; Sutton, R. J.; Haghighirad, A. A.; Snaith, H. J.; Maude, D. K.; Plochocka, P.; Nicholas, R. J. "Impact of the Halide Cage on the Electronic Properties of Fully Inorganic Cesium Lead Halide Perovskites". *ACS Energy Lett.* 2017, *2*, 1621–1627.
5. Hutter, E. M.; Sutton, R. J.; Chandrashekar, S.; Abdi-Jalebi, M.; Stranks, S. D.; Snaith, H. J.; Savenije, T. J. "Vapour-Deposited Cesium Lead Iodide Perovskites: Microsecond Charge Carrier Lifetimes and Enhanced Photovoltaic Performance". *ACS Energy Lett.* 2017, *2*, 1901–1908.


 

6. Lau, C. F. J.; Deng, X.; Zheng, J.; Kim, J.; Zhang, Z.; Zhang, M.; Bing, J.; Wilkinson, B.; Hu, L.; Patterson, R.; Huang, S.; Ho-Baillie, A. W. Y. "Enhanced Performance via Partial Lead Replacement with Calcium for $CsPbI_3$ Perovskite Solar Cell Exceeding 13% Power Conversion Efficiency". *J. Mater. Chem. A* 2018.

7. Liu, C.; Li, W.; Zhang, C.; Ma, Y.; Fan, J.; Mai, Y. "All-Inorganic $CsPbI_2Br$ Perovskite Solar Cells with High Efficiency Exceeding 13%". *J. Am. Chem. Soc.* 2018, jacs.7b13229.

8. Dastidar, S.; Hawley, C. J.; Dillon, A. D.; Gutierrez-Perez, A. D.; Spanier, J. E.; Fafarman, A. T. "Quantitative Phase-Change Thermodynamics and Metastability of Perovskite-Phase Cesium Lead Iodide". *J. Phys. Chem. Lett.* 2017, *8*, 1278–1282.

9. Møller, C. K. "The Structure of Perovskite-Like Cæsium Plumbo Trihalides". *Mat. Fys. Medd. Dan. Vid. Selsk.* 1959, *32*.

10. Heidrich, K.; Künzel, H.; Treusch, J. "Optical Properties and Electronic Structure of $CsPbCl_3$ and $CsPbBr_3$". *Solid State Commun.* 1978, *25*, 887–889.

11. Fröhlich, D.; Heidrich, K.; Künzel, H.; Trendel, G.; Treusch, J. "Cesium-Trihalogen-Plumbates a New Class of Ionic Semiconductors". *J. Lumin.* 1979, *18-19*, 385–388.

12. Linaburg, M. R.; McClure, E. T.; Majher, J. D.; Woodward, P. M. "$Cs_{1-x}Rb_xPbCl_3$ and $Cs_{1-x}Rb_xPbBr_3$ Solid Solutions: Understanding Octahedral Tilting in Lead Halide Perovskites". *Chem. Mater.* 2017, *29*, 3507–3514.

13. Berastegui, P.; Hull, S.; Eriksson, S.-G. "A Low-Temperature Structural Phase Transition in $CsPbF_3$". *J. Phys. Condens. Matter* 2001, *13*, 5077–5088.

14. Eperon, G. E.; Paternò, G. M.; Sutton, R. J.; Zampetti, A.; Haghighirad, A. A.; Cacialli, F.; Snaith, H. J. "Inorganic Caesium Lead Iodide Perovskite Solar Cells". *J. Mater. Chem. A* 2015, *3*, 19688–19695.

15. Sutton, R. J.; Eperon, G. E.; Miranda, L.; Parrott, E. S.; Kamino, B. A.; Patel, J. B.; Hörantner, M. T.; Johnston, M. B.; Haghighirad, A. A.; Moore, D. T.; Snaith, H. J. "Bandgap-Tunable Cesium Lead Halide Perovskites with High Thermal Stability for Efficient Solar Cells". *Adv. Energy Mater.* 2016, *6*, 1502458.

16. Beal, R. E.; Slotcavage, D. J.; Leijtens, T.; Bowring, A. R.; Belisle, R. A.; Nguyen, W. H.; Burkhard, G.; Hoke, E. T.; McGehee, M. D. "Cesium Lead Halide Perovskites with Improved Stability for Tandem Solar Cells.". *J. Phys. Chem. Lett.* 2016, 746–751.

17. Lin, J.; Lai, M.; Dou, L.; Kley, C. S.; Chen, H.; Peng, F.; Sun, J.; Lu, D.; Hawks, S. A.; Xie, C.; Cui, F.; Alivisatos, A. P.; Limmer, D. T.; Yang, P. "Thermochromic Halide Perovskite Solar Cells". *Nat. Mater.* 2018, 1.

18. Lau, C. F. J.; Deng, X.; Ma, Q.; Zheng, J.; Yun, J. S.; Green, M. A.; Huang, S.; Ho-Baillie, A. W. Y. "$CsPbIBr_2$ Perovskite Solar Cell by Spray-Assisted Deposition". *ACS Energy Lett.* 2016, *1*, 573–577.

19. McMeekin, D. P.; Sadoughi, G.; Rehman, W.; Eperon, G. E.; Saliba, M.; Horantner, M. T.; Haghighirad, A.; Sakai, N.; Korte, L.; Rech, B.; Johnston, M. B.; Herz, L. M.; Snaith, H. J. "A Mixed-Cation Lead Mixed-Halide Perovskite Absorber for Tandem Solar Cells". *Science* 2016, *351*, 151–155.


 

20. Eperon, G. E.; Stranks, S. D.; Menelaou, C.; Johnston, M. B.; Herz, L. M.; Snaith, H. J. "Formamidinium Lead Trihalide: A Broadly Tunable Perovskite for Efficient Planar Heterojunction Solar Cells". *Energy Environ. Sci.* 2014, *7*, 982.

21. Travis, W.; Glover, E. N. K.; Bronstein, H.; Scanlon, D. O.; Palgrave, R. G. "On the Application of the Tolerance Factor to Inorganic and Hybrid Halide Perovskites: A Revised System". *Chem. Sci.* 2016, *7*, 4548–4556.

22. Kieslich, G.; Sun, S.; Cheetham, T. "Solid-State Principles Applied to Organic-Inorganic Perovskites: New Tricks for an Old Dog". *Chem. Sci.* 2014, *5*, 4712–4715.

23. Li, Z.; Yang, M.; Park, J.-S.; Wei, S.-H.; Berry, J.; Zhu, K. "Stabilizing Perovskite Structures by Tuning Tolerance Factor: Formation of Formamidinium and Cesium Lead Iodide Solid-State Alloys". *Chem. Mater.* 2015, acs.chemmater.5b04107.

24. Yi, C.; Luo, J.; Meloni, S.; Boziki, A.; Ashari-Astani, N.; Grätzel, C.; Zakeeruddin, S. M.; Röthlisberger, U.; Grätzel, M. "Entropic Stabilization of Mixed A-Cation $ABX_3$ Metal Halide Perovskites for High Performance Perovskite Solar Cells". *Energy Environ. Sci.* 2016, *9*, 656–662.

25. Swarnkar, A.; Mir, W. J.; Nag, A. "Can B-Site Doping or Alloying Improve Thermal- and Phase-Stability of All-Inorganic $CsPbX_3$ (X = Cl, Br, I) Perovskites?". *ACS Energy Lett.* 2018, 286–289.

26. Woodward, P. M. "Octahedral Tilting in Perovskites. II. Structure Stabilizing Forces". *Acta Crystallogr. Sect. B Struct. Sci.* 1997, *53*, 44–66.

27. Klug, M. T.; Osherov, A.; Haghighirad, A. A.; Stranks, S. D.; Brown, P. R.; Bai, S.; Wang, J. T.-W.; Dang, X.; Bulović, V.; Snaith, H. J.; Belcher, A. M. "Tailoring Metal Halide Perovskites through Metal Substitution: Influence on Photovoltaic and Material Properties". *Energy Environ. Sci.* 2017, *131*, 6050–6051.

28. Zhao, W.; Yang, D.; Yang, Z.; Liu, S. (Frank). "Zn-Doping for Reduced Hysteresis and Improved Performance of Methylammonium Lead Iodide Perovskite Hybrid Solar Cells". *Mater. Today Energy* 2017, *5*, 205–213.

29. Eperon, G. E.; Leijtens, T.; Bush, K. A.; Prasanna, R.; Green, T.; Wang, J. T.-W.; McMeekin, D. P.; Volonakis, G.; Milot, R. L.; May, R.; Palmstrom, A.; Slotcavage, D. J.; Belisle, R. A.; Patel, J. B.; Parrott, E. S.; Sutton, R. J.; Ma, W.; Moghadam, F.; Conings, B.; et al. "Perovskite-Perovskite Tandem Photovoltaics with Optimized Band Gaps". *Science* 2016, *354*, 861–865.

30. Akkerman, Q. A.; Meggiolaro, D.; Dang, Z.; De Angelis, F.; Manna, L. "Fluorescent Alloy $CsPb_xMn_{1-x}I_3$ Perovskite Nanocrystals with High Structural and Optical Stability". *ACS Energy Lett.* 2017, 2183–2186.

31. Guria, A. K.; Dutta, S. K.; Adhikari, S. Das; Pradhan, N. "Doping $Mn^{2+}$ in Lead Halide Perovskite Nanocrystals: Successes and Challenges". *ACS Energy Lett.* 2017, *2*, 1014–1021.

32. Liu, W.; Lin, Q.; Li, H.; Wu, K.; Robel, I.; Pietryga, J. M.; Klimov, V. I. "$Mn^{2+}$-Doped Lead Halide Perovskite Nanocrystals with Dual-Color Emission Controlled by Halide Content". *J. Am. Chem. Soc.* 2016, *138*, 14954–14961.

33. Bai, D.; Zhang, J.; Jin, Z.; Bian, H.; Wang, K.; Wang, H.; Liang, L.; Wang, Q.; Liu, S. F. "Interstitial $Mn^{2+}$-Driven High-Aspect-Ratio Grain Growth for Low-Trap-

 

Density Microcrystalline Films for Record Efficiency $CsPbI_2Br$ Solar Cells". *ACS Energy Lett.* 2018, 970–978.

34. Goldschmidt, V. M. "Die Gesetze Der Krystallochemie". *Naturwissenschaften* 1926, *14*, 477–485.

35. Shannon, R. D. "Revised Effective Ionic Radii and Systematic Studies of Interatomic Distances in Halides and Chalcogenides". *Acta Crystallogr. Sect. A* 1976, *32*, 751–767. Available at http://abulafia.mt.ic.ac.uk/shannon/ptable.php.

36. Sharma, S.; Weiden, N.; Weiss, A. "Phase Diagrams of Quasibinary Systems of the Type: $ABX_3$ — $A'BX_3$; $ABX_3$ — $AB'X_3$, and $ABX_3$ — $ABX'_3$; X = Halogen". *Zeitschrift für Phys. Chemie* 1992, *175*, 63–80.

37. Schilling, G.; Kunert, C.; Schleid, T.; Meyer, G. "Metallothermische Reduktion Der Tribromide Und -Iodide von Thulium Und Ytterbium Mit Alkalimetallen". *Zeitschrift für Anorg. und Allg. Chemie* 1992, *618*, 7–12.

38. Schilling, G.; Meyer, G. "Ternäre Bromide Und Iodide Zweiwertiger Lanthanide Und Ihre Erdalkali-Analoga Vom Typ $AMX_3$ Und $AM_2X_5$ (Ternary Bromides and Iodides of Divalent Lanthanides and Their Alkaline-Earth Analoga of the Type $AMX_3$ Und $AM_2X_5$)". *Zeitschrift für Anorg. und Allg. Chemie* 1996, *622*, 759–765.

39. Stoumpos, C. C.; Malliakas, C. D.; Peters, J. A.; Liu, Z.; Sebastian, M.; Im, J.; Chasapis, T. C.; Wibowo, A. C.; Chung, D. Y.; Freeman, A. J.; Wessels, B. W.; Kanatzidis, M. G. "Crystal Growth of the Perovskite Semiconductor $CsPbBr_3$: A New Material for High-Energy Radiation Detection". *Cryst. Growth Des.* 2013, *13*, 2722–2727.

40. Krishnamoorthy, T.; Ding, H.; Yan, C.; Leong, W. L.; Baikie, T.; Zhang, Z.; Sherburne, M.; Li, S.; Asta, M.; Mathews, N.; Mhaisalkar, S. G. "Lead-Free Germanium Iodide Perovskite Materials for Photovoltaic Applications". *J. Mater. Chem. A* 2015, *3*, 23829–23832.

41. Stoumpos, C. C.; Frazer, L.; Clark, D. J.; Kim, Y. S.; Rhim, S. H.; Freeman, A. J.; Ketterson, J. B.; Jang, J. I.; Kanatzidis, M. G. "Hybrid Germanium Iodide Perovskite Semiconductors: Active Lone Pairs, Structural Distortions, Direct and Indirect Energy Gaps, and Strong Nonlinear Optical Properties". *J. Am. Chem. Soc.* 2015, *137*, 6804–6819.

42. McPherson, G. L.; McPherson, A. M.; Atwood, J. L. "Structures of $CsMgBr_3$, $CsCdBr_3$ and $CsMgI_3$— Diamagnetic Linear Chain Lattices". *J. Phys. Chem. Solids* 1980, *41*, 495–499.

43. Zandbergen, H. W. "Neutron Powder Diffraction and Magnetic Measurements on $CsMnI_3$". *J. Solid State Chem.* 1980, *35*, 367–375.

44. Kurihama, T.; Shimizu, F.; Izumi, T. "Powder X-Ray Diffraction Study of $Cs_2CoI_4$ from Room Temperature down to 40 K". *Ferroelectrics* 1998, *217*, 91–98.

45. Loyd, M.; Lindsey, A.; Stand, L.; Zhuravleva, M.; Melcher, C. L.; Koschan, M. "Tuning the Structure of $CsCaI_3$:Eu via Substitution of Bromine for Iodine". *Opt. Mater. (Amst).* 2017, *68*, 47–52.

46. Luo, P.; Xia, W.; Zhou, S.; Sun, L.; Cheng, J.; Xu, C.; Lu, Y. "Solvent Engineering for Ambient-Air-Processed, Phase-Stable $CsPbI_3$ in Perovskite Solar Cells". *J. Phys. Chem. Lett.* 2016, *7*, 3603–3608.

 

47. Kondo, S.; Masaki, A.; Saito, T.; Asada, H. "Fundamental Optical Absorption of $CsPbI_3$ and $Cs_4PbI_6$". *Solid State Commun.* 2002, *124*, 211–214.

48. Bartel, C. J.; Sutton, C.; Goldsmith, B. R.; Ouyang, R.; Musgrave, C. B.; Ghiringhelli, L. M.; Scheffler, M. "New Tolerance Factor to Predict the Stability of Perovskite Oxides and Halides".

49. Sjövall, R.; Svensson, C.; IUCr. "Refinement of Three Caesium Mercury Iodides, $Cs_2Hg_3I_8.H_2O$, $Cs_2HgI_4$ and $Cs_3HgI_5$". *Acta Crystallogr. Sect. C Cryst. Struct. Commun.* 1988, *44*, 207–210.

50. Wells, H. L. "On the Caesium-Mercuric Halides". *Am. J. Sci.* 1892, *3*, 221.

51. Sjövall, R.; Svensson, C.; Lidin, S. "X-Ray Study of $CsCdI_3{\cdot}H_2O$". *Zeitschrift für Krist. - Cryst. Mater.* 1996, *211*.

52. Bansal, S.; Chiu, M. "Atmospherically Processed and Stable Cs-Pb Based Perovskite Solar Cells". *MRS Adv.* 2017, 1–8.

53. Nam, J. K.; Jung, M. S.; Chai, S. U.; Choi, Y. J.; Kim, D.; Park, J. H. "Unveiling the Crystal Formation of Cesium Lead Mixed-Halide Perovskites for Efficient and Stable Solar Cells". *J. Phys. Chem. Lett.* 2017, 2936–2940.

54. Di, X.; Jiang, J.; Hu, Z.; Zhou, L.; Li, P.; Liu, S.; Xiang, W.; Liang, X. "Stable and Brightly Luminescent All-Inorganic Cesium Lead Halide Perovskite Quantum Dots Coated with Mesoporous Silica for Warm WLED". *Dye. Pigment.* 2017, *146*, 361–367.

55. Liu, S.; Luo, Y.; He, M.; Liang, X.; Xiang, W. "Novel $CsPbI_3$ QDs Glass with Chemical Stability and Optical Properties". *J. Eur. Ceram. Soc.* 2018, *38*, 1998–2004.

56. Liao, J.-F.; Rao, H.-S.; Chen, B.-X.; Kuang, D.-B.; Su, C.-Y.; Chan, H. L.; Yan, F.; Kanatzidis, M. G.; Boix, P. P.; Mhaisalkar, S. G.; Snaith, H. J.; Eveb, J.; Alam, M. A.; Gupta, G.; Lou, J.; Ajayan, P. M.; Bedzyk, M. J.; Kanatzidis, M. G.; Mohite, A. D. "Dimension Engineering on Cesium Lead Iodide for Efficient and Stable Perovskite Solar Cells". *J. Mater. Chem. A* 2017, *5*, 2066–2072.

57. Fu, Y.; Rea, M. T.; Chen, J.; Morrow, D. J.; Hautzinger, M. P.; Zhao, Y.; Pan, D.; Manger, L. H.; Wright, J. C.; Goldsmith, R. H.; Jin, S. "Selective Stabilization and Photophysical Properties of Metastable Perovskite Polymorphs of $CsPbI_3$ in Thin Films". *Chem. Mater.* 2017, *29*, 8385–8394.

58. Sun, J.-Y.; Rabouw, F. T.; Yang, X.-F.; Huang, X.-Y.; Jing, X.-P.; Ye, S.; Zhang, Q.-Y. "Facile Two-Step Synthesis of All-Inorganic Perovskite $CsPbX_3$ (X = Cl, Br, and I) Zeolite-Y Composite Phosphors for Potential Backlight Display Application". *Adv. Funct. Mater.* 2017, 1704371.

59. Waleed, A.; Tavakoli, M. M.; Gu, L.; Hussain, S.; Zhang, D.; Poddar, S.; Wang, Z.; Zhang, R.; Fan, Z. "All Inorganic Cesium Lead Iodide Perovskite Nanowires with Stabilized Cubic Phase at Room Temperature and Nanowire Array-Based Photodetectors". *Nano Lett.* 2017, *17*, 4951–4957.

60. Wang, Q.; Zheng, X.; Deng, Y.; Zhao, J.; Chen, Z.; Huang, J. "Stabilizing the α-Phase of $CsPbI_3$ Perovskite by Sulfobetaine Zwitterions in One-Step Spin-Coating Films". *Joule* 2017, *1*, 371–382.

61. Swarnkar, A.; Marshall, A. R.; Sanehira, E. M.; Chernomordik, B. D.; Moore, D. T.; Christians, J. A.; Chakrabarti, T.; Luther, J. M. "Quantum Dot-Induced Phase

 

Stabilization of α-$CsPbI_3$ Perovskite for High-Efficiency Photovoltaics". *Science* 2016, *354*, 92–95.

62. Wang, C.; Chesman, A. S. R.; Jasieniak, J. J. "Stabilizing the Cubic Perovskite Phase of $CsPbI_3$ Nanocrystals by Using an Alkyl Phosphinic Acid". *Chem. Commun.* 2017, *53*, 232–235.

63. Nam, J. K.; Chai, S. U.; Cha, W.; Choi, Y. J.; Kim, W.; Jung, M. S.; Kwon, J.; Kim, D.; Park, J. H. "Potassium Incorporation for Enhanced Performance and Stability of Fully Inorganic Cesium Lead Halide Perovskite Solar Cells". *Nano Lett.* 2017, *17*, 2028–2033.

64. Hu, Y.; Bai, F.; Liu, X.; Ji, Q.; Miao, X.; Qiu, T.; Zhang, S. "Bismuth Incorporation Stabilized α-$CsPbI_3$ for Fully Inorganic Perovskite Solar Cells". *ACS Energy Lett.* 2017, *2*, 2219–2227.

65. Ma, Q.; Huang, S.; Chen, S.; Zhang, M.; Lau, C. F. J.; Lockrey, M. N.; Mulmudi, H. K.; Shan, Y.; Yao, J.; Zheng, J.; Deng, X.; Catchpole, K.; Green, M. A.; Ho-Baillie, A. W. Y. "The Effect of Stoichiometry on the Stability of Inorganic Cesium Lead Mixed-Halide Perovskites Solar Cells". *J. Phys. Chem. C* 2017, acs.jpcc.7b06268.

66. Dastidar, S.; Egger, D. A.; Tan, L. Z.; Cromer, S. B.; Dillon, A. D.; Liu, S.; Kronik, L.; Rappe, A. M.; Fafarman, A. T. "High Chloride Doping Levels Stabilize the Perovskite Phase of Cesium Lead Iodide". *Nano Lett.* 2016, *16*, 3563–3570.

 

# 7.9 Appendices

## 7.9.1 Tolerance factors for metals 'M' in $CsMI_3$: Shannon radii

The tolerance factors for metals 'M' occupying the B-site in $CsMI_3$ are given in Table 7-2 for Shannon's ionic radii of the metals. Here any metal larger than and including Cd satisfies the requirement of an octahedral factor $\mu > 0.41$. Any metal smaller than and including Yb will satisfy the tolerance factor for the formation of a perovskite. This gives the following range of possible metals for $CsMI_3$: Cd, Ca, Hg, and Yb. However, $CsCdI_3$ and $CsHgI_3$ do not form perovskite structures.[49–51]

**Table 7-2. Tolerance factors calculated using Shannon radii for metals 'M' occupying the B-site in $CsMI_3$, where the Shannon radii are taken from Refs 21 and 35. HS denotes high spin.**

| B-site Metal M | Shannon Radii | Octahedral factor μ | Tolerance factor for $CsMI_3$ |
|---|---|---|---|
| Ni | 0.69 | 0.31 | 1.00 |
| Mg | 0.72 | 0.33 | 0.99 |
| Cu | 0.73 | 0.33 | 0.98 |
| Ge | 0.73 | 0.33 | 0.98 |
| Zn | 0.74 | 0.34 | 0.98 |
| Co (HS) | 0.75 | 0.34 | 0.98 |
| Fe (HS) | 0.78 | 0.35 | 0.97 |
| V | 0.79 | 0.36 | 0.96 |
| Cr (HS) | 0.80 | 0.36 | 0.96 |
| Mn (HS) | 0.83 | 0.38 | 0.95 |
| Ti | 0.86 | 0.39 | 0.94 |
| Cd | 0.95 | 0.43 | 0.92 |
| Ca | 1.00 | 0.45 | 0.90 |
| Hg | 1.02 | 0.46 | 0.90 |
| Yb | 1.02 | 0.46 | 0.90 |
| Tm | 1.03 | 0.47 | 0.89 |
| Dy | 1.07 | 0.49 | 0.88 |
| Sn | 1.15 | 0.52 | 0.86 |
| Sr | 1.16 | 0.53 | 0.86 |
| Eu | 1.17 | 0.53 | 0.86 |
| **Pb** | **1.19** | **0.54** | **0.85** |
| Sm | 1.22 | 0.55 | 0.84 |

### 7.9.2 Metal substitution percentages for $CsPbI_2Br$

Figure 7-10 shows the required substitution percentage of $CsMI_2Br$ into $CsPbI_2Br$ for a given overall tolerance factor of the resulting mixed-metal compound. Here effective radii for the metals and for the halide are calculated using a 2:1 ratio of iodide to bromide. Here, the metal substitution percentages required for a stability criterion of $t \geq 0.89$ are smaller by about a third for $CsPbI_2Br$.

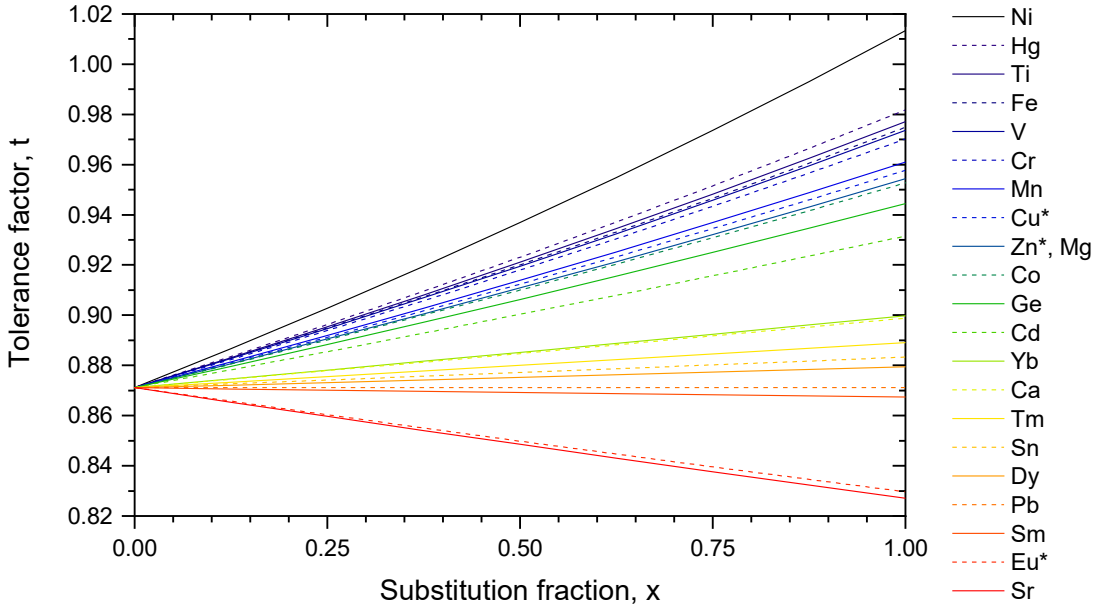


**Figure 7-10. Graphical representation of the required substitution of $CsMI_2Br$ into $CsPbI_2Br$ for a desired overall tolerance factor. Exact percentages for some values of $t$ are provided in Table 7-3, along with the effective radii of the metals used in the calculations.**

**Table 7-3. Substitution percentages of $CsMI_2Br$ into $CsPbI_2Br$ for the overall tolerance factor of 0.892, listed in order of increasing ionic radius for iodide. Revised radii are taken from Travis *et al.*[21] where possible, and otherwise Shannon radii are used (denoted by *).[35] These values are used to calculate effective radii for the metal ions in the mixed halide compound, as well as the relative size compared with the $Pb^{2+}$ cation. Only ions smaller than $Pb^{2+}$ are shown.**

| B-site Metal | Revised ionic radii for iodide compounds | Revised ionic radii for bromide compounds | Effective ionic radii for $I_2Br$ compounds | $R_{Pb} - R_M$ | x (%) t = 0.892 |
|---|---|---|---|---|---|
| Ni | 0.57 | 0.58 | 0.57 | 0.44 | 16.7 |
| Hg | 0.61 | 0.76 | 0.66 | 0.35 | 20.8 |
| Ti | 0.66 | 0.7 | 0.67 | 0.34 | 21.6 |
| V | 0.68 | 0.69 | 0.68 | 0.33 | 22.2 |
| Cr | 0.68 | 0.72 | 0.69 | 0.32 | 22.9 |
| Fe | 0.68 | 0.68 | 0.68 | 0.33 | 22.0 |
| Mn | 0.72 | 0.72 | 0.72 | 0.29 | 25.0 |
| Cu | 0.73* | 0.73* | 0.73 | 0.28 | 25.9 |
| Zn | 0.74* | 0.74* | 0.74 | 0.27 | 26.8 |
| Co | 0.745 | 0.745 | 0.75 | 0.27 | 27.3 |
| Mg | 0.75 | 0.72 | 0.74 | 0.27 | 26.8 |
| Ge | 0.77 | *0.77** | 0.77 | 0.24 | 30.1 |
| Cd | 0.81 | 0.81 | 0.81 | 0.2 | 36.1 |
| Ca | 0.92 | 0.91 | 0.92 | 0.1 | 75.9 |
| Yb | 0.93 | 0.88 | 0.91 | 0.1 | 73.3 |
| Tm | 0.95 | *0.95** | 0.95 | 0.06 | — |
| Sn | 0.97 | *0.97** | 0.97 | 0.04 | — |
| Dy | 0.97 | 1.01 | 0.98 | 0.03 | — |
| Pb | 1.03 | 0.98 | 1.01 | 0 | — |

# 8 Conclusion

## 8.1 Summary and future perspective

The work in this thesis has presented several important steps towards the development of stable inorganic metal halide perovskite materials for optoelectronic applications, with a particular focus on photovoltaics.

Metal halide perovskite materials have been proposed for use in a wide range of cutting-edge technologies, such as photovoltaics, light emitting diodes, lasers, photodetectors, and transistors.[1–4] Regarding photovoltaic applications, power conversion efficiencies for solar cells utilising hybrid organic-inorganic metal halide perovskites continue to increase.[5] However, issues remain with the chemical stability of the perovskite material itself due to the unstable organic component.[6–9] As an approach to increasing the chemical stability of these materials, this thesis investigated full replacement of the organic component with $Cs^+$.

Of the known inorganic metal halide perovskites, $CsPbI_3$ was considered for photovoltaic applications as it has a bandgap of ~1.74 eV.[10] However, this material adopts a yellow non-perovskite polymorph at ambient conditions,[11] with maintenance of the perovskite polymorph only in inert atmosphere, and consequently device efficiencies had reached only 2.9%.[10] In contrast, $CsPbBr_3$ is stable in a perovskite structure at ambient conditions but its wider bandgap is less desirable for single-junction photovoltaics.[12]

As an optimal balance between $CsPbI_3$ and $CsPbBr_3$, Chapter 4 presented the mixed-halide perovskite $CsPbI_2Br$ as a stable perovskite absorber with an ideal bandgap of 1.92 eV for multi-junction photovoltaics. This perovskite was demonstrated to be more structurally stable than $CsPbI_3$ when exposed to ambient moisture, and more compositionally stable than the hybrid perovskite $MAPbI_2Br$ when subjected to thermal stressing at 85 °C. Importantly, the first photovoltaic devices were reported with $CsPbI_2Br$ as the perovskite absorber, with promising J-V scan efficiencies up to 9.8% even with some processing steps in air. The success of the work in this chapter drew the attention of a wide range of science communities to the inorganic perovskites, and further optimisation of solar cells utilising $CsPbI_2Br$ and $CsPbI_3$ has led to efficiencies over 13%.[13,14] Chapter 5 further extended the understanding of the fundamental optoelectronic properties of $CsPbI_{3-x}Br_x$ ($0 \leq x \leq 3$). Specifically, the exciton binding energies, reduced masses, and dielectric constants of $CsPbI_3$, $CsPbI_2Br$ and $CsPbBr_3$ were determined, and found to be comparable to those of the equivalent hybrid perovskites. These fundamental properties emphasised that the limited photovoltaic performance of $CsPbI_2Br$ in particular is due both to insufficient research effort and to the challenge of maintaining the perovskite polymorph in the presence of ambient moisture.

In order to achieve structural stability of the perovskite polymorph of $CsPbI_{3-x}Br_x$, a comprehensive understanding of the polymorphs adopted by these materials is required, along with their relative stability. The polymorph of $CsPbI_3$ and $CsPbI_{3-x}Br_x$ (where $x$ is small) adopted by black thin-films when cooled to room temperature was widely assumed to be the cubic polymorph, as only the structures of the yellow non-perovskite and black cubic polymorphs had been reported with full structural refinement for $CsPbI_3$. However, cubic perovskites usually show symmetry lowering when cooled, which was not evident in the temperature-dependent measurements on black $CsPbI_{3-x}Br_x$ thin-films in Chapter 5. In Chapter 6, the

 

structure of these black thin-films at room temperature was investigated using the neat $CsPbI_3$ perovskite as a model system, as structural refinement is much more complex for mixed-halide compositions. Rather than a cubic perovskite, black thin-films and powders of $CsPbI_3$ were found to adopt an orthorhombic perovskite structure at room temperature, with preferential orientation in the thin-films when prepared from the cubic polymorph. Furthermore, formation energy calculations provided a theoretical basis for the experimental finding that the orthorhombic polymorph is the most stable of the perovskite polymorphs, but metastable in comparison to the non-perovskite polymorph. This agreement of theory and experiment supports the predictivity of these formation energy calculations for the development of structurally-stable perovskites.

While some gains in structural stability of the orthorhombic perovskite polymorph were found possible through halide substitution, this approach was unable to fully stabilise this polymorph for $CsPbI_{3-x}Br_x$ with narrow band gaps ($<2$ eV) for photovoltaic application(s). As an alternative approach, Chapter 7 proposed B-site metal substitution as a theoretical means for achieving structural stability. To assess the validity of this approach, three nontoxic and earth-abundant metals, $Ca^{2+}$, $Mn^{2+}$, and $Mg^{2+}$, were chosen for experimentation. Of the three metals, $Ca^{2+}$ substitution was found to substitute onto the B-site as expected, although without the desired increase in structural stability. In contrast, $Mn^{2+}$ was not found to substitute onto the B-site, but was found to incorporate into the lattice interstitially, with an increase in structural stability. $Mg^{2+}$ substitution was shown to increase the crystallinity of thin-films of $CsPbI_3$. However, none of the three metals was found to promote the preferential adoption of the perovskite polymorph over the non-perovskite polymorph.

In conclusion, inorganic metal halide perovskites have been demonstrated as promising candidates for many optoelectronic applications. Through the full

 

replacement of the organic cation with $Cs^+$, significant gains in chemical stability have been made in comparison to the organic-inorganic hybrid perovskites, without compromising on fundamental optoelectronic properties. Hence with further research it should be possible to achieve comparable power conversion efficiencies to those of the organic-inorganic hybrid perovskites.

However, for commercial application of inorganic metal halide perovskites, full stabilisation of the orthorhombic perovskite polymorph of $CsPbI_{3-x}Br_x$ is the most pressing concern. This thesis has shown that this task is not straightforward. Some structural stabilisation has been achieved with halide substitution, and separately with B-site metal substitution. While independently neither approach is able to fully stabilise the orthorhombic perovskite polymorph of $CsPbI_{3-x}Br_x$, it is postulated that through both approaches together a mixed-metal mixed-halide composition may be found with a perovskite structure that is stable at ambient conditions. With the findings in this thesis as a guide, further research should yield such compositions with both structural stability and excellent optoelectronic properties.

## 8.2 References


1. Grätzel, M. "The Light and Shade of Perovskite Solar Cells". *Nat. Mater.* 2014, *13*, 838–842.
2. Stranks, S. D.; Snaith, H. J. "Metal-Halide Perovskites for Photovoltaic and Light-Emitting Devices". *Nat. Nanotechnol.* 2015, *10*, 391–402.
3. Zhao, Y.; Zhu, K. "Organic–inorganic Hybrid Lead Halide Perovskites for Optoelectronic and Electronic Applications". *Chem. Soc. Rev.* 2016.
4. Sutherland, B. R.; Sargent, E. H. "Perovskite Photonic Sources". *Nat. Photonics* 2016, *10*, 295–302.
5. NREL. Best Research-Cell Efficiencies https://www.nrel.gov/pv/assets/images/efficiency-chart.png.
6. Niu, G.; Guo, X.; Wang, L. "Review of Recent Progress in Chemical Stability of Perovskite Solar Cells". *J. Mater. Chem. A* 2015, *3*, 8970–8980.
7. Patel, J. B.; Milot, R. L.; Wright, A. D.; Herz, L. M.; Johnston, M. B. "Formation Dynamics of $CH_3NH_3PbI_3$ Perovskite Following Two-Step Layer Deposition". *J. Phys. Chem. Lett.* 2016, *7*, 96–102.
8. Sutton, R. J.; Eperon, G. E.; Miranda, L.; Parrott, E. S.; Kamino, B. A.; Patel, J. B.; Hörantner, M. T.; Johnston, M. B.; Haghighirad, A. A.; Moore, D. T.; Snaith, H. J.


 

"Bandgap-Tunable Cesium Lead Halide Perovskites with High Thermal Stability for Efficient Solar Cells". *Adv. Energy Mater.* 2016, *6*, 1502458.

9. Leijtens, T.; Bush, K.; Cheacharoen, R.; Beal, R.; Bowring, A.; McGehee, M. D. "Towards Enabling Stable Lead Halide Perovskite Solar Cells; Interplay between Structural, Environmental, and Thermal Stability". *J. Mater. Chem. A* 2017, *5*, 11483–11500.
10. Eperon, G. E.; Paternò, G. M.; Sutton, R. J.; Zampetti, A.; Haghighirad, A. A.; Cacialli, F.; Snaith, H. J. "Inorganic Caesium Lead Iodide Perovskite Solar Cells". *J. Mater. Chem. A* 2015, *3*, 19688–19695.
11. Trots, D. M.; Myagkota, S. V. "High-Temperature Structural Evolution of Caesium and Rubidium Triiodoplumbates". *J. Phys. Chem. Solids* 2008, *69*, 2520–2526.
12. Stoumpos, C. C.; Malliakas, C. D.; Peters, J. A.; Liu, Z.; Sebastian, M.; Im, J.; Chasapis, T. C.; Wibowo, A. C.; Chung, D. Y.; Freeman, A. J.; Wessels, B. W.; Kanatzidis, M. G. "Crystal Growth of the Perovskite Semiconductor $CsPbBr_3$: A New Material for High-Energy Radiation Detection". *Cryst. Growth Des.* 2013, *13*, 2722–2727.
13. Lau, C. F. J.; Deng, X.; Zheng, J.; Kim, J.; Zhang, Z.; Zhang, M.; Bing, J.; Wilkinson, B.; Hu, L.; Patterson, R.; Huang, S.; Ho-Baillie, A. W. Y. "Enhanced Performance via Partial Lead Replacement with Calcium for $CsPbI_3$ Perovskite Solar Cell Exceeding 13% Power Conversion Efficiency". *J. Mater. Chem. A* 2018.
14. Liu, C.; Li, W.; Zhang, C.; Ma, Y.; Fan, J.; Mai, Y. "All-Inorganic $CsPbI_2Br$ Perovskite Solar Cells with High Efficiency Exceeding 13%". *J. Am. Chem. Soc.* 2018, jacs.7b13229.

 

# 9 Appendices



 

# Publications

By date order, descending:

Sutton, R. J.; Filip, M. R.; Haghighirad, A. A.; Sakai, N.; Wenger, B.; Giustino, F.; Snaith, H. J. "Cubic or Orthorhombic? Revealing the Crystal Structure of Metastable Black-Phase $CsPbI_3$ by Theory and Experiment". *ACS Energy Lett.* 2018, *3*, 1787–1794.

Hutter, E. M.; Sutton, R. J.; Chandrashekar, S.; Abdi-Jalebi, M.; Stranks, S. D.; Snaith, H. J.; Savenije, T. J. "Vapour-Deposited Cesium Lead Iodide Perovskites: Microsecond Charge Carrier Lifetimes and Enhanced Photovoltaic Performance". *ACS Energy Lett.* 2017, *2*, 1901–1908.

Yang, Z.; Surrente, A.; Galkowski, K.; Miyata, A.; Portugall, O.; Sutton, R. J.; Haghighirad, A. A.; Snaith, H. J.; Maude, D. K.; Plochocka, P.; Nicholas, R. J. "Impact of the Halide Cage on the Electronic Properties of Fully Inorganic Cesium Lead Halide Perovskites". *ACS Energy Lett.* 2017, *2*, 1621–1627.

Eperon, G. E.; Leijtens, T.; Bush, K. A.; Prasanna, R.; Green, T.; Wang, J. T.-W.; McMeekin, D. P.; Volonakis, G.; Milot, R. L.; May, R.; Palmstrom, A.; Slotcavage, D. J.; Belisle, R. A.; Patel, J. B.; Parrott, E. S.; Sutton, R. J.; Ma, W.; Moghadam, F.; Conings, B.; et al. "Perovskite-Perovskite Tandem Photovoltaics with Optimized Band Gaps". *Science (80).* 2016, *354*, 861–865.

Milot, R. L.; Sutton, R. J.; Eperon, G. E.; Haghighirad, A. A.; Martinez Hardigree, J.; Miranda, L.; Snaith, H. J.; Johnston, M. B.; Herz, L. M. "Charge-Carrier Dynamics in 2D Hybrid Metal–Halide Perovskites". *Nano Lett.* 2016, *16*, 7001–7007.

Sutton, R. J.; Eperon, G. E.; Miranda, L.; Parrott, E. S.; Kamino, B. A.; Patel, J. B.; Hörantner, M. T.; Johnston, M. B.; Haghighirad, A. A.; Moore, D. T.; Snaith, H. J. "Bandgap-Tunable Cesium Lead Halide Perovskites with High Thermal Stability for Efficient Solar Cells". *Adv. Energy Mater.* 2016, *6*, 1502458.

Li, W.; Zhang, W.; Van Reenen, S.; Sutton, R. J.; Fan, J.; Haghighirad, A. A.; Johnston, M. B.; Wang, L.; Snaith, H. J. "Enhanced UV-Light Stability of Planar Heterojunction Perovskite Solar Cells with Caesium Bromide Interface Modification". *Energy Environ. Sci.* 2016, *9*, 490–498.

Eperon, G. E.; Paternò, G. M.; Sutton, R. J.; Zampetti, A.; Haghighirad, A. A.; Cacialli, F.; Snaith, H. J. "Inorganic Caesium Lead Iodide Perovskite Solar Cells". *J. Mater. Chem. A* 2015, *3*, 19688–19695.

 

Eperon, G. E.; Habisreutinger, S. N.; Leijtens, T.; Bruijnaers, B. J.; van Franeker, J. J.; DeQuilettes, D. W.; Pathak, S.; Sutton, R. J.; Grancini, G.; Ginger, D. S.; Janssen, R. A. J.; Petrozza, A.; Snaith, H. J. "The Importance of Moisture in Hybrid Lead Halide Perovskite Thin Film Fabrication". *ACS Nano* 2015, *9*, 9380–9393.

# Conference presentations

Oral presentations entitled '*Fully-inorganic caesium lead halide perovskites*', with progressively more content, given at:

1. The first International Conference on Perovskite Solar Cells and Optoelectronics (PSCO), Lausanne, Switzerland, 2015.
2. The 12th Photovoltaic Science, Applications and Technology (PVSAT) Conference, Liverpool, United Kingdom, 2016.
3. The 8th International Conference on Advanced Materials and Nanotechnology (AMN8), Queenstown, New Zealand, 2017.

Poster presentation entitled '*Caesium Lead Halide Perovskites with High Thermal Stability for Efficient Solar Cells*', at The 8th International Conference on Hybrid and Organic Photovoltaics (HOPV16), Swansea, United Kingdom, 2016. See Figure 9-1.

Poster presentation entitled '*Vapour-Deposited Cesium Lead Iodide Perovskites: Microsecond Charge Carrier Lifetimes and Enhanced PV Performance*', at the 3rd International Conference on Perovskite Solar Cells and Optoelectronics (PSCO), Oxford, United Kingdom, 2017. See Figure 9-2.

 

# Caesium Lead Halide Perovskites with High Thermal Stability for Efficient Solar Cells

R. J. Sutton*, G. E. Eperon, L. Miranda, E. S. Parrott, B. A. Kamino, J. B. Patel, M. T. Hörantner, M. B. Johnston, A. A. Haghighirad, D. T. Moore, and H. J. Snaith.
Department of Physics, University of Oxford, Clarendon Laboratory, Oxford, OX1 3PU, U. K., and Oxford PV Ltd. Begbroke Science Park, Woodstock Road, Oxford, OX5 1PF, U. K.

## Introduction

- Methylammonium (MA) lead halide perovskites have increasingly impressive solar cell performance.[1]
- However, these materials thermally degrade at relatively low temperatures.[2]
- The inorganic caesium (Cs) analogues are more thermally stable.[3]
  - $CsPbI_3$ has an **ideal bandgap** for tandem solar cells but is unstable in the perovskite phase in ambient conditions.[4]
  - $CsPbBr_3$ is **stable** in ambient conditions but has a wider bandgap.[5]
- Here we show **increased stability** and **bandgap tunability** for a mixed-halide composition, and the **highest efficiency** inorganic perovskite **solar cells.**

Cs MA

## Perovskite Phase Transition

- $CsPbI_2Br$ transitions to the perovskite phase at a **lower temperature** than $CsPbI_3$.
- Both films stay in the perovskite phase when cooled in nitrogen. Ref. patterns from [6].

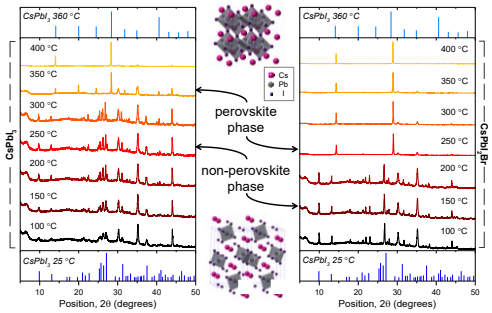


## Tuneable Bandgap with $CsPb(I_xBr_{1-x})_3$

- For mixed halide $CsPb(I_xBr_{1-x})_3$ films with varying iodide concentration 'x':
- **Bandgaps** (c) from absorbance (a) and PL (b) **change linearly** with bromide content.
- $CsPbI_2Br$ is **more stable** than $CsPbI_3$ in a slow flow of air at 50% (d).

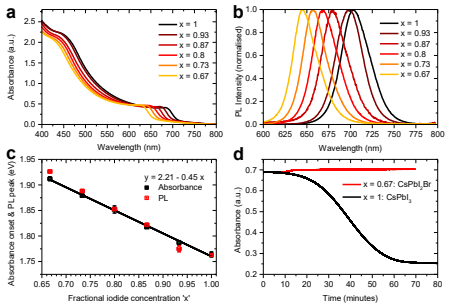


## Compositional Stability Test

- We heated $CsPbI_2Br$ and $MAPbI_2Br$ at 85 °C in 20-25% RH for 270 minutes.
- $CsPbI_2Br$:
  - Little change in absorption over time.
  - Little change in XRD before and after heating.
- $MAPbI_2Br$:
  - Decrease in absorption at band edge.
  - Decrease in perovskite peak in XRD; appearance of $PbI_{2-x}Br_x$ peak.
- Here $CsPbI_2Br$ is **compositionally stable** while $MAPbI_2Br$ thermally degrades.

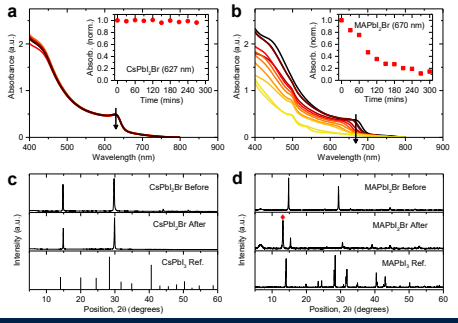


## Solar Cells with $CsPbI_2Br$ absorber

- With the structure FTO/$TiO_2$/$CsPbI_2Br$/HTM/Ag (HTM = P3HT/SWNT-PMMA)[7] we made solar cells with highest reported efficiencies for inorganic perovskite solar cells.

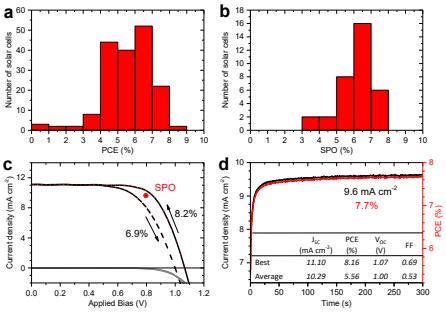


## Conclusions

- Caesium lead halide perovskites have a reversible phase transition.
- The bandgap of $CsPb(I_xBr_{1-x})_3$ depends linearly on the bromide content.
- $CsPbI_2Br$ is more **structurally stable** in air than neat iodide $CsPbI_3$.
- $CsPbI_2Br$ is more **compositionally stable** than $MAPbI_2Br$.
- With a one-step solution process we achieved the **first solar cells** with $CsPbI_2Br$, with over 8.2% current-voltage scan efficiency and 7.7% stabilised PCE.

***Email:*** rebecca.sutton@physics.ox.ac.uk ***Acknowledgements:*** The authors thank EPSRC and MESO; R. S. is a Commonwealth Scholar, funded by the UK government. ***References:*** [1] Zhou *et al.*, *Science* **345**, 542 (2014); [2] Conings *et al.*, *Adv. Energy Mater.* **5**, DOI 10.1002/aenm.201500477 (2015); [3] Sutton *et al.*, *Adv. Energy Mater.* **6**, (2016) DOI 10.1002/aenm.201502458; [4] Eperon, Sutton, *et al.*, *J. Mater. Chem. A* **3**, 19688 (2015); [5] Kulbak *et al.*, *J. Phys. Chem. Lett.* **6**, 2452 (2015). [6] Trots and Myagkota, *J. Phys. Chem. Solids* **69**, 2520 (2008). [7] Habisreutinger *et al.*, *Nano Lett.*, **14**, 5561 (2014).

**Figure 9-1. Poster presented at HOPV16.**

# Vapour-Deposited Cesium Lead Iodide Perovskites: Microsecond Charge Carrier Lifetimes and Enhanced PV Performance

Eline M. Hutter,† Rebecca J. Sutton,*‡ Sanjana Chandrashekar,† Mojtaba Abdi-Jalebi,§ Samuel D. Stranks,§ Henry J. Snaith,‡ and Tom J. Savenije*†

†Department of Chemical Engineering, Delft University of Technology, van der Maasweg 9, 2629 HZ Delft, The Netherlands
‡Clarendon Laboratory, University of Oxford, Parks Road, Oxford OX1 3PU, United Kingdom
§Cavendish Laboratory, University of Cambridge, JJ Thomson Avenue, Cambridge CB3 0HE, United Kingdom

## Introduction

- Metal halide perovskites are highly promising materials for photovoltaics.[1]
- But does the cation need to be organic for high optoelectronic properties?
- Here we investigate the optoelectronic properties of fully inorganic perovskite $CsPbI_3$ made by either vapour-deposition or spin-coating
- We use the time-resolved microwave conductivity technique to determine charge carrier mobilities and charge carrier lifetimes
- We then make solar cell devices with films prepared using the two deposition methods

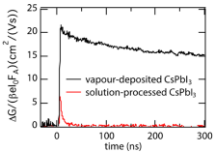


## Absorption and X-ray Diffraction

- Our vapour-deposited films are made by alternating deposition of very thin layers of CsI (~2 nm) and $PbI_2$ (~2.5 nm) to build up a film of ~260 nm.[2]
- This process forms yellow-phase $CsPbI_3$, which we anneal briefly at 310 °C to convert to black-phase $CsPbI_3$.


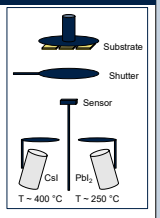


- We compare these vapour-deposited films with spin-coated films prepared from a 0.8 M solution of stoichiometric precursors in DMF:DMSO 0.65:0.35.

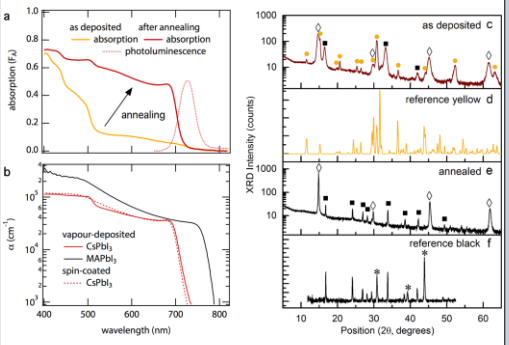


- The films' absorption, PL, and XRD shown above match well to $CsPbI_3$ films in the literature.[3,4] The background-subtracted XRD (Co Kα radiation, λ = 1.79 Å) was measured at room temperature using an airtight sample holder. ■ denotes the black phase $CsPbI_3$, ◊ denotes $PbI_2$, and * denotes $SnO_2$.
- AFM measurements show micron-sized grains for both deposition methods.

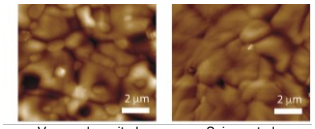


## Time-Resolved Microwave Conductivity

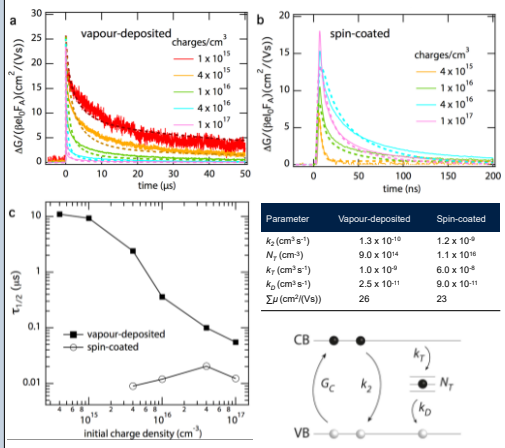


| Parameter | Vapour-deposited | Spin-coated |
|---|---|---|
| $k_2$ ($cm^3 s^{-1}$) | $1.3 \times 10^{-10}$ | $1.2 \times 10^{-9}$ |
| $N_T$ ($cm^{-3}$) | $9.0 \times 10^{14}$ | $1.1 \times 10^{16}$ |
| $k_T$ ($cm^3 s^{-1}$) | $1.0 \times 10^{-9}$ | $6.0 \times 10^{-8}$ |
| $k_D$ ($cm^3 s^{-1}$) | $2.5 \times 10^{-11}$ | $9.0 \times 10^{-11}$ |
| $\sum \mu$ ($cm^2/(Vs)$) | 26 | 23 |




We use the time-resolved microwave conductivity technique to determine the following optoelectronic parameters for $CsPbI_3$ thin films prepared via different routes: rate constants for second-order recombination ($k_2$), trap filling ($k_T$) and trap depopulation ($k_D$), the overall trap density ($N_T$) and mobilities for electrons ($\mu_e$) and holes ($\mu_h$).

## Photovoltaic Devices

- We made solar cells with the structure FTO/$SnO_2$/$CsPbI_3$/HTM/Ag (HTM = P3HT/SWNT-PMMA).[5] We measured them in air without encapsulation.

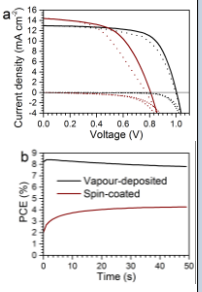


| Parameter | Vapour-deposited Best Cell | Vapour-deposited Mean ± std. dev. | Spin-coated Best Cell | Spin-coated Mean ± std. dev. |
|---|---|---|---|---|
| $J_{sc}$ (mA $cm^{-2}$) | 13.0 | 12.6 ± 1.2 | 14.4 | 11.6 ± 2.6 |
| $V_{OC}$ (V) | 1.00 | 0.95 ± 0.06 | 0.80 | 0.74 ± 0.13 |
| FF | 0.68 | 0.61 ± 0.05 | 0.56 | 0.51 ± 0.07 |
| PCE (%) | 8.80 | 7.27 ± 0.96 | 6.40 | 4.4 ± 1.5 |
| SPO (%) | 7.8 | 6.0 ± 1.3 | 4.3 | 2.5 ± 1.1 |
| SPO Ratio | 0.89 | 0.82 ± 0.09 | 0.67 | 0.56 ± 0.14 |

## Conclusions

- Caesium lead halide perovskites can have optoelectronic properties comparable to hybrid organic-inorganic lead halide perovskites.
- We find mobilities ~25 $cm^2/(V\,s)$ for both vapour-deposited and spin-coated $CsPbI_3$ films. Furthermore, in vapour-deposited $CsPbI_3$, we observe lifetimes on the order of tens of microseconds – exceptionally long for a metal halide perovskite thin film.
- With the highly-controlled vapour-deposition process we obtain solar cells with $CsPbI_3$ with 8.8% current-voltage scan efficiency and nearly 8% stabilised PCE.

*Email: rebecca.sutton@physics.ox.ac.uk or T.J.Savenije@tudelft.nl **Acknowledgements:** This work was supported by The Netherlands Organization for Scientific Research (NOW, 712.014.007), the EU's Seventh Framework Programme (FP7/2007-2013, PIOF-GA-2013-622630), Nava Technology Limited and Nyak Technology Limited. R.S is a Commonwealth Scholar, funded by the U.K. Government.
**References:** [1] Zhou *et al.*, *Science* **345**, 542 (2014); [2] Hutter *et al.*, *Adv. Energy Mater.* **7**, 1602349 (2017) [3] Eperon, Sutton, *et al.*, *J. Mater. Chem. A* **3**, 19688 (2015); [4] Trots and Myagkota, *J. Phys. Chem. Solids* **69**, 2520–2526 (2008). [5] Habisreutinger *et al.*, *Nano Lett.*, **14**, 5561 (2014).

**Figure 9-2. Poster presented at PSCO 2017.**